HIGH TEMPERATURE TRIBOLOGY PERFORMANCE OF NICKEL ALLOYS UNDER HELIUM ATMOSPHERE

A Dissertation

by

MD SAIFUR RAHMAN

Submitted to the Office of Graduate and Professional Studies of
Texas A&M University
in partial fulfillment of the requirements for the degree of

DOCTOR OF PHILOSOPHY

Chair of Committee,	Andreas A. Polycarpou
Committee Members,	Cynthia Hipwell
	Homero Castaneda-Lopez
	Adolfo Delgado
Head of Department,	Andreas A. Polycarpou

May 2021

Major Subject: Mechanical Engineering

ABSTRACT

Currently the health and well-being of the global society are affected by energy source efficiency, reliability and enviromental impact. Nuclear power is one of the realiable energy resources with low greenhouse gas emissions per unit energy generated. Findings from the current research directly result in more reliable and efficient nuclear power plants. The objective of this research is to systematically evaluate the tribological response of 800HT and 617 alloys at relevant reactor operating temperatures (700-950 $^{\circ}$C) and in the presence of helium (He) coolant. This research aims to address the need for a clear and inclusive understanding of the tribological performance of Nickel (Ni) based alloys in high temperature (HT) gas cooled reactors HTGR/VHTR operational environment that will clarify the necessity of further enhancement in HT durability and environmental compatibility of tribological components operating in HTGR-He coolant. The fundamental knowledge in high temperature tribology, especially in controlled gas atmosphere is limited, mainly due to complexity of experimental tests and analytical/numerical methods. The present work is pushing the boundaries of in-situ multiscale (nano/micro/macro) characterization of tribological materials in air/non-air ambient conditions at very high temperatures through novel experimental setups (e.g., very high temperature tribometer and very high temperature nano-indenter, under controlled Helium conditions). Also, comprehensive surface layer composition studies using advanced electron microscopy and other material characterization techniques, provide insght into prevention and failure mechanisms. Using a custom-built high temperature tribometer, helium cooled reactor environment was simulated at room and 950 ^{o}C temperatures. Microscopy and chemical analyses are carried out to explain the tribological performance of the alloys. At elevated temperatures, both alloys show higher friction in helium, compared to air environment. Both alloys exhibit high wear resistance in all experimental conditions, except at

high temperature helium environment. The formation of glazed and mechanically mixed layers of oxides were found to be important causes for the lower friction and wear in high temperature air atmosphere. The in-depth chemical analysis of the oxide layer using techniques like EDS, XRD, RAMAN and SIMS were performed to link the tribochemical aspects to the evolution of mechanical properties under contact. This work provides new knowledge in the form of scientific papers, technical reports, and presentations that benefits a wide range of communities, and individuals. Most importantly this work is showcasing the important tribological issues encountered in suture state-of-the-art nuclear reactors.

ACKNOWLEDGEMENT

First and foremost, I would like to convey my sincere gratitude to my advisor Dr. Andreas A. Polycarpou for his support, patience, motivation, and above all his encouragement. I am also grateful to him for his valuable suggestions and guidance not only on my research but also on personal life by sharing his personal experiences. I could not have imagined having a better advisor and mentor in my life. Without his unwavering guidance and persistent help this dissertation would not have been possible. I am immensely grateful to my collaborator, my mentor and the person who motivated me to pursue doctoral degree at Texas A& University, Dr. Ali Beheshti from George Mason University. I am grateful for his guidance, motivation, and a whole lot of time that he spent discussing research and personal life with me.

I am grateful to my committee members: Dr. Cynthia Hipwell, Dr. Adolfo Delgado and Dr. Homero Castaneda-Lopez for their valuable suggestions and insightful comments.

All the research group members in the Microtribodynamics laboratory have been of great help with their discussions and suggestions. I would like to especially thank Pixiang Lan, Youfeng Zhang, Reza Gheisari and Mohammad Humood for their guidance in the beginning of my research. I would be forever indebted to Jevon Phandi for his help, especially in other aspects of my graduate life. I would also like to thank all other individuals who in different ways have contributed to the realization of this thesis.

I would like to acknowledge the support of US DOE Office of Nuclear Energy's Nuclear Energy University Program (NEUP) (Contract No. DE- NE0008549) for providing the financial support for this research. The materials, Inconel 617 and alloy 800HT were provided by Idaho National Laboratory (INL) and Oak Ridge National Laboratory (ORNL), respectively. I would like to thank

Dr. Richard Wright of INL, Dr. Sam Sham of ANL and Dr. Yanli Wang of ORNL useful data as well as helpful discussions. I am thankful to Dr. S. Verkhoturov of Texas A&M University for the TOF-SIMS data analysis and thoughtful discussions. I would like to thank Materials Characterization Facility (MCF) at Texas A&M University for the access to SEM, EDS, SIMS, Raman instruments. I would like to extend my sincere thanks to my collaborator: Dr. Kyriaki Polychronopoulou for helping me to analyze the XRD and Raman data. I am also grateful to Jie Ding and Dr. Xinghang Zhang from Purdue University for the Ni/Cr coating preparation and the TEM in Figure 76. I am immensely grateful to my collaborator, my mentor, the person who Dr. Ali Beheshti from George Mason University for his guidance, motivation, and a whole lot of time he spent discussing with me.

I cannot thank enough my wonderful parents, Din Mohammad and Sufia Begum, for their faith in me and supporting me to follow the path I wanted. I also want to mention my elder brother Shafiqur Rahman, because of whom I started my career as Mechanical Engineer and my elder sister, Delwara Begum, who encouraged me to pursue higher studies in US university. Also, I thank my in-laws for providing me unending encouragement. I am and will always be grateful to my wife, Farjana Yeasmin and my son, Ateeb Saif, for being patient, supportive and enduring all the troubles of graduate student life.

CONTRIBUTORS AND FUNDING SOURCES

Contributors

This work was supervised by a dissertation committee consisting of Professor Andreas Polycarpou, Cynthia Hipwell, and Adolfo Delgado of the Department of Mechanical Engineering and Professor Homero Castaneda-Lopez of the Department of Material Science & Engineering.

The analysis of Raman and XRD data in Chapter V and VI was supported by Professor Dr. Kyriaki Polychronopoulou, a visiting professor of the Department of Mechanical Engineering. The TOF-SIMS analysis in Chapter V and VI was conducted by Dr. S. Verkhoturov of the Department of Chemistry.

All other work conducted for the dissertation was completed by the student independently.

Funding Sources

This work was made possible in part by US DOE Office of Nuclear Energy's Nuclear Energy University Program (NEUP) under Grant Number DE- NE0008549. Its contents are solely the responsibility of the authors and do not necessarily represent the official views of the US DOE Office of Nuclear Energy.

TABLE OF CONTENTS

LIST OF FIGURES

LIST OF TABLES

CHAPTER I
INTRODUCTION

The cost of energy generated from fossil fuels and their detrimental environmental effects has mandated major steps to escalate energy production from alternate sources more extensively and efficiently. One such energy resource is nuclear power with low greenhouse gas emissions per unit energy generated. Operating at high temperature (HT) is critical for nuclear reactors as it results in substantial thermal efficiency improvement. Therefore, in view of design demands, materials that can withstand HTs and harsh environment are deemed necessary for reliable and effective nuclear reactor operation. Alloy 800HT and Inconel 617 are principal candidates in high temperature gas cooled reactors (HTGR) and very high temperature gas cooled reactors (VHTR) with outlet temperatures of 700-950°C, which should be licensed for a 60-year life [5–7]. Of course, not all of the designed components can be targeted for such a long period of time; nonetheless, time intervals between two replacements should be sufficiently long and more importantly lifetime should be estimated as accurate as possible. Thus, there is no surprise that significant efforts have been made to characterize and predict the behaviors of these alloys. The literature is relatively abundant with works pertaining to mechanical behavior studies (mostly fatigue, fracture, and creep) [8–12] as well as oxidation and corrosion [3,6,7,13–17], for 800HT, Inconel 617 and other nickel alloys. Yet, before this study and similar projects funded by the Department of Energy in 2016, tribological studies of alloy 800HT and Inconel 617 interfaces were limited [18,19].

Sliding motion and its consequent friction and wear between metallic components at elevated temperatures can lead to severe surface damage and are important considerations for the effective performance of moving parts in nuclear reactors and power generation components. The VHTRs

uses Helium (He) as coolant as shown in the schematic diagram in Fig. 1a. HT tribology is challenging on its own, and in the case of nuclear reactor conditions, the complexity is further compounded by the fact that the interface between metallic surfaces at HT remains non-lubricated with low water or oxygen partial pressure in the presence of Helium (He) and other minor gaseous ingredients [20]. Tribo-pairs in HTGR mainly include isolation valves as shown in Fig. 1b, valve seats, valve shafts, He circulator shaft and bearings, and control rods [21]. For these rubbing surfaces, accelerated friction and surface damage (mostly wear and small motion fretting wear) can have detrimental effects on component performance and life. Besides, owing to the HT inert operating conditions along with extended dwell times, static/kinetic friction transition as well as self-welding are major concerns in moving components. During steady-state operation in HTGR/VHTR, the He coolant contains low levels of impurities including H_2, O_2, H_2O, CH_4, CO, CO_2, and N_2. Due to the presence of these impurities, the structural alloys used in the reactors can experience significant long-term corrosion involving oxidation, carburization or decarburization depending on temperature, oxygen partial pressure, carbon activity, and alloy composition at elevated temperatures.

The objective of this research is to systematically evaluate the tribological response of 800HT and 617 alloys at relevant reactor operating temperatures (700-950 °C) and in the presence of He coolant. This research aims to address the need for a clear and inclusive understanding of the tribological performance of Ni based alloys in HT gas cooled reactors HTGR/VHTR operational environment as well as a further enhancement in HT durability and environmental compatibility of tribological components operating in HT He-coolant. This dissertation summarizes the work carried out investigating the tribological behavior of Ni-based alloy, Inconel 617 and 800HT in simulated HTGR/VHTR atmosphere of He, the nano/micro and macro tribological experiments in

a novel HT tribology setup, the microscopy characterization and development of wear protective coatings, and extracting mechanical properties at HT.

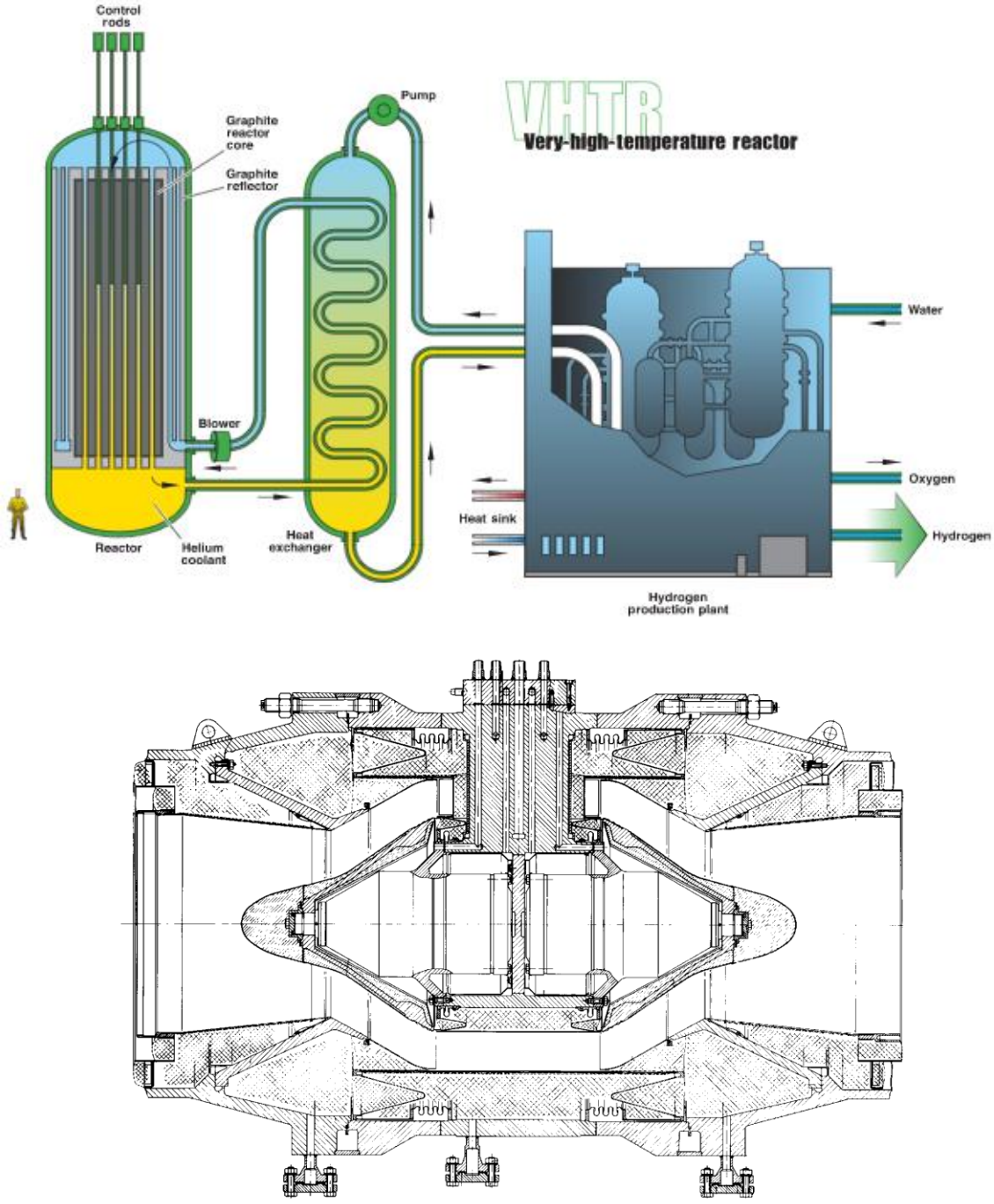

Fig. 1 Schematic diagram of (a) VHTR [1] (b) DN 700 Isolation valve used in VHTR [2]

1.1. Research Objective and Outline

The objective of this research project is to systematically evaluate the tribological response of 800HT and 617 alloys at relevant reactor operating temperatures (700-950^{o}C) and in the presence of helium (He) coolant. This research aims to address the need for a clear and inclusive understanding of the tribological performance of Ni based alloys in high temperature (HT) gas cooled reactors HTGR/VHTR operational environment as well as a further enhancement in HT durability and environmental compatibility of tribological components operating in HTGR-He coolant.

Two alloy blocks of Alloy 800HT and Inconel 617 were provided by Idaho National laboratory (INL) and Oak Ridge National Laboratory (ORNL) to perform the experimental studies. This work describes the contact response of tribo-pairs including friction, wear, self-welding, oxidation, chemical and nanomechanical property measurements of the alloys surface at HT (up to 950^{o}C) in simulated HTGR/VHTR He (and also in air, for comparison). In addition, experimental and numerical simulations for the micro/nano scale properties characterization of alloy surfaces and their oxide layers under HT, are presented through nano/micro indentation and scratch studies. The research project also investigated different solutions such as optimizing the operating conditions, and surface modifications, such as surface treatments, and HT super hard coatings to mitigate tribological problems under HTGR/VHTR conditions. The Flowchart of this research is showed in Fig. 2 and it shows the three major parts of these research in three boxes on the left side: Sample conditioning as Aging, HT tribology experiments and Nanomechanical property characterization. On the right three boxes in the flow chart, it explains how the conditions were created, what was the objective, and at last the reasoning behind the results by answering the question by why.

Detailed description of the experiments, materials development and modification and simulations, along with their results and discussion are presented in the following chapters.

HT aging and testing process (Chapter 2): The effect of long exposure to HT was studied by aging the samples inside a furnace. The as-received materials were exposed to HT condition of HTGR/VHTR to investigate the effect of oxidation on the surfaces of the samples. The HTGR/VHTR He condition was simulated in a vacuum furnace to prepare the aged samples to be used in the tribological experiments.

HT unidirectional and oscillatory tribology experiments (Chapter 3-4): The response time as well as the capability to control the stroke of reactor's elements such as control rods/bearings and valves is highly critical for safety and reliable performance of nuclear reactors. This is mainly controlled by the state of friction between the component's interfaces. Hence, the values of kinetic and static coefficient of friction (COF) and the transitional COF from static to kinetic sliding are of a great concern for the tribo-pairs in contact. Unidirectional and oscillatory (fretting) macro tribological experiments were carried out in a custom made high-temperature tribometer (HTT) which simulates the reactors operating conditions. Tests were carried out for temperatures up to 950 °C for different normal loads and sliding velocities to study static/kinetic friction as well as wear volume.

Tribo-Chemical analysis (Chapter 5-6): To understand the underlying mechanisms behind the friction and wear behaviors of the alloys in He HT, it is essential to investigate the complex tribo-chemical activity at the contact. The as-received, aged and tested samples were investigated thoroughly using techniques such as, cross section SEM/EDS, XRD, Raman, SIMS and nanoindentation to analyze the surface topography, tribo-chemical changes and their effects on the tribological behavior of the alloys.

HT nano/micro indentation and scratch (Chapter 7-8): The nano-mechanical properties of the bulk and oxide surfaces of aged samples were investigated using HT nano/micro indentation and scratch techniques.

Tribological response enhancements (Chapter 9): To improve the friction and wear properties of alloy 800HT and Inconel 617, multiple combinations of Ni/Cr multilayer coatings were developed and investigated, where the hardness values of the multilayers were tailored effectively by varying the individual layer thickness. Several other alternatives to coatings for alloy 800HT and Inconel 617 were searched in the literature and Laser Shock Peening (LSP) was selected as a potential promising remedy. Nano/macro-tribology investigations were performed on Ni/Cr multilayer coatings using both nanoscratch and macro tribology experiments at very HTs. In addition, LSPed alloys were tested at HT using the macro tribometer to investigate the tribological benefits of the treatment process.

High Temperature Tribology of Nickel Alloys

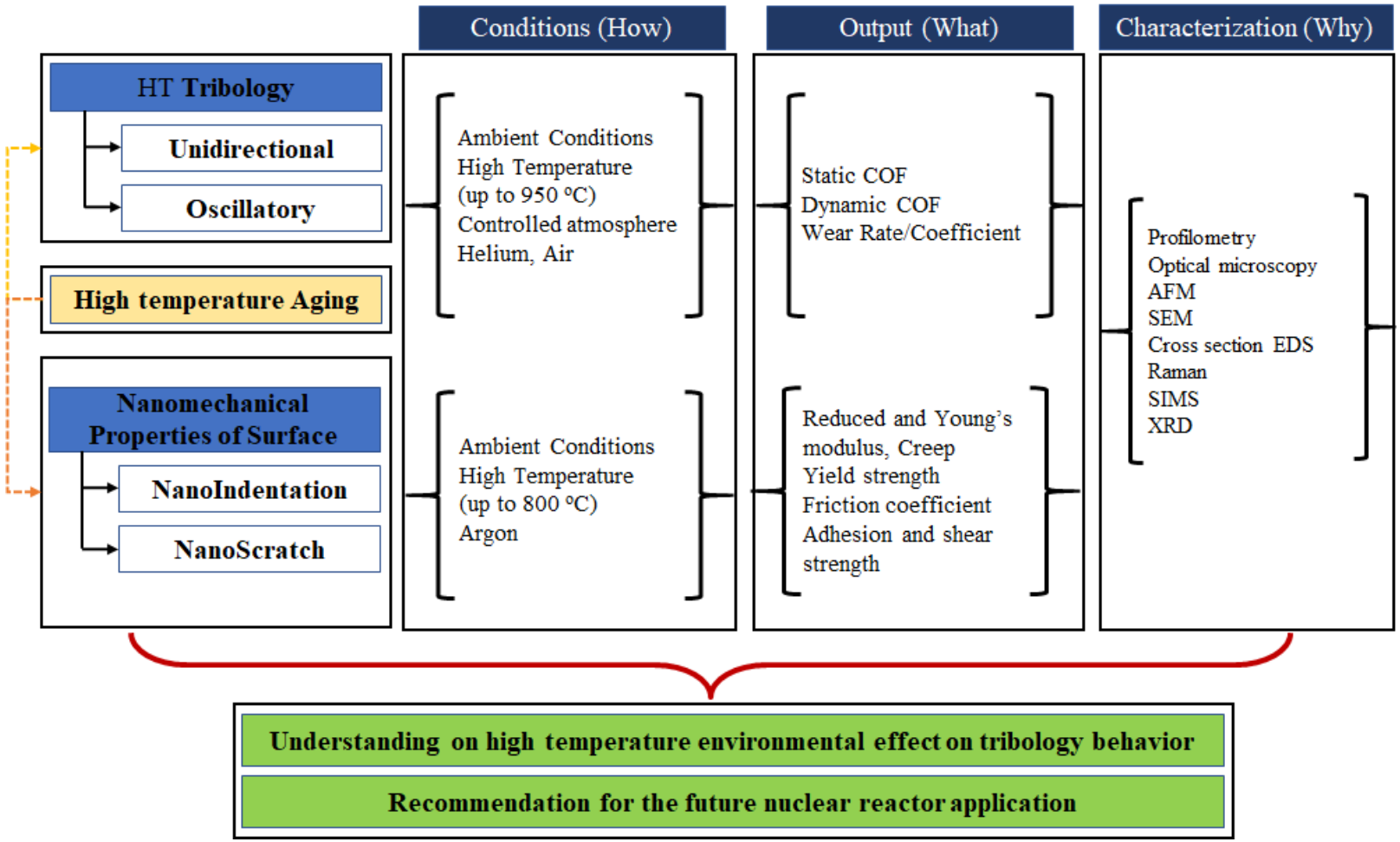

Fig. 2 Research outline

CHAPTER II
MATERIALS, AGING PROCESS, TRIBOLOGY TESTING AND ANALYSIS [1]

2.1. Materials and Samples

The materials used in this study, Inconel 617 and alloy 800HT were received from Idaho National Laboratory (INL) and Oak Ridge National Laboratory, respectively. The chemical composition of the as-received alloys, given by the manufacturer, are shown in Table 1. Alloy 617 is strengthened by solid solution hardening provided by chromium, cobalt, and molybdenum as well as by intra and inter-granular carbide precipitates. The high-temperature oxidation resistance of the alloy is due to the high nickel and chromium content. Alloy 800HT was solution annealed at 1150^{o}C and has a yield strength of 90 MPa at 750 °C, while Inconel 617 has a yield strength of 189 MPa at 800^{o}C.

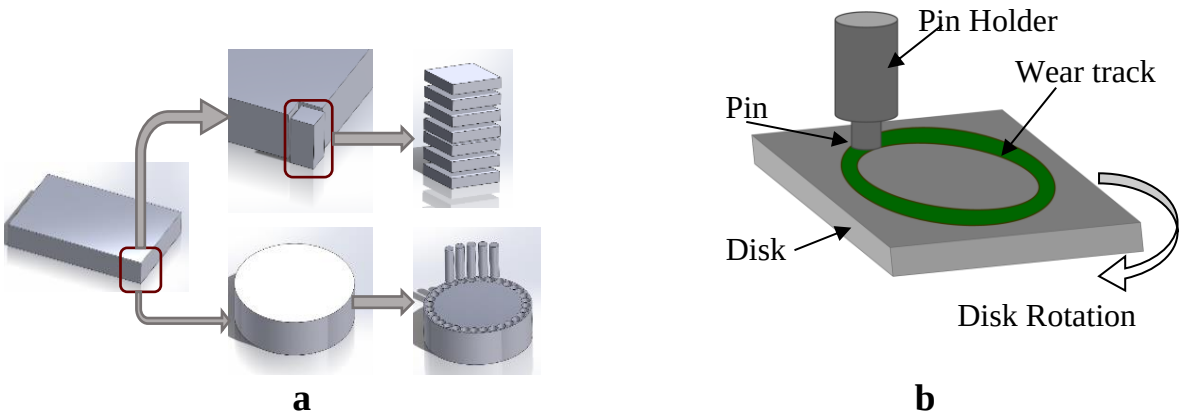

Fig. 3. (a) Sample preparation process, (b) Schematic of flat pin-on disk experimental configuration.

[1] Reprinted with permission from "Elevated temperature tribology of Ni alloys under helium environment for nuclear reactor applications." by Rahman MS, Ding J, Beheshti A, Zhang X, Polycarpou AA. Tribol Int 2018;123:372–84. Copyright 2018 by Elsevier Ltd.

Fig. 3 shows the sample preparation and testing schematic of the pin-on-disk configuration. The material was received in the form of a rectangular bar and then machined to desired specifications. The disk samples (25.4mm x 25.4mm x 3.8mm) and flat cylindrical pins (6.3mm diameter and 19mm length) were machined using wire EDM (Electric Discharge Machining) process from the bulk material. The disk and pin contact surfaces were then polished to reach a surface roughness of approximately 0.3 µm (root-mean-square) for the unidirectional tribological experiments. For the nanoindentation experiments at HT, the surface was polished with 400, 600 and 800 grit SiC paper and then by mechanical polishing with 3µm diamond grits to have 30-40nm rms values.

Fig. 4a shows the microstructure of the as-received Inconel 617 disk where it is evident that the grain size is not homogenous, and the inhomogeneous distribution of carbide is present. The average grain size is around 30-40 µm, which agrees with the findings of Ref. [7]. The microstructure of the as-received alloy 800HT, etched by 1:3 solution of nitric acid and hydrochloric acid is shown in Fig. 4b. The grain size is generally not homogenous, where twinning is observed.

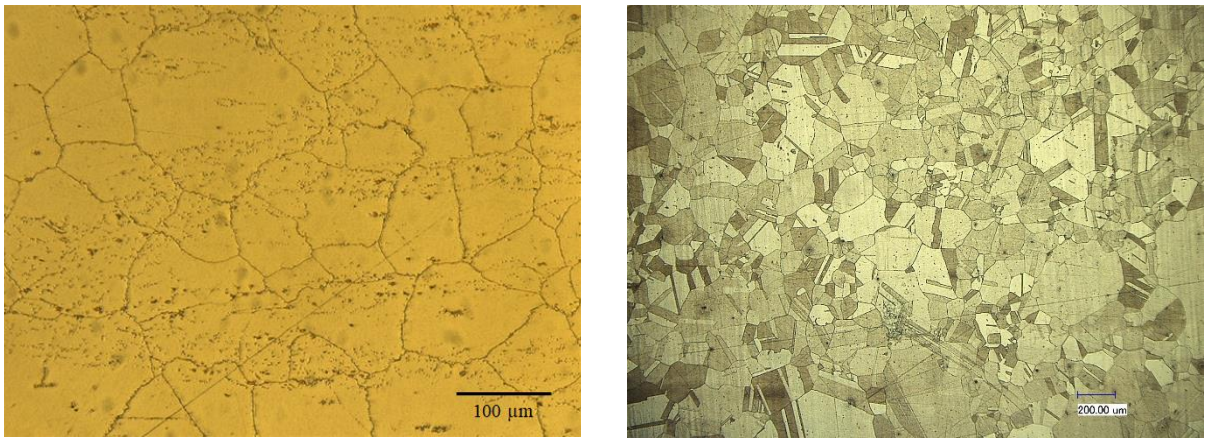

Fig. 4. Optical micrograph illustrating carbide distribution and grain size in as-received (a) Inconel 617, and (b) Alloy 800HT.

Table 1
Chemical composition of Inconel 617 and 800HT (in wt%)

Element	C	Mn	Fe	S	Si	Cu	Ni	Cr	Al	Ti	Co	Mo	P	B
Inc 617	0.08	0.23	1.46	0.001	0.2	0.02	53.27	22.02	1.10	0.32	11.91	9.38	0.005	0.002
800HT	0.061	1.27	46.24	0.001	0.42	0.2	30.65	19.7	0.56	0.54	0.1	-	0.024	-

2.2. Helium Coolant

All high-temperature reactor systems operated to date using He coolant, have had extensive gas cleanup systems to keep the total impurity level in He typically below 10 ppm [6]. To create similar VHTR environment, three impurity combinations of He have been used in this study: 99.99% (*He3*), 99.999% (*He2*), and 99.9999% (*He1*) purity. He gas was injected during the He environment wear experiments as well as aging in HT furnace. The composition of He gas used in the current project and the impurity levels reported for the steady-state operation for several of the VHTR are given in Table 2 [6,7].

Table 2
Composition of impurities in Helium (in ppm by volume) [2,3]

	He	O_2	H_2O	CH_4	CO	CO_2	H_2	N_2
Present research *He1*	Bal	0.5	0.2	0.1	0.1	0.1	-	0.5
Present research *He2*	Bal.	1	1	0.5	1	1	-	5
Present research *He3*	Bal	-	-	10	-	20	200	-
Dragon	Bal.	0.1	0.1	0.1	0.05	0.02	0.1	0.05
Peach Bottom	Bal.	-	0.5	1	0.5	<0.05	10	0.5
Fort St. Vrain	Bal.	-	1	0.1	3	1	7	-
AVR	Bal.	-	0.15	1	45	0.25	9	22
THTR	Bal.	-	<0.01	0.1	0.4	0.2	0.8	0.1

During the initial comparative study, no significant difference was observed on the tribological behavior for the alloys in these three categories of He. So, the detailed study on the alloys has been performed using *He2*. Hereafter in this document anywhere mentioning He will refer to *He2* unless mentioned otherwise.

2.3. Aging Process

An atmosphere-controlled furnace, GFC1400 was used for the aging of the samples in air and He environments. The furnace is capable of reaching a maximum temperature of 1400 °C. Before the He aging experiments, the furnace was purged with He after achieving -14.4 psi vacuum pressure in the chamber and the process was repeated three times. Then, a constant He flow rate was maintained at 5 scfh. The furnace is heated up to the test temperature in 2 hours while during cool down (at the completion of the experiments) the cooling rate is maintained at 1 ^{o}C/min or lower. Digital weighing balance (Satorius-CPA225D) of 0.01 mg accuracy was used for the weight measurements for all the samples before and after the experiments to measure the oxidation and wear rate. In this study, to simulate VHTR environment, 99.999% pure He is used in furnace aging. The supplied He contains very small amounts of impurities in (ppm): O_2(1), H_2O(1), CO_2(1), CH_4(0.5), CO(1), N_2(5), which is similar to VHTR operational environments (refer to Table 2). The purging protocol ensured minimum (~35ppm) presence of oxygen content in the chamber. The oxidation rate is calculated as weight gain per unit surface area (g/m^2), using the following equation:

$$\Delta W/S = (W - W_o)/S_o \quad (2.1)$$

where *Wo* is the weight before oxidation, *W* is the weight after oxidation, and *So* is the surface area before oxidation.

As shown in Fig. 5a, for Inconel 617, the weight gain follows a parabolic curve as a function of time at 950 °C as reported in the literature [15] (note that it is linear with respect to square root of time). Oxidation rate is almost similar to what was presented by Kim et al. at 1000 ºC in two different types of He environments [3]. In the current study, higher initial oxidation weight gain is indicated by the short time aging of 1 hr and 10 hrs. The oxidation rate is higher than what the trend line indicated. The main reason can be the presence of oxygen as impurity in the current He environment, whereas none of the He environment had O_2 content in the work of Kim et al. at. Although O_2 and H_2O contents are significantly different in air and He environments, the weight gain behavior in air follows the same trend line as He.

As shown in Fig. 5b, the weight gain of alloy 800HT at 750 °C in air and He also followed a parabolic trend over time for both He and air environments. Unlike Inconel 617, the rate of weight gain in air is higher than in He for alloy 800HT. The weight change curves follow a parabolic law of oxidation governed by a relationship of the type $\Delta W/S = k^{1/2}t^{1/2}$ where k is the parabolic rate constant, and *t* is the oxidation time in hours. The parabolic rate constants were calculated from the fitting oxidation data sets to straight lines. The parabolic rate constants for alloy 800HT in air and He conditions are 1.23×10^{-12} and 3.87×10^{-13} $g^2\,cm^{-4}\,s^{-1}$, respectively. For Inconel 617, the rates are 2.27×10^{-12} and 2.31×10^{-12} $g^2\,cm^{-4}\,s^{-1}$ in He and air respectively for aging in 950 °C.

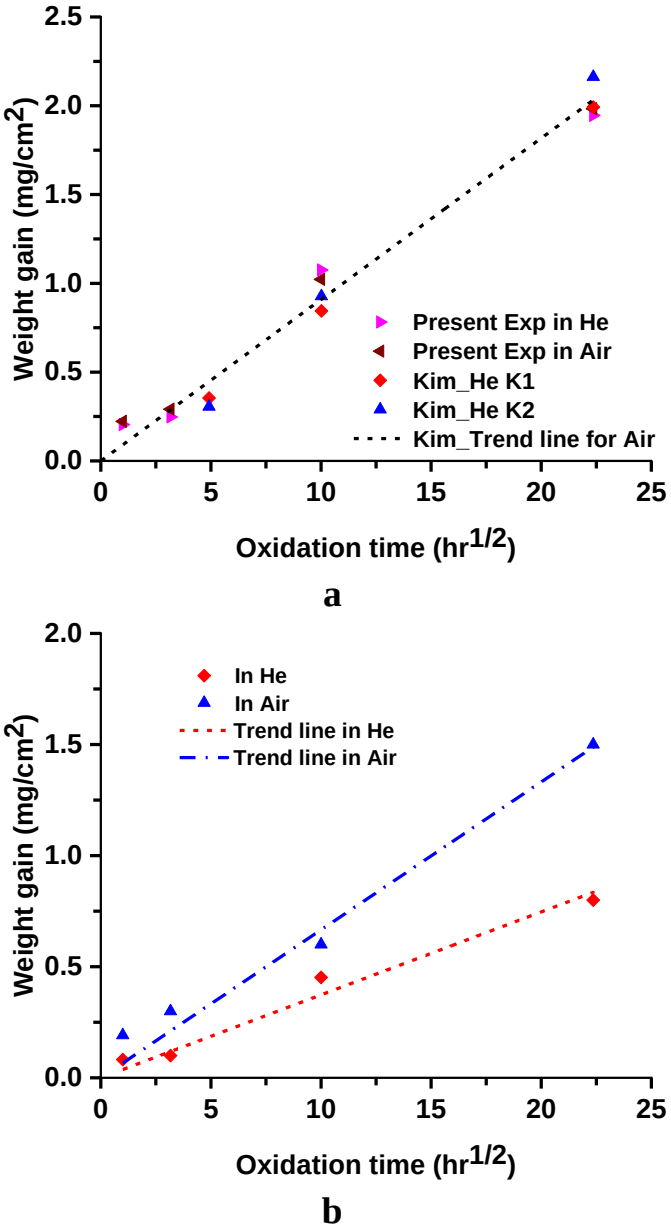

Fig. 5. (a) Weight gain with oxidation time for Inconel 617 in He at 950 °C and comparison with oxidation behavior at 1000 °C by Kim et. al. [3] with impurities of H_2, H_2O, CO, C_2O, CH_4 (He K1) and H_2O, CO, C_2O (He K2); (b) Weight gain in He and air over oxidation time of Alloy 800HT at 750 °C.

2.4. High Temperature Tribometer (for Helium)

A custom-built high temperature tribometer (HTT) is modified to perform unidirectional HT tribological experiments for alloy 800HT and alloy 617 in controlled environments (e.g., He with impurities). The HTT mimics the complex environmental conditions of nuclear reactors, and is

capable of exploring the tribological characteristics of the alloys in HT gas cooled HTGR/VHTR operational environments.

The HTT is a specialized tribometer (shown in Fig. 6a) with pin-on-disk (ball-on-disk, flat pin-on-disk, and cylinder pin-on-disk) configurations that can perform wear and friction experiments for samples with a diameter up to 95 mm. The tribometer has the capability of unidirectional and oscillatory motions: rotational speeds up to 1000 rpm and oscillation frequencies up to 5 Hertz. The force transducer records the in situ normal (up to 45 N) and friction forces and uses them to calculate the in-situ COF. It has an enclosed chamber (Fig. 6b), which enables the control of the test atmosphere. Using a vacuum pump and ports, the chamber can be evacuated and then gas (e.g., He with different impurities) can be introduced. It is equipped with a "Transparent Furnace" based on the invention of Thomas Reed in 1970, which uses the infrared radiation to heat up the sample by reflecting substantially all infrared radiation on a thin gold coated quartz tube (Fig. 6c). Yet, sufficient visible radiation is transmitted so that the inside of the furnace can be viewed from the outside [22].

Fig. 6c shows a schematic view of the furnace with section views taken parallel and vertical to the rotational axis of the furnace. The outermost quartz muffle is a transparent quartz enclosure coated on the inner side with a thin gold film. The gold film enables the attainment of high operating temperatures as it has high reflectance for infrared radiation, while being thin allows visible light transmittance. The transparent furnace has the capability of reaching 1000 ^{o}C in reasonably short period of time with efficiency, comparable to the conventional infrared heated muffle furnace encased by conventional packed insulation, with the additional advantage of visibility. Beside the outermost quartz tube mentioned above, the furnace consists of an innermost clear quartz muffle in which the tribo-pair is inserted. These two quartz tubes are concentric creating a 4 mm annular

space in-between, called the dead air space. The heating elements are located in the annular space wrapped around five alumina tubes in helical formation. Two ends of the heating wire are connected to the power source, well-protected from the metal body by alumina tubes. The heating wires are passed through slots on the alumina tubes to avoid reduction in the resistance of the heating element and effectiveness of the furnace due to heating wires connecting each other during operation. A ferritic iron-chromium-aluminum alloy (Fe-Cr-Al alloy) is used as the heating wire which is an advanced powder metallurgical, dispersion strengthened alloy with melting temperature of 1500 °C. Although originally 1 mm diameter heating wire was used in the furnace, as we seek to reach temperatures as high as 950 °C, especially in the presence of He coolant, the heating wire diameter was increased to 1.2 mm. A third quartz clear tube is placed in between the heating elements and the outer gold-coated quartz tube to avoid contact and damage to the gold coating.

The disk holder is placed on the plate supported by four pins connected to the rotating shaft of the servo motor which is surrounded by a jacket of cooling fluid to ensure safe operation of the servo motor at HTs. The shaft near the furnace also has fins to increase heat transfer during rotation. The whole setup of the disk holder and motor (lower part) has vertical movement capability using another servo motor to move the sample in and out of the furnace. The pin is connected to the upper unit consisting of a pin holder made of Inconel 625, which is connected to a two-axis force transducer. The entire upper setup is mounted on a jack screw drive system and a servo motor to control the normal load and movement into and out of the furnace. Additionally, to have a precision control of the normal load, an electromagnetic actuator is placed in between the force transducer and the servo system bringing the resolution control of the normal load to 0.05 N. The force transducer is also jacketed by a cooling fluid to ensure correct measurement of forces at HTs. It is

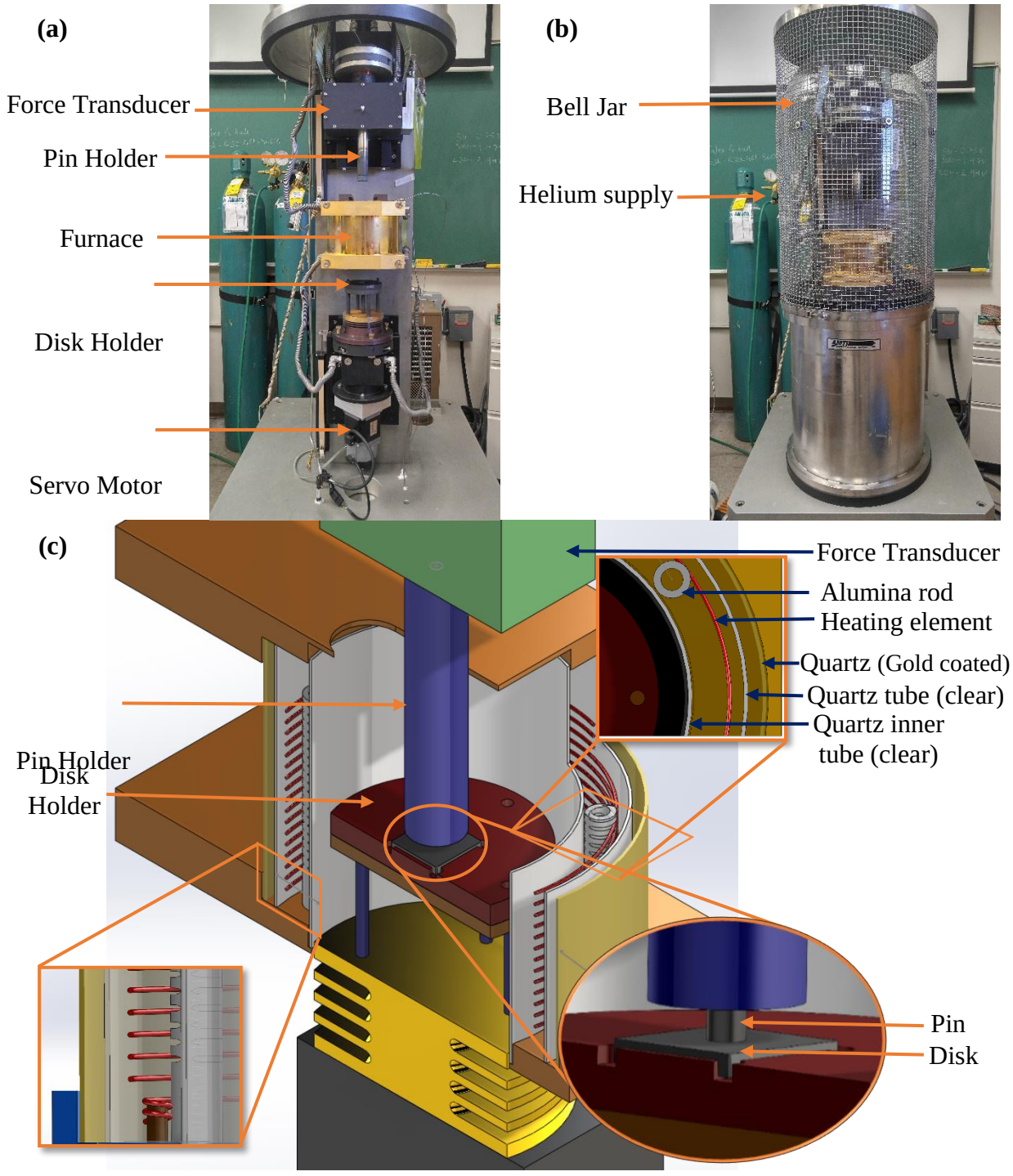

Fig. 6. High temperature tribometer (a) Tribometer setup, (b) Bell jar chamber for vacuum and controlled environment, (c) Furnace construction.

possible to measure and record the in-situ friction and normal loads along with the COF with the data acquisition system at 100 Hz.

2.5. Tribology Experimental Conditions

The experimental conditions for unidirectional sliding are summarized in Table 3. Two different tribo-pairs, Inconel 617 pin sliding on Inconel 617 disk and 800HT pin sliding on 800HT disk and two different gas environmental conditions (air and He) were selected for each tribo-pair. The HT tribological study was carried out at three different temperatures with the highest being 950 °C for Inconel 617. However, for alloy 800HT, the highest temperature was 750 °C as its mechanical properties degrade drastically beyond 800ºC [8,11]. All the experiments were performed at three different normal loads and three sliding velocities along a circular path with 17.5 mm mean diameter. The tests were performed for a duration of 600 seconds with 24 m sliding distance.

Table 3
Tribology experimental conditions

Disk	Pin	Ambient	Temperature (ºC)	Normal Force (N) [MPa]	Sliding velocity (m/s)
Inc 617 800HT	Inc 617 800HT	Air, He	25, 500, 950 25, 500, 750	5 [0.16], 10 [0.32], 20 [0.64]	0.04, 0.1, 0.15

For all the experiments in He environment, the exact same experimental protocol was followed as described in Table 4. Before each HT test, the bell jar needs to be full of He and free of air. Accordingly, the ball jar chamber was vacuumed to -14.3±0.1 psi and then followed by flushing He in the chamber until the chamber has a positive pressure. To assure minimum possible amount of air in the bell jar chamber, the vacuum and flushing process were carried out three times. The He pressure in the chamber was maintained at 0.1 psi during heating up, during the experiment, and during the cooling down processes.

Table 4
Protocol for HTT experiments with Helium flow

Time (min)	State	He volume flow rate (l/min)	Relative Pressure (psi)
0	Initial condition	0	0
1-5	Test chamber vacuumed	0	-14.0 ~ -14.3
6-15	Helium flushed the test chamber	~25	0.1±0.02
16-45	Vacuum and flushing of He (Two times)	~25	-14.3 / 0.1
46-55	Create positive pressure and execute test	~60 (Full Open)	0.1±0.05
56-85	Heating the chamber	5-10	0.1±0.02
86-95	Test	5-10	0.1±0.02
96-185	Cooling	5-10	0.15±0.02

2.6. Tribo-Chemical analysis

Sliding contact under HT conditions is influenced by both mechanical and chemical changes of the surfaces coming in contact, as well as the bulk material properties. The tribological behavior is further affected by the environment and gaseous content present during the HT contact. There are several studies which showed the chemical changes under He impurity at HT (thermal load only) [14,15,23] but there is none showing the effect of simultaneous presence of tribological action and gas atmosphere on the chemical changes of Inconel 617 and 800HT (co-presence of thermal/chemical/mechanical load). The present study focuses on the tribo-chemical changes taking place at the surface/interface contact of Inconel 617 under He and air atmospheres at HT of 950 °C, and 800HT at 750 °C. Subsequently we explain how these changes may have affected the tribological behavior of the alloys. To deconvolute the contribution of wear and temperature, characterization study has been performed on the aged samples as well. Following the tribological studies, the surfaces inside and outside the wear tracks of the alloy were studied using detailed characterization tools including Scanning Electron Microscopy (SEM), Energy Dispersive

Spectroscopy (EDS), X-ray Diffraction (XRD), Raman spectroscopy, and Secondary Ions Mass Spectroscopy (SIMS) and nanoindentation.

SEM and EDS

SEM and EDS were performed on the disk sample surfaces along with optical microscopy. For the cross-sectional EDS analysis, a layer of Nickel (Ni) coating, deposited using electrodeposition technique, was used on some of the sample's surface to protect the oxide layer from delaminating during grinding. SEM and EDS analyses were performed in a JEOL JSM-7500F that was equipped with EDS and BSE detectors. All the SEM images and the EDS scans have been taken using 5 KV and 20 KV operational voltages, respectively.

X-ray diffraction

X-ray difraction spectroscopy (XRD) was performed using a Bruker D8 Discover having Copper sealed tube X-ray source with angular resolution of 0.01^{o}. The energy of the incident X-ray beam used was 40 keV, 40 mA (λ=1.54056 Å) with collimator of 0.5 mm and step size of 0.005^{o} on an area of 1 mm^2.

Weight changes during oxidation

Digital weighing balance Metter Toledo-AG245 with 0.01 mg accuracy was used for the weight measurements for all the samples, before and after the experiments, to measure the oxidation and correlate with the wear rate.

Raman Spectroscopy

Horiba Jobin-Yvon LabRam HR Raman is used as a complementary method for chemical characterization of the surface materials. It is equipped with an Olympus BX 41 confocal microscope and two different wavelength laser sources of 633 nm and 785 nm. For the current research, 633 nm wavelength laser was used for the Raman shift range of 100 – 2000 cm^{-1}.

Secondary Ion Mass Spectroscopy (SIMS)

A CAMECA IMS 4f ion microprobe was used in the dynamic mode, for identification of materials through the depth of the oxide layers inside and outside of the wear tracks. Profiling was performed with 14.5 keV Cs1 ion beam (raster 50 x 50 μm^2, image collimation diameter of 50 μm, and variable sputtering rate from 2.73 nm/s to 3.73 nm/s). Time-of-Flight (ToF) SIMS spectra were collected over selected samples.

CHAPTER III
TRIBOLOGY OF INCONEL 617 [2]

In this chapter, the tribological behavior of Inconel 617 will be analyzed. The custom-built high temperature tribometer (HTT) was used to perform parametric sliding (unidirectional) HT tribological experiments in controlled environments (e.g., He with impurities) simulating the environmental conditions of the nuclear reactors up to 950 °C on unaged as-received samples. Thermal aging over time brings changes to the top surface of the alloy which might influence the tribological results. Previous study has showed that stress-assisted and stress free thermal aging has different effect on microstructure and mechanical properties of Inconel 617 [24,25]. In what follows, the effects of temperature, normal load, and sliding speed, sliding distance and experimental atmosphere on the tribological behavior of Inconel 617 are presented and discussed. The oxide layer formation plays a key role in the friction and wear behavior at HT, and hence, to better understand the mechanisms of oxide layer formation and its mechanical properties, the experimental results are complemented with detailed characterization including scanning electron microscopy (SEM), energy dispersive spectroscopy (EDX), and X-ray diffraction (XRD).

3.1. Effect of Temperature and Normal Load

Fig. 7 depicts the COF of Inconel 617 tribopair in He environment as a function of sliding time and temperature. Every experiment discussed, hereinafter, has been carried out at least twice to assure repeatability. All the mean COF values reported were obtained from the stable average of

[2] Reprinted with permission from "Helium Tribology of Inconel 617 at Elevated Temperatures up to 950° C: Parametric Study." by Rahman MS, Ding J, Beheshti A, Zhang X, Polycarpou AA. Nuclear Science and Engineering (2019): 1-15. Copyright 2019 by Taylor & Francis.

the in-situ results during the last 40% portion of the runtime. As seen, the COF values at RT and HT in He are all generally high and stable. In He environment, the COF is 1.42 at 950 °C, which is significantly higher than at 500 °C (0.85) and RT (1.09) under 5 N normal load (nominal contact pressure of 0.16 MPa). As shown in Fig. 7b, the tribopair exhibits the lowest COF at 500 °C in He environment while the COF values at 800 °C and 950 °C are higher. Interestingly no considerable change is observed comparing the COFs at 800 °C and 950 °C, implying the same mechanisms at very HT from 800 °C to 950 °C. It is noted that with the rise of temperature, the fluctuation of the COF increases under He environment (Fig. 7a) which is also seen in the increasing trend for the standard deviation values depicted in Fig. 7b.

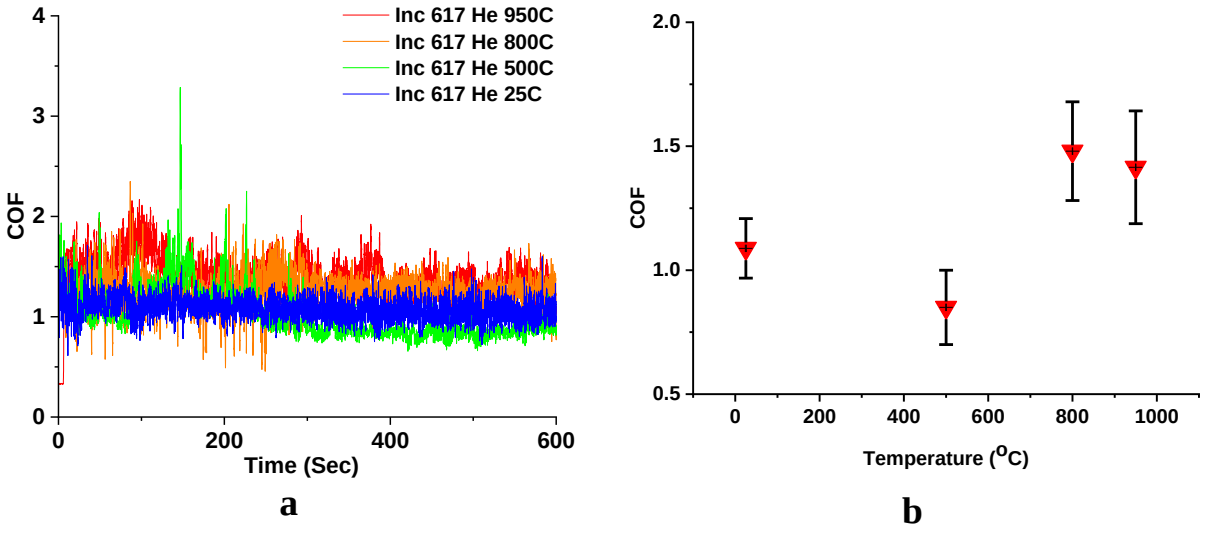

Fig. 7. Inconel 617 in He under 5 N normal load (0.16 MPa) and sliding velocity of 0.04 m/s (a) In situ COF, (b) average COF versus temperature showing ± 1 standard deviation.

Fig. 8 shows the dependency of the COF on the contact pressure (normal load) at three different temperatures under He conditions. The COF is minimum under the intermediate load of 10 N at all temperatures. The COF is highest at 950 °C for all loads, while minimum COF values are observed at the intermediate temperature. At the intermediate temperature of 500 °C, the alloy starts to become softer and very small oxide layer starts to form, that also can be confirmed by the

change in the color of the surface to brownish yellow. This is also observed in previous studies and it is suggested that the COF is lowest at the intermediate temperature during when mechanically mixed layer (MML) starts to form [26,27]. On the other hand, in previous studies on Ni-Cr alloys it is found that at this intermediate temperature NiO is dominant , whereas Cr_2O and $NiCr_2O_4$ was found to be the reason of lower COF at 600 °C and above temperatures [28]. Lower melting temperature of NiO could enable softening under the contact pressure at intermediate temperature which can be attributed to the formation of a more stable tribolayer or MML by chemical reaction with the impurities present in He, during the experiments at the intermediate temperature. At HT (800 °C and above), however, the formation of more brittle and harder composite layer can lead to COF increase. Moreover, adhesive wear strongly depends upon interfacial bonding between the solids. In the case of two metals in contact, they can overlap, leading to large electron exchange interactions [29]. The adhesion between the pin and the bare metal surface on the wear track in He environment is considerably higher than the adhesion force with the thicker oxide layer (see Section 3.5) in air atmosphere.

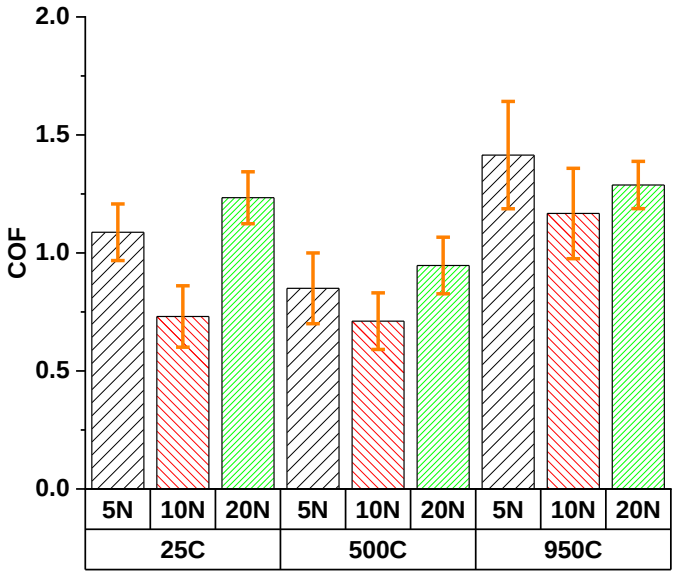

Fig. 8. Average COF at sliding velocity of 0.04 m/s for various normal loads in He (the nominal contact pressures are 0.16. 0.32. 0.64 MPa for 5, 10, 20 N, respectively).

The influence of temperature and normal load on the wear rate in He atmosphere is shown in Fig. 9. Under He environment, at all temperature conditions, the wear rate increases with applied normal load. The wear rate also increases with the rise of temperature under all contact pressures. At RT the wear loss is mostly through adhesive-abrasive burnishing by the metallic contact between the pin and disk. During testing, periodic evaluation of the contacting surfaces sliding at RT confirmed no sign of material transfer or layer formation. At 500 °C, oxidation and transfer of wear debris to the pin from the disk wear track increases the wear rate. At 950 °C, high oxidation and formation of a composite layer on the wear track accelerated the wear rate at the beginning of the sliding period and continued at a steady rate afterward by high plastic deformation, crack nucleation and propagation in more brittle rubbing surfaces. The wear rate at the intermediate temperature of 500 °C is slightly higher than that of the RT experiments under all loads, while it increases significantly at 950 °C. The wear mechanisms at 500 °C He remains similar as RT with powdery abrasive wear particles whereas, at 950 °C the wear is mostly adhesive generating larger delaminated oxidized wear particles. But due to the presence of higher temperature of 500 °C, the particles are oxidized and increased hardness ratio of oxide to metal substrate might have slightly raised the wear rate [26,27,30,31]. On the other hand, the presence of very fine powdery wear particle in the contact kept the COF lower. Although similar behavior is observed by several investigators as mentioned before, for better understanding of this phenomenon of low friction-high wear rate at intermediate temperatures, further in-depth study is required. Specific wear rate values (wear rate normalized by the normal load) in Fig. 9b show an increase in the wear volume for high load of 20 N. Like typical metallic wear phenomena where specific wear rate does not change considerably with load, here the values are close to each other at RT and 500 °C. At HT

the trend changes which can be attributed to the formation of a brittle substrate that is more prone to cracking damage under high contact pressure.

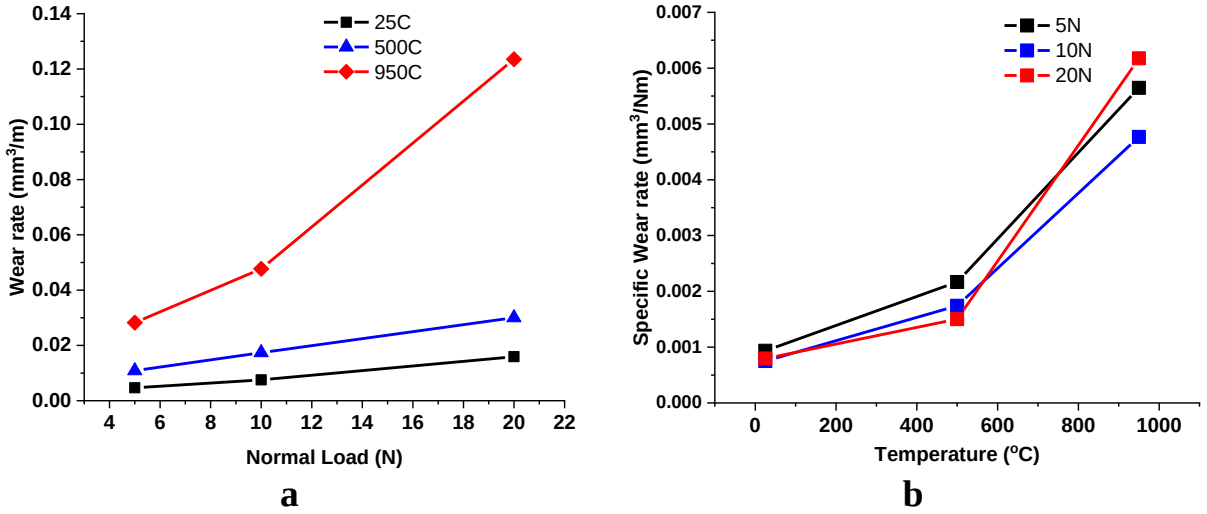

Fig. 9. (a) Average wear rate versus normal load and (b) specific wear rate versus temperature (In He at 0.04 m/s).

3.2. Effect of the Environment

To understand the effect of the He environment on the sliding wear, experiments were carried out under similar loading and temperature conditions in air. Fig. 10 shows the in-situ COF at different temperatures in air environment and also the average COF values as a function of temperature under different normal loads. At 950 °C in air, the COF drops significantly (about 60% reduction) after few cycles and it is stabilized at lower values as also observed in previous studies [18,32]. Contrary to He environment, in air atmosphere, as the temperature increases, the steady-state COF monotonically decreases from 0.69 at 25 °C to 0.45 at 950 °C, which is similar to the behavior shown at 800 °C and in Ref. [19]. The COF value at 10N at RT and 500 °C in air environment remains almost in the same range and standard deviation. The reason behind not having lower COF at 10N like other loads, is still not clear and further investigation is required in future. The COF decreases with the increase in temperature for all loads (with exception of 10N at 500 °C) due to the stable protective glazed layer generated by compaction of the wear debris

trapped in the contact area. At HT in air, the oxide layer becomes softer and at higher loads, the glazed layer becomes relatively more consistent along the wear track. However, in He environment, no such layer was observed even at higher load, which eventually led to higher observed COF and wear.

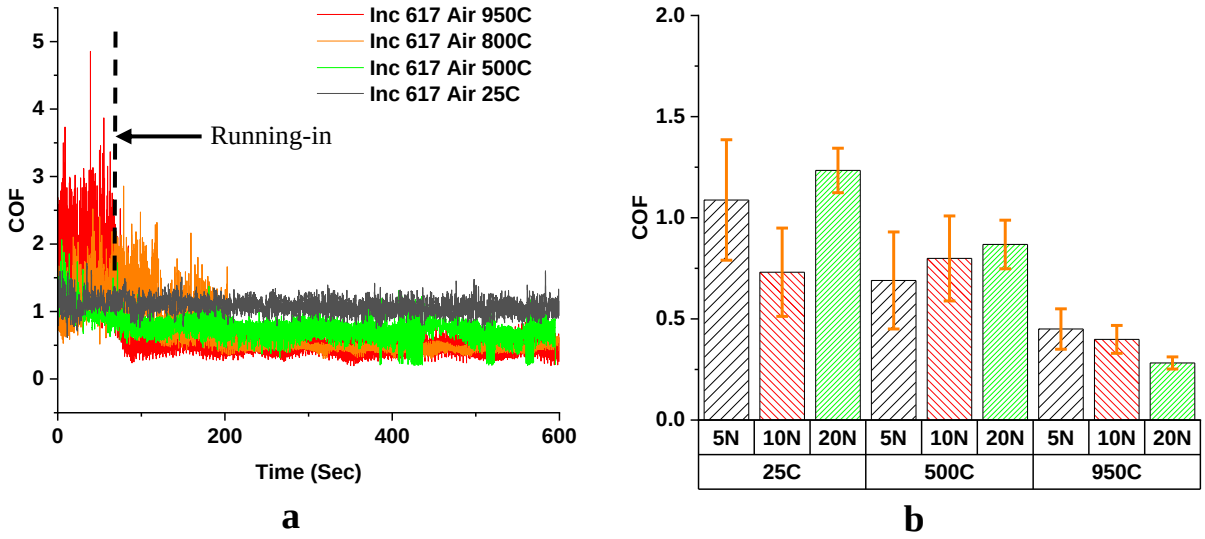

Fig. 10. (a) In-situ COF for 5 N load, (b) average COF at sliding velocity of 0.04 m/s for various normal loads in air.

Fig. 11 compares the wear rates in both air and He environments at 950 °C. At all loading conditions, the wear rate in He is higher than in air, which is in line with the observed frictional behavior. Although the wear rate, similar to He environment, increases at almost constant rate with load in air, the rate of increment is much lower and consistent between different loads, implying the same specific wear rate (wear coefficient) and the same wear mechanism. The wear rate in HT air is dominated by the initial running in period of the experiment (high COF values for 950 °C in Fig. 10a) where the metal pin slides on the oxidized surface breaking into wear particles. Subsequently, some portion of the wear debris and the newly oxidized surface create the compacted glaze load bearing layer protecting the surface, which leads to reduced friction and wear. Such transitional period (running-in) was not observed for the test carried out in He

environment. The wear at HT air is also affected by the reduction in the mechanical properties such as hardness and modulus of elasticity, as the maximum elastic contact strength drops significantly with temperature [33].

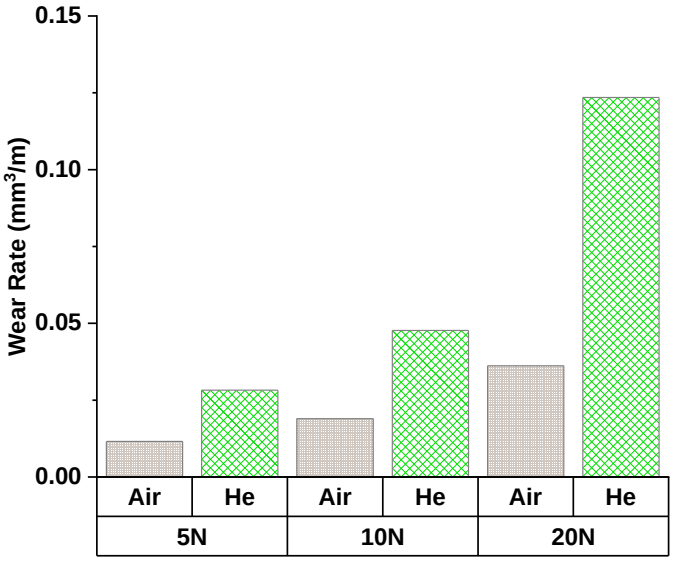

Fig. 11 Wear rate in Air and He environments at 950 °C for different normal loads at 0.04 m/s.

3.3. Effect of Sliding Velocity

Fig. 12 presents the effect of sliding velocity on the COF and wear rate under 5 N normal load at 950 °C, in He and air environments. Both in air and He environments, the COF remains similar at all sliding velocities, although, in He the standard deviation decreased with the increase in sliding speed. In the case of air, although stable COF values, the transition to achieve stable COF increases with sliding velocity (see Fig. 12c). As compared to the situation in air, for samples tested in He, no difference or transition was observed at any velocity. The interaction time between the pin and any point on the disk wear track is inversely proportional to the velocity. Hence, as the sliding velocity increases the interaction time decreases. At low velocity, the surface has more time to get oxidized and thus the compacted layer is formed earlier than at high velocity. Moreover at higher velocity, there is a higher probability of removing the wear debris out of the wear track that is

required to form the protective layer. The wear rate of Inconel 617 is somewhat independent of velocity, and significantly lower in air.

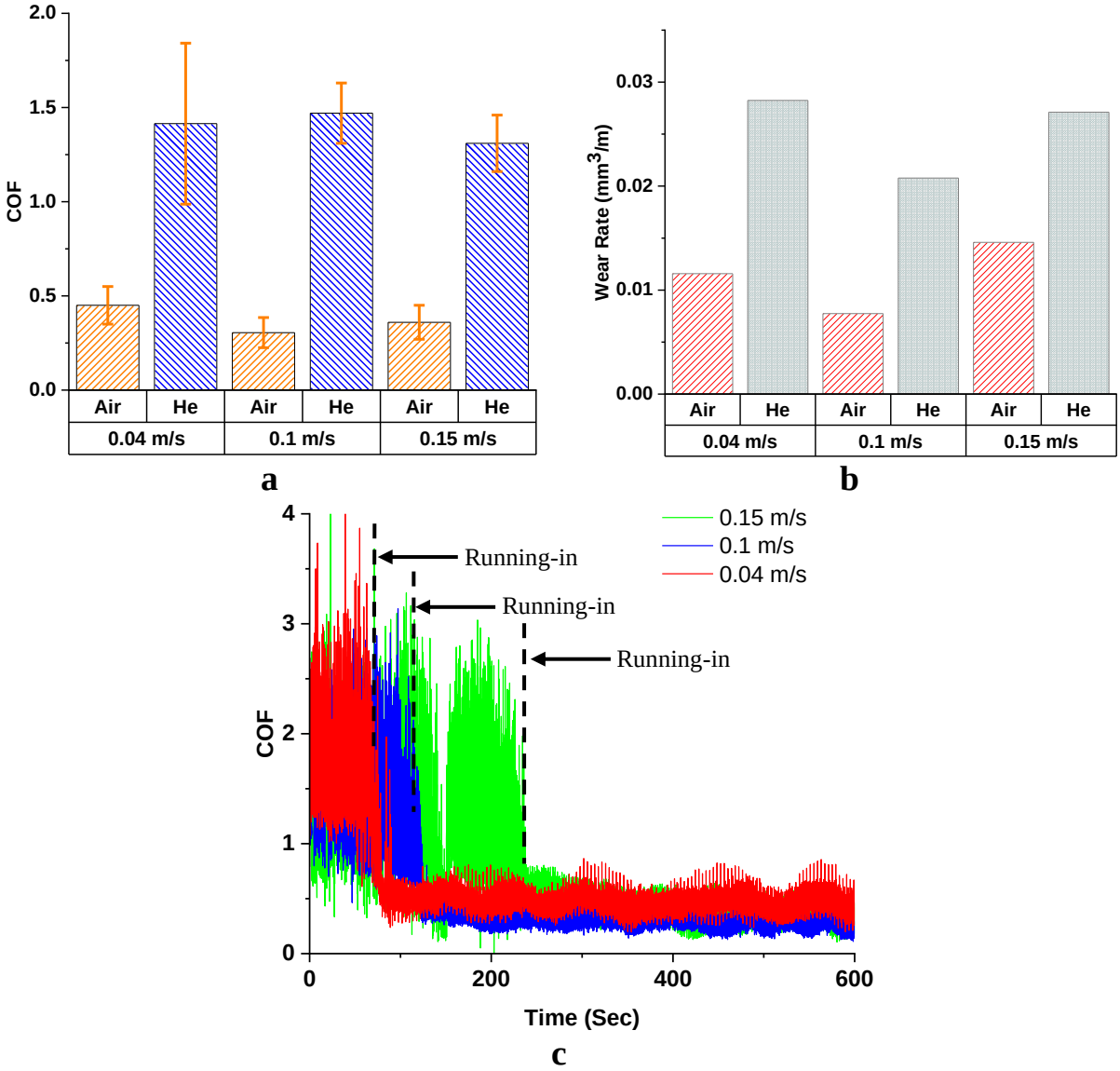

Fig. 12 Effect of sliding velocity at 950 °C under 5 N load and duration of 10 minutes: (a) COF, (b) wear rate, (c) in situ COF in air.

3.4. Effect of Sliding Distance

Fig. 13 shows the experimental results of Inconel 617 for different sliding distance values with the same constant load of 10 N under He, 950 °C and 0.04 m/s. The average COF is reported for the final 200 s of the experiment, where the COF is stabilized. The 500-cycle experiment exhibits

almost the same average COF as 1400 and 2700 cycles. This is in line with the fact that unlike experiments performed in air, no considerable transitional (running-in) period was observed during sliding of the Inconel tribo-pair in He. The 500-cycle experiments are sufficient to investigate the friction/ wear behavior under nuclear HT He conditions. The wear rate at HT He is constant at 0.04 mm^3/m. Although the wear rates are fairly close for all test durations, their standard deviation decreases with increasing number of cycles. This is expected as the initial oxidation and removal of oxide layers, although has marginal effect on the average values, they impact the variability of the wear rate. It is noted that despite exhibiting very high COF, Inconel 617 has very low wear rate showing strength retention capability as well as the oxide stability at HT He atmosphere.

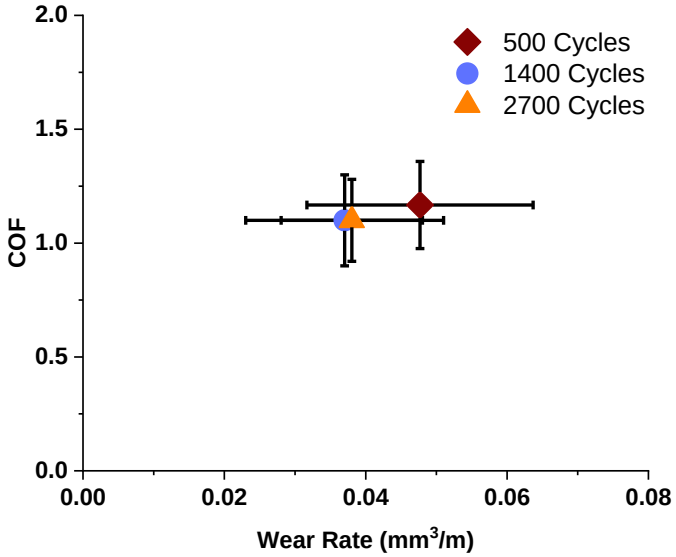

Fig. 13 Comparison of COF and wear rate for Inconel 617 under 10 N at 950 °C in He and 0.04 m/s.

3.5. Effect of Aging

The Inconel 617 samples were aged for different durations as mentioned in previous chapter section 2.3. The aged samples were used for tribological experiments to mimic the contact surface movements in nuclear reactor after being in operation for long duration at high temperature. The disks and pins aged for 10 hours in Helium were used for the tribology experiment under 5N

normal load and 0.04 m/s sliding speed at 950 °C helium environment. As shown in Fig. 14, the in-situ COF for He-aged sample remains high for the whole experiment period. The oxide on the aged sample did not change the frictional behavior of Inconel 617.

Considering the lower friction behavior of Inconel 617 in air HT, another set of samples were aged in Air 950 °C and then used for tribology experiments in He environment at 950 °C keeping other experimental parameters constant. As shown in Fig. 14, the Air-aged sample did exhibit lower friction behavior for approximately the initial 60 seconds of the experiment and then the friction jumped higher to the similar value of He-aged sample. It does prove the possible effectiveness of the surface treatment in air as a solution of reducing friction of Inconel 617. But further study is required to be done to attain a sustainable improved frictional behavior.

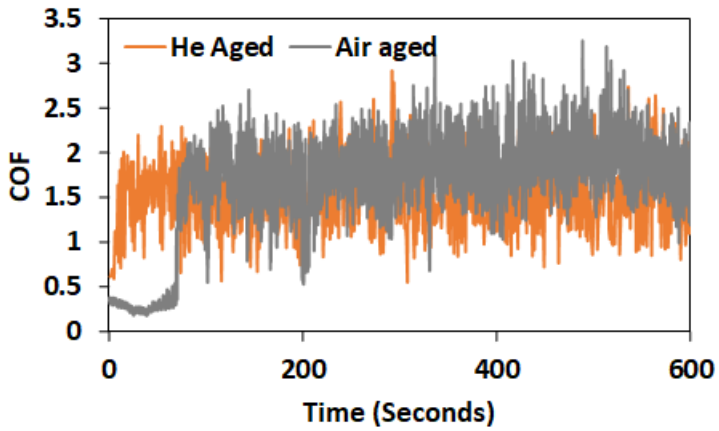

Fig. 14 Comparison of in-situ COF for Inconel 617 aged in He and air under 5 N at 950 °C in He and 0.04 m/s.

3.6. Oscillational (Fretting) Experiments

The HT oscillation (fretting) study was carried out at 950 °C for Inconel 617 using the same specialized high-temperature tribometer (HTT). All experiments were performed at 10 N normal loads (contact pressure of 204 MPa) with an oscillation angle of 120° and max sliding speed of 0.025 m/s along a circular path of 17.5 mm mean diameter. In this configuration, one complete cycle is completed in two seconds, which allows us to obtain enough data to accurately capture

the static COF. Data acquisition was collected at 120 Hz for all the tests performed for 10 and 100 cycle oscillations.

All conditions are repeated for at least two experiments to ensure consistency. Similar to unidirectional experiments presented above, at RT, the static COF is lower than the static COF at HT He environment. The COF value remains almost the same for both 10 and 100 cycles. The static COF in HT He atmosphere for Inconel 617 is 2.13±0.22 during the 10 cycle experiments, whereas it is 2.28±0.26 during the 100 cycle experiments. All the data reported here for 100 cycle experiments are taken by averaging the value of the final 10 oscillations. The spherical pin with 55.3 mm radius curvature was used in these experiments to ensure better contact. The final contact area on the pin increases with oscillations and is larger after 100 oscillations. But the consistency of the static COF at RT proves that the contact area does not have a considerable effect on the COF in this case. In the case of HT experiments, the contact area is larger than its corresponding RT experiments for all conditions.

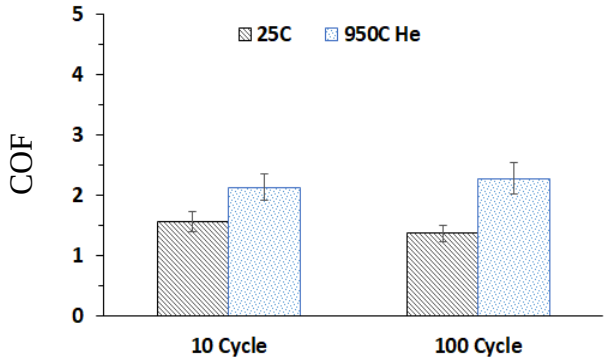

Fig. 15 Average static COF in RT and HT He environment for Inconel 617.

Fig. 15 shows the average static COF values for Inconel 617 under 10 N normal load. It shows higher static COF values at HT He condition, similar to the dynamic COF. It is noted that the static COF is around 1.5 to 2.5 times higher than the dynamic COF reported in the previous sections for unidirectional experiments. The dynamic COF values during these oscillation experiments are

within the error limits reported, which will stabilize over time as mentioned in the previous sections. According to the static COF values reported here, Inconel 617 has better agreement with the previously reported dynamic COF values.

3.7. Characterization and Discussion

3.7.1. Surface morphology

The SEM images in Fig. 16 show the morphology of the oxides formed on the matrix surface as well as in the wear track under different magnifications at 950 °C in both air and He. The thicker yellow arrows in the middle micrographs indicate the sliding direction. The SEM images reveal that the oxides formed on the matrix surface in air (Fig.16a) and He (Fig.16c) atmospheres have similar morphologies. On the wear track, however, the compacted glazed layer of oxide debris is more continuous and clearly visible on the wear track of the disk at 950 °C in air (Fig. 16b), whereas no such layer is observed under He environment. This clearly explains the higher COF and wear values observed for He. A closer look in the wear track reveals areas with two different surface morphologies under both air and He. Designated area-I exhibits a more continuous contact with the counter surface and eventually carrying most of the contact pressure, which made the surface “cleaner” and smoother. This is the result of the initial material transfer to the pin surface in He, and the “glazed” layer formed by compacted oxide debris in air. Designated area-II shows a rougher surface with partially compacted adhesive wear debris, which is also a transitional phase towards Area-I. Area-II on the wear track in He (Fig. 16d) shows similar morphology as on the surface outside the wear track and fewer signs of adhesive wear than in Area-I, which indicates reduced contact with the counter surface.

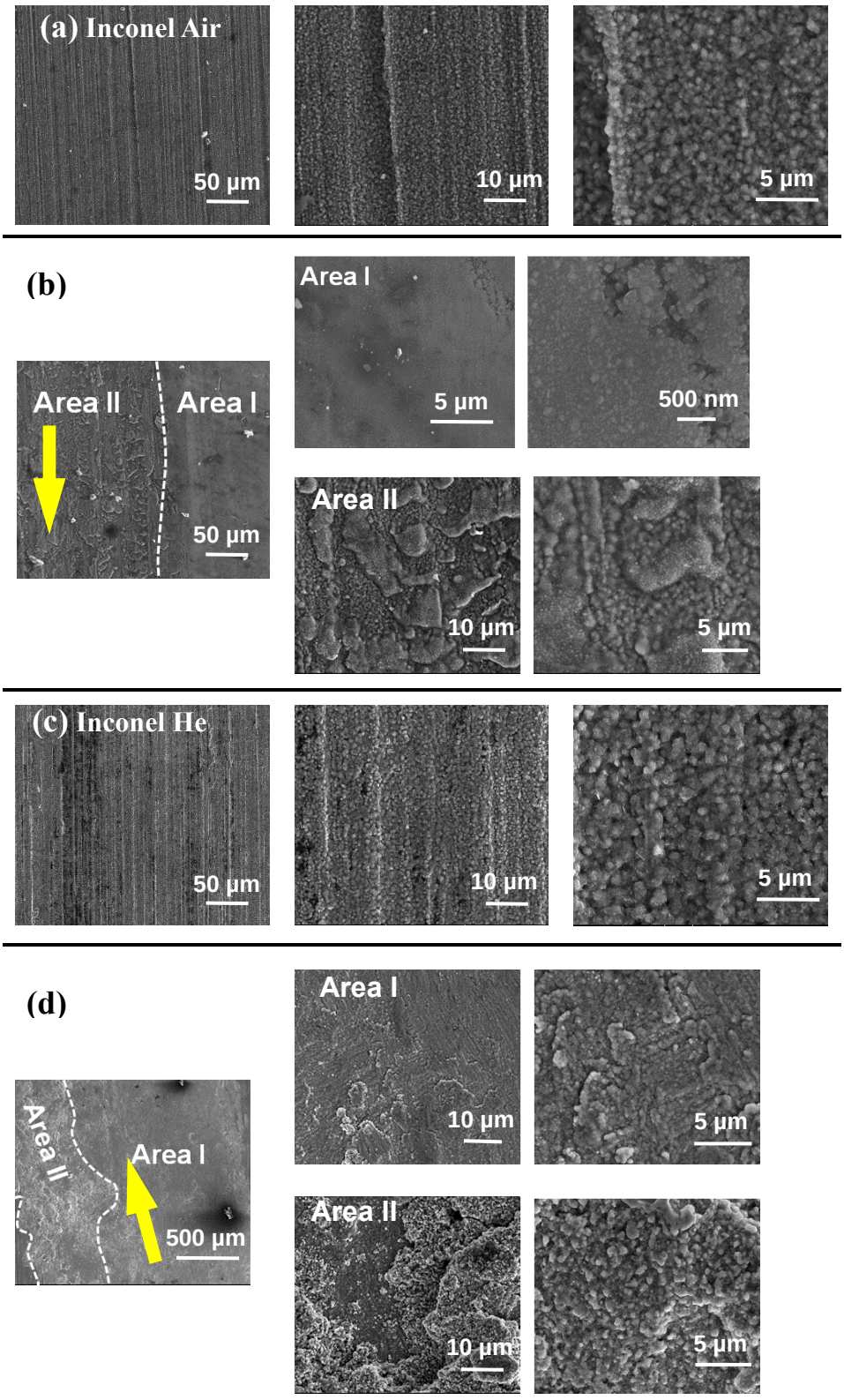

Fig. 16. SEM images of samples under 5 N normal load, 950 °C, 0.04 m/s; in air (a) outside the wear track (matrix) and (b) inside the wear track; in He (c) outside the wear track (matrix) and (d) inside the wear track.

The XRD technique was also performed on samples exposed in He and air at 950 °C and both samples show peaks for Cr_2O_3 as well as the metal substrate of Inconel 617 (Fig. 17). The peaks of the oxides in air are further developed and sharp, implying that the oxide is more crystalline and also the size of the particles is larger, compared to the oxide developed in He, which is in agreement with the observations from the SEM images, Fig. 16.

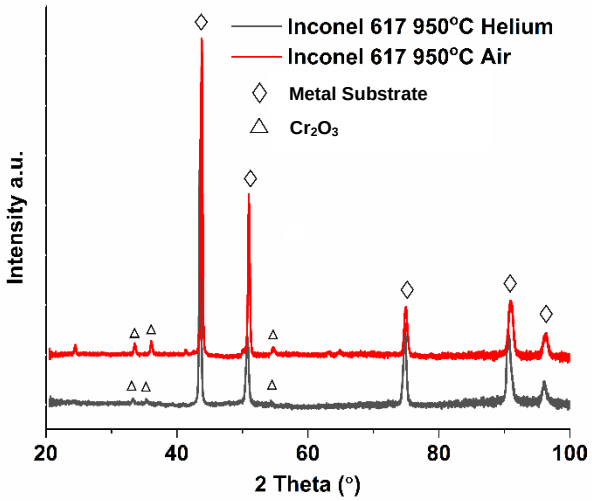

Fig. 17. XRD data outside the wear track for Inconel 617 at 950 °C, 0.04 m/s in He and Air.

3.7.2. SEM/EDS

Cross section SEM and EDS analyses for the samples tested at 950 °C show a surface oxide reach of Cr with the presence of subsurface oxides of Aluminum (Fig. 18) [34]. From the cross-section SEM images of the matrix outside the wear track, it is evident that the oxide layer thickness exposed in air is higher than the samples tested in He. Also, the surface oxide in air is relatively rougher than in He. Once pressurized in the contact region, this thick and stable layer of compacted oxides in HT air protects the Inconel surface from excessive wear.

According to Fig. 18, the oxide layer thickness outside the wear track is approximately 4 μm in air at 950 °C, but it should be noted that it varies depending on location and could be up to 10 μm thick. Nonetheless, outside the wear track in He the oxide layer thickness is only around 1.5 to 2 μm. For the wear tracks at 950 °C, the cross section EDS results show that the thickness of the mechanically mixed layer varies between 1 to 10 μm in both air and He environments depending on the area (I and II) of the wear track. The EDS maps on the wear track in Fig. 18 reveal the layer in HT air to be a mixture of Cr-Ni-Co-Mo with a higher concentration of Cr. However, in the case of the mixed layer in HT He, it mostly consists of high concentration of Cr at the top layers with a small trace of Ni, Co and Mo. Significant amount of molybdenum and aluminum traces are found at the inner edge in the interface of the mechanically mixed layer and the bulk. At 950 °C air, complete recrystallization occurs and $M_{23}C_6$ carbide precipitates, rich in chromium and molybdenum are found on the surface and along the grain and subgrain boundaries [15,35]. The presence of Mo in the MML and moisture in the air can help the formation of compact layers and reduce the COF and wear at HT air environment.

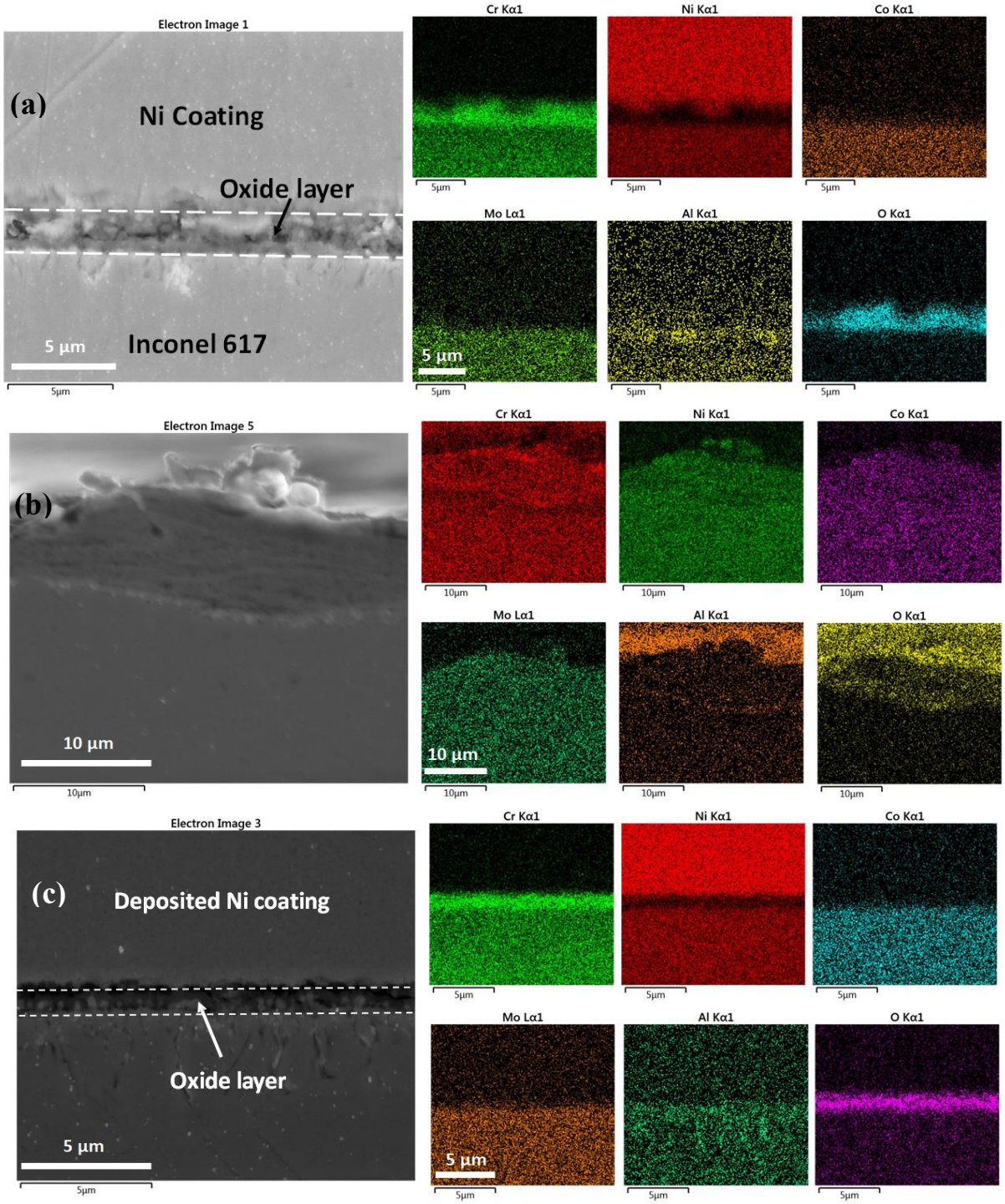

Fig. 18. Cross section SEM images and EDS maps of Inconel 617 at 950 °C under 5N load, (a) Air outside the wear track, (b) Air inside the wear track, (c) He outside the wear track and (d) He inside the wear track.

Figure 18 Continued

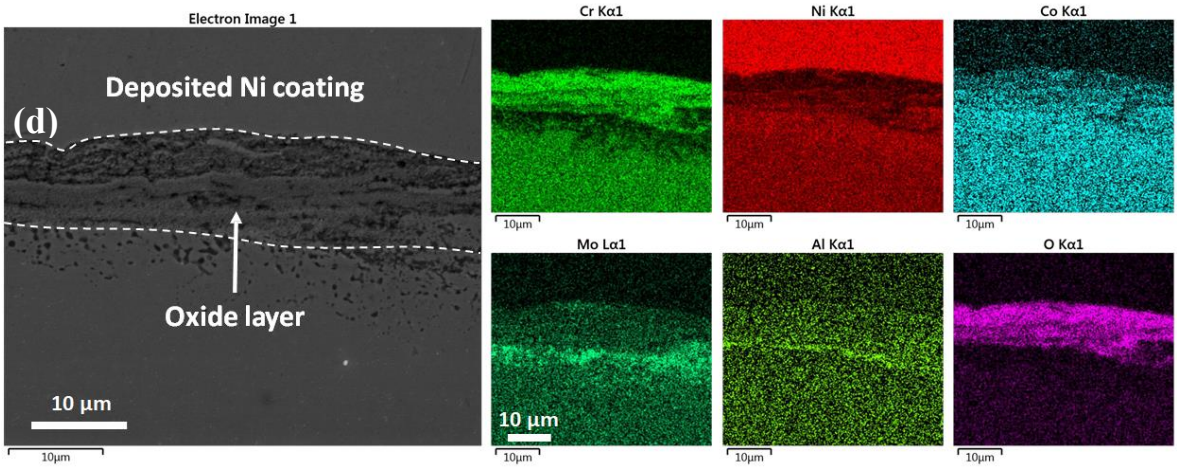

At a lower load of 5 N, patches of "glazed" layer are observed on the wear track in HT air (Fig. 19), whereas at higher loads the glazed layer becomes consistent and continues along the wear track (see SEM images shown in Fig. 19a, b, c). It should be emphasized that in He, no such layer is present at any condition. At higher load, the wear track is clear of any wear debris particles and shows only small patches of adhesive contacts which eventually lead to higher COF and wear (Fig. 19d, e, f). With increasing load in HT He, the higher contact pressure easily generates and propagates cracks through the mixed layer at a higher rate than its formation and eventually, the thickness of the mixed layer reduces. This observation is further supported by the EDS line scans presented in Fig. 19(g, h) for the sample cross section under 10 N and 20 N loads.

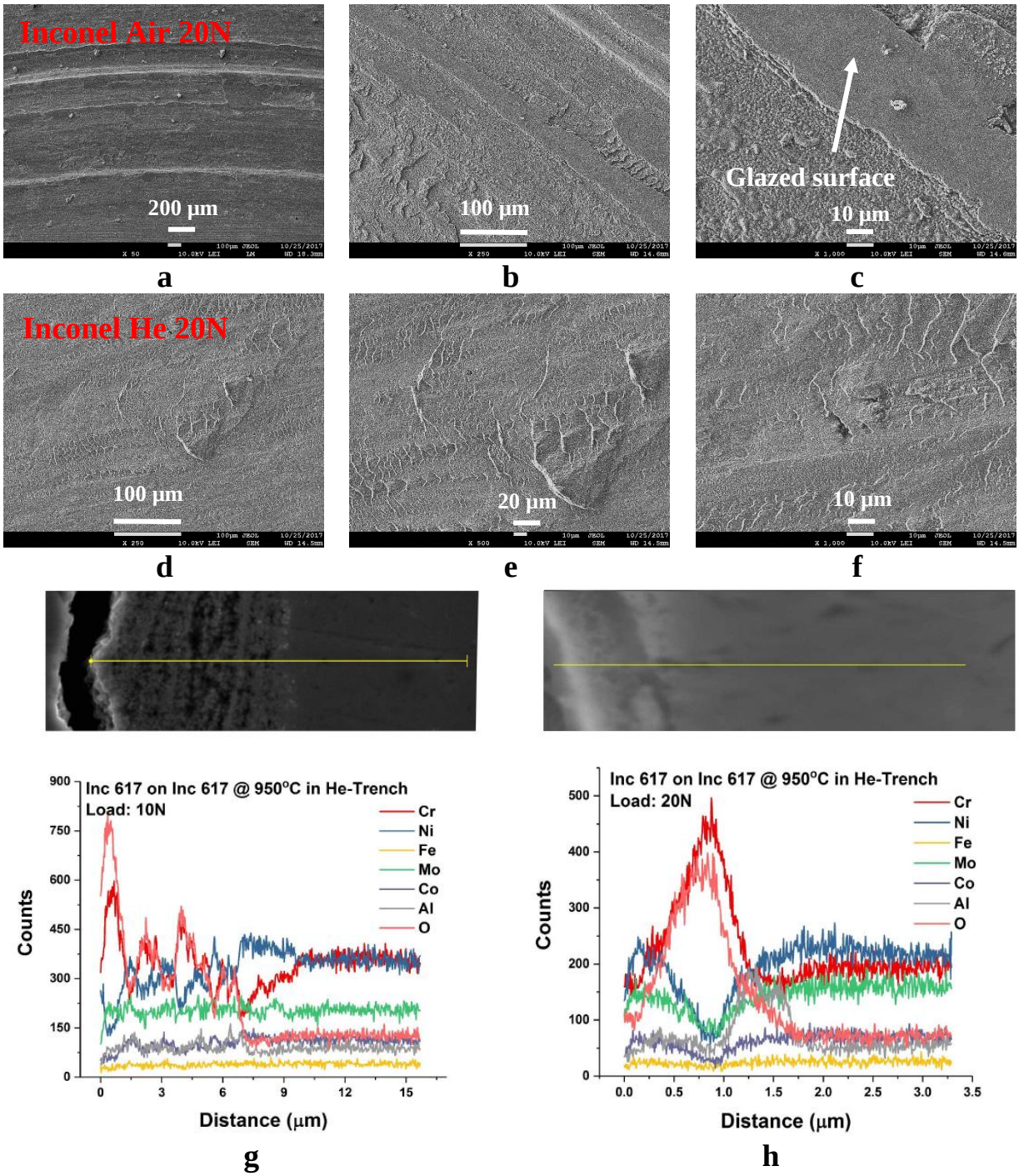

Fig. 19. SEM images of 20 N, 0.04 m/s samples (a, b, c) at 950 °C, air; (d, e, f) 950 °C, He. EDS line scan on the cross section of the wear track at 950 °C in He (g) 10 N load sample, (h) 20 N load sample.

Obvious differences are observed between the worn surface and the wear debris produced in HT He and air environments. The amount and size of the wear debris produced in He at 950 °C is larger than in air, under similar loading conditions. To further evaluate the wear particles, debris

produced during the experiments were examined by SEM and EDS techniques and the results are shown in Fig. 20. At the temperature of 500 °C as well as RT at both environments, the size of the wear particles is small in the rage of 20-100 µm, and particles are flake-like. However, at 950 °C in He, the quantity of wear debris increases drastically with larger chunky particles up to 300 µm. The size of the debris particles is defined by both mechanical and chemical effects during sliding, and also the partial pressure of oxygen has a significant influence on their size.

It has been shown experimentally by Soda et al. that the diameter of the wear debris particles increases with the decrease in oxygen partial pressure [36,37], which is in agreement with this work. The chemical activity of the gases was systematically investigated by Mishina to correlate the influence of atmosphere on the wear of metals [38]. Three categories of wear behavior were identified based on chemisorption affinity for metals and, accordingly, a correlation between the wear debris size/ quantity and gas pressure was established. The wear behavior is classified as Type I: gases with high chemisorption affinity of metals, Type II: gases with low chemisorption affinity of metals and Type III where chemisorption of gases on metal surfaces does not occur. In the case of type I, at the low-pressure end, strong adhesion and metal transfer occurs. With the increase in gas pressure, the wear debris particle size decreases. According to the observation of wear debris produced here, the wear behavior can be classified as Type I. The generation of rolling fine wear debris particles promotes faster agglomeration and formation of wear-protective layer in HT air environment, whereas the larger particles in He are not suitable and jump out of the wear track, or go through further plastic deformation under contact and can potentially lead to harder substances and may even result in more abrasive wear.

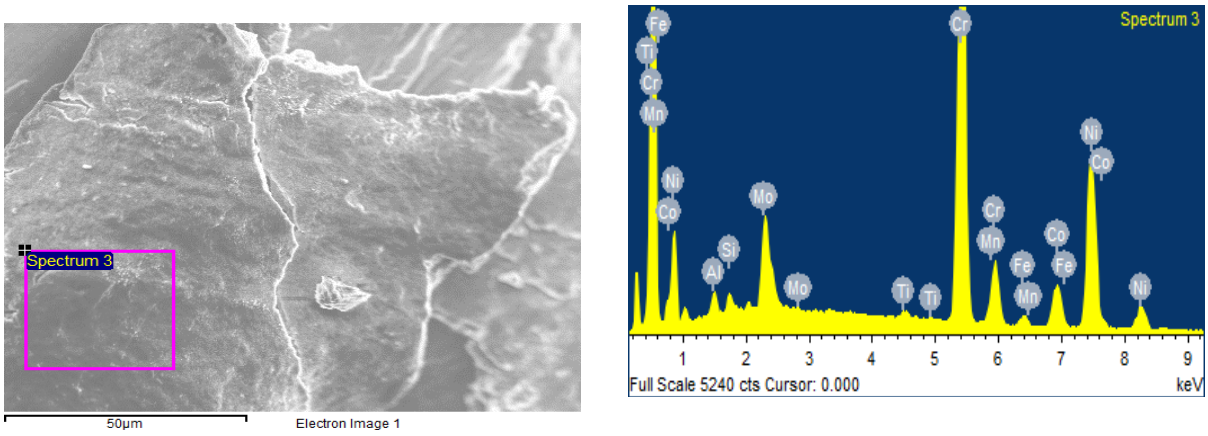

Fig. 20 SEM and EDS of typical wear debris at 950 °C in He, 5 N, 0.04 m/s.

3.7.3. Nanoindentation

Fig. 21(a, b) presents the nanoindentation hardness data on and outside the wear track generated at 950^{o}C in both air and helium environments. It has been shown before that the adhesive and abrasive wear introduce surface hardening [12] and it has been proven by micro hardness testing in previous study [39]. Although the polished virgin sample shows a stable hardness value 5.87±0.27 GPa, after the HT experiment in both air and He, the top oxide layer outside the wear track shows very low hardness and reduced elastic modulus value. To ensure the data belongs to the oxide and no significant effect comes from the substrate, the indentation depth was kept in between 50 nm to 300 nm. For the matrix, the average hardness and reduced elastic modulus are around 1-2.5 GPa and 40 -100 GPa, respectively. On the Area II of the wear track in air and He, hardness of the top layer is similar to the hardness of the area outside the wear track, which proves the presence of similar oxide layer on Area II. However, the Area I of wear track in air exhibits a very high hardness of average 16.45±3.93 GPa with a decreasing trend with contact depth whereas on wear track of He, the average hardness is 4.29±1.23 GPa with almost constant trend till 300nm contact depth, which is almost same as the virgin material hardness. The extreme high hardness of

the glazed layer on the wear track in HT air along with its stability and high adhesion to the substrate increases the wear resistance of the material [40]. However, the bare metal contact

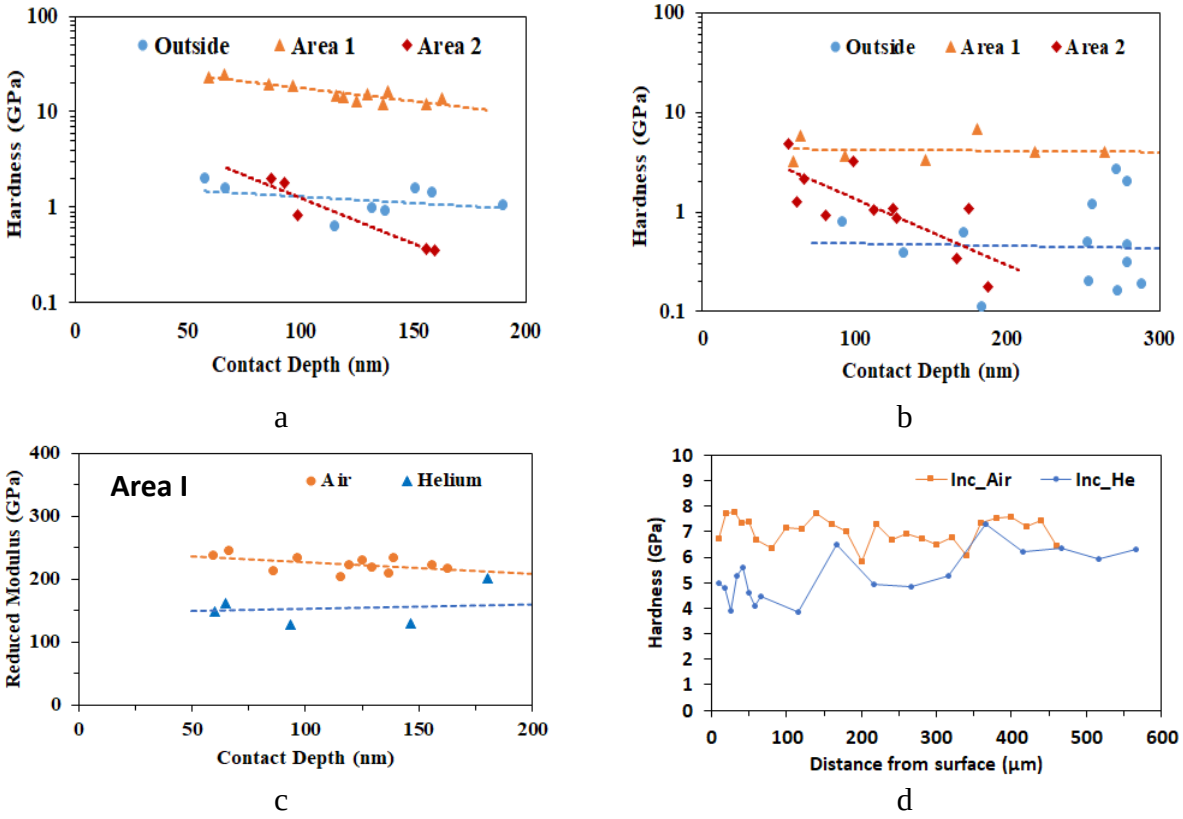

Fig. 21 Nanoindentation hardness of the top surface of Inconel 617 wear samples at 950°C (a) Air, (b) Helium; (C) Reduced modulus of Area 1 in Air and Helium, (d) Cross section subsurface layer hardness of samples under 10N normal load.

surface of Area-I in HT He environment shows lower hardness as well as reduced elastic modulus as can be seen in Fig. 21c compared to Area-I in air atmosphere. High elastic modulus enables the surface ability to support higher load with lower strain. Generally, it has been shown that the higher modulus of the tribofilm generated on the wear surface provide superior friction and wear properties [41]. The higher reduced modulus of Area-I in air increases the wear resistance and load bearing capacity comparing to He environment. The cross-sectional hardness measurement again reconfirms the physical properties at He environment close to the surface of wear track in Fig. 21d. The closest indentation from the surface is at 10 µm away and further away from the wear surface the hardness value reaches close to the bulk material hardness. On the other hand, for air, the

hardness on the cross section shows similar value from near-surface into the bulk away from the wear track. The depletion of carbide on the grain boundary at HT He could be the reason for this observation, whereas the formation of protective glazed layer may have slowed the process of diffusion in HT air environment.

3.8. Summary

The friction and wear behavior of Inconel 617 was investigated using a custom-built HT tribometer simulating He cooled reactor environments up to 950 ºC. Understanding the complete tribological behavior of Inconel 617 requires experiments covering multiple variables affecting the results. Interestingly, even though the alloy exhibits very large COF values (>1), high wear resistance was observed for the alloy at HT, which demonstrates the strength resilience of the alloy even at HT He environments. The following conclusions could be drawn from this work:

(1) In air, as temperature increases, friction decreases due to the formation of a protective glazed layer on the tribo-surface, formed by wear debris compaction;

(2) In HT He, friction and wear are higher than in air due to the instability of the surface oxide layer and crack initiation/propagation in low oxygen partial pressures, generating larger size wear debris;

(3) Under different contact pressures, the wear rate increases linearly with pressure, while the COF is almost independent of pressure;

(4) Sliding velocity (in the range of nuclear reactor applications) does not have a significant effect on the wear rate and COF values in both air or He environments. However, the transition time in HT air increases with increasing velocity;

(5) At HT air, Cr-rich oxide layer is present with a mixture of CO-Ni-Mo. The thickness of the oxide layer outside the wear track varies significantly between 1 to 10 µm.

(6) At HT He, the oxide is Cr-rich with minor presence of CO-Ni-Mo and the thickness of the oxide layer outside the wear track remains almost the same; and

(7) The thickness of the mechanically mixed layers inside the wear track varies for both He and air, and two different areas with very different properties and topographies are observed.

(8) The nanoindentation data shows the presence of very hard protective layer on the wear track of HT air, whereas in HT He wear track shows deterioration of properties such as hardness and reduced modulus compared to virgin Inconel 617.

After gathering all the detail tribological characteristics of Inconel 617, the competitor material alloy 800HT is next to be analyzed under similar VHTR conditions. This will be explained in the next chapter.

CHAPTER IV
TRIBOLOGY OF ALLOY 800HT [3]

In this chapter, detailed parametric tribological experiments with unidirectional motion were performed for alloy 800HT in a controlled environment (He with impurities) up to 750 °C to simulate the conditions of the nuclear reactor. In the following, the effects of experimental environment, temperature, contact pressure, sliding distance and sliding speed on the tribological behavior and surface morphology of 800HT have been studied and discussed. The tribological measurements were complemented with characterizations including contact/optical confocal profiling of the wear and matrix surfaces, scanning electron microscopy (SEM) and energy dispersive spectroscopy (EDS) to better understand the mechanisms involved in the formation of oxide layer as well as its synergic effects on the tribo-pair friction and wear properties.

800HT is considered one of the main candidate alloys for nuclear reactors with gas cooled high-temperature environment and, therefore, it is necessary to have a thorough understanding of the alloy tribological response for obtaining optimum operating and loading conditions. This chapter entails the detail investigation of the wear and friction behavior of alloy 800HT using a customized high temperature tribometer to simulate the environment of helium cooled reactor up to 750 °C. The effect of temperature contact load, environment, sliding distance and sliding speed on the alloy friction and wear were studied. The friction and wear coefficients have the highest values at high temperature helium atmosphere where the formation and stability of the oxide scales play an

[3] Reprinted with permission from "Tribology of incoloy 800HT for nuclear reactors under helium environment at elevated temperatures." by Rahman MS, Ding J, Beheshti A, Zhang X, Polycarpou AA. *Wear* 2019;436–437:203022. Copyright 2019 by Elsevier B.V.

important role. Optical and contact profiling, scanning electron microscopy, as well as energy dispersive spectroscopy techniques were utilized to study the surface oxide. The analysis showed the presence of Fe-Cr-Ni rich oxide both in air and helium. The protective glazed layer did not form in helium in any condition, whereas in air and under specific conditions a stable protective oxide layer was observed.

4.1. Effect of Temperature and Normal Load

Fig. 22 shows the COF results in He atmosphere as a function of temperature and sliding time (distance). The error bars presented in Fig. 22b were obtained from experiments carried out under the same condition repeated for at least two times to assure repeatability, as well as to determine the range of variation which is true for all the data hereinafter. The steady-state runtime of the in-situ results is considered to obtain all the mean COF values. In He environment, the COF values at all temperatures (RT and HTs) are high and generally stable, albeit with fluctuations. In He atmosphere, the COF is 1.65 at 750 °C, which is considerably higher than at both 500 °C (0.97) and RT (1.28) under 5 N normal load equivalent to 0.16 MPa nominal contact pressure. The tribo-pair demonstrates the lowest COF value at 500 °C in He. Similarly, from the in-situ COF data in Fig. 22a it is noted that the fluctuation of the COF is highest at 750 °C and lowest at 500 °C, under He environment, which can also be inferred by the standard deviation values depicted in Fig. 22b.

Generally, with the increase in temperature and in the absence of major oxidation, the material becomes softer and is expected to have lower resistance to sizable deformation and thus, lower COF values. Here, the sample surface color changes to brownish yellow at 500 °C, confirming oxidation phenomena. However, further investigation showed that the oxide layer is very thin and not even detectable under cross sectional EDS. At this temperature, the alloy is softer compared to RT which in the absence of major oxidation leads to lower COF. This trend is also observed in

previous reports for HT alloy [28,29]. At HT (750 °C), nonetheless, the formation of a harder, brittle and thicker composite layer and its frequent failure leads to an increase in the COF [26].

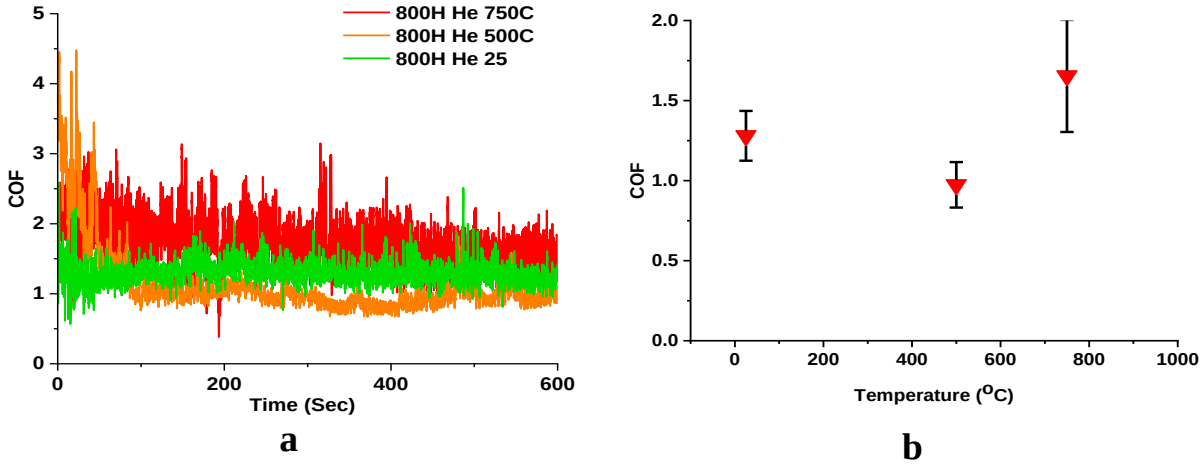

Fig. 22. Alloy 800HT (a) In situ and (b) average COF values for different temperatures in He environment and under 0.04 m/s sliding velocity and 5 N normal load (0.16 MPa).

Fig. 23 shows the average COF values for different normal loads in He condition and under three different temperatures. No specific trend can be concluded for the variation of COF with load (contact pressure), especially taking the standard deviation into consideration. Although the COF is minimum for the middle load of 10 N at RT, it is the maximum at the same load at a high temperature of 750 °C, while at an intermediate temperature of 500 °C the average COF is almost in the same range for all load conditions. Still, the COF has the highest values at 750 °C for all loads, whereas lowest values are measured at the temperature of 500 °C. The reduction of the COF values at 500 °C, compared to RT for 5 N and 20 N load is noticeable. At 750 °C, the COF behavior becomes more extreme where with the combination of higher adhesive wear debris generation and surface roughness on the wear track, the COF at 10 N is the highest. This behavior at 750 °C can be attributed to a mechanically mixed composite layer formation from a brittle oxide layer generated by chemical reaction with the impurities present in He during the experiments at HT.

This composite layer starts breaking and delaminating with continuous unidirectional motion leading to higher roughness on the wear track.

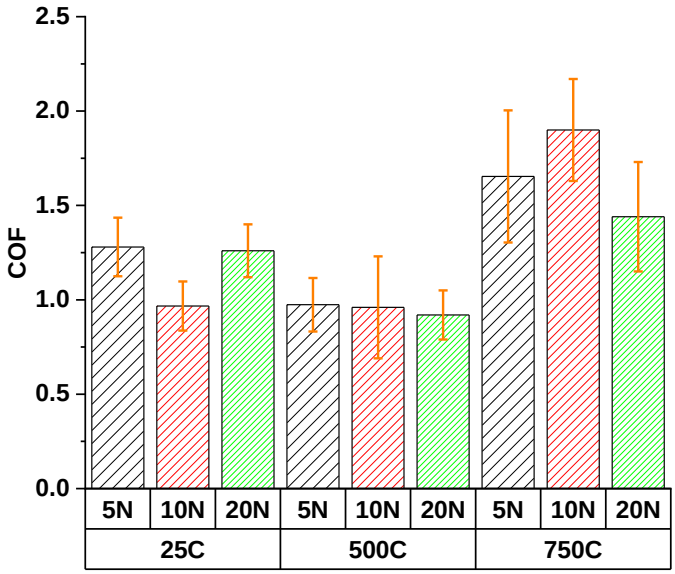

Fig. 23. Average COF for different normal loads in He (sliding velocity of 0.04 m/s, normal contact loads of 5, 10, 20 are equal to 0.16. 0.32. 0.64 MPa, respectively).

The effect of normal load as well as temperature on the wear rate is illustrated in Fig. 24, under He atmosphere. The results clearly show wear rate increase with the increase in applied normal load, as expected. Under this condition and for all contact pressures, the wear rate increases with temperature. Adhesive-abrasive burnishing wear, caused through the disk and pin metallic surface interactions, is predominant at RT. During the RT experiment, no sign of layer formation or material transfer was observed which is confirmed by periodic assessment of sliding surfaces. The wear at 500 °C in He becomes larger slightly since the material softens compared to RT while retaining the COF value lower with the generation of similar type of finer wear debris. At 750 °C, high oxidation rate, and formation and delamination failure of the composite oxide layer on the wear track resulted in enhanced surface wear during the running-in period. The wear rate is then continued with high steady value through large plastic deformation, as well as nucleation and propagation of cracks in more brittle surfaces. The change in wear rate under 10 N is slightly

steeper than that of other loads at 750 °C, which is also more pronounced from the values of wear rate normalized by normal load (specific wear rate), shown in Fig. 24b. The reported values are for 500 cycle experiments and the steep change in wear rate for 10 N load is investigated for higher cycles in a later section.

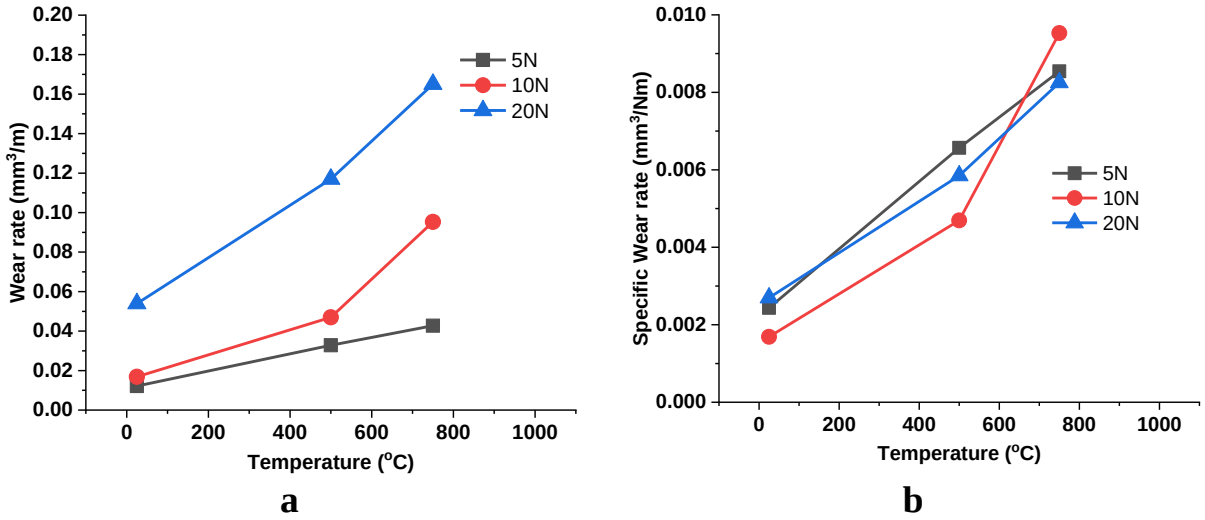

Fig. 24 (a) Average and (b) specific wear rates for different temperatures (0.04 m/s, He, 500 cycles).

4.2. Effect of Environment

The influence of He environment on the sliding wear can be better explained through comparing the He environment data with experiments carried out in air under the same loading and temperature conditions. Fig. 25a depicts the in-situ COF values at three different temperatures in air under 5 N normal load, whereas the average COF values at 750 °C under different normal loads at sliding speed of 0.04 m/s are compared with He atmosphere in Fig. 25b. The in-situ data suggests that the COF stabilizes around the same range of values for both 500 °C and 750 °C in air for 5 N normal load with a longer period of running-in at 750 °C. At 500 °C, the average COF values reduce in a similar fashion to He environment, but the COF values in air are slightly lower compared to He. Under 5 N load, the COF in air 500 °C is 0.71 whereas in He, the value was 0.97. At 750 °C in air, the COF continues dropping after several cycles (running-in period) and stabilizes

at 0.66 for 5 N load. Although this trend in air is not observed in He, similar behavior was, in fact, observed in air according to Refs. [18,19] for nickel alloys. On the contrary, for higher loads of 10 N and 20 N in air, such significant reduction was not identified. The reduction of COF with the increase in temperature for 5 N load is attributed to the glazed layer formed by compacting the wear debris under contact pressure. At HT in air and under higher contact pressures, the glazed layer becomes unstable, cannot sustain the high contact pressure and fails to provide effective wear resistance, which leads to higher COF and wear.

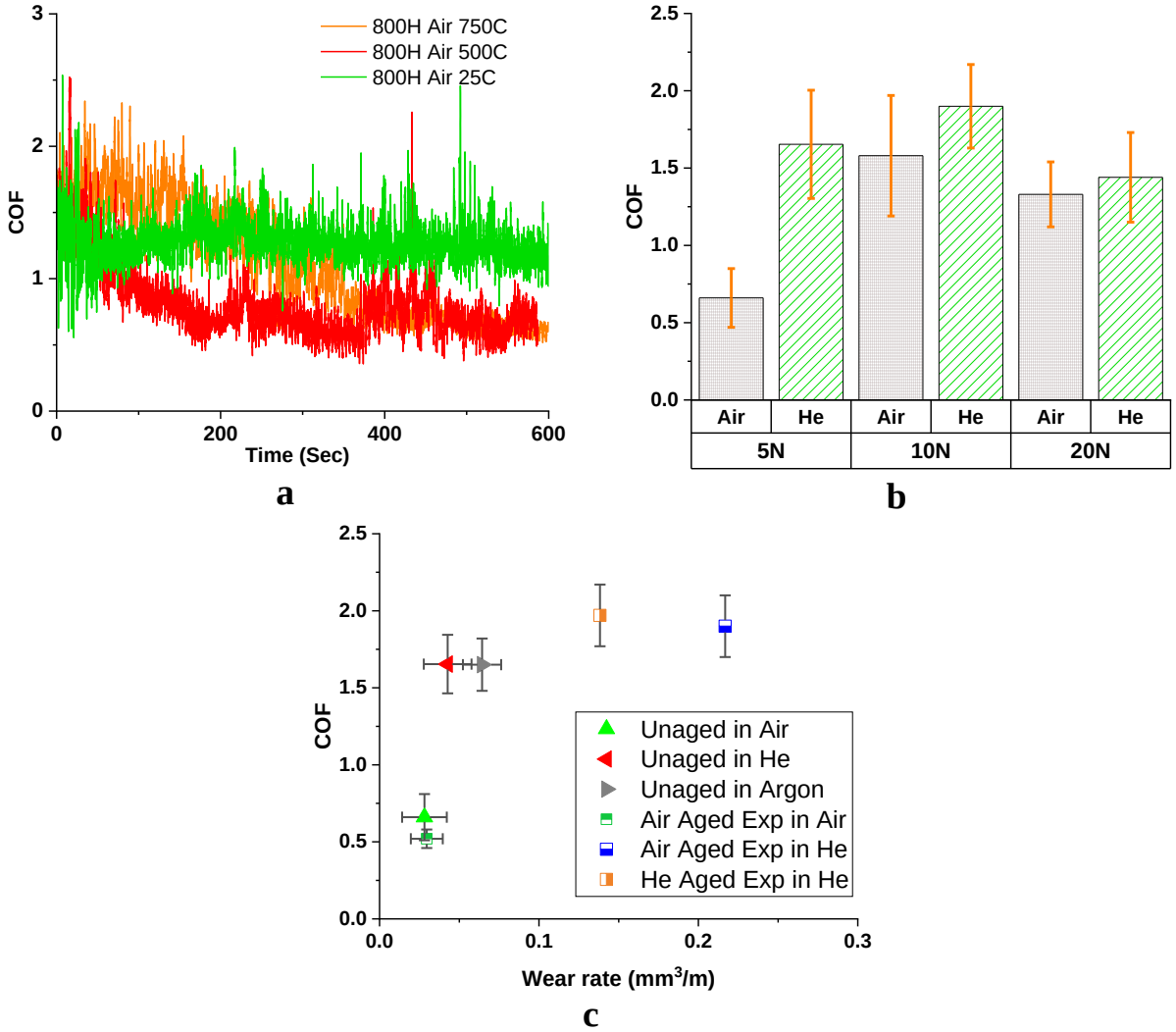

Fig. 25 (a) In-situ COF values in air for 5 N load and sliding velocity of 0.04 m/s, (b) average COF at 0.04 m/s for different normal loads in air compared with He at 750 °C; (c) COF and wear rate comparison of unaged and aged samples tested at 750 °C under 5N and 0.04 m/s. Each experiment was performed for 30 minutes

Furthermore, the 100 hour aged disks and pins are tested under similar parameters in the tribometer to study the effect of aging on friction and wear. The unaged sample is also tested in Argon atmosphere, as shown in Fig. 25c. The tests in Argon exhibited similar friction behavior as He, but slightly higher average wear, with overlapping standard deviation. This indicates that the impurities in He gas has limited effect on friction and wear behavior. The He-aged samples tested in He HT showed high COF of 1.97 with slightly higher deviation. The wear debris consists of the existing oxide from aging, which acted as third body particles during sliding, and increased the wear rate. Comparatively easy removal of the pre-formed oxide on the surface during sliding added to the higher wear. For Air aged samples when tested in HT air, they exhibited low wear rate similar to the unaged samples, and even 20% lower COF. The preformed thick oxide on the surface supported the formation of a load-bearing layer. Afterwards, the air aged samples were tested in He HT, and it resulted in high COF, similar to the He aged sample, but even higher wear. The wear mechanism remained the same as before in both He and air.

The comparisons of the wear rates in air and He environments are presented in Fig. 26a for the temperature of 750 °C at 0.04 m/s sliding speed for different normal loads. A typical 3D confocal optical profiling image of a wear track in shown in Fig. 26b. The wear rate steadily increases with load at 750 °C, irrespective of the atmosphere. Interestingly, under all normal loading conditions, the wear rate values are in very close proximity in He and air, which indicates similar oxidative adhesive wear mechanism in action. The wear rate in HT is dominated by adhesion, crack propagation and delamination of the mechanically mixed oxide layer. The layer on the wear track in both environments shows brittle behavior with low adherence to the bulk metal leading to higher wear rate at higher temperatures.

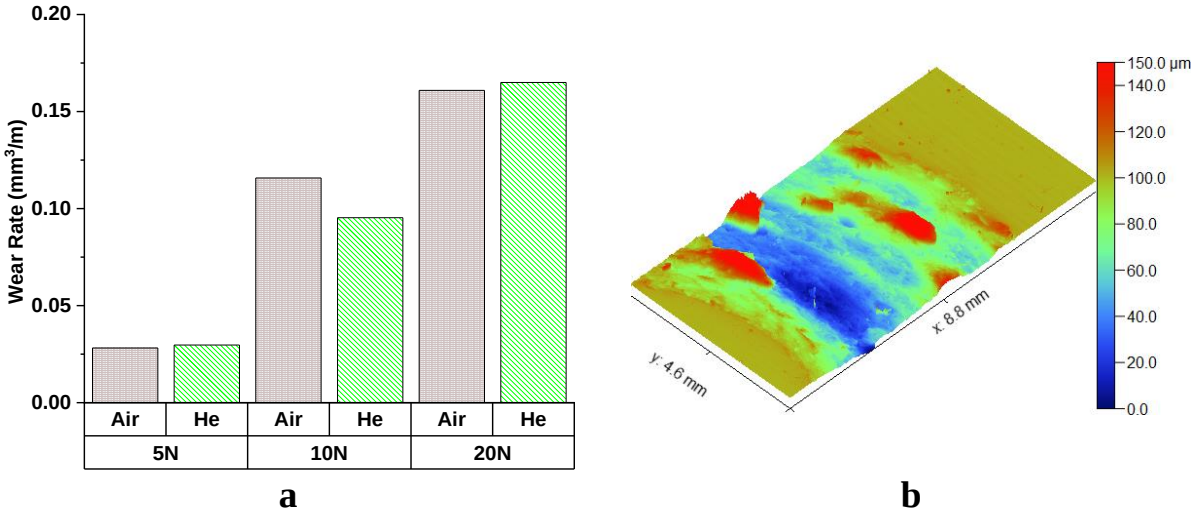

Fig. 26 (a) Wear rate in Air and He environments at 750 °C for various normal loads at 0.04 m/s, 500 cycles, (b) Confocal optical profiling images of wear track in He under 10N, 0.04m/s at 750 °C.

4.3. Effect of Sliding Velocity

Fig. 27 presents COF values as a function of sliding velocity under all normal loading conditions at 750 °C, in both He and air conditions. In HT air atmosphere the COF settles to a lower average value for 5 N load in 0.04 m/s sliding speed, but cannot maintain this value for the higher loads. As shown in Fig. 27a, a similar trend is observed for the sliding speed of 0.1 m/s where the COF is low for 5 N but higher for other load conditions. However, at a higher sliding speed of 0.15 m/s, change in the behavior is observed with lower COF for both 5 N and 10 N, and higher COF under 20 N load. In He, as shown in Fig. 27b, the COF still remains in the higher range above 1.0 for all conditions but shows a slight steady decreasing trend at a high load of 20 N with the increase of sliding speed, and remains in the same range for the other two loading conditions without showing any specific trend.

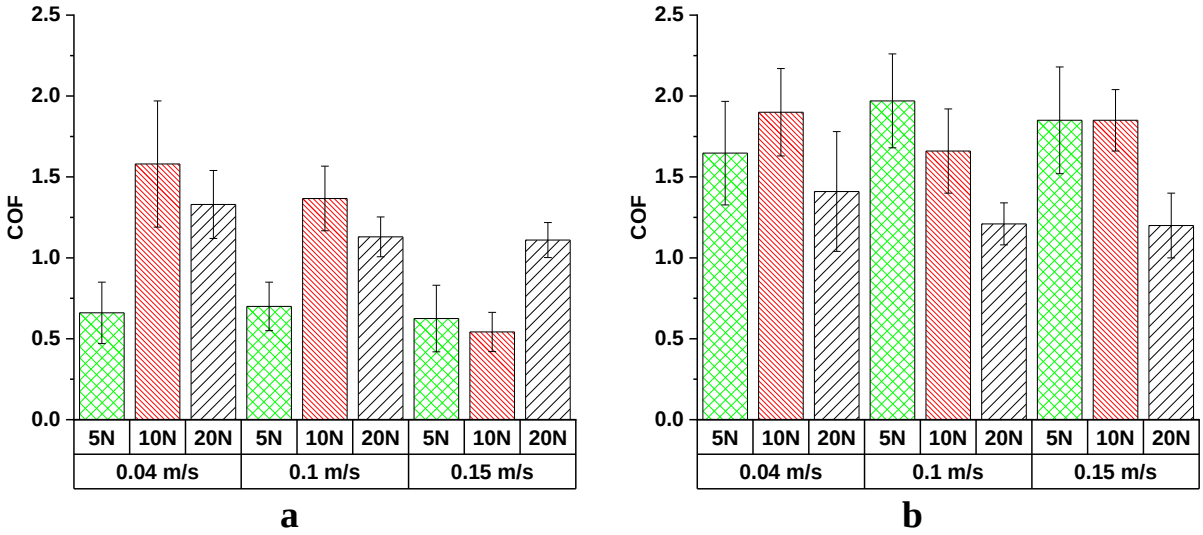

Fig. 27 Effect of sliding velocity on COF at 750 °C for 500 cycle experiments: (a) in air, (b) in He.

4.4. Effect of Sliding Distance

Experiments were performed for three different test durations in He, while other parameters were kept constant at normal load of 10 N, temperature of 750 °C, and sliding speed of 0.04 m/s. The average COF is calculated for the final 30% of the experimental duration, when the COF value is stabilized and is shown in Fig. 28. The 500-cycle test demonstrates almost similar value for average COF as the 1400 and 2700 cycle experiments. In fact, unlike the tests performed in air, the experiments in He atmosphere do not show any clear running-in period with sudden change in COF. Considering the constant and stable test conditions, where COF and wear rate values are stabilized, one can conclude that from a tribological perspective, 500 cycles is adequate duration to accurately quantify and understand the steady-state sliding friction behavior of alloy 800HT at the current experimental conditions.

Nonetheless, specific applications in reactors might involve contacting surfaces in idle conditions for long duration followed by few slow sliding movements. In view of such scenario, it is then worth mentioning that it might never be possible to reach the steady state condition and, therefore, in some practical applications (viz. nuclear reactors) aging is an important factor. In fact, aging

over time changes the top layer of material surface influencing its short-term tribological behavior. Particularly, when a long idle duration is followed by limited number of slow sliding movements, the system can always stay in running-in mode. Aging is not the focus of the current investigation, however, a separate investigation looking into the frictional behavior of samples aged for different durations in He atmosphere is sought in future studies. The wear rate shows a high standard deviation at 500 cycle experiments with a higher average value of 0.09 mm^3/m, compared to other test durations. However, this by itself does not contradict the conclusion of steady-state conditions for 500 cycles. This, in fact, is due to the inclusion of the running-in period (initial oxidation and oxide layer removal) in the total wear rate calculation. As seen, with the increase in the experimental cycles, the deviation in wear rate diminishes as steady-state wear rate gradually overshadows the running-in effect.

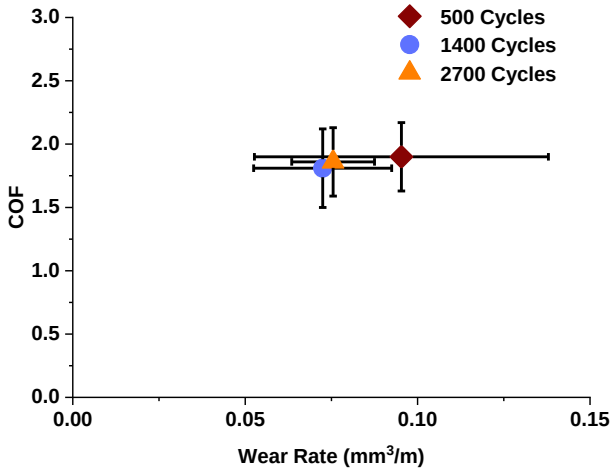

Fig. 28 COF and wear rate comparison under 10 N at 750 °C in He and 0.04 m/s.

4.5. Oscillational (Fretting) Experiments

The HT oscillation experiments were carried out at 750 °C for alloy 800HT using the HTT, which has the capability of unidirectional and oscillatory motions: rotational speeds up to 1000 rpm and oscillation frequencies up to 5 Hertz. Similar to Inconel 617, all experiments were performed at 10 N normal loads (contact pressure of 204 MPa) with an oscillation angle of 120° and max sliding

speed of 0.025 m/s along a circular path of 17.5 mm mean diameter. Data acquisition was collected at 120 Hz for all the tests performed for 10 and 100 cycle oscillations.

Fig. 29 shows representative in-situ COF for the oscillation experiment for an 800HT pin against 800HT disk in both room temperature (RT) and HT under He environment. All conditions are repeated for at least two experiments to ensure consistency. Similar to unidirectional experiments, presented above, at RT, the static COF is lower than the static COF at HT He environment. The COF value remains almost the same for both 10 and 100 cycles (Fig. 29a). In the case of HT He atmosphere, the static COF of alloy 800HT increases with time over the 100 cycles. The static COF in HT He atmosphere for 800HT is 2.98±0.38 during the 10 cycle experiments, whereas it is 3.74±0.59 for 800HT during 100 cycle experiments. All the data reported here for 100 cycle experiments are taken by averaging the value of the final 10 oscillations. The spherical pin with 55.3 mm radius curvature was used in these experiments to ensure better contact. The final contact area on the pin increases with oscillations and is larger after 100 oscillations. But the consistency of the static COF in RT proves that contact area does not have a considerable effect on the COF in this case. The final contact width after 100 oscillations is approximately 1.5 mm at RT and 3 mm at 750 °C. Fig. 29b and c show the optical images of the wear tracks on the disk and pin at HT, respectively. The image shows the presence of adhered wear debris on the wear surface of both pin and disk, which is not seen on the surface of the RT wear track.

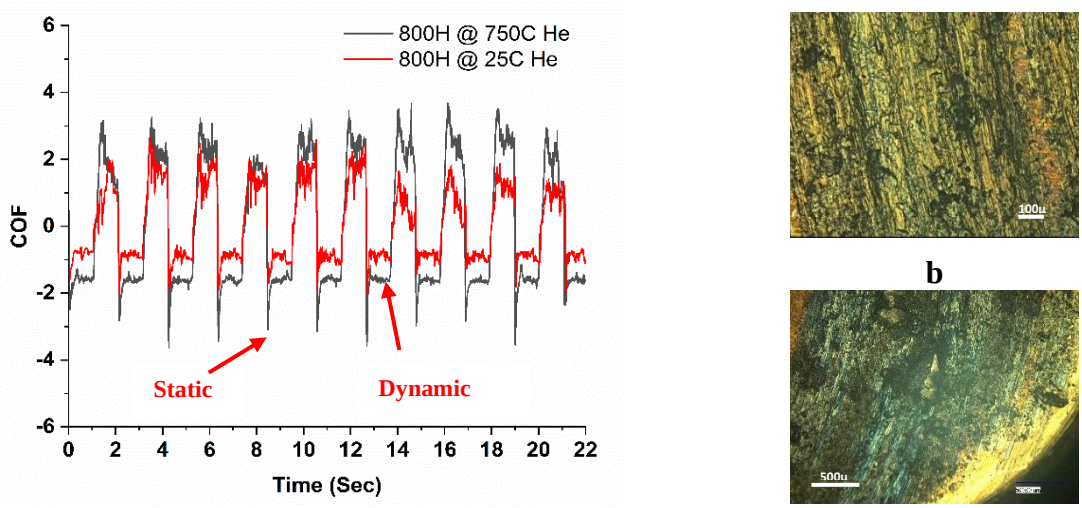

Fig. 29 (a) In-situ oscillation experiment data of alloy 800HT, Alloy 800HT disk (b) and pin (c) surface after 750 °C He experiment.

The SEM images shown in Fig. 30 show the wear track of both RT and HT experiments. The HT wear track shows higher adhesive contact features with a lower amount of loose debris than in RT. The increase in adhesive force between the pin and disk surface at HT along with the increase in contact area could be the reason for the higher static COF in HT He environment [42]. The contact depth at HT He for 800HT is around 25 µm, and 6 µm at RT. The higher contact depth also increases the resistance to sliding and accordingly the static COF.

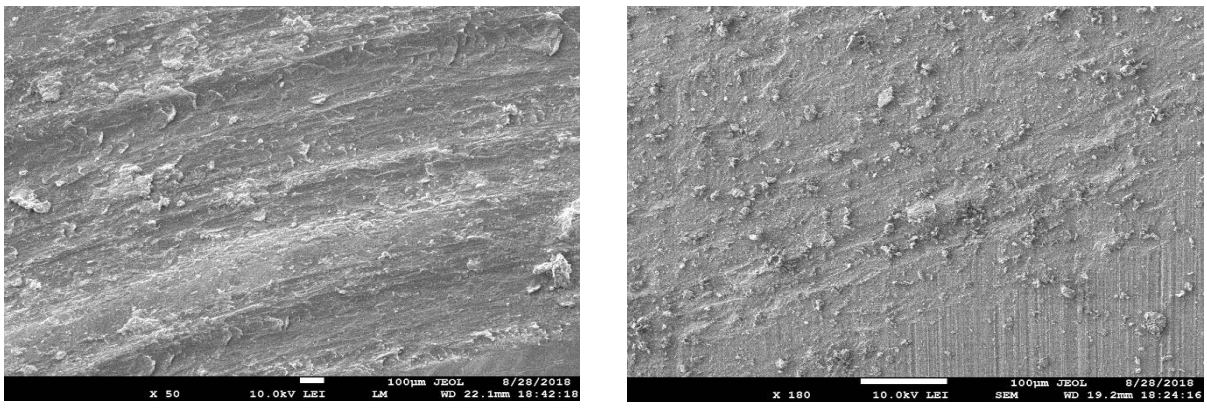

Fig. 30 SEM images of alloy 800HT wear track (a) At 750 °C He (b) At room temperature.

Fig. 31 shows the average static COF for alloy 800HT under 10 N normal load. The possible reason for the increase in the static COF at HT He environment for alloy 800HT could be the higher wear rate leading to higher contact depth and increased plowing resistance. It is noted that the static COF of both alloys is around 1.5 to 2.5 times higher than the dynamic COF reported above for unidirectional experiments. The dynamic COF values during these oscillation experiments are within the error limits reported, which will stabilize over time as mentioned earlier. According to the static COF reported here and in section 3.5, Inconel 617 has proven its superior performance over alloy 800HT.

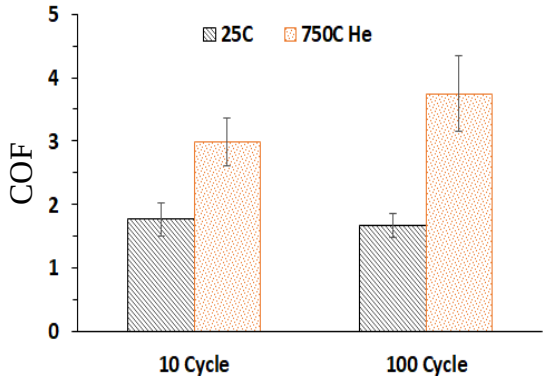

Fig. 31 Average static COF in RT and HT He environment for Alloy 800HT.

4.6. Characterization and Discussion

4.6.1. Surface Morphology

Fig. 31 shows the SEM images of the surface oxides on the sample surface as well as on the wear track (at different magnifications) in both air and He at 750 °C (10 N normal force and 0.15 m/s sliding speed). The arrows on the micrographs denote the sliding direction. The SEM pictures show the matrix oxide surfaces with fairly analogous morphologies in air (Fig.28c) and He (Fig.28i) atmospheres except that the surface oxide particles in air are more crystalline and larger in size, as compared to the oxide formed in He. A scattered and discontinuous compacted glazed layer formed by oxide debris is found (Fig. 32d, e, f) on the wear track in HT air. Similar patches

of the compacted glazed layer are seen on the pin surface which resulted in lowering the COF even with discontinuous glazed layer on the disk.

This form of compacted surface is found only on the samples showing lower COF in HT air atmosphere, namely for 5 N load at all three speed conditions and for 10 N load at 0.15 m/s sliding velocity. Therefore, the observed compacted oxide layer seems to be the key factor to reduce the COF on alloy 800HT at HT environments. For other loads and sliding velocities, the conditions are not favorable to generate a compacted oxide that can support the contact pressure, as explained in section 3.3. The wear track surface morphology of these conditions is similar to the HT He samples, as shown in Fig. 32(j, k, l) where no such layer is observed. The clear presence of adhesive wear patches are seen on the wear track with the surface almost free of wear particles, implying the dominance of adhesive wear mechanism for successive process of repeated sliding [43,44].

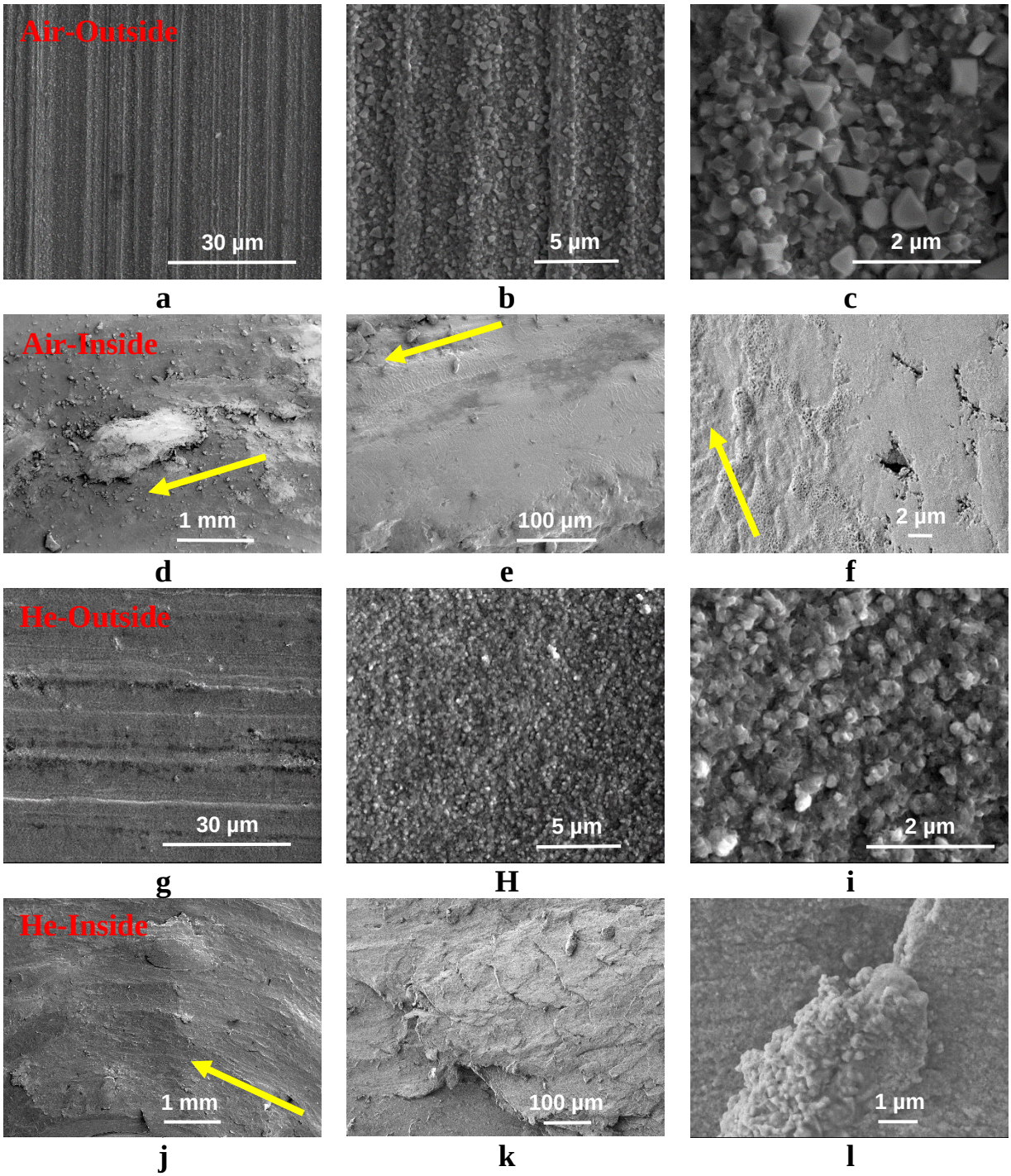

Fig. 32 SEM images of specimens at 750 °C under 10 N load at 0.15 m/s sliding speed (a, b, c) in air outside the wear track (matrix), (d, e, f) in air inside wear track, (g, h, i) in He outside the wear track, (j, k, l) in He inside wear track.

4.6.2. SEM/EDS

Examining the wear track cross-section SEM images shown in Fig. 33, it is clear that for the same duration experiments, the mixed oxide layer generated in air is thicker than the one in He (~10.0 μm in air and ~4.0 μm in He). Note that layer thickness varies from point to point depending on the location of the wear track, as the surface is changing during sliding. The mixed layer thickness is observed to vary from 1 μm to 20 μm in air and from 0.8 μm to 10 μm in He. The lamellar formation of the metal bulk and oxide mixed layer is evident for both He and air conditions in Fig. 33, which happens mainly due to the repeated unidirectional sliding under adhesive contact. The formation of cracks under the layer is also visible in both conditions. The initial wear of the surface is dominated by abrasive wear mechanism at HT, caused by crack nucleation, and propagation in the hard and brittle oxide layers. Removal of the oxide layer increases the adhesive contact between the bare metal surfaces and consequently, adhesive wear becomes dominant. Tangential shear during sliding motion and under compression at the strongly bonded adhesive contact generates flake-like particles followed by nucleation and propagation of cracks in combined compression and shear fracture modes [43]. The subsurface crack seen in Fig. 33 a, c is an example of crack propagation after continuous sliding under compressive and shear load.

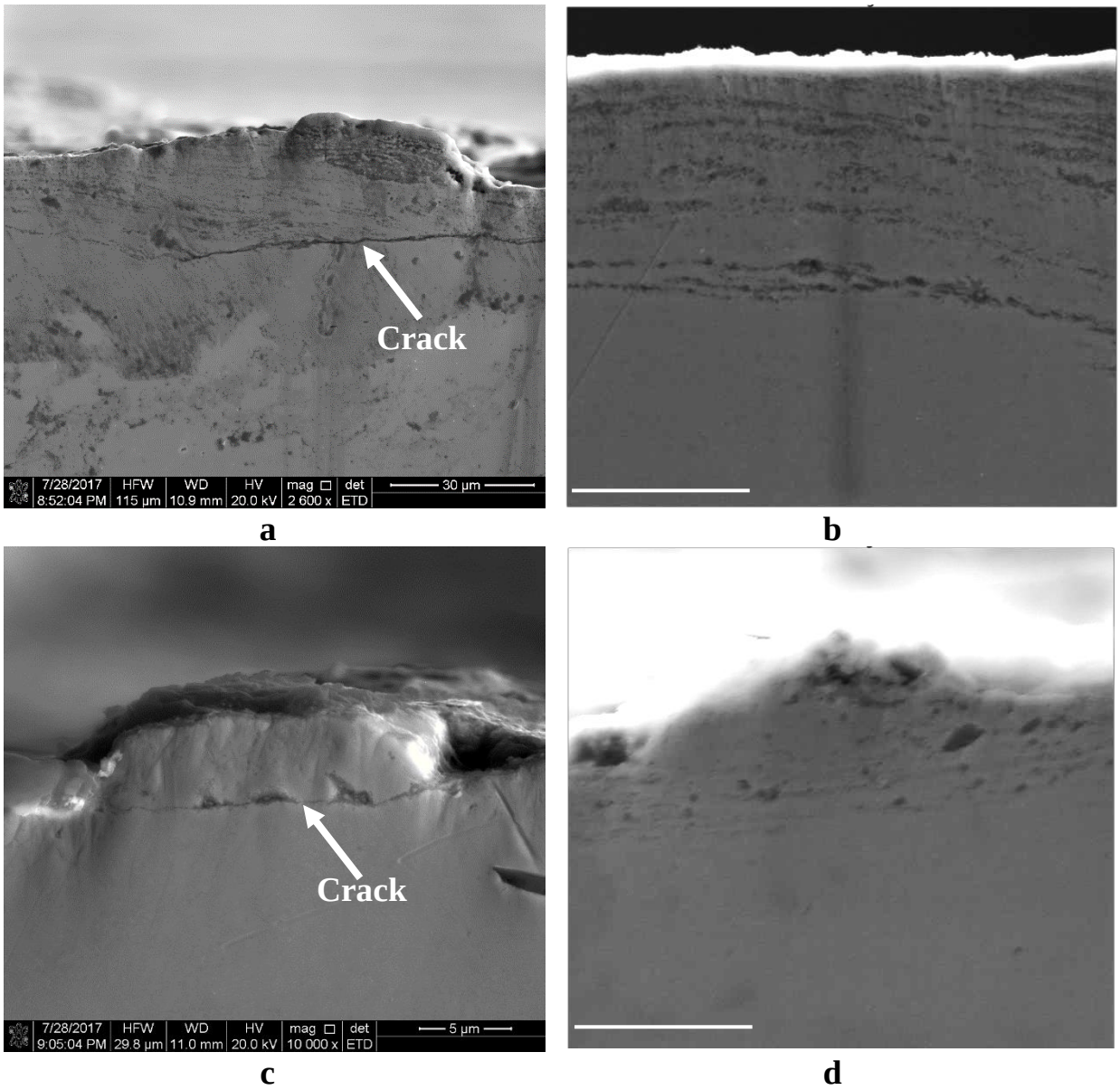

Fig. 33 Cross section SEM images on the wear track at 750 °C, 5 N, 0.04 m/s (a, b) air, (c, d) He.

The EDS results at the cross-section of the wear tracks show thicker oxide penetration in air at HT, compared to He environment. The cross-section SEM images in Fig. 34 show the top surface of the wear track which is a mixing zone of oxides and alloy elements creating non-uniform layers. This mixing zone is referred to as mechanically mixed layer (MML) [26,45]. The thickness of this MML for alloy 800HT at 750 °C under 5N normal load is 18 µm and is observed only in air, whereas in He environment more brittle composite layer (CL) is observed. The MML has better

interface strength with the substrate, as compared to CL and, therefore, CL has the tendency to get detached from the wear surface leading to higher wear rates [26]. This diffused adhesive interface of MML and ability to transfer the load to the substrate reduces the wear rate. The quick removal of the oxide debris from the wear track in He at 750 °C is likely the reason of higher thickness of oxygen penetration depth on alloy 800HT wear track.

EDS analysis was performed on different areas of the wear track and surfaces outside the wear track to investigate the chemical composition of the oxide layers (see Fig. 35 for the case of 750 °C, 5N, 0.04 m/s). The EDS analysis on the area outside the wear track shows evidence of the oxide layer enriched by Fe, Cr and Ni in both air and He atmospheres. The chemical composition of the surface oxide layer in air inside and outside the wear track areas are similar, except a slight increase of the oxygen content. This is indicative of the oxide formed on the parallel distributed needle-like phases outside the wear track and the compacted debris in the trench as seen in Fig. 32c, f. For the samples tested in He, the composition remained similar both inside and outside the wear track surfaces, except for the wear debris scattered over the track. Inside the wear track surface in He, the oxygen content is found to be reduced, compared to some areas outside the wear track. At some of the points on the area outside the wear track, high amount of titanium is also found which is believed to be the titanium oxide generated in the grain boundaries. Comparing the wear surfaces in air and He in Fig 31(b, d) it is seen that the compacted oxide debris on the surface in air has higher oxygen content, confirming the retention of oxide on the track, resulting in lower COF values observed in air.

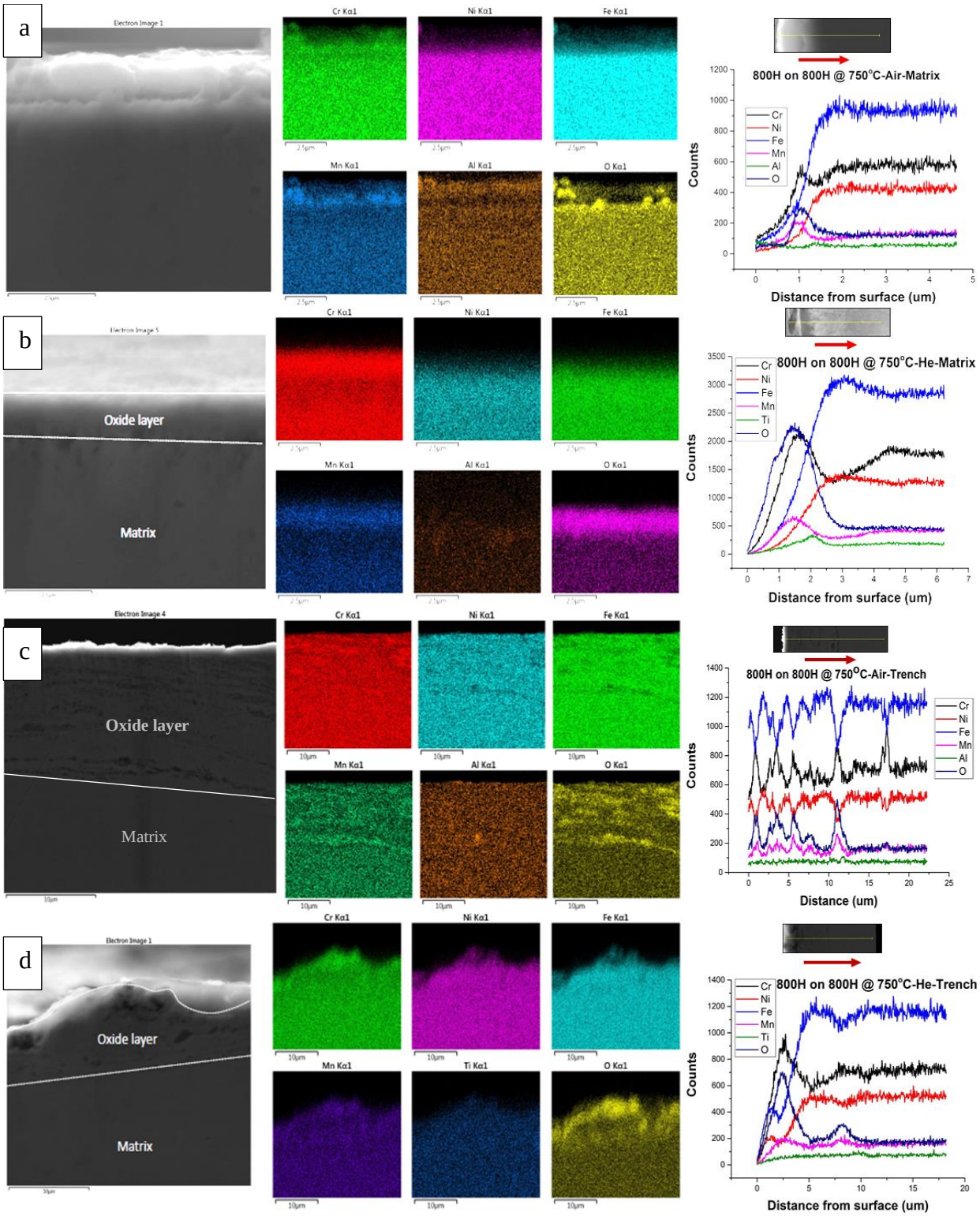

Fig. 34. Cross section SEM images and EDS map of alloy 800HT at 750 °C, (a) Air outside wear track, (b) He outside wear track, (c) Air on wear track and (d) He on wear track.

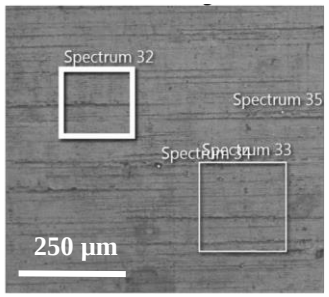

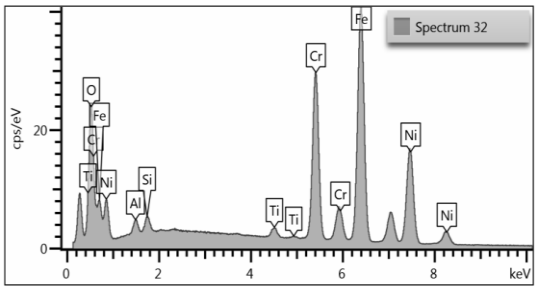

Element	Wt%	Wt% Sigma	Atomic %
O	10.17	0.12	27.75
Al	1.14	0.03	1.84
Si	1.02	0.03	1.59
Ti	0.87	0.03	0.79
Cr	20.14	0.07	16.91
Fe	41.30	0.10	32.28
Ni	25.35	0.09	18.85
Total:	100.0		100.0

a

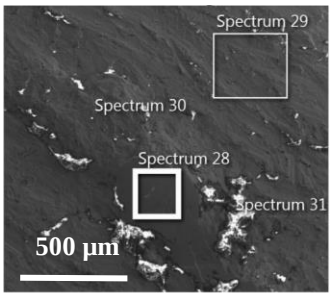

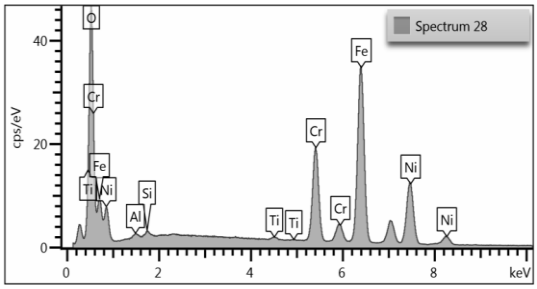

Element	Wt%	Wt% Sigma	Atomic %
O	24.54	0.13	52.87
Al	0.41	0.03	0.52
Si	0.37	0.02	0.46
Ti	0.31	0.02	0.22
Cr	14.18	0.06	9.40
Fe	39.33	0.11	24.28
Ni	20.86	0.09	12.25
Total:	100.0		100.0

b

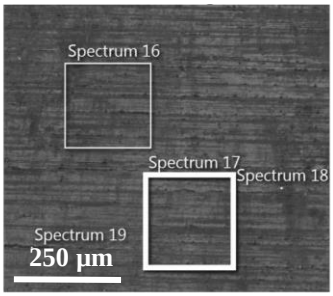

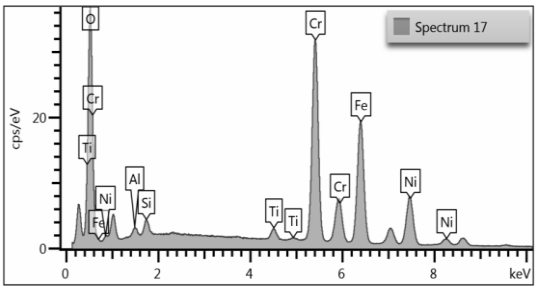

Element	Wt%	Wt% Sigma	Atomic %
O	22.10	0.14	48.60
Al	0.81	0.03	1.06
Si	1.12	0.03	1.41
Ti	1.21	0.03	0.89
Cr	31.21	0.10	21.11
Fe	27.68	0.10	17.44
Ni	15.86	0.10	9.50
Total:	100.0		100.0

c

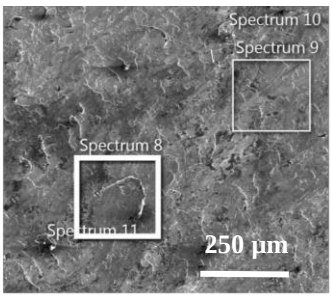

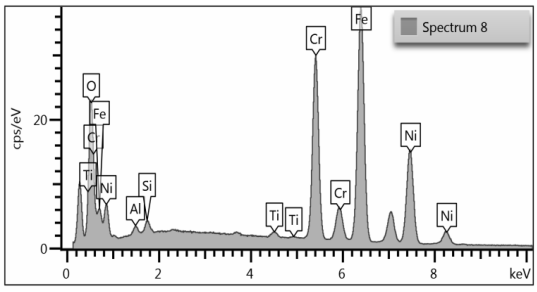

Element	Wt%	Wt% Sigma	Atomic %
O	10.52	0.12	28.66
Al	0.68	0.03	1.10
Si	0.77	0.03	1.19
Ti	0.49	0.02	0.45
Cr	21.63	0.07	18.13
Fe	41.05	0.10	32.03
Ni	24.86	0.10	18.45
Total:	100.0		100.0

d

Fig. 35. SEM pictures and EDS analysis of samples (a) in air and outside wear track, (b) in air and inside wear track, (c) in He and outside wear track, (d) in He and inside wear track (750 °C, 5N, 0.04m/s).

4.7. Summary

A comprehensive study of the tribological performance of superalloy 800HT in the complicated environment of VHTR requires covering multiple variables in the experimental tests. The conditions evaluated in this study may not cover the whole spectrum of applications but provide helpful guidelines in finding optimum operating conditions for nuclear reactor applications. The following conclusion can be drawn from this study:

(1) In air and with the increase in temperature, the formation of a protective glazed layer in conjunction with the increase in material softness results in lower friction. This is true only for lower contact pressures, while the layer fails at higher contact pressures. The stability of this protective layer increases at higher sliding speed;

(2) At 500 °C and 750 °C He, friction and wear stay high for all conditions due to the surface oxide instability, its brittleness and subsequent crack initiation/propagation through oxide layer in low oxygen partial pressure, resulting in the generation of larger size wear debris;

(3) In He atmosphere, under all contact loads studied here, the specific wear rate shows a linear increasing trend with load, while the COF does not show any specific correlation with contact force;

(4) No significant change in wear rate or COF values in He atmosphere is observed for the sliding velocities examined here (in the range of typical VHTR applications). However, in air environment, higher sliding velocities influence the formation of the compacted glaze layer and as a result, reduce friction and wear; and

(5) At 500 °C and 750 °C in both air and He, Fe-Cr-Ni rich oxide layer is present. The variation of the mixed oxide layer thickness is significant under the wear track (between 1 to 20 μm) independent of the environment for the 500 cycle experiments.

In chapters III and IV the detail tribological behavior of the two alloys were explained with fundamental characterization. But to understand and answer the fundamental reason behind their behavior, it required more detail characterization of the sample surfaces undergone tribological experiments, meaning the wear tracks. In the next chapter the tribochemical changes of the Inconel 617 sample surfaces will be explained.

CHAPTER V
TRIBO-CHEMICAL ANALYSIS OF INCONEL 617 [4]

Sliding contact under HT conditions is influenced by both mechanical and chemical changes of the surfaces coming in contact, as well as the bulk material properties. The tribological behavior is further affected by the environment and gaseous content present during the HT contact. The influence of temperature and He environment on the tribological characteristics of Inconel 617 have been presented in a previous chapter. There are several studies which showed the chemical changes under He impurity at HT (thermal load only) [14,15,23] but there is none showing the effect of simultaneous presence of tribological action and gas atmosphere on the chemical changes of Inconel 617 (co-presence of thermal/chemical/mechanical load). This chapter focuses on the chemical study performed on the surface of Inconel 617 under He and air atmospheres at HT of 950 °C and the tribochemical changes taking place at the surface/interface contact. Subsequently we explain how these changes may have affected the tribological behavior of Inconel 617. To deconvolute the contribution of wear and temperature, aging experiments were performed at 950 °C for different times to follow the kinetics of oxide formation. Following the tribological studies, the surfaces inside and outside the wear tracks of the alloy were studied using detailed characterization tools including Scanning Electron Microscopy (SEM), Energy Dispersive Spectroscopy (EDS), X-ray Diffraction (XRD), Raman spectroscopy, and Secondary Ions Mass Spectroscopy (SIMS).

[4] Reprinted with permission from "Tribo Chemistry of Inconel 617 during sliding contact at 950 °C Under Helium Environment." by Rahman MS, Polychronopoulou Kyriaki, Polycarpou AA. J Nucl Mater 2019;521:21–30. Copyright 2019 by Elsevier B.V.

5.1. Surface Morphology

Fig. 36a shows an optical image of the microstructure of as-received Inconel 617. Figs. 32b-d show the microstructure evolution (SEM) images due to oxidation in air and He environments. The average grain size in the as-received material is 30-40 μm, in agreement with Ref. [7]. The samples were polished to 30-40 nm root-mean-square roughness, before the oxidation experiments. The roughness of the sample surfaces was measured using a Tencor P-6 stylus profilometer. Formation of grain boundary ridges is observed on the oxidized samples, both in air and He atmospheres. The rate of growth is different in He, compared to air, which is evident from Figs. 32c and 32d. Specifically, the grain boundary ridges are more evident in air than in He, after 100 hr. On the other hand, the width of the ridges is wider in He. After 500 hr of oxidation, the width of the ridges increases further and the amount of grain boundary visible in a specific area has also been reduced, compared to the 100 hr aged sample.

From the EDS analysis it is found that the grain boundary ridge is mainly formed by Ti-oxide along with Cr-oxide. It is also limited by the amount of Ti available until depletion. It is believed that, over time, some of the grain boundary ridge growth slowed down and got covered by the Cr-oxide, and only few of the grain boundary ridges grew to be visible. For the case of the 500 hr aged sample, spallation of oxide is observed on few places near the grain boundary regions (Fig. 36d inset), which might have occurred during the cooling process due to the difference in thermal expansion of metal compared with oxide, and the internal stress difference between the oxide on the grain boundary and the nearby surface. Spallation reveals the presence of dense Cr-

oxide in layer formation below the irregular morphology on the surface, as shown in the inset of Fig. 36d.

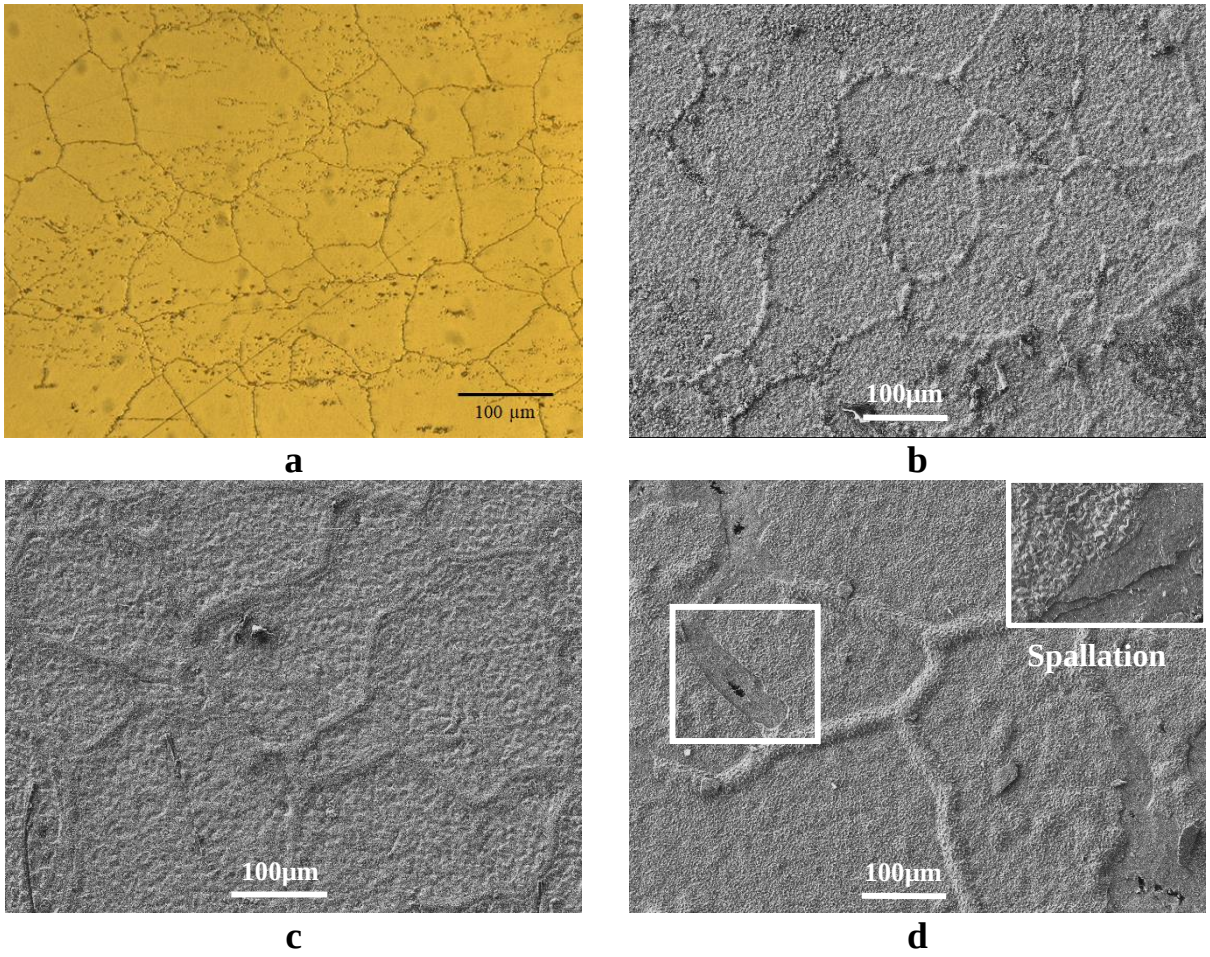

Fig. 36. Microstructure evolution of Inconel 617: (a) optical image of virgin sample; SEM images of samples aged at 950 °C (b) 100 hr air, (c) 100 hr He, (d) 500 hr He. All images obtained at the same magnification.

Fig. 37 shows magnified surface morphologies inside and outside the grain boundary ridges. At HT air atmosphere after 100 hr, the presence of high oxygen content helps the formation of larger nodular grains of oxides on the surface. On the grain boundary, the oxide shows the presence of more porosity than the other areas. At low oxygen partial pressure of He atmosphere, the formation of oxide is influenced greatly by the chemistry of impurities present. SEM image of the 100 hr aged samples in He (Fig. 37d) shows the presence of less nodules and less crystalized

regions, compared to the surface exposed in air environment. The surface oxide shows the presence of few larger nodules on an oxide layer with mode intergranular gaps. The grain boundary shows comparatively larger crystalized oxide. The presence of minute quantities of CO_2 and H_2O in He is believed to be the control parameter of creating nodular oxide particles facilitating the crystallization of oxides, as discussed in Refs. [46–49]. The 500 hr aged samples in Fig. 37g-i show growth in the crystal size and is similar to what is observed for the100 hr aged samples in air. Both grain boundary and surface show similar morphology and crystal size with no intergranular gaps.

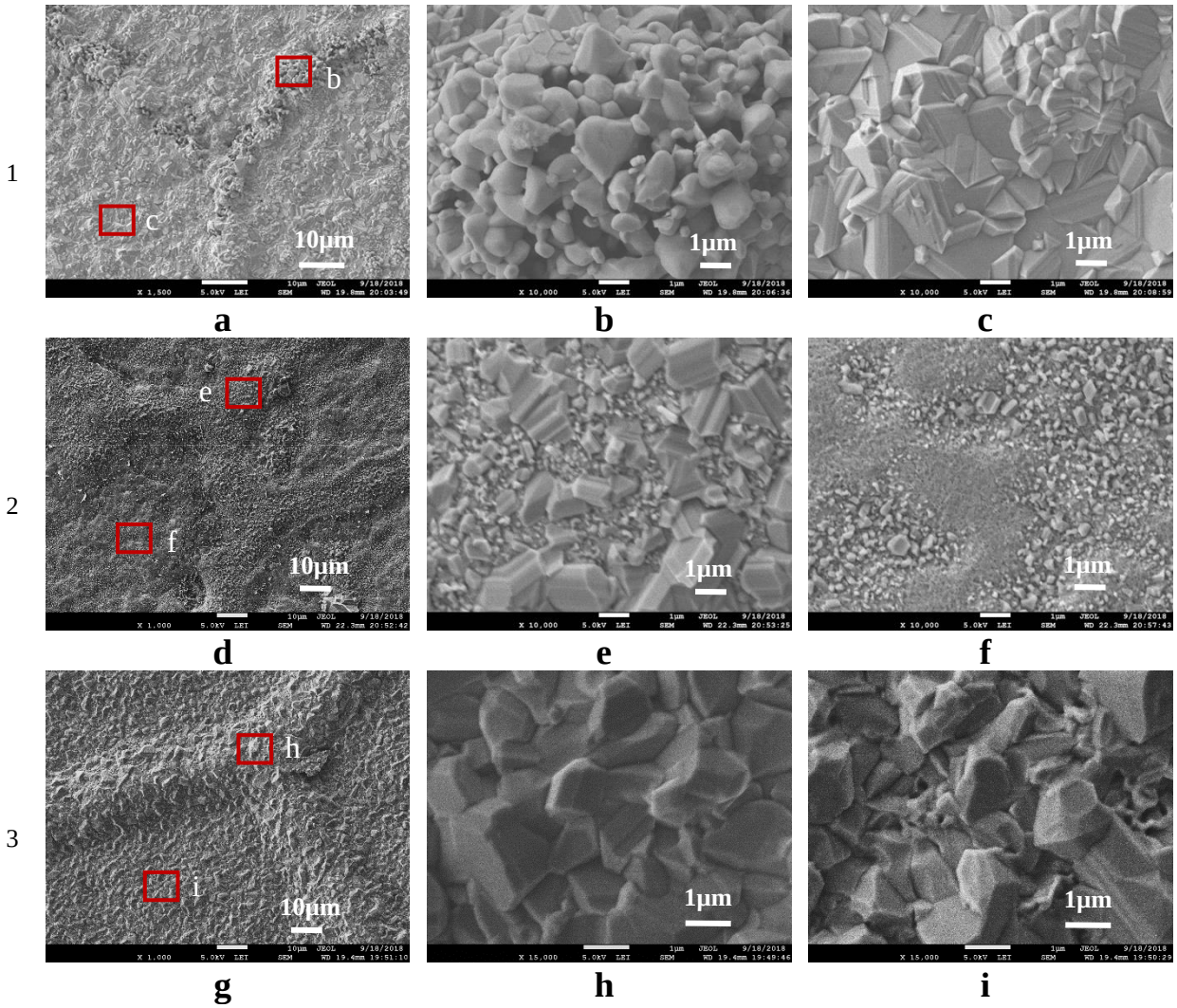

Fig.36. Surface morphologies after oxidation for Inconel 617 at 950 °C: (1) 100 hr air, (2) 100 hr He, (3) 500 hr He. Images shown in (b,e,h) are taken on the grain boundary ridges, and (c,f,i) are taken on the surface.

Cross-section backscatter (BS) SEM images in Fig. 38 show the presence of internal oxidation of aluminum along the grain boundary, and Cr-oxide on the surface. Fig. 39 shows the

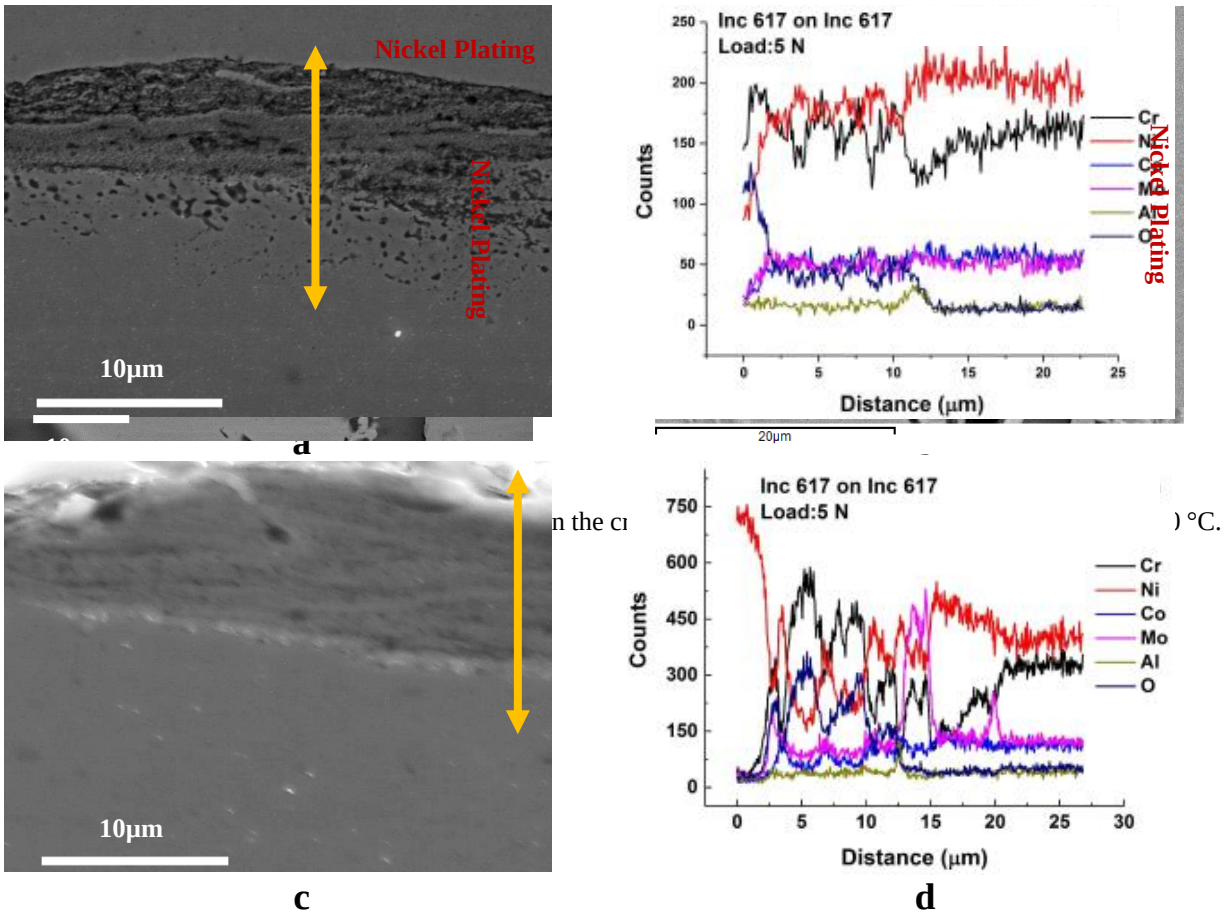

Fig. 39. Cross section SEM images and EDS line scans of Inconel 617 at 950 °C under 5N load inside the wear tracks: (a, b) He, (c, d) Air.

cross-section SEM and EDS line scans for the samples undergone tribological experiments. The EDS line scan in Fig. 39b, which is along the grain boundary, shows a spike of Ti on the surface, which is in line with the EDS data on the grain boundary. On the other hand, EDS on the cross section of the samples following HT tribological experiments in both air and He atmospheres reveal the presence of Cr-rich oxides on the wear track, with internal oxidation of aluminum. On the wear track, the thickness of the oxide layer varies between 1 – 10 µm. In case of air atmosphere,

at the end of the oxide layers there is high concentration of Mo, whereas in He atmosphere the concentration is the same as the matrix after the oxide layer.

5.2. XRD Analysis

Fig. 40a presents the XRD patterns obtained over the 100 hr aged Inconel 617 samples. X-ray diffraction patterns are collected over a 1 mm^2 area for 30 min duration using an X-ray beam energy of 40 keV 40mA (λ=1.54056 Å) and step size of 0.005º. The X-ray patterns indicate that the diffraction peaks for the underlying metal substrate are clearly noticed for all samples. This means that X-rays completely penetrate the oxide layer thickness, and all the oxide phases are detected. Inconel 617 at 500 °C in He or air atmospheres, did not show any prominent peaks other than the substrate. Some of the previous works indicated the presence of small amount of Cr_2O_3 and $(Ni/Mn)Cr_2O_4$ spinel close to the substrate peaks [50–52]. The oxide scales of Inconel 617 at 950 °C in Fig. 37a are strongly composed of Cr_2O_3 and $(Ni/Mn)Cr_2O_4$, whereas other oxides such as TiO_2 and $MnTiO_3$ are clearly detected in He, but weakly detected in air.

In contrast to the previous results in air [14], NiO peaks are not detected. Fig. 40b presents the XRD patterns obtained over the Inconel 617 specimen following the tribotesting under different conditions as described above. X-ray diffraction patterns are collected inside and outside the wear tracks. By comparing the XRD patterns obtained inside and outside the wear track at 500 °C, no changes are observed under He. On the contrary, when the testing is performed at 950 °C drastic differences can be observed. The diffraction peaks that are observed outside the wear track

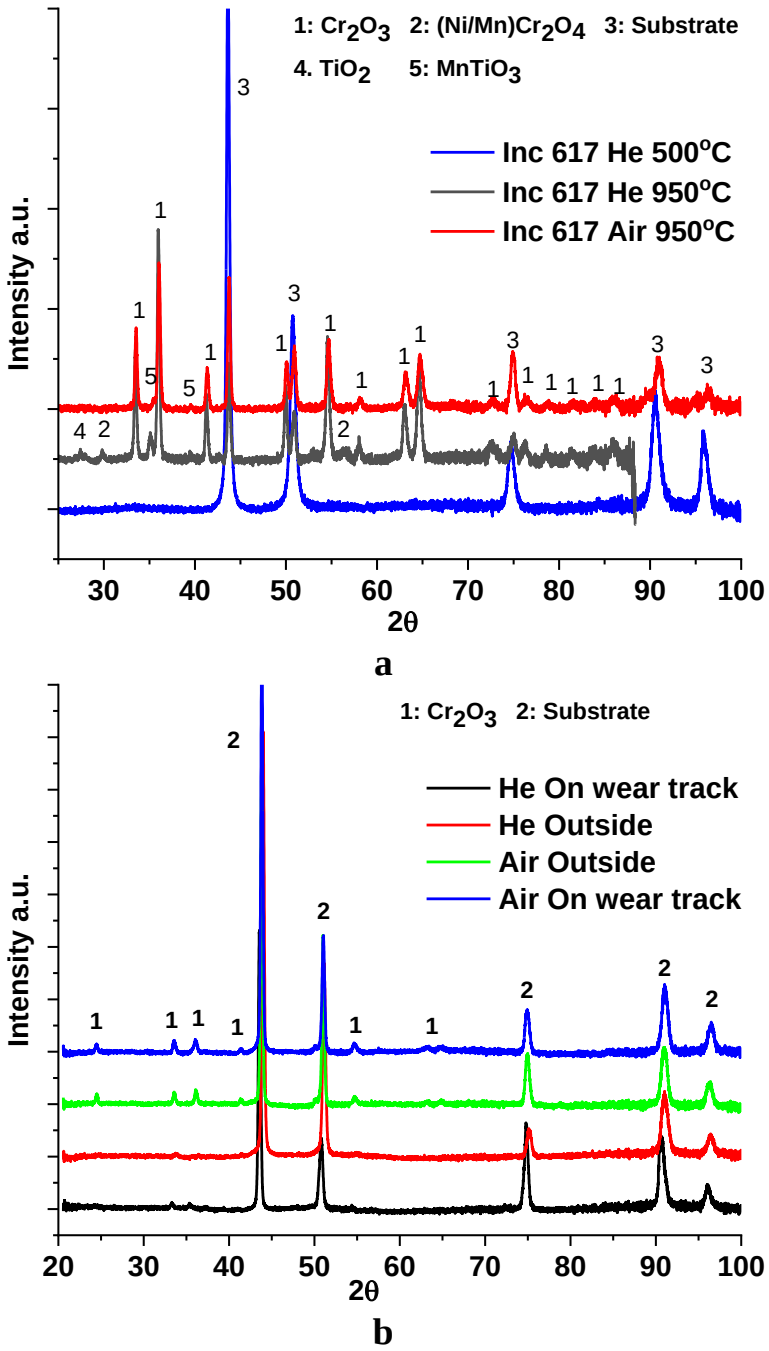

Fig. 40. XRD data on (a) samples aged for 100 hr; (b) inside the wear tracks created at 950 °C tribotesting.

corresponding to the Cr_2O_3 are not present in the diffraction patterns inside the wear track. This can be understood on the basis of Cr_2O_3 being a sacrificing mediator to contribute to reduce or increase the COF. The easy cracking and removal of oxide indicates that the oxides in He have lower shear strength compared to the oxides generated in air.

At 500 °C, there is neither sign of significant formation of Cr_2O_3 (likely due to the slower kinetics of oxidation), nor any other oxide on the surface, which indicates that the reduced COF is the result of only thermal softening. Also, inside the wear track, the XRD pattern appears shifted to higher diffraction angles, a result that implies that the lattice of Inconel 617 phase has contracted under compressive stresses. On the contrary, under air, Cr_2O_3 particles are continuously formed and thus replacing the ones that have been exhausted and retained on the wear track, as compacted layer. Thus, Cr_2O_3 particle XRD peaks can still be traced at the end of the experiments. This can be the reason for the lower COF of 0.45 in the case of air, compared to 1.4 in He.

5.3. Raman Analysis

Raman spectroscopy is a unique tool to investigate the oxygen sublattice and provide complimentary structure information to the XRD analysis. Fig. 41a presents the Raman spectra acquired over the specimens received from the above described tribotesting, under different gas and temperature conditions. Fig. 41b presents the Raman spectra of samples aged in He over different durations of time. Referring to Fig. 41a, the Raman bands at 554 cm^{-1}, 616 cm^{-1} and 685 cm^{-1} include contributions from formed phases, such as Cr_2O_3, $NiCr_2O_4$, $FeCr_2O_4$ spinels, and/or $(Ni/Fe)Cr_2O_4$ mixed spinel phase. As the duration of tribotesting is increased, the crystallization/ formation of the spinel type oxides is becoming more developed [53,54]. This is expected as a spinel solid solution requires more time to be formed. The spinel disordering is obvious based on the asymmetry of the bands (e.g., band at 685 cm^{-1}). A possible reason for this disordering can be the presence of oxygen vacant sites as the metal oxides are mixed towards the formation of the spinel structure, as well as the short duration of the experiment, compared to the time scale of formation of the spinel structure.

Given that the tribotesting and the aging tests were both conducted in He at 950 °C, by comparing Figs. 37a and 37b there is a clear effect of the wear mechanism in the phases formed. The latter is clear based on the differences on the peaks at <1000 cm^{-1} (different population of oxides) and on the peaks at high wavenumber (>1200 cm^{-1}). Also, in Fig. 41a, a red shift can be observed in the Raman spectra as the aging is prolonged. This coincides with enhanced diffusion of some of the constituent metal atoms (Cr, Co, Ni), enhancing their incorporation into the Cr_2O_3 crystal structure.

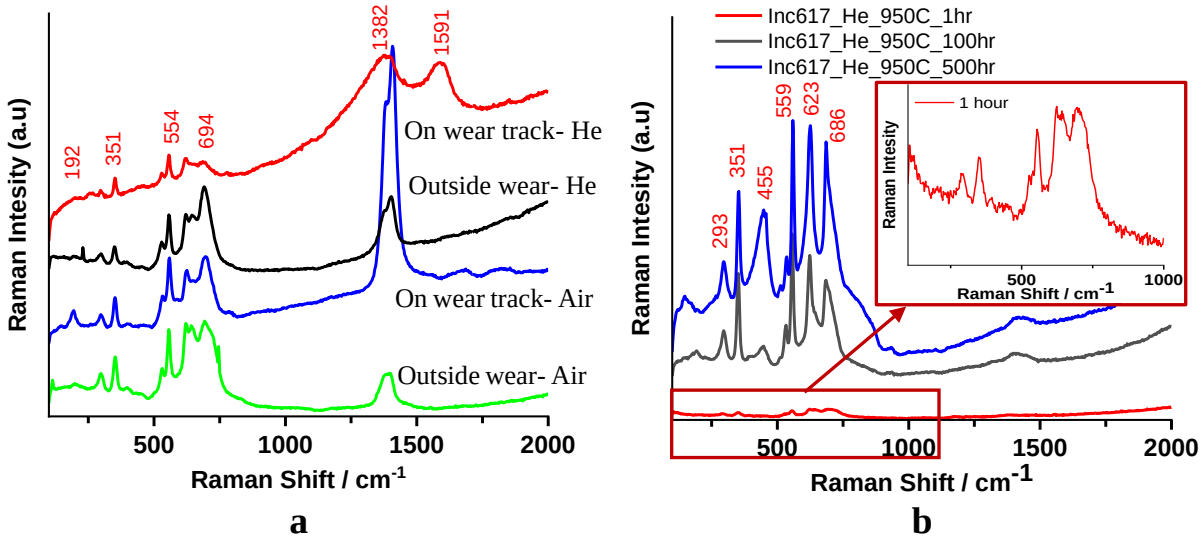

Fig. 41. Raman spectroscopy data on (a) tribotested samples, (b) He 950 °C aging samples of Inconel 617.

5.4. TOF-SIMS Depth Profiling

Fig. 42 presents the TOF-SIMS depth profiles that were acquired over the Inconel 617 specimens, following tribotesting under He and air environmental conditions, both outside and inside the wear tracks. Outside the wear tracks of Inconel 617 (in He atmosphere), the presence of high Cr and O concentration was noticed, which corroborates for a Cr_2O_3-rich surface, in agreement with the XRD and Raman results. At intermediate depths (sub-surface), Cr_2O_3 depletion is noticed, where Ni and Co-rich oxides start revealing. This behavior of the outward diffusion,

temperature-driven of Cr, is in agreement with the literature for Inconel 617 [15]. Inside the wear track, the profiles are different, as Cr_2O_3 and CoO are observed. The latter is most likely diffused on the surface from greater depths.

Similar trend with CoO, is observed for NiO. The diffusion profile with depth explains the coexistence and concomitant formation of the mixed spinel structures observed using Raman spectroscopy. It is interesting to note that Cr_2O_3 depletion rate, as we move to sub-surface, follows fast kinetics inside the wear track under He, whereas in air the depletion is lower. This suggests that while performing the tribo-experiments under air, the Cr_2O_3 has formed in greater depths as well, and thus can be detected. Under air, on the very top surface of the oxide, enrichment of Ni and Co-based oxides was observed, along with dominant Cr_2O_3 at a very thin layer.

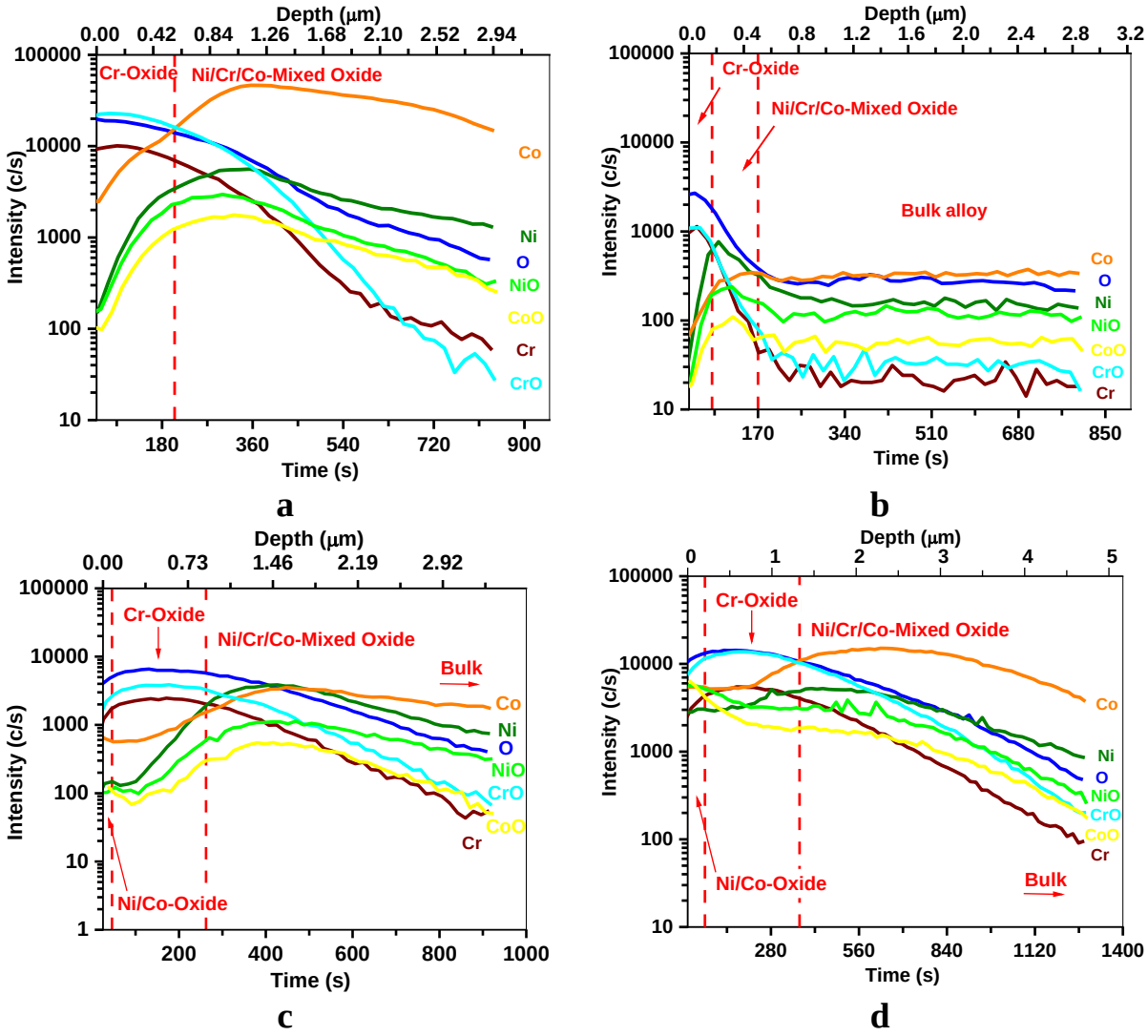

Fig. 42. TOF-SIMS elemental depth profiles of Inconel 617 tribotested samples at 950 °C (a) He outside wear track, (b) He inside wear track; (c) Air outside wear track, (d) Air inside wear track.

5.5. Summary

The combined mechanical and chemical changes of Inconel 617 surfaces are uncoupled through designed tribological (mechanical and chemical) and aging (chemical only) experiments. From the tribological experiments, both the COF and wear rare values were higher in He environment, compared to air atmosphere. The aging studies highlighted the oxidation processes and how they contributed to the evolution of different types of oxides (e.g., spinels and simple oxides). An evolution from asymmetric to more symmetric Raman peaks, demonstrated the

transition to less disordered spinels. As metal oxides are vital in the tribological behavior their depth distribution was measured using TOF-SIMS. Cr_2O_3 was predominant on the surface, while in sub-surface Ni/Co/Cr oxides were found. Cr_2O_3 depletion rate follows fast kinetics in the sub-surface inside the wear track under He, whereas in air the depletion is lower. The next chapter will detail the tribochemical analysis of alloy 800HT.

CHAPTER VI
TRIBOCHEMICAL ANALYSIS OF ALLOY 800HT [5]

6.1. Surface Morphology

The surface morphology of the alloy aged in He and air environments for 100 hours is shown in the SEM images of Fig. 43. Two very different ways of the grain boundary (GB) ridge evolution is observed for He and air environments. From Fig. 43a (air atmosphere), it is clearly visible that the area on the GB is lower in height, compared to the surrounding surface. On the other hand, under He atmosphere, the GB ridge rises higher than the surrounding area. The surface of the oxide in air, other than the GB, shows multiple number of holes on the surface of different size and shape (Fig. 43c). These openings are believed to be the result of gaseous product discharge during the formation of the oxide. The grain boundary valley does not show similar structure. The surface is mostly covered by nodular-like structures with several larger openings, as seen in Fig. 43b.

The oxide generated on the surface in He does not show any such formation of openings at the investigated magnification of SEM. The surface in He, as seen in Fig. 43f, is more homogeneous with nodules of around 1 μm size created by small oxide crystals attached together shown by red dashed square. The nodules might have gaps between them, and two or more nodules can merge together to generate larger (aggregated) nodules over time. The surface on the GB shows oxides with merged nodules. The crystals on the GB are larger compared to the surface oxide crystals.

[5] Reprinted with permission from "Tribochemical changes of alloy 800HT under sliding contact at elevated temperature in impure helium environment." by Rahman MS, Polychronopoulou Kyriaki, Polycarpou AA. *Wear* 2020. Copyright 2020 by Elsevier B.V.

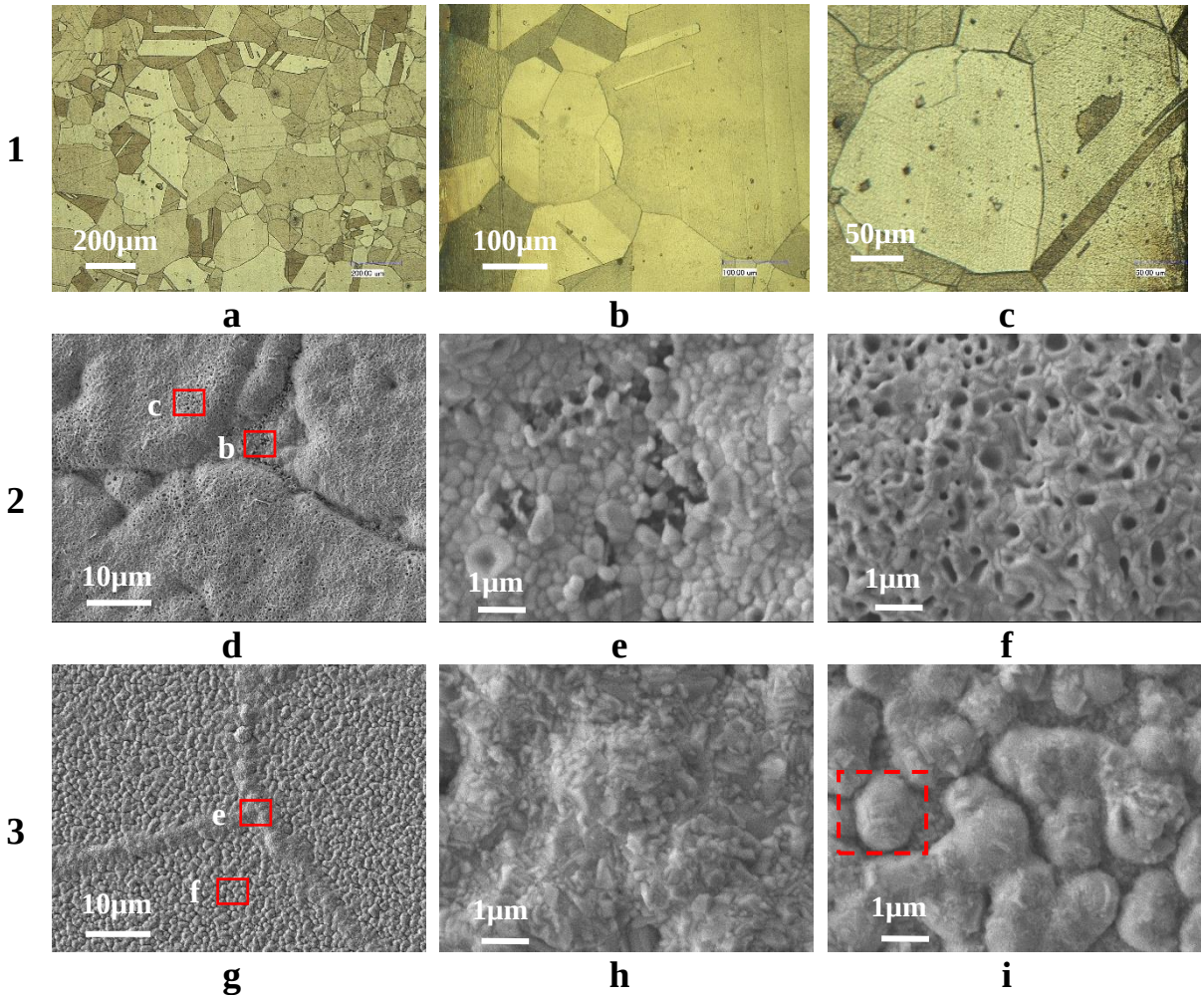

Fig. 43. (1) Optical micrograph of as-received alloy 800HT polished and etched (a-c). SEM surface morphologies after oxidation of Alloy 800HT at 750 °C: (2) 100 hr air, (3) 100 hr He. Images shown in (e and h) are taken on the GB ridges, and (f and i) are taken on the surface. The red dashed square in (i) is showing the nodule-like structure of the oxide.

Fig. 44 depicts the EDS map performed on the GB and surrounding surface of 100 hour aged samples showing the dominant elemental distribution. The elemental distribution map in Fig. 44a, for the sample in air confirms the presence of oxygen on the GB region with a rich presence of chromium (Cr), titanium (Ti), manganese (Mn), and nickel (Ni), compared to the surrounding surface. The surface other than the GB is mostly covered by iron-rich oxide along with Mn. Ni is found all over the sample surface but with very small concentration.

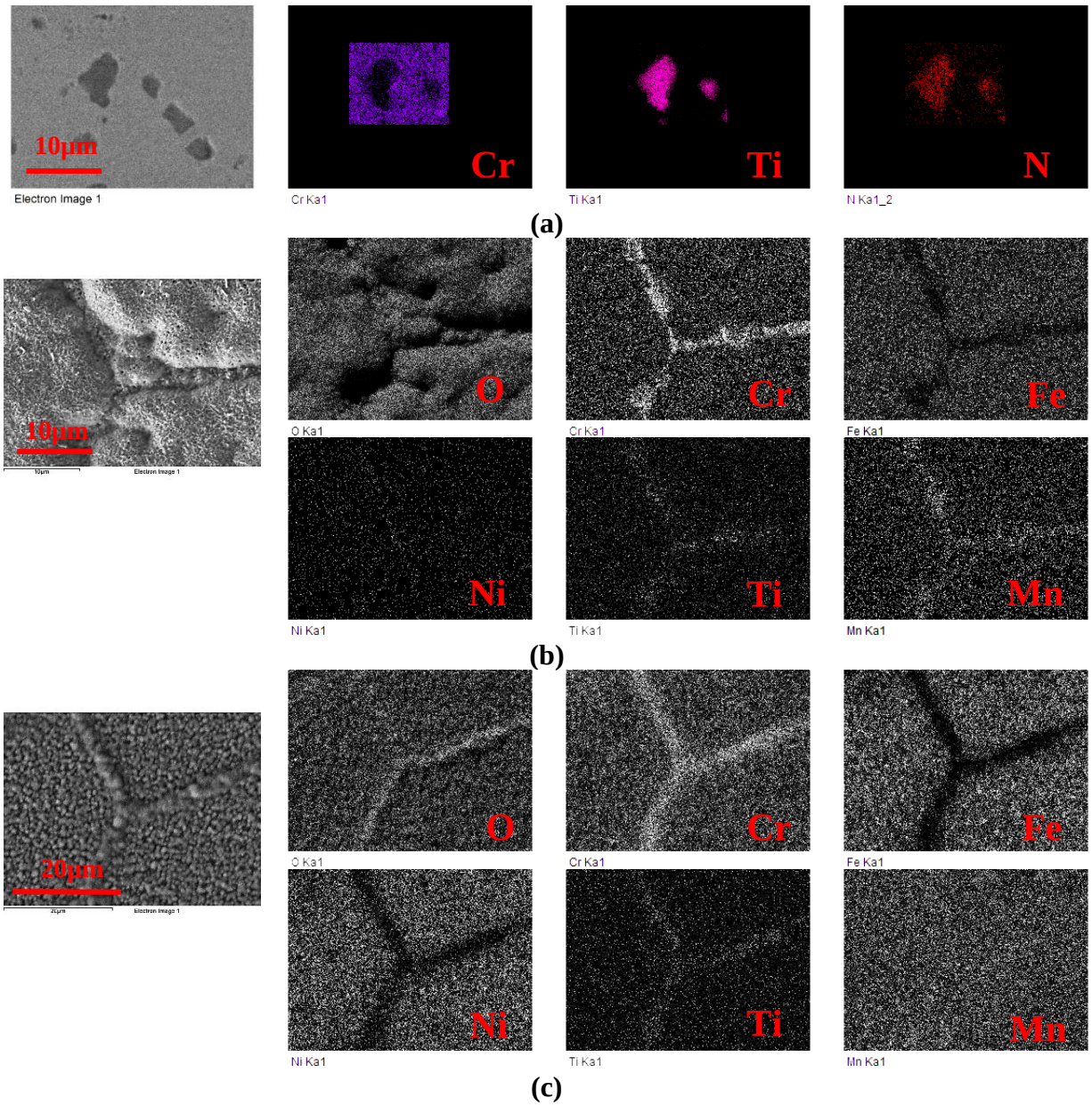

Fig. 44. SEM images and EDS analysis of samples (a) virgin 800HT, aged at 750 ºC for 100 hr: (b) in air, (c) in He.

The EDS map analysis of the sample in He shows different qualitative elemental presence. The presence of oxygen is found all over the sample surface and with slightly higher concentration on the GB region, indicating higher oxidation in the area which could be the reason of height gain of the GB. The GB shows high concentration of Cr with presence of Ti and Mn, but minimum presence of Fe. The rich presence of Ti on the GB, compared to the surface, is evidence that the

GB is rich with Ti-based oxide. The surface oxide in He shows presence of Fe and Cr with Mn and Ni. The surface map in He shows comparatively higher amount of Ni present than in air.

For more insight, quantitative EDS analysis is performed on and outside the GB locations showed in Fig. 45 and the outcomes are listed in Table 5. As expected during EDS map, in air, Iron (Fe) is more dominant on the surrounding areas with 56.87 wt.%, whereas on the GB it is only 27 wt.%. On the other hand, composition of Cr jumped to 22 wt.% on the GB, whereas it is only 4% on the surrounding area. Wt.% of Ni is also increased on the GB with traces of Ti, Si, and Al, which is not found on the areas other than GB. For the sample aged in He, the oxygen wt.% is about 44% on the GB and 29% on the surrounding surface. The surface oxide is rich with Fe (23.89%) and Cr (25.76%) with the presence of Ni, Mn and Ti whereas, the GB oxide is mostly Cr rich (44.2%) with presence of Ti. So, the major difference between the GB oxide in air and He is the composition of Fe, Cr and Ti.

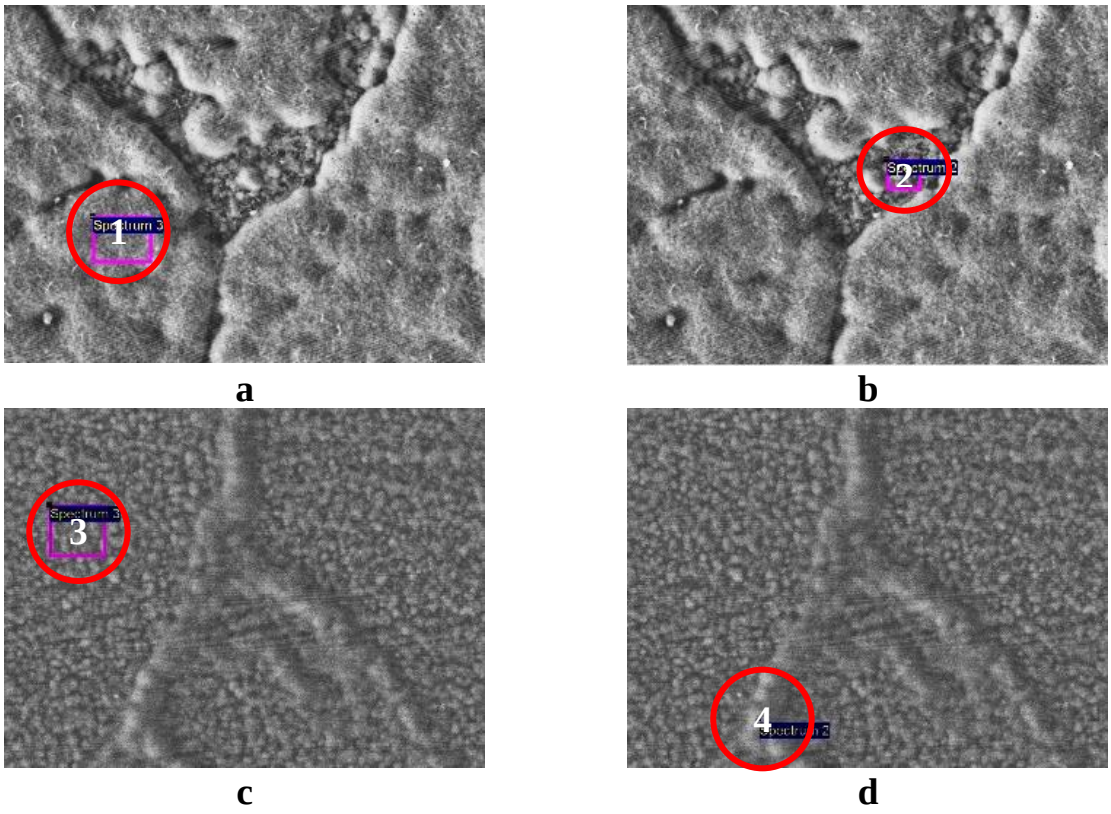

Fig. 45. SEM images showing quantitative EDS analysis locations of samples aged at 750 °C for 100 hr: (a) outside grain boundary in air, (b) on grain boundary in air, (c) outside grain boundary in He, (d) on grain boundary in He.

Table 5
Quantitative EDS analysis of Alloy 800HT aged at 750 °C for 100 hr on locations showed in Fig. 45

Location (Fig. 45)	1	2	3	4
Composition (wt%)				
O	33.48	32.59	29.12	44.33
Al	-	0.45	0.86	-
Si	-	0.81	1.06	-
Ti	-	1.33	0.69	4.34
Cr	4.45	22.10	25.76	44.20
Mn	1.51	4.31	4.50	2.71
Fe	56.87	27.72	23.89	2.97
Ni	3.10	10.02	14.11	1.45
Cu	0.59	0.67	-	-
Total	100	100	100	100

6.2. XRD Analysis

Fig. 46a presents the XRD patterns obtained over the 100 hr aged samples. The X-ray patterns clearly show the diffraction peaks for the underlying metal substrate for all samples, indicating the complete penetration of the X-ray through the oxide layer thickness, and all the oxide phases are detected. Comparison of the XRD data acquired following oxidation in He at 500 °C, He at 750 °C and air at 750 °C is shown in Fig. 46a. It demonstrates that phases only from the substrate can be observed when the experiments were performed at 500 °C (mild conditions), whereas temperature raise to 750 °C caused acceleration of oxidation and thus Cr_2O_3, Fe_2O_3 and other spinel phases peaks emerged. Previous studies on alloy 800HT oxidation, in supercritical water, superheated steam and in He, mentioned the presence of Fe-Ni spinel and Cr2O3 [50,52,55–57].

In the case of the samples after tribo-experimentation under air at 750 °C, the oxidation was more pronounced as it can be seen by the sharper peaks. In Fig. 46b, the 20-100 2theta diffraction patterns can be seen for the cases where the experiments were run under, He and air, for both inside and outside the wear tracks. In Fig. 46c and 45d, a zoom in for the peaks at 43^o and 51^o of Fig. 45b is presented. For the experiment under air, it is seen that the peak at 43^o is shifted to lower angles inside the track, whereas in He the opposite is valid. This type of shift is associated with the different type of stresses, tensile or compressive developed during the thermal treatments, respectively. Tensile stresses are due to the oxides' formation and lattice volume expansion favored in the air atmosphere. The oxide-related phases were noticed only outside the wear track. It seems that inside the wear track during the contact/sliding the oxides formed were purged away under He atmosphere. This coincides with the higher COF measured under He atmosphere and the known role of oxides in tribo-chemistry and lubrication (decrease of the COF) [58]. On the contrary, in the case of air the purged-out oxide is being replenished.

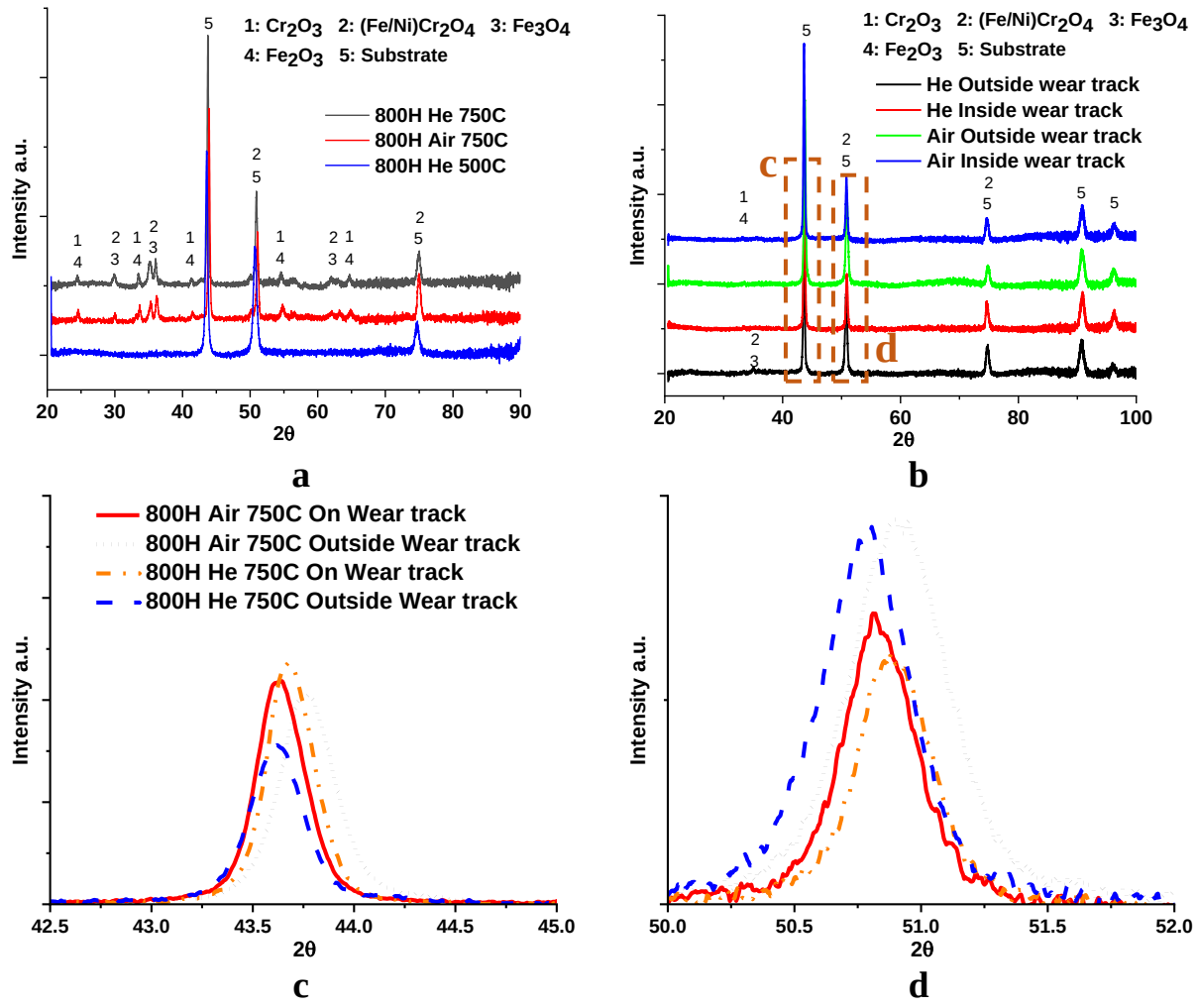

Fig. 46. XRD data on (a) samples aged for 100 hr; (b) inside and outside the wear tracks after tribotesting at 750 °C; (c and d) zoomed-in XRD data from the wear track showing the shift of peaks.

6.3. Raman Spectroscopy Studies

Raman spectroscopy is a unique tool to investigate the oxygen sublattice and provides complimentary structural information to the XRD analysis. Fig. 47a presents the Raman spectra for samples oxidized (aged) at different conditions (He and air) for 100 hr and also at two different temperatures, namely 500 °C and 750 °C. Literature suggests identical Raman shifts at around 550-556 cm^{-1} for Cr_2O_3, at 295 and 408-414 cm^{-1} for Fe_2O_3, at 671 cm^{-1} for Fe_3O_4, at 693-707 cm^{-1} for $NiFe_2O_4$, and at around 686 cm^{-1} for $FeCr_2O_4$[59–65]. The main Raman shift of $(Fe,Cr)_3O_4$

or $Fe_{3-x}Cr_xO_4$ spinel oxide varies from 671 cm^{-1} to 686 cm^{-1} and $(Fe,Cr)_2O_3$ or $Fe_{2-x}Cr_xO_3$ corundum oxide varies from 502 cm^{-1} to 553 cm^{-1} based on the x-value in between 0.0 to 2.0 [66].

As showed in Fig. 47, characteristic peaks corresponding to Cr_2O_3 were found; namely at 353 and 558 cm^{-1}. Furthermore, for the mixed spinel $(Fe,Ni)Cr_3O_4$ the characteristic peak was found at 683 cm^{-1}. It seems that the temperature affects dramatically the kinetics of metal oxides formation (500 vs. 750). In particular, during aging, the crystallization/ formation of the spinel type oxides is becoming more developed/increased under air at the extreme conditions of temperature (750 °C) [54,67]. The sample aged at 500 °C shows the characteristic peaks of Fe_2O_3 at 219 cm^{-1}, 289 $cm^{-1}$and 408 cm^{-1} along with the $(Fe,Ni)Cr_3O_4$ spinel but not the Cr_2O_3 peaks. There is presence of $(Fe,Cr)_2O_3$ corundum peak in 512 cm^{-1} to 538 cm^{-1} for both 100 hr aged sample in He and air at 750 °C. The formation of spinel is more dominant and under He at the extreme temperature of 750 °C it is more pronounced. This is expected as a spinel solid solution requires more time to be formed. The spinel disordering is obviously based on the asymmetry of the peaks (e.g., band at 683 cm^{-1}). A possible reason for this disordering can be the presence of oxygen vacant sites as the metal oxides are mixed towards the formation of the spinel structure, as well as the short duration of the experiment, compared to the time scale of formation of the spinel structure. Fig. 47b presents the Raman spectra obtained under He and air inside and outside the wear track. In the presence of He, at 750 °C some of the oxides have been 'spent' during the sliding (e.g., the double peak in the region (1000-1600 cm^{-1}). These peaks correspond to some type of carbonization that took place in the presence of impurities in He gas. In the presence of air, under sliding conditions new oxide phases are formed as indicated by the emerged peaks at <500 cm^{-1} and 1250-1500 cm^{-1}, which is identical to the Raman peaks of Fe_2O_3 (at 222 cm^{-1}, 289cm^{-1}, 414 cm^{-1} and 1333 cm^{-1}).

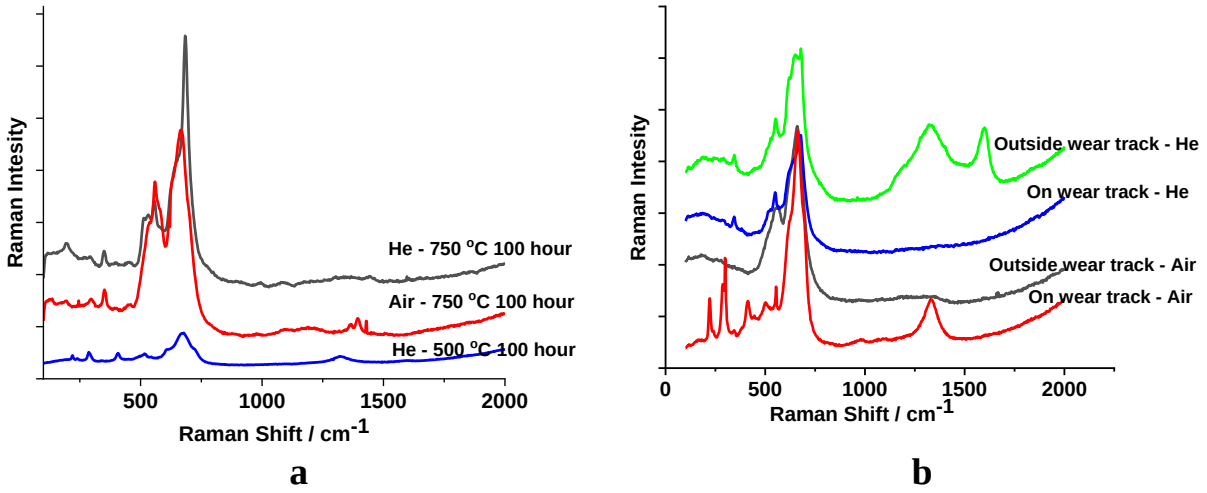

Fig. 47. Raman spectroscopy data on (a) 100 hour aged samples at 750 °C , (b) tribo-tested samples at 750 °C under 5N normal load.

6.4. TOF-SIMS Depth Profiling

Fig. 48 presents the TOF-SIMS depth profiles that were acquired over the 800HT specimen, following tribotesting at 750 °C in He (a and b) and air (c and d) environments on both outside and inside the wear tracks. The profile depths in (a) and (b) show that under He, outside the wear track the surface has a very thin layer of Fe-rich oxide with a peak of Mn. Afterward, Cr peaks immediately indicating Cr_2O_3 rich zone (simultaneous high O and Cr concentrations), which are in agreement with the XRD, and Raman studies. At intermediate depths, Fe/Mn and FeO depletion can be noticed, whereas NiO start revealing. This phenomenon is linked with a temperature-driven diffusion. At the inner layer, before the bulk, a combined peak of Ni-Fe with a decreasing layer of Cr indicating a mixed oxide layer.

Inside the wear track (Fig. 48b) the FeO/Mn depletion is more intense. It is interesting to notice that the Fe/Ni/Cr depletion follows fast kinetics as we move to greater depths inside the wear track (Fig. 48b). This is not the case inside the wear track under air (Fig. 48d). It is believed that the rubbing process during the sliding in air caused accumulation of oxide debris on the wear track, which did not happen in He condition. That is why the depth profile up to 600 nm could not reach

the bulk of the alloy. The formation of this accumulated oxide is the reason for lower COF in HT air condition.

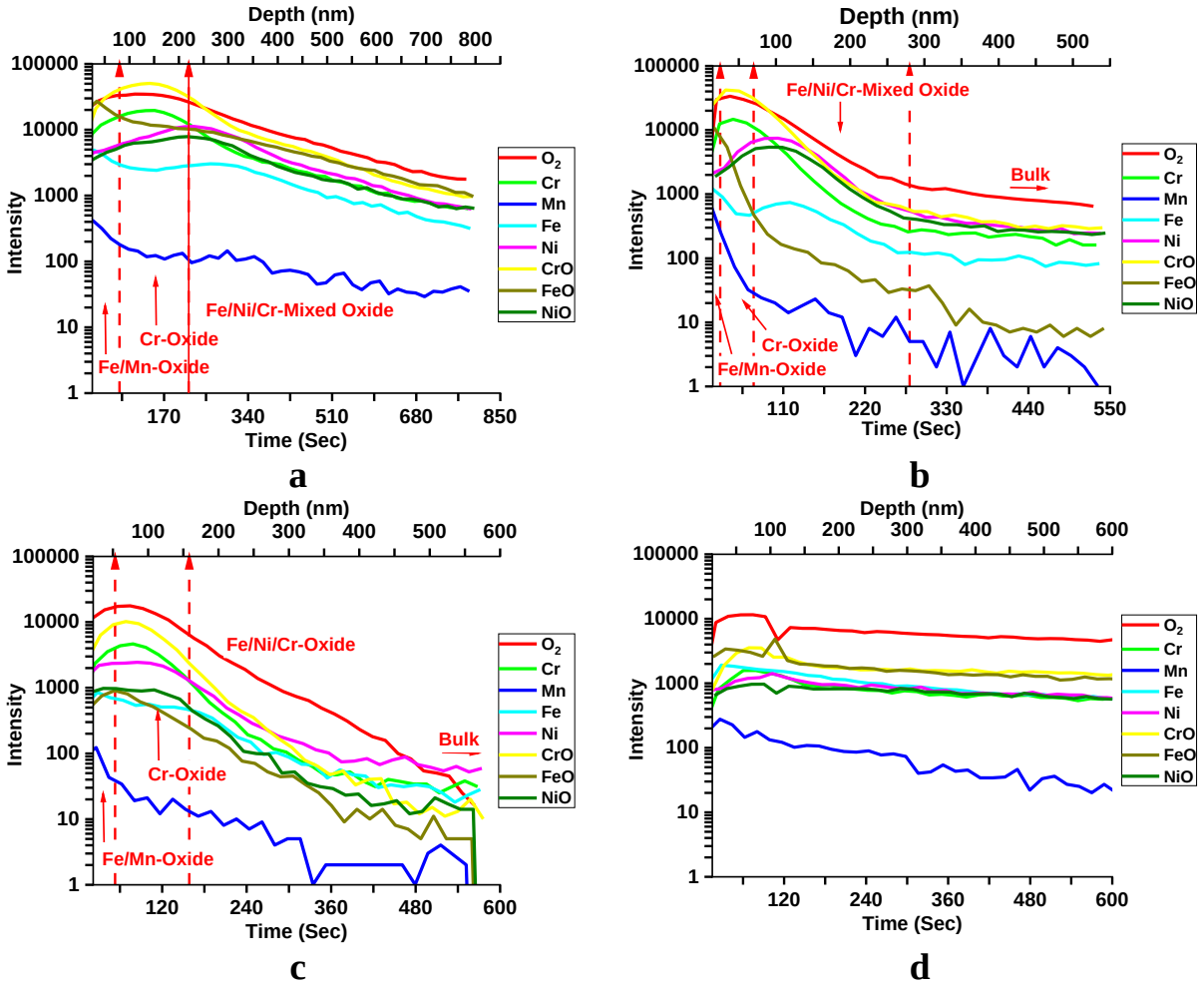

Fig. 48. SIMS elemental depth profiles of tribotested samples at 750 °C (a) He outside wear track, (b) He inside wear track; (c) Air outside wear track, (d) Air inside wear track.

Different metal oxides were formed as a result of the oxidation of the constituent elements in the alloy under investigation. The weight-gain due to the oxidation proceeded at different rates due to the different atmospheres (i.e., He vs. air), with air being moisture and oxygen-rich environment. Based on the XRD and Raman studies the oxide phases were identified, such as Cr_2O_3, $(Fe,Ni)Cr_3O_4$ and $(Fe,Cr)_2O_3$. Raman showed stronger corundum signals with the dominant spinel peaks in air-aged sample, which is again more clarified from the Raman spectra on the wear track

showing multiple strong corundum peaks on the surface of wear track in air. This is in line with the known fact that higher oxygen content favors formation of Fe_2O_3 and oxygen deficiency favors that of Fe_3O_4 [30]. Similar multilayered oxide structure was described in the literature for 800HT in a separate study for oxidation in dry and wet (5% water) oxygen at 850 ^oC for 50 hours [68]. In that study, the outer layer shows the presence of Cr_2O_3 and Fe_3O_4 whereas, the inner layer had Cr_2O_3 and Cr-rich $(Fe,Cr)_3O_4$ in dry oxygen. On the other hand in wet oxygen, the top layer showed presence of Cr-rich $(Fe,Cr)_3O_4$ and the inner layer had Cr-rich $(Fe,Cr)_2O_3$, which is in line with our findings in this work.

The thickness of the formed oxide layers is different in He vs. air atmosphere as it can be seen by comparing the TOF-SIMS results (Fig. 48a and 47c). Also, TOF-SIMS studies proved that the oxide layers are continuously consumed under He sliding conditions, whereas they are replenished in the case of air atmosphere (Fig. 48b and 47d). Some first evidence about this finding was discussed earlier in the Raman studies by comparing the spectra inside and outside the wear track. Also, from the TOF-SIMS, the formation of some internal oxides is observed (depth >100 nm). The formation of these oxides is facilitated by the voids of the thin surface oxides, the latter being incapable to protect the structure against oxidation. The TOF-SIMS profiles under air have a higher increase slope (outside the wear track) up to 150 nm depth as the changes in the oxide layers are expected to be steeper due to the much abundant oxygen and its diffusion through the layer. Following this trend and beyond 200 nm, drop of oxides can be noticed in air atmosphere, due to possible spallation or oxides evaporation, whereas in He atmosphere due to much slower kinetics of oxidation (less abundant oxygen) oxide layers keep taking place even beyond 200 nm depth.

6.5. Summary

The chemical changes in alloy 800HT during HT oxidation in He compared to air atmosphere during tribocontact are decoupled through multiple analyses techniques. The oxidation study exposed the evolution of oxides on the surface at different temperature, exposure time, and atmosphere. SEM/EDS analysis showed the formation of Cr-Ti rich oxide on the grain boundary. In addition, XRD and Raman spectroscopy confirmed the presence of oxides, some of them in spinel structures, the disordering of which is dependent on the oxygen level and the presence of tribocontact. SIMS depth profiling confirmed the presence of Fe-rich thin layer of oxide on the top surface with a thicker Cr-rich oxide and a mixed spinel-based inner layer on the bulk. The wear track in air showed the presence of thicker oxide, whereas in He the oxide depleted from the wear track. TOF-SIMS profiles in air and He atmospheres exhibited a distinct difference in their slope (different layer composition as the depth is increasing) due to the oxygen abundance in air and different diffusion rates.

After analyzing the chemical changes on the surfaces and the tribological behavior, it is imperative to analyze the mechanical properties of the material in the simulated atmosphere. In this part of the research, nano/micro scale experiments were selected. It is well understood that tribology is dominated by the surface or interface properties of the material, and not the bulk properties. Thus, nano/micro scale probing will provide a more reasonable explanation and correlation to the tribological behavior. In the next chapter, the nano mechanical properties of the surface oxide generated under very high temperatures will be analyzed using nano/micro indentation and scratch techniques.

CHAPTER VII
HIGH TEMPERATURE NANOMECHANICAL PROPERTY CHARACTERIZATION [6]

Operating at HT is vital for several types of emerging and highly efficient nuclear reactors including HTGR and VHTR. The main coolant of HTGR/ VHTR reactors is He which contains low levels of impurities including H_2, O_2, H_2O, CH_4, CO, CO_2 and N_2 [69]. Due to the presence of these impurities, the metallic alloys can develop inevitable and unique surface oxides that are highly controlled with temperature, oxygen partial pressure, carbon activity, and alloy composition. The presence of this oxide can highly influence surface friction, wear and contact properties which in turn impacts the performance of the components. For example, the precise motion of the control rods is mission-critical for reactors' performance and safety. Control rods surface can be affected by the high-temperature contact creep and self-welding during long idle intervals resulting in unpredictable high static friction and often surface damage [70]. In general, contact, friction, wear and adhesion behavior of control rods' surfaces, as well as other tribo-pairs in HTGR/VHTR, are governed by the oxide layer properties and it is thus imperative to understand and quantify their nanomechanical responses/properties.

Instrumented nanoindentation has become a common method of measuring mechanical properties of thin films [71] and oxides [72] with the ability of measuring several material time independent [71–77] and time dependent behaviors [78–81]. Interpreting and measuring mechanical properties at HT through instrumented nanoindentation is, however, very challenging due to the temperature

[6] Reprinted with permission from "Elevated temperature mechanical properties of Inconel 617 surface oxide using nanoindentation." by Salari, Sepehr, Md Saifur Rahman, Andreas A. Polycarpou, and Ali Beheshti. Materials Science and Engineering: A (2020): 139539. Copyright 2020 by Elsevier B.V.

effect on the compliance of the system, thermal expansion of the tip, tip damage as well as complexity of the contact at HT. Hence studies at HT and especially over 500 ºC are scarce with limited measured mechanical properties [78–84]. For instance, Gibson et al. used high HT to measure effect of He implantation on tungsten hardness at temperatures up to 750°C [82]. Due to the hardening effect of He, implanted tungsten retains its hardness at HTs, which was contributed to pinning effect of trapped He in small vacancies. Wang et al. measured temperature dependent mechanical properties of additively manufactured Inconel 718 up to 650°C where HT nanoindentation was used to measure hardness, Young's modulus and creep stress exponent [83]. Zhang et al. reported elastic modulus, hardness, indentation creep exponent, and thermal activation of Inconel 617 bulk at HT using instrumented nanoindentation. They observed slight decrease in elastic modulus and significant reduction in indentation hardness as temperature increases [84]. Applying high loads, Zhang's study was focused on the bulk rather the oxide layer, and more importantly, oxidation in their study, if any, formed in air for a short period of time.

Generally, constitutive equations of creep based on uniaxial tests cannot be directly used for nanoindentation parameters requiring systematic modifications. This is due to the complicated stress/strain status during indentation, contact evolution, and continuously changing stress and strain fields in indentation tests resulting in inaccurate estimation of creep properties. Theoretical modeling, numerical simulation, and experiments, when performed collectively, can resolve some of the issues and more importantly can be used to measure time dependent mechanical properties at HT by relating the strain-stress during the creep of indentation to the uniaxial test [78,81–83,85–87].

Su et al. build up a correlation between nanoindentation creep parameters and uniaxial tests using an analytical model of Bower et al. [87] and improved it to include conical indenters using

iterations of finite element analysis with varying half angles of the indenter. The improved model validated by the results of amorphous selenium at room temperature (RT) [78]. Nonetheless, the verification was performed with selenium having elastic-creep behavior only at RT. The problem gets more complex when plasticity and creep are both involved. Kang et al. combined the experimental indentation data at HT and corresponding FEA to find the elastic-plastic and creep parameters of P91 steel and XN40F at 600 °C and 900 °C, respectively [80]. There are also other iterative use of FEA to measure yield strength, work hardening rate and creep parameters [88–90]. However, these measurements are only applicable for specific creep mechanisms and should be implemented with care when used for unknown material e.g., metal oxides. It also required precise measurements of the indented surface which is difficult at HTs.

This chapter evaluates the HT mechanical properties of the surface oxide, formed after aging, of IN617 through nanoindentation. This experimental analysis is employed to find the time independent properties, elastic modulus and yield strength of the oxide layer along with creep exponent, creep coefficient and activation energy. These properties are important to understand and highlight the main contributors to static and kinematic COF of Inconel 617 at HT and to predict the top layer frictional behavior.

7.1. Sample Preparation

As received samples are mechanically polished to reduce the roughness and remove initial oxides on the surface. The polished samples are then cleaned with acetone and iso-propyl alcohol in an ultrasonic cleaner and dried. To simulate the effect of the He-cooled reactor environment, the samples are then placed in a He filled furnace at 950 °C and aged for 100 hours. The samples are then cut where the nanoindentation tests are performed on the oxide from the cross section of the aged samples (called Aged Inconel 617 and symbolized as AIN, hereinafter). Nanoindentation on

the cross section is highly beneficial compared to the surface, mainly, due to the high roughness of the surface oxide surface after aging, and also it prevents the ambiguity of having bulk substrate effect on the extracted property. For the cross-sectional sample preparation, a layer of Ni coating is deposited using the electrodeposition technique on the samples' surface to protect the oxide layer from delaminating during grinding (Fig. 49). A small section is cut and polished from the AIN gradually to get a mirror polished surface with approximate roughness (Rq) of 40 nm. Cross-section SEM image in Fig. 49b shows the oxide layer formed on bulk IN617. The oxide thickness of AIN after 100 hr of aging in He is around 6 to 10 µm, and attests to the fact that the contact mechanics of aged IN617 depends mainly on the oxide properties.

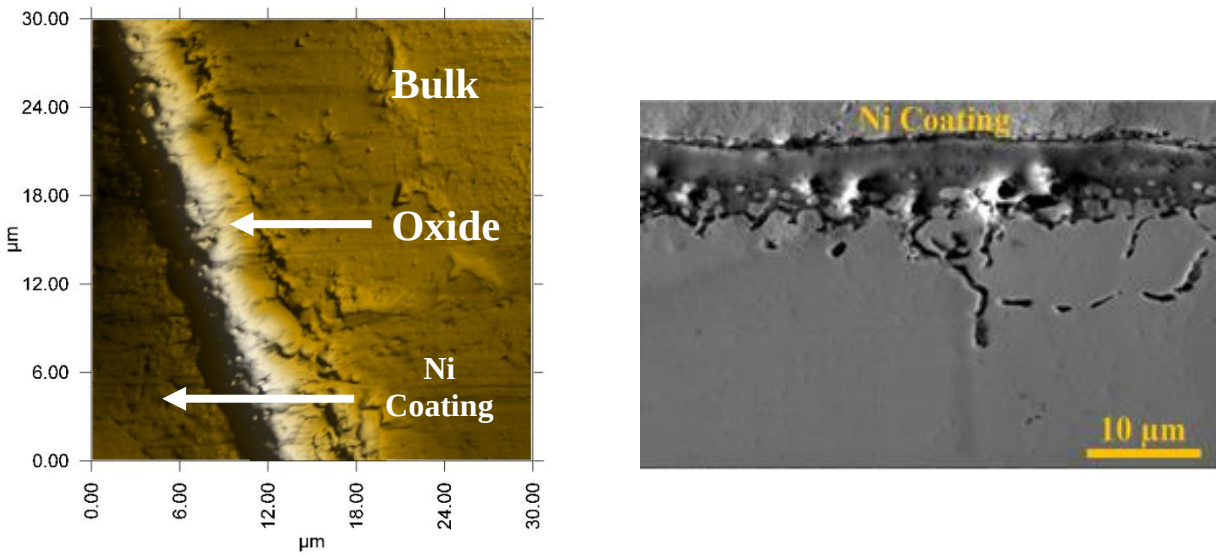

a **b**

Fig. 49(a) SPM image, and (b) SEM image of aged Inconel 617 at cross section.

7.2. Instrumented Nanoindentation

Nanoindentation experiments were conducted using a commercial nanoindenter (Triboindenter TI Premier, Bruker) shown in Fig. 50. Indentation tests are performed at RT, 200 °C, 400 °C and 600 °C, on the oxide cross-section of AIN samples. Fig. 50 shows the indenter with the HT chamber,

which is heated by two sets of heating elements on the top and bottom of the sample holder. A constant flow of 95% Argon and 5% Hydrogen is introduced through the hot chamber as cover gas, which acts as the convective heat transfer medium to achieve thermal equilibrium. The cover gas also protects the tip from oxidative damage and further oxidation to the sample.

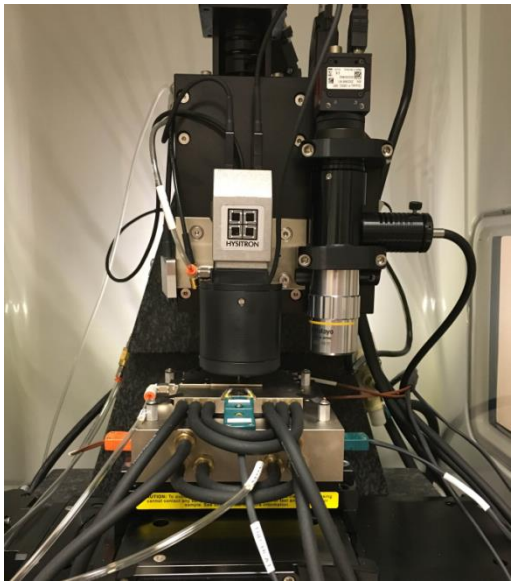

Fig. 50 Bruker-Hysitron TI Premier nanoindenter with high temperature stage.

In the current work, a Berkovich type indenter probe made of diamond is used for nanoindentation tests up to 400 °C and a Berkovich cBN (Cubic Boron Nitride) probe is used for 600 °C tests. The load is ramped from zero to the peak load at 0.5 mN/s rate before it is held at peak load for 100s (for indentation creep measurements) and then it is unloaded at 1.0 mN/s rate. A maximum load of 6 mN is used for experiments up to 400 °C, and 500 µN is used for 600 °C due to softening of the oxidized sample. The load and holding time are selected after evaluating nanoindentation test results for different holding stages, maximum loads and load patterns. Indentations are repeated 5 times at each temperature.

7.3. High Temperature Parameter Modifications

To obtain an accurate result for elastic modulus and hardness at high temperatures, the effect of machine compliance, thermal drift and samples creep should be eliminated from the raw results. Compliance of the machine is calculated by integrated software at the beginning of each test through calibrating in air and standard Fused Quartz sample. During unloading the load is held for 120s at 10% of its peak for 120s to calculate thermal drift correction from the fraction of displacement [91–93]. It should be mentioned that for high temperature indentations, the sample and the probe are held at high temperature for half an hour to achieve thermal stability.

Creep influence on hardness depends on the loading pattern used to measure the creep properties. The common technique, also used in this research, is constant load and hold (CLH) which is loading to a maximum load and maintaining the load for a specific time. Phani et al. shows this method of loading limits the range of depth during creep which reduces its influence on hardness and at the same time can cover a wide range of creep strain rates. In fact, it is shown that the creep displacement during holding time in CLH is closer to real uniaxial creep tests in comparison to other loading patterns [93].

Hardness is measured using the maximum load as well as the associated projected area of the contact and is given by:

$$H = \frac{P_{max}}{A} \tag{7.1}$$

where P_{max} is the maximum indentation load and A is an area function at the contact depth, h_c. The area function can be estimated by the following function:

$$A(h_c) = C_0 h_c^{\,2} + C_1 h_c + C_2 h_c^{\,1/2} + C_3 h_c^{\,1/4} + C_4 h_c^{\,1/8} + C_5 h_c^{\,1/16} \tag{7.2}$$

where C_o represents a constant, which is a function of tip geometry and for a perfect Berkovich tip equals to 24.5 and coefficients C_1-C_5 account for the geometrical imperfection and are calculated based on known properties of fused quartz standard sample. Contact depth h_c, can be defined as [73]:

$$h_c = h_{max} - \varepsilon \frac{P_{max}}{S_u} \tag{7.3}$$

where h_{max} is the maximum depth at the end of loading step, ε denotes the geometry correction factor which is 0.75 for Berkovich tip and S_u is the contact stiffness at the onset of unloading.

Following Oliver-Pharr method, the reduced elastic modulus E_r can be calculated through measurement of contact stiffness, S_u , and projected contact area [94]:

$$E_r = \frac{\sqrt{\pi} S_u}{2\sqrt{A}} \tag{7.4}$$

Using reduced elastic modulus from Eq. 4, and known mechanical properties of the diamond tip (E_i,ν_i), elastic modulus of oxide at the cross section of the samples can be calculated based on:

$$\frac{1}{E_r} = \left(\frac{1-\nu_i^2}{E_i} + \frac{1-\nu_s^2}{E_s}\right) \tag{7.5}$$

where E_s and ν_s are elastic modulus and Poisson' ratio of oxide, respectively.

The creep influence on elastic modulus can be eliminated following Feng et al. method [95]. Feng et al. suggested a correction for Oliver-Pharr method (Eq. 4) to exclude the effect of creep on elastic modulus [95] by introducing a modified stiffness parameter, S_m, given by:

$$\frac{1}{S_m} = \frac{1}{S_u} + \frac{\dot{h}_h^c}{|\dot{P}|} \tag{7.6}$$

where $\dot{h}_h^c$ represents indenter's creep rate at the end of the load hold stage, and $\dot{P}$ is the unloading rate at the beginning of the unloading stage. Following Feng et al.'s suggestion, in the current study, the unloading stiffness, S_u, is replaced by S_m in Eq. 3 and 4 to mitigate the effect of creep at higher temperatures.

Implementing these corrections to calculate the true mechanical properties at HT is essential, however, they can only be used when specific criteria is satisfied. [78,95]. Accordingly, Feng et al. introduced a creep factor, *C*, and a threshold for unloading rate, $\dot{P}$, in which Eq. 6 is valid and can be used to eliminate the creep influence on elastic modulus [95]. The factor defined as:

$$C = \frac{\dot{h}_h^c}{|\dot{P}|} < 0.1 \tag{7.7}$$

Here, for measuring the Young's modulus and hardness of IN617, unloading rate of indenter is kept constant at 1 mN/s. Considering indenter displacement rate at the end of load holding stage for each tests and temperatures, the maximum creep factor calculated as $C = 0.027 < 0.1$. This condition shows that Eq. 6 can be used to calculate Young's modulus and the proposed holding time is sufficient even at elevated temperatures to effectively reduce the creep influence [95]. Su et al. also defined a threshold for minimum creep displacement (or similarly time during holding stage), below which the elastic modulus can significantly influence steady state creep strain rate and named it elastic transient. Elastic transient related to strain propagation through unyielded material below the indenter postponing the steady state section of creep. This is important since creep rates measured at this stage (holding stage) and should be surpassed to reduce its effect on creep parameters. Su et al. suggested a minimum indentation depth beyond which the results are not affected by the elastic transient and it is given by [78]:

$$h_{min} = 10\sqrt{\frac{\pi P_{max}}{2E_r tan\theta}} \quad (7.8)$$

where θ is half angle of the indenter (70.3º for Berkovich) [78]. The calculated elastic transient for the current indentation tests is between 15 to 20 nm based on the maximum load and reduced elastic modulus for all the tested temperatures. Here, the measured creep displacements are beyond the elastic transient and hence minimal influence of elastic transient on creep displacement is expected.

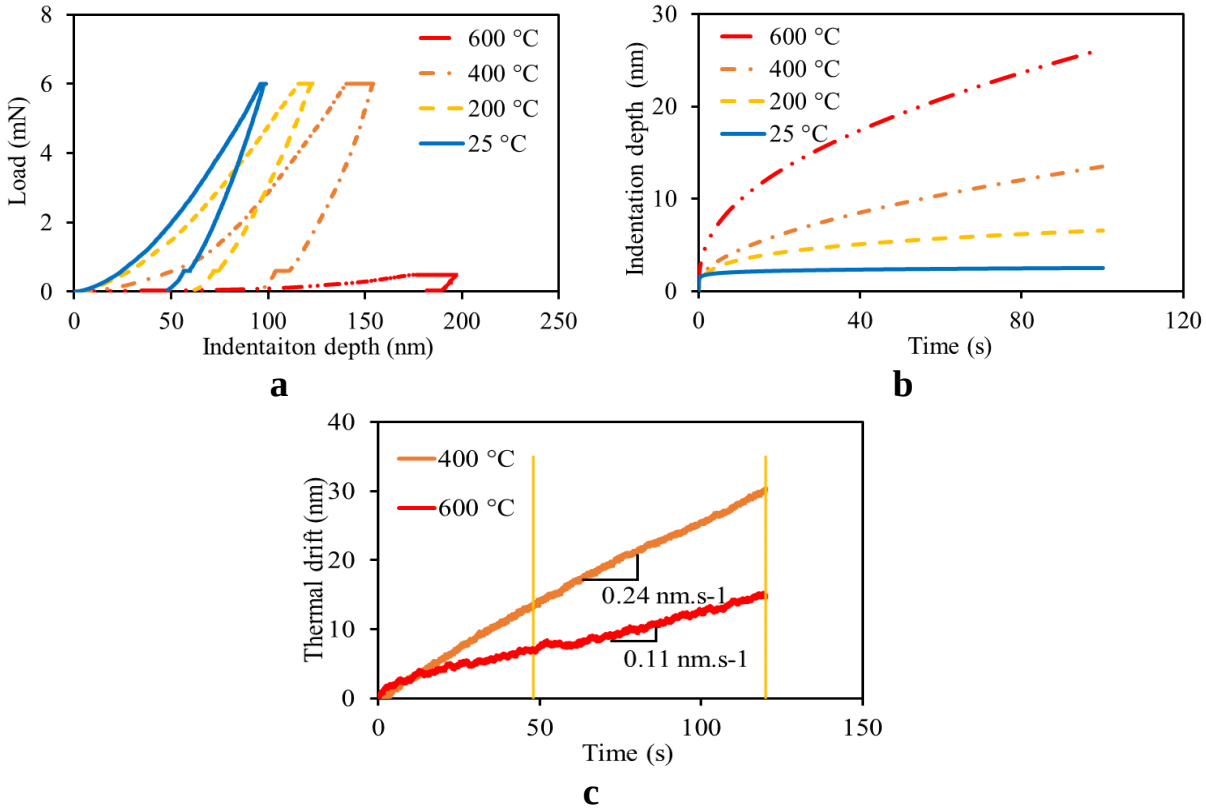

Fig. 51 Average results of 5 indentations for (a) load displacement and (b) creep displacement at the holding time and maximum load of 6 mN for RT to 400 °C and 500 µN for 600 °C, and (c) thermal drift of oxide on AIN at RT - 600°C. It is noted that at higher temperature of 600 ° the thermal drift is lower compared to 400 °C. It can be attributed to cBN material having lower thermal conductivity, ~700 $W/m°K$, compare to Diamond, 2000 $W/m°K$ [4]

Indentation load-displacement curve for the oxide on AIN cross-section is presented in Fig. 51a at different temperatures where creep displacement is taken out from the holding period at maximum load (Fig. 51b). Thermal drift graphs of nanoindentation test are depicted at 400 °C and 600 °C as it is insignificant in other temperatures. At this temperatures, the thermal drift rate is 0.11-0.24 nm/s which is relatively low and similar to what is reported in Ref. [96] for fused silica.

7.4. Results and discussion

Fig. 52 shows the indentation hardness and elastic modulus (after considering and excluding creep influence on the stiffness) for bulk virgin IN617 at 25 °C to 800 °C. Nanoindentation results are compared with the recently published macro indentation results from Zhang et al. on the IN617, where the indentation depths were very high around 2 to 3 µm using high loads of 200 mN to 400 mN. The nanoindentation results are higher (27-51%) than the published data which may resulted from indentation size effect and also surface treatment effect as the samples used in this research were not electropolished to remove the polishing effect on the surface.

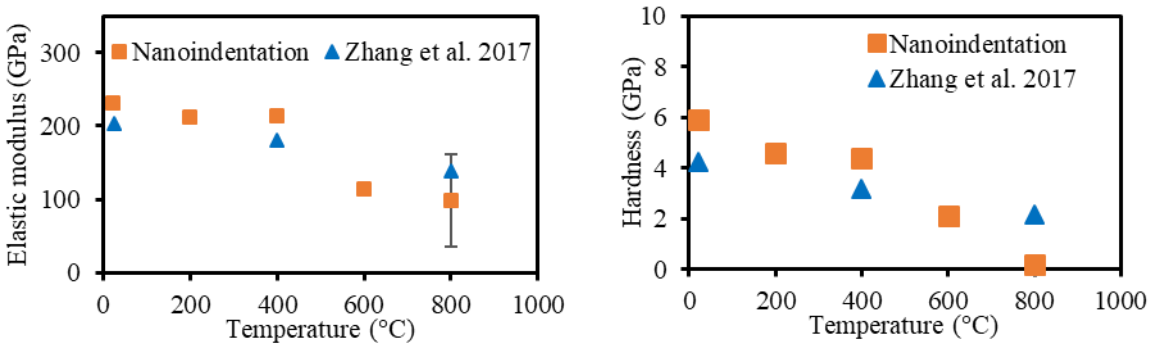

Fig. 52 Results of nanoindentation for (a) hardness (b) elastic modulus calculated from Eqn. 6 in comparison with Zhang et al. 2007 results of IN617 at different temperatures

Fig. 53 shows hardness of the cross section of IN617 at different distances from the surface. There is a sudden drop through the top oxide layer to the bulk of the material. It is interesting that the

hardness of the cross section is close to the hardness of the bulk of chromium oxide. The size effects as well as the preparation process which compact the oxides at the cross section may result in higher hardness values similar to chromium oxide packed coat [75].

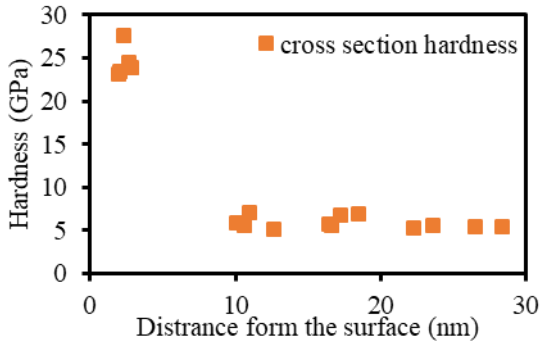

Fig. 53 Hardness of the cross section of IN617 at different distances form the surface

Fig. 54 shows Young's modulus and hardness (excluding creep influence) for oxide layer at 25 °C and up to 600 °C along with those obtained by Zhang et al for bulk IN617. They used high loads of 200 mN to 400 mN on the surface after heating the sample in air for 8 hours, which indented the surface down to the depth of 3 μm including around 400 nm of oxide [84]. Therefore, the results are represented as the properties of the bulk of IN617 (BIN) at 25 °C and 400 °C as tested by Zhang et al. [84]. Young's modulus of the oxide layer is 1.4 times of BIN [84] at RT to 400 °C and closer to Young's modulus of similar metal oxides (Table. 6). However, hardness is 8 times of BIN at RT which decrease significantly to 3 times of hardness of BIN at 400 °C. This may due to softening at elevated temperatures and/or diffusion of other metal ions into the surface. Hardness and Young's modulus of BIN were only measured for RT, 400 °C and 800 °C in [84]. Table 6 compares the Young's modulus, hardness and yield strength of manufactured metal oxides which build up the oxide on AIN. It shows that despite having different morphologies and scales, nanoindentation results are comparable with similar metal oxides. Based on the EDS results in

chapter 6, the oxide mostly consist of Cr_2O_3 validating the high yield strength and elastic modulus of the AIN.

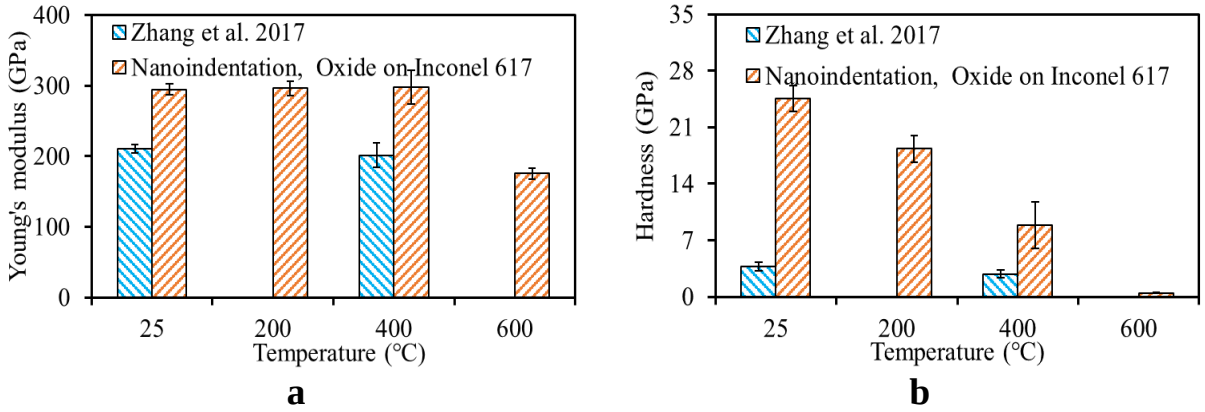

Fig. 54 Results of nanoindentation for (a) elastic modulus (b) hardness calculated from Eq. 6 in comparison with Zhang et al. 2017 results of BIN at different temperatures

Table 6 Mechanical properties of metal oxides similar to oxides of aged IN617 at room temperature

Oxide	E (GPa)	σ_y (GPa)	H (GPa)	Reference
Al_2O_3	344-408	15.4	19.6-25.5	[97,98]
Cr_2O_3	260-370	10-14.5	20 & 30	[75,99]

Fig. 55 shows hardness of AIN from the cross section at different distances from the surface at RT. There is a sudden drop when indentation pass the top oxide layer to the bulk of the material. It is interesting that the hardness of the top of the cross section is close to the hardness of chromium oxide coatings measured by nanoindentation reported in [99] at RT.

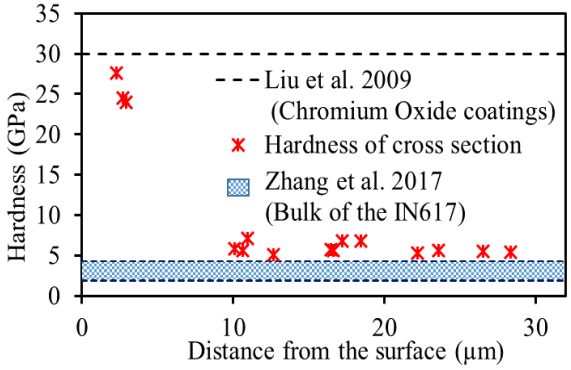

Fig. 55 Hardness of the cross section of IN617 at different distances form the surface

The yield strength of the oxide at RT is estimated through combined experimental and numerical analyses and is depicted in Fig. 56, along with the yield strength of bulk IN617, measured with uniaxial tests, as well as the yield strength of the oxides listed in Table 6. The oxide strength is significantly higher than the bulk, and closer to that of similar oxides, especially Cr_2O_3. However, the oxide strength is lower compared to Cr_2O_3, which can be attributed to the surface diffusion of $NiCr_2O_4$ discussed above. The oxide yield strength and strain hardening exponent are plotted vs. temperature in Fig. 57. As seen, both the yield strength and strain hardening exponent decrease with temperature rise, which can be due to the activation of slip systems [100]. It is noted that the strain hardening exponent decrease is relatively linear with temperature rise. Based on the results of Young's modulus (Fig. 54), yield strength, and strain hardening exponent (Fig. 57) it can be concluded that plastic deformation rate is changing rapidly from 400°C to 600°C. Also depicted in Fig. 57a is the oxide hardness to yield strength ratio showing an increase as the temperature increases from RT to 600°C, due to lower hardness reduction rate compared to yield strength. Similar behavior has been observed for Al_2O_3 up to 700°C, as reported in Ref. [101].

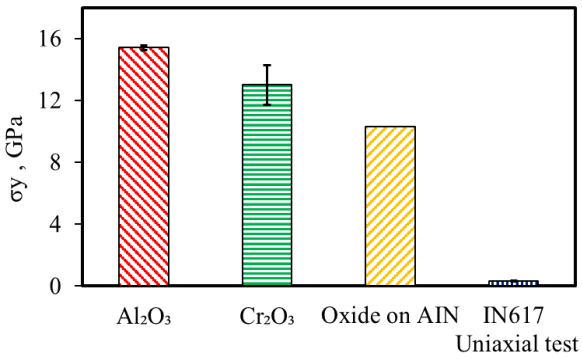

Fig. 56 Yield strength of oxides Al_2O_3, Cr_2O_3 in comparison to extracted yield strength of oxide and IN617 measured by uniaxial test [102,103]

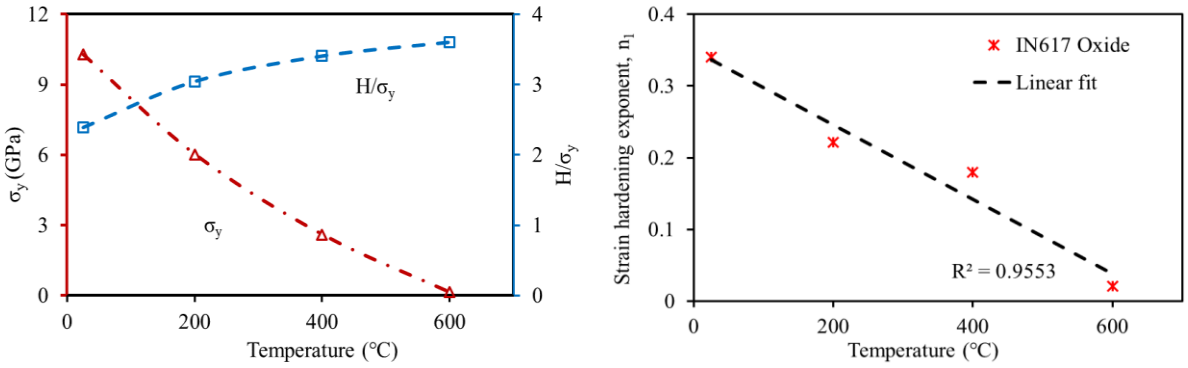

Fig. 57 (a) Evolution of yield strength and hardness to yield strength ratio and (b) strain hardening exponent for oxide of aged IN617 from 25°C to 600°C extracted using current numerical method.

Fig. 58 presents a comparison of creep stress exponent of BIN from reference [84] and oxide at the cross section of AIN from current study. The stress exponent above 5 generally shows that the main mechanism of creep for BIN is dislocation climb [84], however, for the oxide layer, the lower creep exponent, $n \approx 2$, showing that creep deformation is dominated by diffusion through the grains [104,105]. Diffusional creep is reported to be the main creep mechanism of Al_2O_3 and Cr_2O_3 [86], though, diffusion through the grain is dominant for lower stresses and temperatures $T < 0.5\,T_m$ [86]. It is believed that due to complex stress/strain below the indenter and elastic transient during creep, the shear stress drops and creep is dominant by diffusion through boundary (Fig. 59). Surface heat treating in order to have coarser grains can increase the creep resistance of the surface since creep rate varies with inverse of square of grain size [104]. This can be further studied with surface heat treatment and modifying the grain size of the oxide.

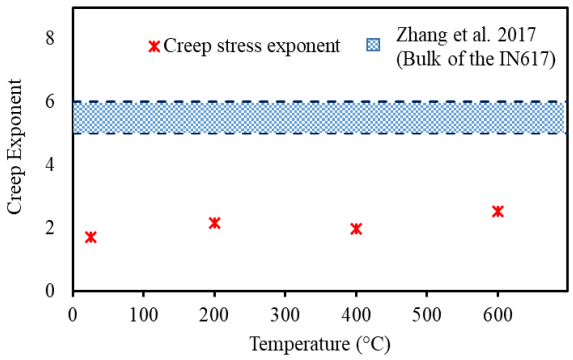

Fig. 58 Comparison of creep stress exponent of oxide on AIN with Zhang's study [84]

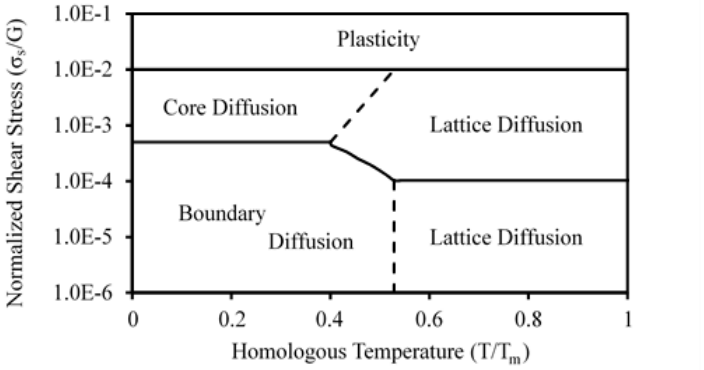

Fig. 59 Deformation mechanism map of creep based on normalized shear stress, $\sigma_s/_G$, with shear modulus versus homogenous temperature, T/T_m (T_m=2435 °C for Cr_2O_3) [86]

Another important parameter in creep deformation is activation energy, *Q*,. An Arrhenius equation for creep strain rate during steady state creep of oxide is presented by:

$$\dot{\varepsilon} = \acute{A} \exp(-Q/kT)\sigma^n \tag{7.11}$$

where $\dot{\varepsilon}$ symbolizes the steady state creep rate, $\acute{A}$ is a material constant, σ represents the creep stress, n is the stress creep exponent, Q denotes the activation energy, k is the universal gas constant, and T is thermodynamic temperature in the unit of kelvin. Activation energy can be calculated by gradient of logarithm of creep strain vs *1/T* based on Eq. 11. Results (Fig. 60) show slope remain mostly constant over the tested temperature providing that the creep mechanism is not changing and for oxide on the AIN is~23 $kJ/mole$. This activation energy is much lower than 291 $kJ/mole$ reported by [84] for IN617, however, it is close to the boundary creep mechanism in which less energy is needed to move through the boundaries [104,106]. Also, similar activation energy (29 $kJ/mole$) calculated from creep coefficient, A. At high temperatures, creep rate is controlled by the slowest species in solids which in the case of metal oxides is controlled by the oxygen activity [107].

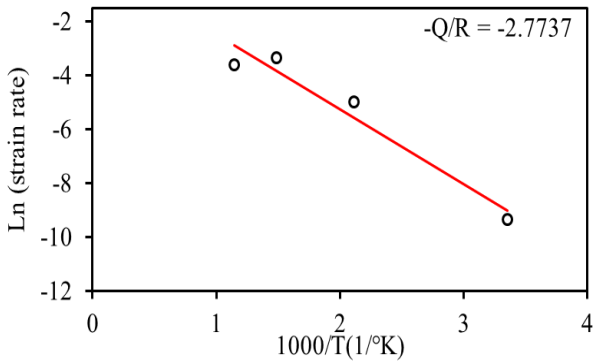

Fig. 60 Depiction of how activation energy calculated from the gradient

7.5. Challenges

Elevated temperature nanoindentation on a complex multi element alloy like Inconel 617 presents with the challenge of tip material and alloy reactivity along with the most common and well-known challenges of instrumented nanoindentation: thermal drift and indenter damage due to oxidation. Diamond is the obvious choice for tip material with the highest hardness, but it loses its effectiveness at higher temperature above 400C due to graphitization. It is popular indentation and scratch probe material up to 400 °C, although oxidation can be avoided in high vacuum technique even for higher temperature. The next choice is cBN for its high hardness, and it requires 700 ^{o}C to oxidize and create a B_2O_3 layer. On the other hand, sapphire is popular as it is inert at high temperature. Both this material has been successfully used at high temperature for indentation in several cases.

The diamond tip is successfully used on Inconel 617 up to 400 °C without any major damage to the tip. When the tips were used above 400 °C, the exhibited severe damage although the indentation were performed in Argon gas environment. As shown in Fig. 61a, the first diamond tip was corroded and broken off during indention at 800 °C. The second tip in Fig.60b shows a chunk of material adhered on the tip. The first tip in Fig. 61a was used at 800 °C and then it was used to indent on standard FQ to check the status as per the HT indentation protocol explained

earlier. But for the second tip, it was imaged under SEM before indenting on FQ. It is assumed that the similar material adhesion might have occurred on the first tip after indentation at 800 °C and afterward during the indentation on FQ at room temperature the potion of the tip might broke off that had adhered material.

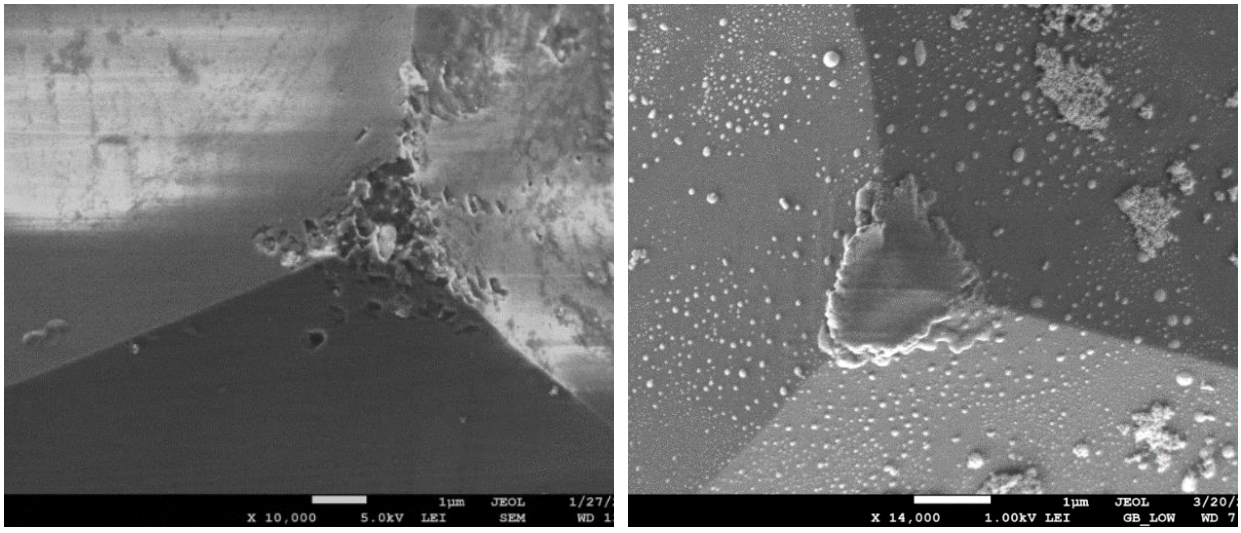

a **b**

Fig. 61 SEM images of damaged diamond Berkovich probes after indenting on Inconel 617 at 800 °C.

The cBN tip was then used to perform the indentations at HT. Although the indentations at 600 °C were successfully executed with very little damage to the tip, it produced similar result at 800 °C as diamond. Fig. 62a shows the cBN tip after 600 °C indents, where the tip is mostly clear of material. But after 800C indents, in the SEM images the tip is found to be covered with the transfer material. The sapphire probe is used on Inconel 617 at 800 °C resulted in similar outcome. Fig. 63a and 62b shows the SEM images of the tip before and after performing the HT indentations on Inconel 617.

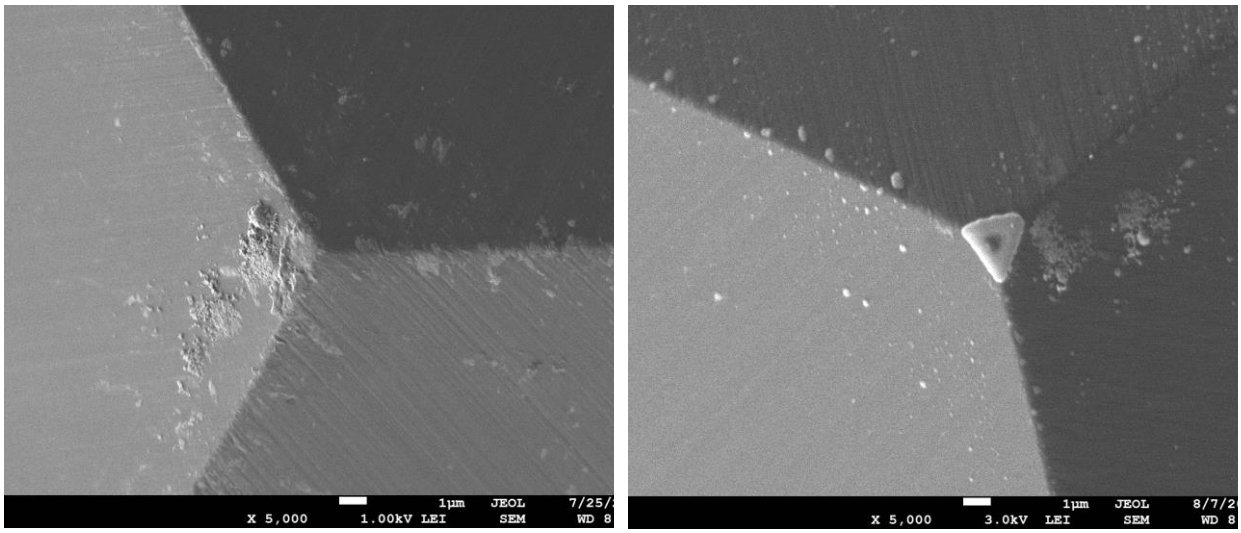

a **b**

Fig. 62 SEM images of cBN Berkovich probes after indenting on Inconel 617 at (a)600 °C; (b) 800 °C.

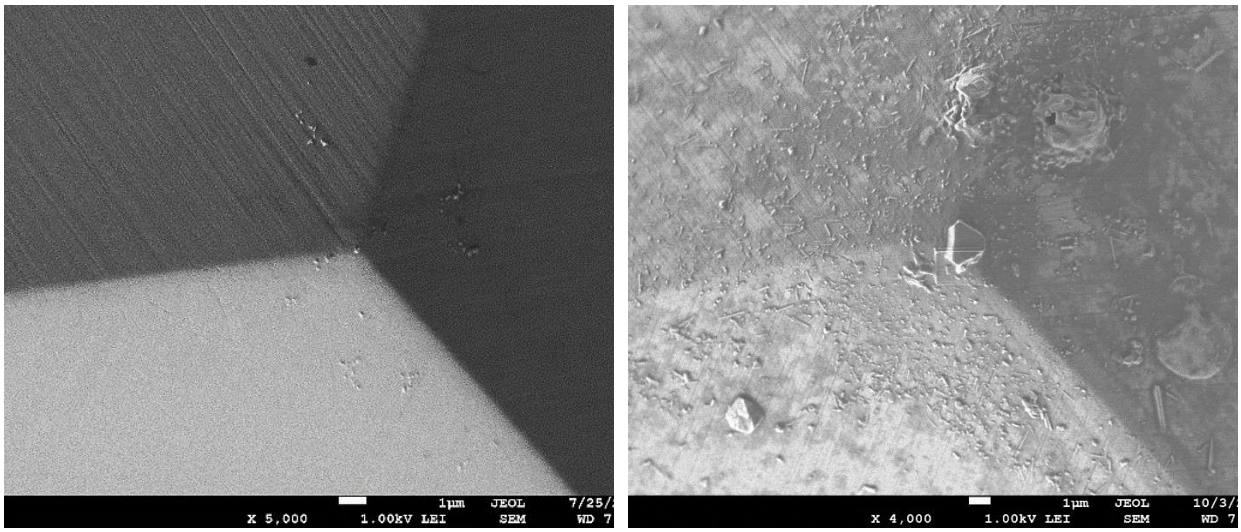

a **b**

Fig. 63 SEM images of sapphire Berkovich probe (a)before; (b)after indentation on Inconel 617 at 800 °C.

The combination of these experiments suggests, although the tip material is protected from oxidation, the indenter-sample interaction/reactivity poses the highest challenge. Carbon is known to be dissolved in elements like Cr, Ni, Mn, Co, Fe and other early transition metals at high temperature. cBN and sapphire is also prone to be dissolved or redused to oxides, borides or

nitrides in presence of the Cr or Ni at HT. This reactivity does not only depend on the environment but also the increased diffusion at HT. This highly reactive interaction at HT caused the adherence of material on the tips. This type of material transfer during indentation has been reported before even at room temperature while in-situ TEM indentation of copper by sharp tungsten tip[108]. The adhesion property between the tip and sample is responsible for the material transfer[109].

7.6. Summary

In this study experimental nanoindentation tests are performed to investigate the mechanical response of top layer oxide of Inconel 617 which is one of the main candidates for components such as heat exchanger, control rods and valves in HTGR/VHTR. Elevated temperature nanoindentation is performed on the cross section of oxide after aging Inconel 617 for 100hrs at 950 °C environment filled with He. The results are further investigated with an optimization algorithm to fit the FEA data and extract the time independent and dependent constants. Oxide exhibits different mechanical properties than the bulk of Inconel 617 at RT to 600 °C. The following conclusive remarks can also be made:

(1) Young's modulus of the oxides is 1.3-1.6 times of IN617 and closer to metal oxides. Hardness of the oxide layer at the top most layer of IN617 is much higher than that of the bulk of Inconel 617. This is due to formation of several hard oxide layers on top of Inconel 617 during aged process.

(2) The yield strength through of the oxide of aged Inconel is 10 GPa at RT and reduced to 120 MPa at 600 °C. The high yield strength at RT is close to other metal oxides at RT.

(3) Activation energy of oxide is much lower than the bulk of Inconel as less energy is needed for ion/voids to move through the boundaries.

(4) Creep deformation at high temperature is dependent on diffusion through the grain rather than dislocation climb dominant for the bulk of Inconel 617 and depend on oxygen diffusivity in the oxide.

(5) Based on the extracted properties, mechanical properties of the bulk cannot be used to measure the tribological response of the surface which oxidized during holding stages.

The success of instrumented high temperature indentation on complex alloys like Inconel 617 is limited by the tip material available. Other tip material like, SiC and WC can be explored, but dissolution of SiC in the presence of metals (Fe, Ni, Mn, Co) and loosing carbon through diffusion is well known. So, it is imperative to explore suitable tip materials to produce successful, reliable and reproducible HT instrumented nanoindentation data.

If the oxide is treated as a coating on the bulk surface, adhesion and shear strength of the oxide is very important to identify the limitation of the coating in tribology applications. With the nano-mechanical properties of the surface oxide analyzed in this chapter, the next chapter will show the friction, adhesion and shear strength of the oxide formed on the Inconel 617 surface using the scratch technique.

CHAPTER VIII
NANOMECHANICAL AND NANOSCRATCH BEHAVIOR OF OXIDE FORMED ON INCONEL 617 AT 950 °C

Instrumented nanoindentation and scratch are common methods of measuring nanomechanical properties of thin films [71] and oxides [72], including the measurement of time dependent and independent properties. Nanoindentation is predominantly used for measuring the elastic modulus and hardness of materials, especially thin films. For fracture toughness measurements, Vickers indentation is widely used for brittle materials where the length of the radial cracks is known to correlate with the fracture toughness. However, in the nanoindentation regime, the method is not very useful as the crack generation and measurement is not as straight forward. Bhushan and collaborators studied the fracture toughness of amorphous carbon film using different probe shapes in nanoindentation based on the analysis of the energy release in cracking [110,111]. Lepienski et al. proposed another method of calculating fracture toughness based on the nucleation of cracks instead of propagation, following the idea developed by Lawn and Marshal [112,113].

In general, the tribological behavior of thin films and oxides can be explained with the combined knowledge of mechanical properties of the substrate and the film. In case of HT oxides on the surface, they have the tendency to delaminate due to residual stresses. In addition to hardness, elastic modulus, and nanoscale scratch friction coefficient (COF) that are used to explain thin film tribological behavior, adhesion and shear strength of the oxide film at the interface can also provide valuable information for the robustness of these films.

In this work, in order to better understand the tribological behavior of the oxidized Inconel 617 in both He and air, the thin oxide film on the surface that is generated at 950 ^{o}C He and air is characterized using nanoindentation and scratch experiments. Hardness, modulus and COF were

measured, and then extended to fracture toughness calculation from nanoindentation, shear and adhesion strength from ramp loading scratch measurements.

8.1. Scratch

The scratch experiments on the oxide layers were executed using the same TI Premier equipped with a 3D Omni probe, which has the ability to scratch at any direction by the movement of the sample holding stage. A conospherical geometry diamond tip with 60^o included angle and tip radius of 5 μm was used to conduct the scratch experiments. The area function for a spherical and conical part of the tip is given by [114]

$$A_{sph} = \pi h_c(2R - h_c) \quad \text{for } h_c \leq h_a \quad (2)$$
$$A_{con} = \pi \tan^2\theta (h_c + h_o)^2 \quad \text{for } h_c > h_a \quad (5)$$

where h_o is the distance between the apex of the indenter tip and the apex point of the equivalent conical indenter and h_a is where the change from spherical to conical region occurs and is expressed by

$$h_a = R - R\sin\theta \quad (6)$$

Where, θ is the semi-vertical angle for the conospherical tip. Based on the geometry of the current tip, to calculate the hardness from scratch, the maximum depth during scratch, while staying within the spherical region of the tip is 2.5 μm.

All scratch experiments were performed in load-controlled mode under two different modes: constant load and continuously increasing ramp loading profiles. The constant load up to 500 μN was used to investigate the COF (ratio of friction force to applied force) and wear property of the oxide layers. The ramp loading scratch was performed to identify the discontinuity at the onset of oxide layer delamination, with applied load varying from 250 mN to 750 mN.

8.2. Results and discussion

8.2.1. Surface morphology and oxide layer thickness

Fig. 64 shows the SEM images and AFM topographical images of the Inconel 617 samples aged in He (a, b) and air (c, d) for 100 hours. The surface of the HT air atmosphere sample after 100 hour has larger nodular grains of oxide, whereas the nodules are smaller in the He aged sample. The presence of impurities and low partial oxygen pressure has modified the oxidation chemistry. The grain boundaries are also formed differently based on the oxidation atmosphere. The oxidation kinetics and the grain boundary evolution was discussed in Ref. [115]. The surface roughness, based on the AFM images, has changed significantly from the polished clean surface. The sample surface roughness after polishing was 0.04 µm, whereas after aging in He for 100 hours, the surface roughness of the oxide became 0.4 µm and in air it became 0.8 µm. The higher roughness in air atmosphere resulted from the larger nodules on the surface.

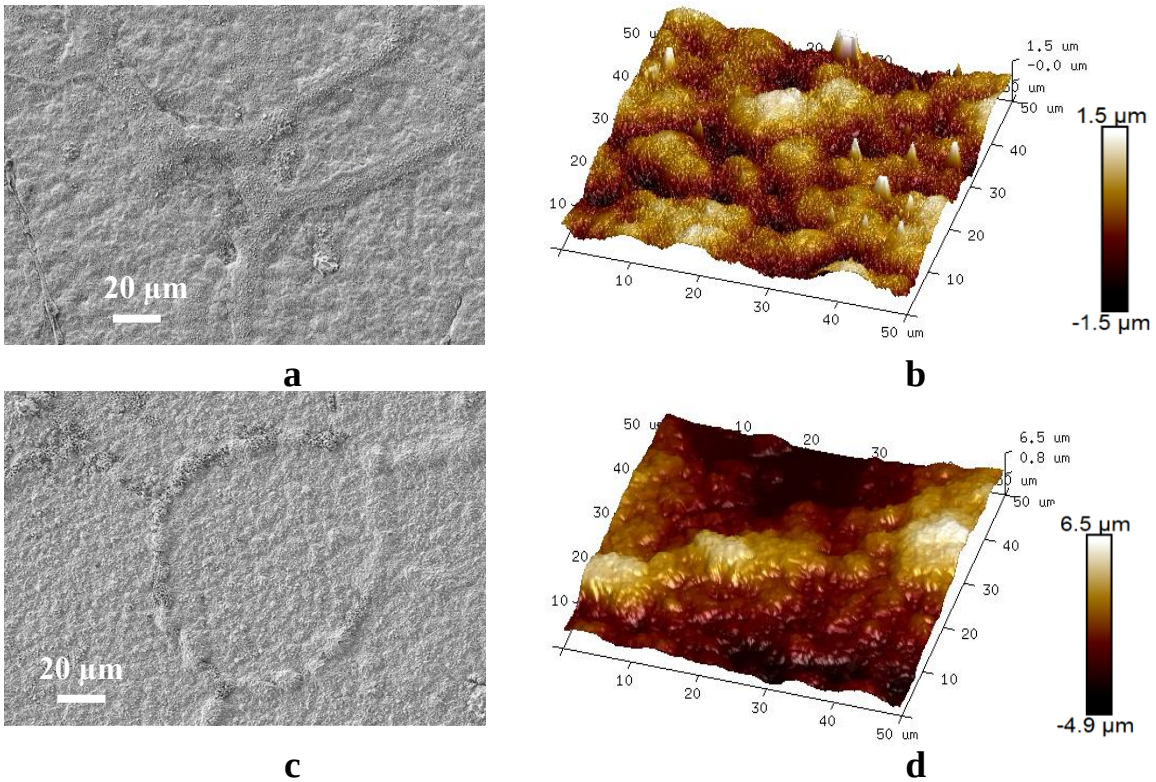

Fig. 64. SEM and AFM images of oxide surfaces grown at 950°C for 100 hours in He (a, b) and in air (c, d).

The thickness of the oxide layer is investigated using optical microscopy and cross section SEM images, as showed in Fig. 65. Cross-sections show the surface morphology and the top payer consisting of Ni platting as part of the cross-section preparation, then the main oxide layer that is primarily Cr_2O_3, and after that the aluminum rich internal oxidation along the grain boundary. The thickness of the primary oxide layer varies from point-to-point on the surface of the sample for all conditions. The oxide thickness of A100 varies from 5.5 μm to 6.5 μm, having a mean value of 6.1 μm. For H100, the average thickness was measured to be 5.7 μm, while the thickness increases to 8.4 μm for H500. The maximum thickness was found up to 8 μm in H100 and 10 μm for H500 sample in some cross section spots, especially near the grain boundary. For these measurements, intentionally the spots near the grain boundary were avoided, as was the case for the indentations and scratch data, which are focused in the middle of the grains. The thickness reported here are only for the surface oxides, avoiding the internal oxidation through grain boundary. The maximum oxidation penetration depth including the internal oxidation is observed to be ~ 35 μm for A100, ~20 μm for H100 and ~30 μm for H500 samples.

The chemical characterization of H100 surface oxide is explained elsewhere [115]. The cross-section EDS showed the presence of high concentration of Ti on the surface. The XRD analysis confirmed the presence of $MnCr_2O_4$ and TiO_2 on the surface along with rich Cr_2O_3. Similar results were reported by Jang et al. [3,15] for He-aged Inconel 617. This result is again confirmed in Fig. 66 by the EDS map of the H500 sample. The Ti-map in Fig. 66 shows rich presence of Ti on the surface. The presence of Mn was observed throughout the oxide along with Cr_2O_3, not only on the surface. Internal oxidation of Al is more prominent for the 500-hour aged sample.

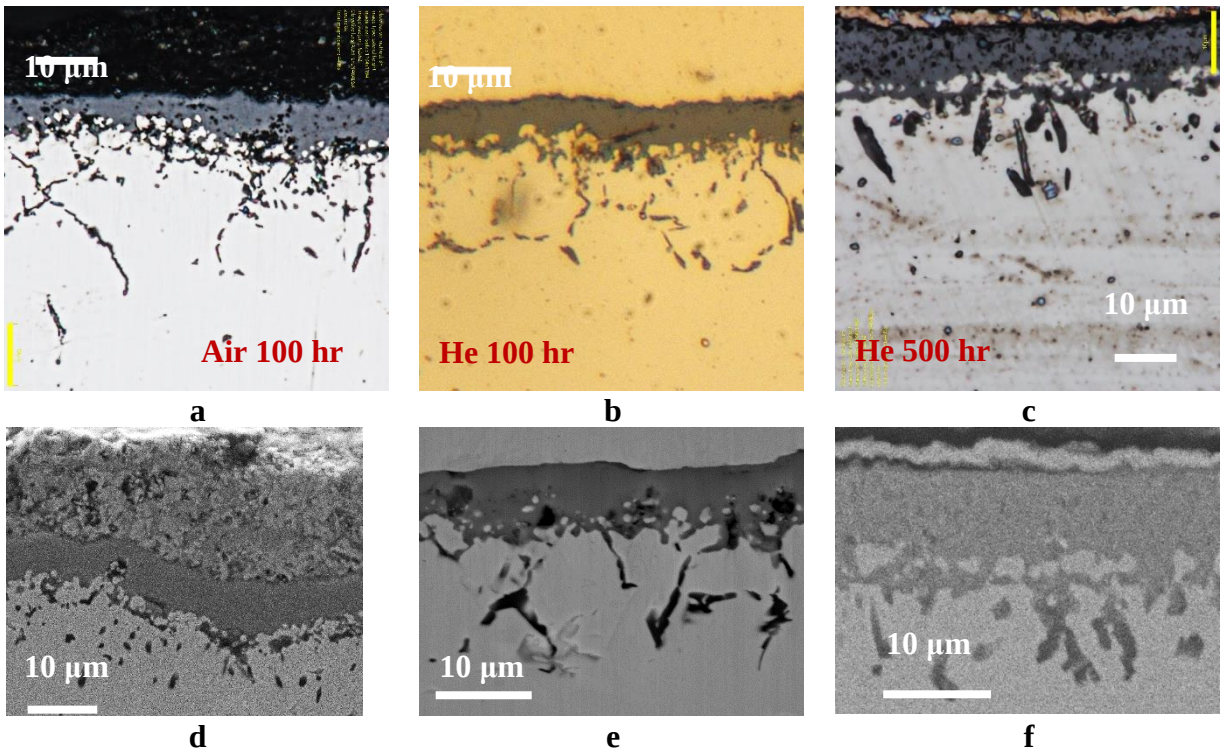

Fig. 65. Optical images (a, b, c) and SEM images (d, e, f) of Inconel 617 cross section aged at 950 ºC in air for 100 hours (a,d), in He for 100 hours (b,e) and in He for 500 hours (c,f).

On the other hand, A100 showed Ni/Co oxide on the surface along with Ti in the EDS. The low partial oxygen pressure in helium condition was not favorable to form NiO according to Ellingham diagram at 950ºC, but in air, NiO was generated at 950ºC, and was transformed to $NiCr_2O_4$ [3]. Thick layer of $NiCr_2O_4$ is formed on top of Cr_2O_3 with NiO nodules on the surface. This is confirmed by the SEM/EDS, XRD and SIMS (Secondary ion mass spectroscopy) depth profiling data in Refs. [14,115]. These characterizations confirmed the multilayer oxide layer on the bulk metal surface as showed in Fig. 67. Fig. 67a shows the H100 oxide layer with TiO_2 on the top, whereas Fig. 67b shows the A100 oxide layer schematic having $NiCr_2O_4$ on the top surface with NiO nodules above, generating the rough morphology.

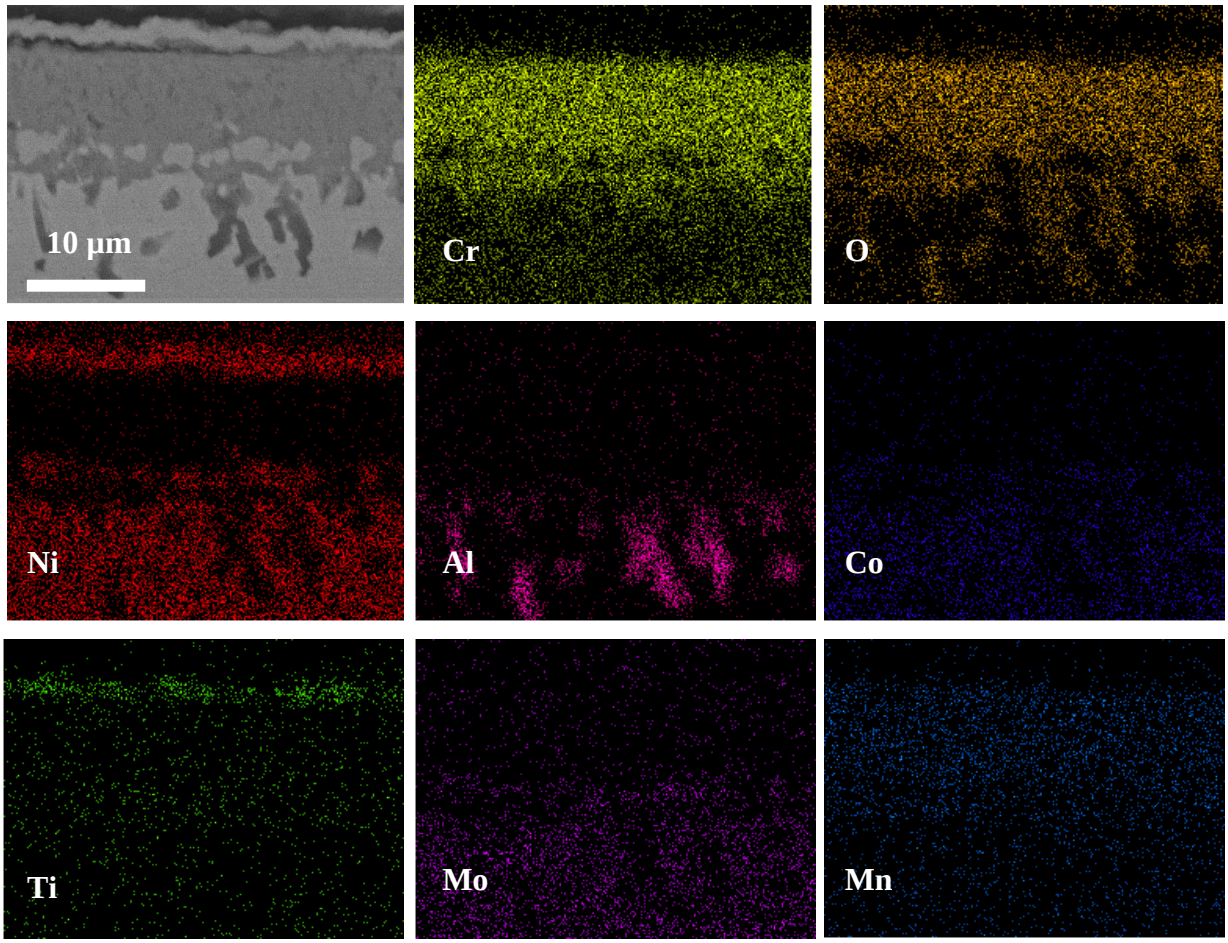

Fig. 66 SEM and EDS results measured on the cross section of Inconel 617 after aged at 950°C in He environment for 500 hr.

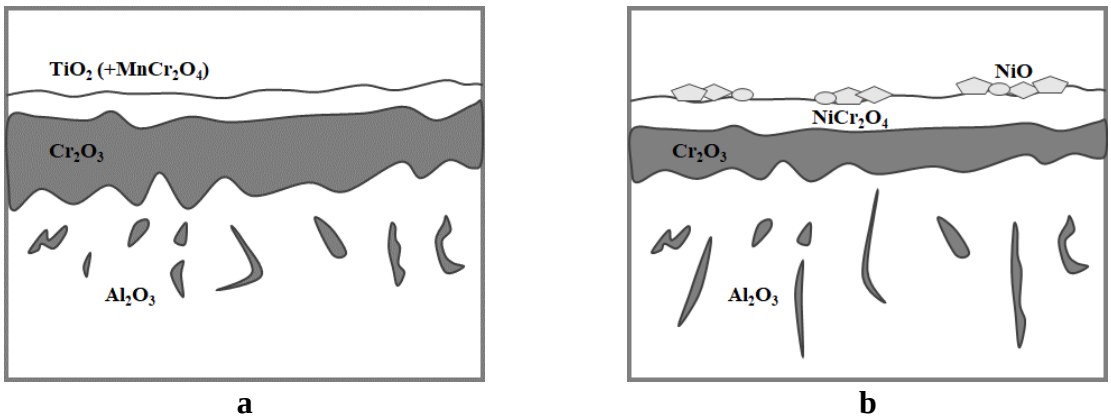

Fig. 67 Schematic diagrams of the multilayer oxide formation (a) H100, (b) A100.

8.2.2. Indentation Hardness and reduced modulus of elasticity

Indentation hardness and reduced modulus if elasticity measurements for the top surface oxide formed on A100 and H100 using the cube corner probe at very shallow depths are shown in Fig. 68. The average values are also summarized in Table 7. For H100, the hardness was measured to be 26.32 GPa and the reduced modulus 211.65 GPa, whereas for A100, the hardness was 15.75 GPa and the reduced modulus 175.38 GPa. The confidence band has a bowed appearance as it is calculated based on the mean of the contact depths of the entire data set and is thus dependent on the distribution of maximum indentation depth data. The wider confidence band indicates more data points away from the mean value and thus higher uncertainty in determining the true mean value. Similarly, the narrow band suggests higher degree of certainty.

Fig. 68 shows comparatively narrow confidence band for the reduced modulus data and negligible variation with contact depth suggesting the elastic modulus of the material is independent of the tested contact depth (within the oxide layer). The hardness data on the other hand shows more wider confidence band, especially H100. This is due to the nonuniform surface, microstructural differences and mostly due to the complex surface chemistry variation. Indentation was performed on the rough oxide surface peaks, based on SPM imaging, to minimize significant roughness effects. The shallow indentations performed with the cube corner probe had the highest contact depth of 60 nm. In order to obtain the thin film's hardness value, the indentation depth needs to be less than 10% of the thickness [116]. The hardness value of the deeper (inner) Cr_2O_3 was obtained by indentation performed from the cross section and obtained as 24.55 GPa, which was reported earlier in Ref [117].

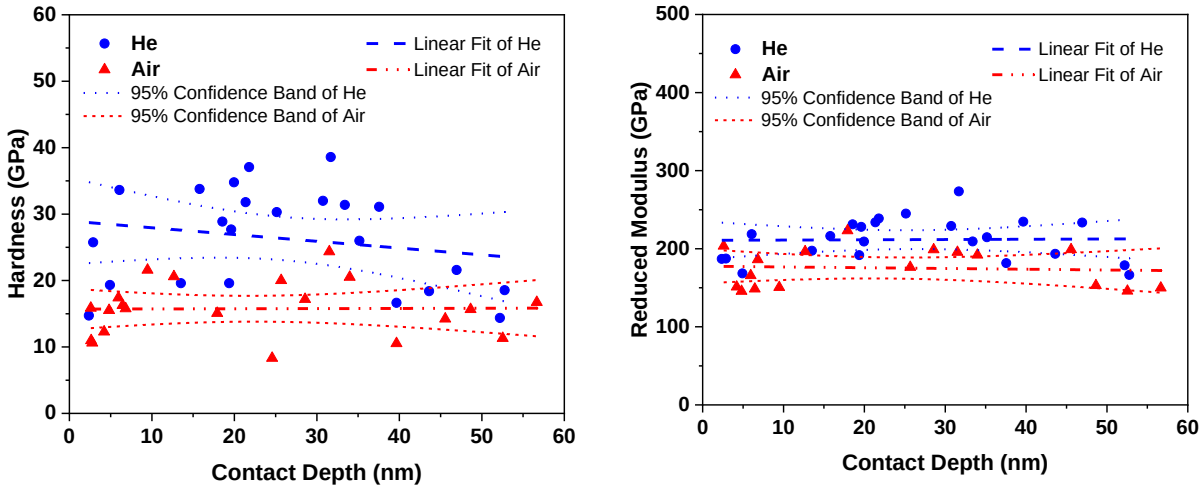

Fig. 68. Nanoindentation (a) hardness and (b) reduced modulus of elasticity of the surface oxide measured with a cube corner probe as a function of contact depth (h_c).

Table 7
Oxide surface properties

Oxides	Thickness (µm)	R_{rms} (µm)	H_c (GPa)	E_r (GPa)
H100	5.7	0.4	26.32	211.65
A100	6.1	0.8	15.75	175.38

8.2.3. Indentation Fracture toughness

To determine the fracture toughness of the oxide layer, higher load nanoindentation measurements were performed using the Berkovich probe. Figure 68(a) shows a representative in -situ load versus displacement curve from a indentation experiment on the oxide surface. During the indentation experiments, under the high stress of the indenter probe, several discontinuities were observed around a load of 20-70 mN at 300-500 nm depth range for the surface oxide generated in He. These discontinuities exist when a sudden increase in depth occurs due to lateral displacement of material under the probe. Some of the discontinuities are observed in the load-displacement curve shown in Fig. 69(a). These dislocations indicate the nucleation of the crack of the oxide surface layer. Here the fracture toughness of the oxide layer is calculated based on the model proposed by Lepienski et al. considering the model developed by Lawn and Evans on crack nucleation [112,118]. As the smallest fractures are difficult to identify, the events are detected in the *dP/dh*

curve versus *P*. Several other discontinuities are observed under lower load, shown in Fig. 69(b). These events follow Weibull statistics and cumulative probability function corresponding to the probability of these events calculated from the fracture events in *dP/dh* vs *P* curves. The cumulative probability function P_f is given by

$$P_f = 1 - \exp\left[-\left(\frac{P - P_u}{P_o}\right)^m \right. \quad (7)$$

where P_f is the cumulative probability function, m is the Weibull modulus, P_0 is the scale parameter and P_u is the location parameter defined as the minimal load for crack nucleation. P_f is estimated as (n-0.5)/N, where n is the n^{th} result in the set of a total N number of *dP/dh* versus *P* curves analyzed. From the experimental indentation data, fracture events were not observed for loads lower than 3 mN for H100 and 40 mN for A100. A good linear fit of the first fracture events in the $Ln\left(Ln\left[\frac{1}{1-P_f}\right]\right)$ versus ln(P-P_u) as shown in Fig. 69(c), confirming the Weibull statistics.

The Weibull modulus or the shape parameter, also known as the Weibull slope (m) and the scale parameter (P_o) were calculated from the plot. The critical load (P_c) is calculated as the load at which 50% fracture probability from the mean value of the Weibull distribution function, given by [119,120]

$$P_c = P_o.\Gamma\left(\frac{1}{m} + 1\right) \quad (8)$$

where $\Gamma(x)$ is the gamma function defined by $\Gamma(x) = x!$

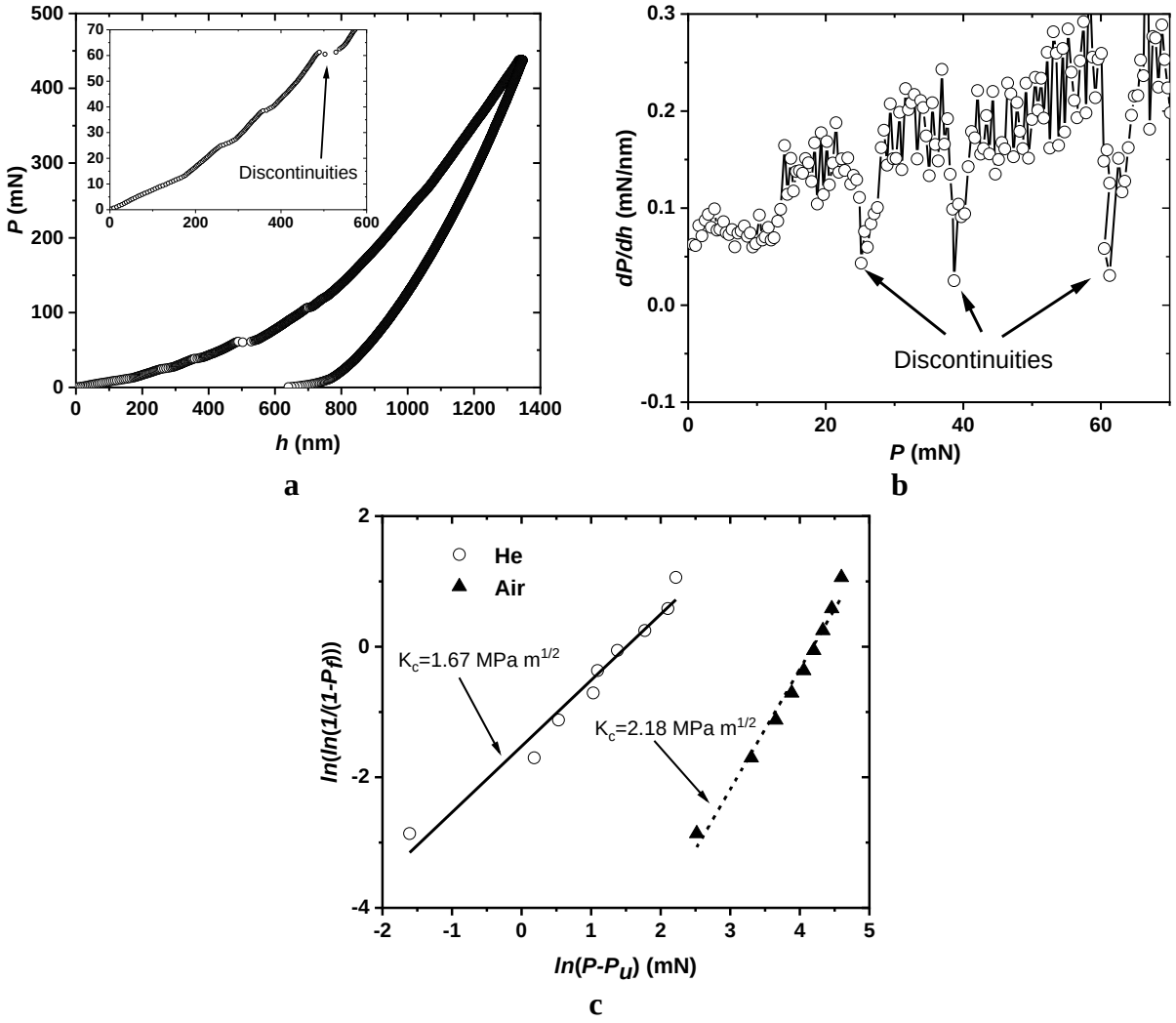

Fig. 69. (a) Typical nanoindentation loading-unloading curve on the oxide using a Berkovich probe, (b) derivative of the load with respect to the contact depth versus indentation load on oxide showing the discontinuities, (c) Weibull plots for the loads associated with the occurrence of first discontinuity due to crack nucleation.

The minimum load P_c to propagate fracture by Lawn and Evan's model is considered arbitrarily as the critical load of a probability of 50% determined by Eq. (8). The fracture toughness calculation is given by the equation

$$K_c = \frac{P_c^{1/4} H_c^{3/4}}{\beta^{1/4}} \tag{9}$$

where H_c is the hardness of the top surface oxide layer, β is an empirical constant for the indenter tip, which is 1.6×10^4 for the Berkovich probe. Considering the values P_o = 6.81 mN, and m = 2.43

for H100, obtained from the *dP/dh* vs *P* curves using Weibull statistics, and the hardness value from Table 7, K_c is obtained for the oxide scale of H100 as 1.67 MPa.m$^{1/2}$ using Eq. (8). For A100, the value of K_c is calculated to be 2.18 MPa.m$^{1/2}$ based on the values of P_o = 91.97 mN and m = 2.83. Higher value of K_c indicates more ductile behavior.

8.2.4. Friction behavior

Scratch experiments were carried out using different normal loads in the range of (50-500) mN to study the scratch friction behavior, while keeping the sliding velocity and number of passes constant. Due to high surface roughness, higher hardness and tip radius, higher scratch load was selected to obtain consistent data. The in-situ COF during scratch and variation of COF with normal load for both A100 and H100 is shown in Fig. 70. The error bars in Fig. 70c indicate ±1 standard deviation obtained from the average COF values of four to six scratch experiments. The COF for A100 gradually increased with increasing load as shown in Fig. 70(c), whereas the COF is stable in between 0.21-0.25 for H100 up to 250 mN load and jumped to much higher value of 1.23 at 500 mN. For the normal load of 50 mN and 100 mN, A100 showed similar COF values between 0.29-0.33. As the friction behavior is highly dominated by the asperity interaction, the roughness of the surface can contribute in increasing the COF. As the A100 surface had higher roughness, it could be a contributing factor in the in-situ fluctuation and higher average COF for A100. The variation on COF between A100 and H100 could be attributed to the hardness difference. Also, the COF increase with load indicated the dominance of ploughing friction component with load.

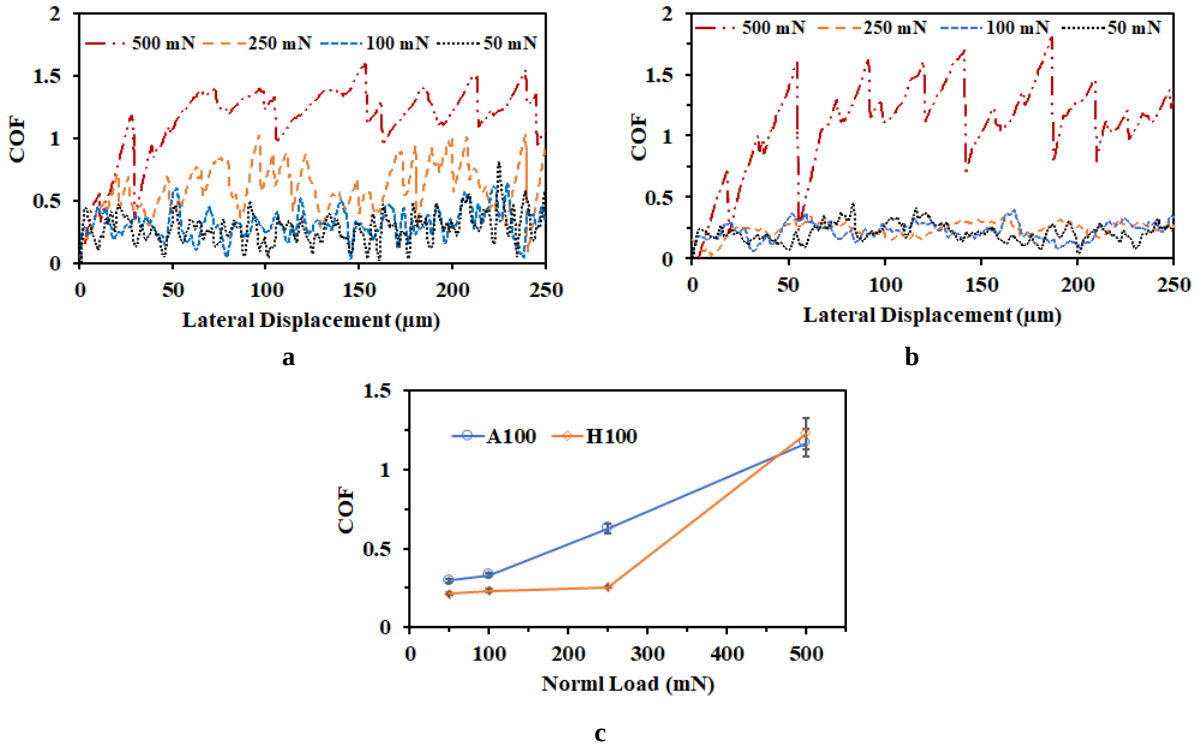

Fig. 70. In-situ COF as a function of lateral displacement during scratch for multiple loads for (a) A100, (b) H100 and average COF as a function of normal load (c).

Fig. 71(a) shows the COF variation with number of passes for both oxides under normal load of 50 mN. Both oxides have similar COF trend showing initial decrease in COF and reaching steady state condition after four passes. The COF in the first pass is dominated by the asperity interaction with the probe. The drop of COF in the second pass indicates the removal of rough asperities. In the later passes at steady-state condition, H100 shows more elastic deformation, whereas A100 deforms plastically and residual depth is much higher due to less recovery. The steady state COF for A100 was 0.23 and 0.18 for H100. Fig. 71(b) shows the change in contact depth with number of passes for both oxides. In this case, H100 does not show much change in contact depth after four passes, and contact depth remains constant for the rest of the passes. However, for A100, the contact depth increases gradually with the number of passes and shows over 100% increase after eight passes. Even with such high increase in contact depth, the change in COF remained very minimal for A100 after twelve passes. This behavior indicates that the friction behavior of H100

oxide surface is dominated by the adhesion friction portion and for A100 ploughing friction portion is dominant. Similar behavior as H100 was reported for macro tribology experiments on pearlitic steels due to work hardening behavior [121]. These results indicate that the oxide in helium will reach steady-state condition for both friction and wear, but in air the wear did not. As reported in Fig. 70, for higher contact pressure, both samples show similar behavior, with H100 showing more resistance to plastic deformation and thus wear resistance, even up to 250 mN.

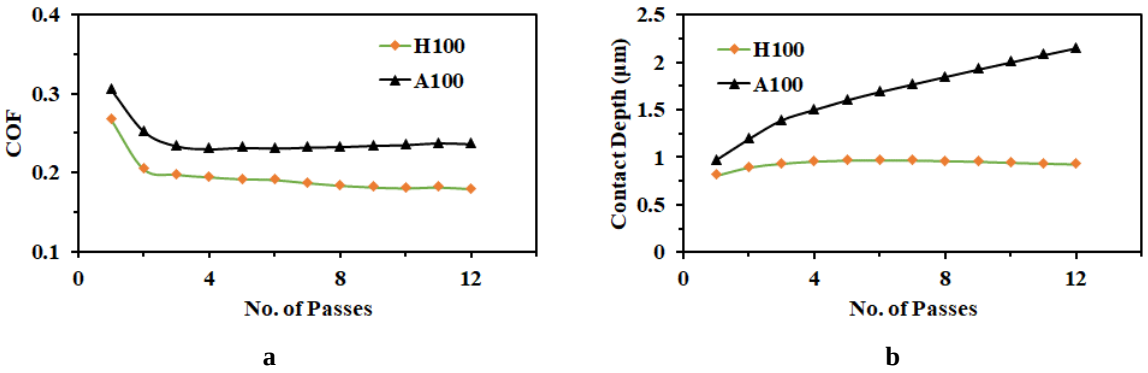

Fig. 71. Variation of (a) COF and (b) residual contact depth with number of passes at normal load of 50 mN.

Two components of the COF, adhesion and ploughing, can be separated using the simple formula

$$\mu_d = 0.6 \times \sqrt{\frac{h}{R}} \quad (10)$$

$$\text{Total friction coefficient } \mu \approx \mu_a + \mu_d \quad (11)$$

where μ_d is the ploughing COF, μ_a is the adhesion COF, h is the in-situ scratch depth, R is the radius of the tip (5 μm) and $R \gg h$. The in-situ scratch depth is measured during the scratch experiments. For 50 mN single pass scratch, the in-situ scratch depth was 628 nm for H100 and 949 nm for A100 sample. The calculated ploughing component for H100 was 0.21 for 50 mN and for A100 it was 0.26. This indicates that the adhesion portion of the COF is 15% for A100 sample, whereas for H100 sample it is only 3%. This data contradicts the conclusion from multi-pass scratch behavior. These simplified calculated values are corresponding to the first pass, which is

dominated by the asperity roughness of the surface. In the first pass both materials deformed plastically and the steady state is not achieved. So, as a caution, the adhesion and ploughing friction portion calculated here are only applicable for the first pass of scratch and can not be considered as general behavior of the material.

The SEM images of the scratches in Fig. 72 on H100 reveal that till 250 mN load the indenter did not break into the top oxide surface and stayed intact. Under higher load of 500 mN the top surface layer is penetrated and delaminated. This increased the indentation depth and also delamination of the layer is the source of higher COF jump observed in the in-situ COF of Fig. 70(b).

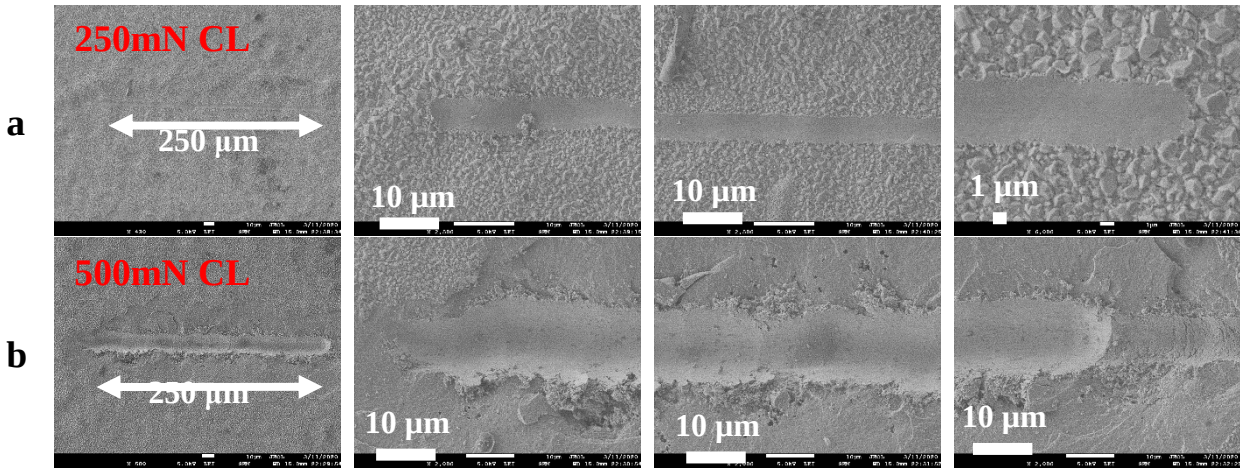

Fig. 72. SEM images of constant load scratch experiments on H100 (a) 250 mN, (b) 500 mN.

The high load scratch experiments on the oxide surface caused delamination of the top surface and eventually expose the multilayered structure of the oxides. The first delamination mainly occurred for the failure of the top spinel oxide layer from the lower dense Cr-oxide. The failure of this top layer is the main reason of COF increase. Fig. 73(a) shows a higher magnification SEM image of the delaminated multilayer structured oxide surface. The inner oxide surface exposed after delamination had lower roughness, compared to the top surface of the oxide. Fig. 73(b) shows a typical SPM image of the delaminated area of the oxide, which was used to measure the thickness

of the delaminated layer. The delaminated layer thickness of the spinel oxide was measured to be 1.2 μm for H100 and 1.8 μm for A100.

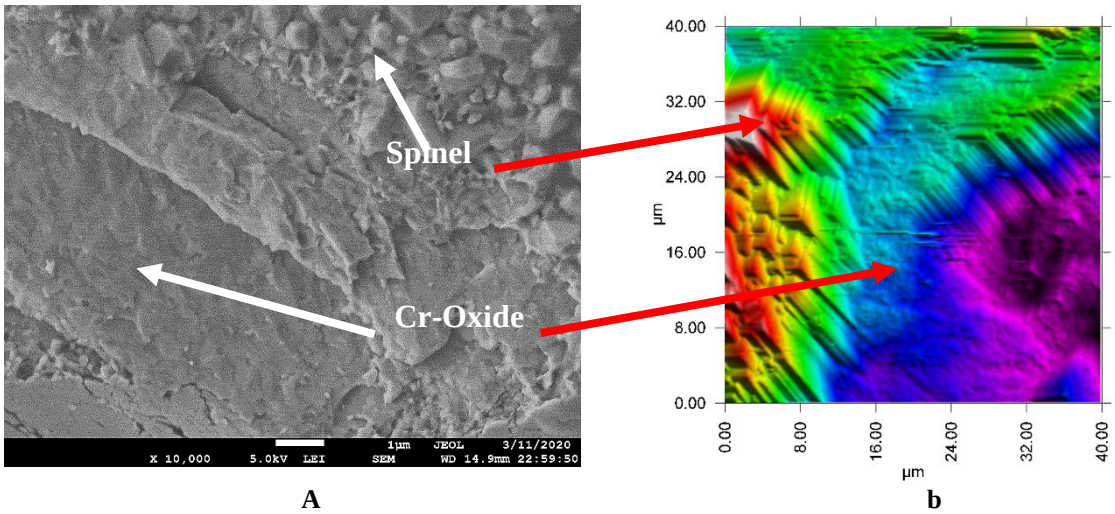

A **b**

Fig. 73. (a) SEM and (b) SPM images of a typical delaminated area after scratch on H100.

8.2.5. Adhesion and shear strength measurements

To investigate the adhesion and shear strength of the oxide layer, penetrative ramp-load scratch experiments were performed. Fig. 74 shows optical and SEM images of the ramp-load scratched H100 surface under three different peak loads. As seen from the optical images, the 250 mN peak load scratch did not delaminate the oxide layer, while under both 500 mN and 750 mN loads the oxide layer was penetrated. To make sure the oxide layer delaminates and for consistent comparison between H100 and A100, the scratch experiments under 750 mN were used for the investigation of interfacial adhesion strength.

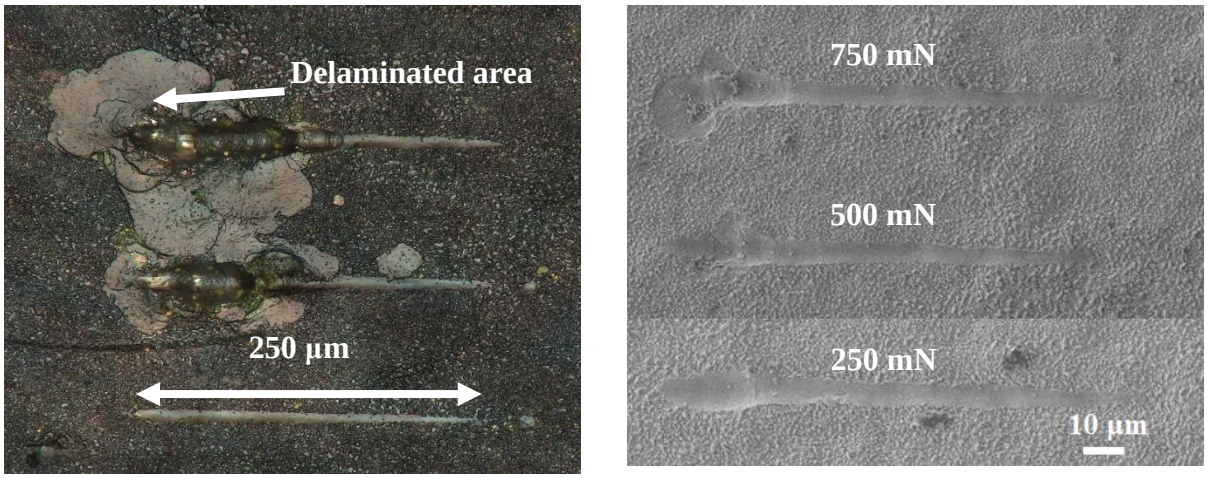

a b

Fig. 74. (a) Optical and (b) SEM images showing the 250 µm long ramp-load scratches on H100 under three different peak loads.

In this study, interfacial failure of the top surface spinel oxide from the internal oxide was observed with spallation ahead of the indenter. The failure event of the oxide scale is identified by the probe movement in the vertical and horizontal direction along the surface. The critical load is recognized by a sudden jump in the normal displacement (Fig. 75(d)) and the location of the failure can be verified by SEM images as shown in Fig. 75(a-c). Fig. 75 shows the SEM images, in-situ normal displacement, normal force, lateral force and COF for a typical ramp-load scratch experiment on H100. Fig.74(d) shows the normal displacement plot against time for the scratch test. A large discontinuity is observed during the failure of the oxide as shown by the arrow. The critical load is obtained corresponding to this time of the failure from the normal force curve shown in Fig. 75(e). For the example shown in Fig. 75, the critical load is measured to be 596.16 mN, and the corresponding critical scratch width was measured from the SEM image to be 5.95 µm.

The experimental results are summarized in Table 8. The oxide layer thickness, hardness and modulus values were obtained according to the process explained earlier. The Poisson's ratio for the top oxide layer of A100 is considered as 0.44, which is the value for $NiCr_2O_4$ and for H100 top layer it is considered 0.27, which is the value of TiO_2, reported by Tromans and Meech based on

theoretical estimation [122]. Considering these values of Poisson's ratio, the Young's modulus of the layers was calculated using Eq (2) and were found to be close to the values reported in Ref. [122] with some deviation from the mixture of other types of oxide elements. The inner Cr_2O_3 is assumed to be the substrate for the top delaminated layer and accordingly the substrate hardness H_s is for Cr_2O_3.

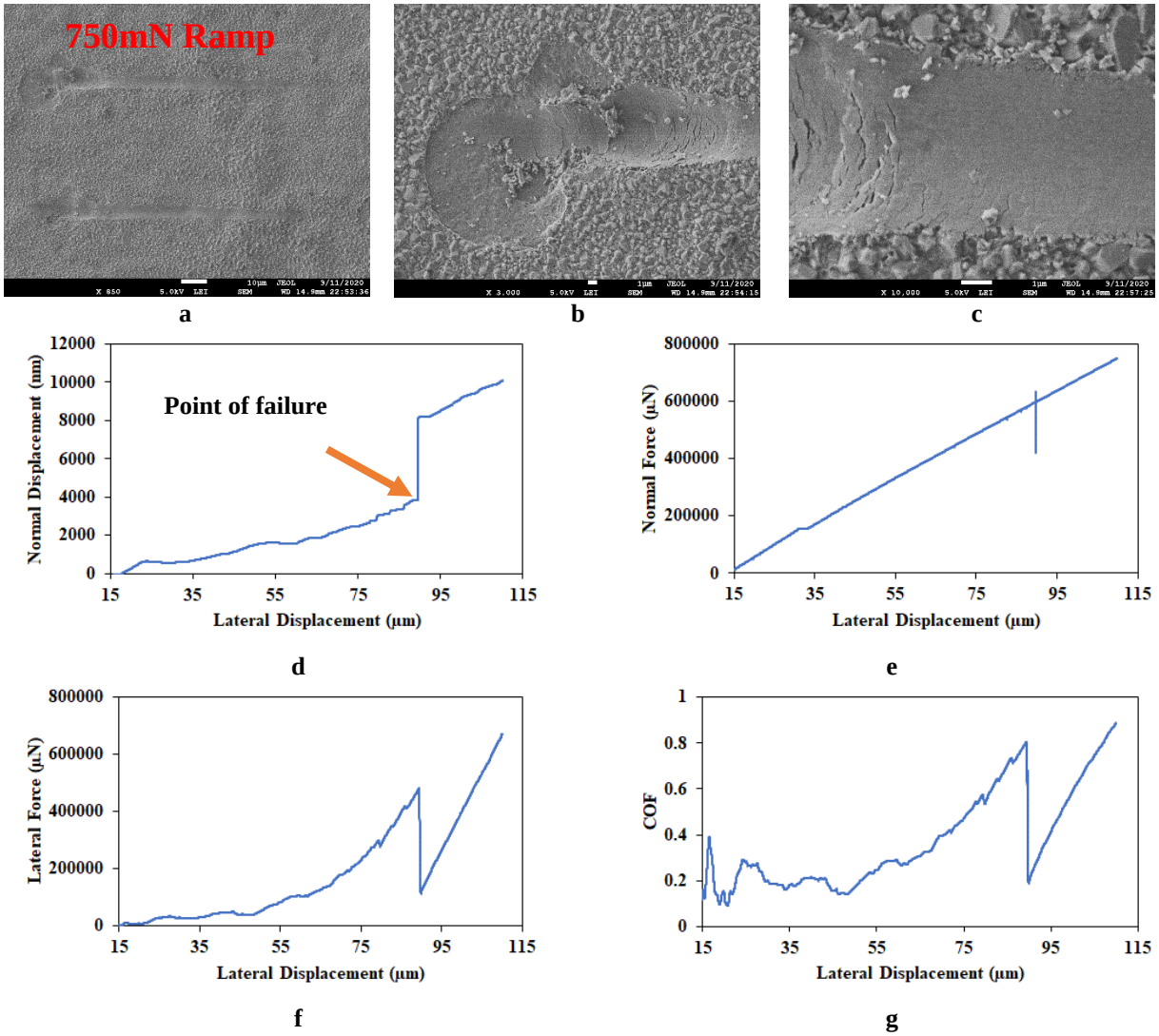

Fig. 75. (a) SEM images of a typical ramp load scratch on H100; Higher magnification SEM images of the scratch track (b) showing spallation failure and (c) the critical load zone; (d) in-situ displacement; (e) in-situ normal force; (f) in-situ lateral force and (g) in-situ COF.

From the data in Table 8, based on Appendix C, it is observed that A100 had lower value for the critical load than H100 and the shear strength value according to Eq. (9) follows the same trend. The critical applied stress ahead of the indenter or adhesion strength of H100 is more than three times the value of A100. This indicates that the chemical bond strength of the H100 top surface oxide is much stronger that A100 with the underlying Cr_2O_3 layer.

Table 8

Average values of calculated and measured properties of the oxides based on indentation and scratch

Oxides	Layer thickness t (μm)	H_s (GPa)	H_c (GPa)	E_c (GPa)	P_c (mN)	d_c (μm)	μ_c	τ_c (GPa)	σ_a (GPa)	Work of adhesion W (Jm^{-2})	
										Eq. (13)	Eq. (15)
A100	1.80	24.55	15.75	166.56	332.29	7.60	0.73	11.20	11.47	715.08	325.83
H100	1.20	24.55	26.32	239.78	552.22	5.80	0.82	15.55	37.32	2753.08	760.07

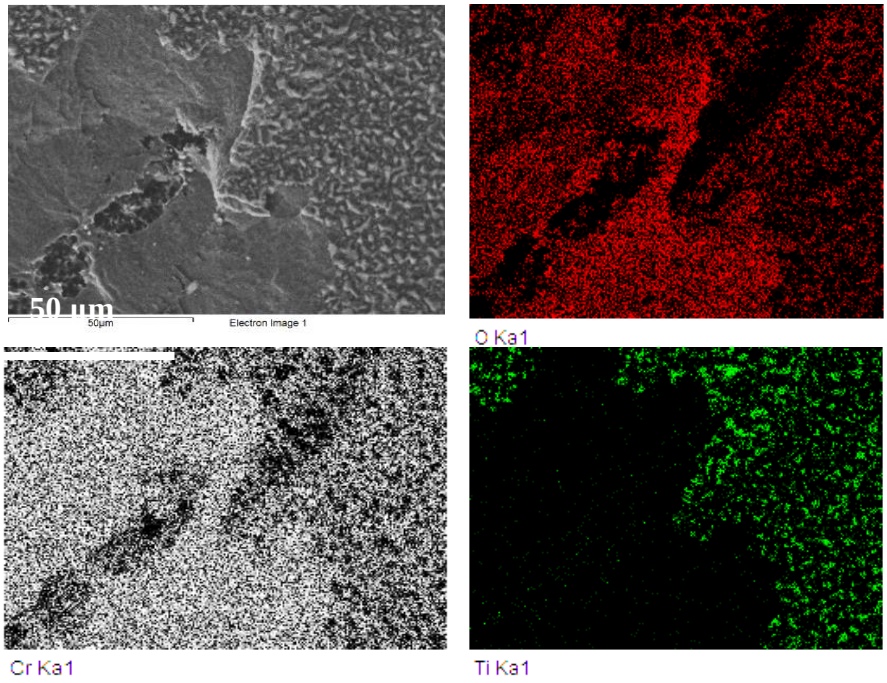

Fig. 76. SEM and EDS map of the spalled area of the H100 oxide layer.

The difference in work of adhesion values for the two models are significant and this is due to the difference in assumptions made for the models. However, both models indicated higher work of adhesion value for H100. The adhesion parameter is mostly affected by the chemical difference in

the thermal oxide. Fig. 76 shows the SEM image and EDS map of a delaminated area from the surface of H100 sample. It clearly shows the spalling of the top Ti-oxide exposing the lower Cr-oxide. The shear stress calculated for this oxide is higher than the $NiCr_2O_4$ on A100.

The residual stresses generated on the oxide surface after cooling of the sample can have effect on the results calculated using Eqs. 13 and 15. So the residual stresses of the oxides have been measured using X-ray diffraction data employing the $Sin^2\psi$ technique. The calculated residual compressive stresses were found to be 1.78 GPa for A100 and 2.08 GPa for H100. Using these values, summed with the critical stress for failure, the work of adhesion is recalculated and found to be 787.65 J/m^2 [Eq. 13] and 358.9 J/m^2 [Eq. 15] for A100 and 2836.88 J/m^2 [Eq. 13] and 782.99 J/m^2 [Eq. 15] for H100. The values increased for both of them with the addition of the residual stress, but the trend remained the same.

8.3. Summary

The thermally grown oxide layers on Inconel 617 under two different environments were examined using nanomechanics techniques, namely nanoindentation and scratch experiments. The results showed that the oxidation environment resulted in the growth of two unique oxide layers on the surface having a common basic Cr-rich oxide layer. Having this difference in chemistry also changed the nanomechanical properties of the surfaces, which is important from a contact, corrosion and tribological perspective. From the current study, we can conclude the following:

1. The oxide layers of Inconel 617 aged in Air showed lower hardness and elastic modulus, than the sample aged in He;
2. Both environments developed multilayer oxides. Air had a dominant presence of $NiCr_2O_4$ on the top surface, whereas the sample aged in He had Ti-rich surface oxide;

3. Ti-rich surface oxide in He-aged sample showed more brittle fracture behavior with K_c of 1.67 MPa.m$^{1/2}$ and the air-aged sample top surface had K_c of 2.18 MPa.m$^{1/2}$;
4. The top oxide layers failed by wedge spallation mode;
5. The He oxide required much higher critical load, compared to the oxide in air, in order to be penetrated;
6. Using the elastic model by Laugier, the adhesion strength of air-aged sample was calculated to be 11.47 GPa, whereas the He-aged sample's adhesion strength is 37.32 GPa;
7. The work of adhesion was higher for He- aged samples. The Attar and Johanneson model calculated the work of adhesion of the Ti-rich top surface layer to be 760.06 Jm^{-2} and the $NiCr_2O_4$ layer on air-aged sample was 325.83 Jm^{-2}.

The oxide formed on the surface in the harsh conditions of VHTR does not support stable tribological behavior which is reflected by the high adhesion and friction data. To lower the friction, and eventually achieve a smooth operation of the valves and other moving parts in the reactors, the surfaces can be coated with special coating or treated with special techniques. In the next chapter we will look into the effects of some techniques on the tribological behavior.

CHAPTER IX
TRIBOLOGICAL PROPERTY ENHANCEMENT

Coatings have been used in several applications to improve the contact performance and increase the service life of components. Metallic multilayers with various individual layer thickness have drawn considerable attention from the community for their promising mechanical properties and surface enhancement capabilities [1–5]. Recent studies have shown that certain metallic multilayers with nanoscale individual constituent layer thickness exhibit extremely high strength close to their theoretical values [4–10]. To mitigate the observed high friction of alloy 800HT and Inconel 617, multiple combinations of Ni/Cr multilayer coatings were investigated where the hardness of multilayers were tailored effectively by varying the individual layer thickness [11-12]. Nano/micro-scratch was utilized for the study of thin films and surface layers to help explain the tribological behavior with correlation to the properties extracted by the nanoindentation. Nanoscratch at high temperature also helped in the selection of the most suitable coating to be deposited on the Ni-alloy surface. This report presents the nano/macro-tribology of Ni/Cr multilayer coatings on Ni-alloys (Inconel 617 and 800HT) at high temperature using both nanoscratch and macro tribology experiments at very high temperatures.

9.1. Coating Preparation

Ni/Cr multilayers with individual layer thickness of h = 50 nm and h = 200 nm were deposited on Si 110 and SiO_2 substrates for the preliminary nanomechanical and microstructural property study. The 50 nm layered coating (noted as NiCr50 hereinafter) has individual Ni and Cr layer of 50 nm thickness reaching to 1.5 μm total thickness, whereas the 200 nm layered coating (noted as NiCr200 hereinafter) has individual layer thickness of 200 nm and total film thickness of 4.0 μm.

For the macro-tribology experiments, NiCr50 and NiCr200 coatings were then deposited on Inconel 617 and 800HT nickel-based alloy substrates by direct current magnetron sputtering at room temperature. Before sputtering, the alloy substrates were mechanically ground and polished, followed by ultrasonic cleaning using ethanol. The sputtering chamber was evacuated to a base pressure of less than 5×10^{-8} torr before deposition. The total film thickness was kept similar, ~1.6 μm for both Ni-based alloy specimens. For this multilayered structure, the first layer is always Cr and the topmost layer is always Ni.

9.2. Nano-tribological Properties

A bright-field XTEM micrograph of NiCr50 multilayer coating (on Si 110 substrate) is shown in Fig. 77a. The inset selected area diffraction (SAD) pattern clearly demonstrates the formation of polycrystalline structure after deposition and no preferable texture is observed. The EDS mapping results (Fig. 77b) and its corresponding line profiles (Fig.76c) verify the chemically alternating layer structure.

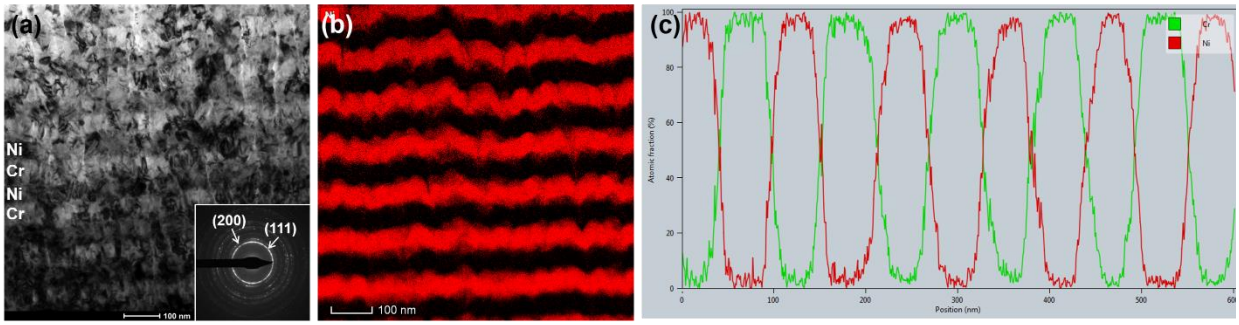

Fig. 77 An XTEM micrograph of Ni/Cr 50 nm multilayer showing the polycrystalline structure. (b) EDS mapping result of Ni and (c) the corresponding line profiles verify the chemically modulated multilayer structure.

The coatings grown on SiO_2 substrate were tested by nanoindentation and nanoscratch. The SPM images in Fig. 78 shows the clear difference in asperity distribution of the coating surfaces. The roughness values, R_{rms} of 5.41 nm and 10.94 nm is calculated from the images for NiCr50 and NiCr200 coatings, respectively.

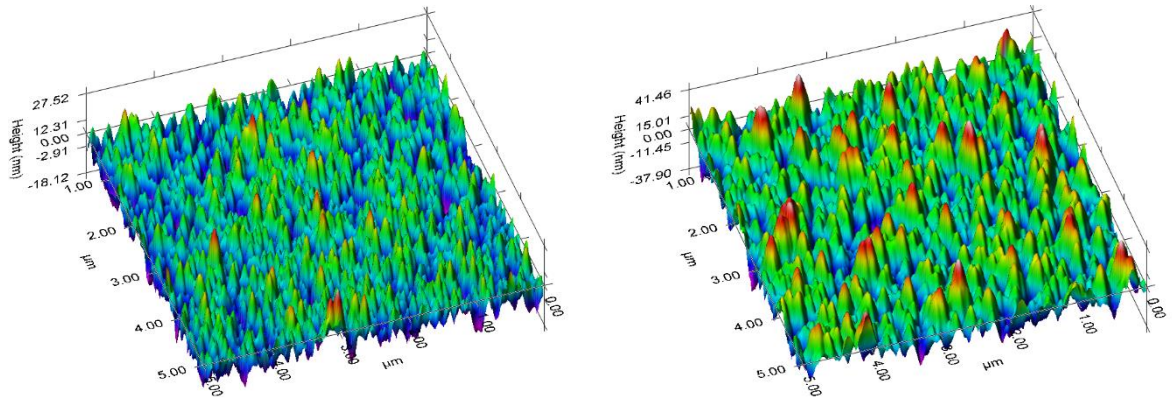

a **b**

Fig. 78 SPM images of (a) NiCr50 and (b) NiCr200

The high temperature indentation and scratch experiments were performed using the Tribo Premier nanoindenter by Bruker (Hysitron) under cover gas of 95% Argon and 5% Hydrogen. The indentations were performed using a Berkovich geometry probe having a tip radius of around 180 nm. The indentation depth range for the data presented here and was in between 50 and 300 nm, which is within 20% of the total coating thickness. For each loading condition the indentation was repeated at least four times. The indentation results showed that the average hardness values were 6.00 GPa and 3.57 GPa for NiCr50 and NiCr200, respectively at room temperature, where the reduced elastic modulus for both coatings stabilizes around 150 GPa. These results are summarized in Table 9, where it should be noted that these values are the composite properties of the multilayer coating, not the individual layers. To identify the individual layer properties, pure Ni and pure Cr coatings of 1.0 µm thickness were also deposited on the same substrate. Pure Cr coating exhibits higher hardness and reduced modulus compared to pure Ni coating, as listed in Table 9.

Table 9
Film parameters measured prior to nanotribological testing

Coatings ID	Layer Thickness (nm)	Total thickness (μm)	R_{rms} (nm)	H (GPa)	E_r (GPa)
Pure Ni	1000	1.0	19.66	2.09 ± 0.67	142.94±19.26
Pure Cr	1000	1.0	2.95	5.44 ± 0.56	153.94 ± 6.75
NiCr50	50	1.5	5.41	6.02 ± 0.67	150.22±7.7
NiCr200	200	4.0	10.94	3.57± 0.30	158.96±12.02

Similar indentations were repeated at elevated temperatures of 200 °C and 400 °C, shown in Fig. 79. The hardness value for NiCr50 reduces gradually by a small amount. The average hardness at 400 °C was found to be 4.92 GPa, which is 18% lower than the RT hardness. The effective modulus reduces insignificantly and remains almost in the same range. On the other hand, for NiCr200 coating, the hardness and reduced modulus show reduction at 200 °C, but it increases again at 400 °C, which could be attributed to the generation of oxide on the surface.

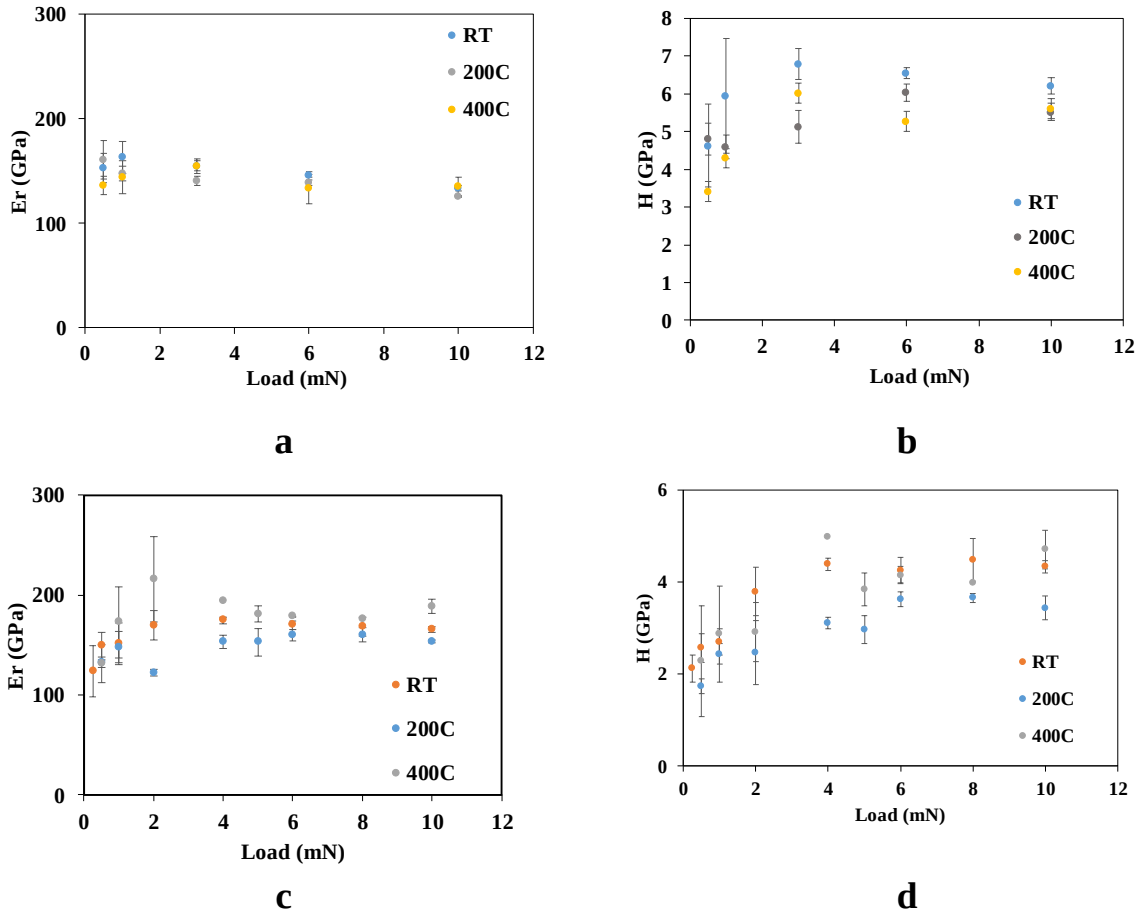

Fig. 79 Extracted nanoindentation properties of (a) reduced modulus of NiCr50; (b) hardness of NiCr50; (c) reduced modulus of NiCr200; (d) hardness of NiCr200 at different temperatures.

The friction behavior was studied at different normal loads (10–100 μN) keeping the sliding velocity and scratch length constant. The variations of COF with temperature and normal load are shown in Fig. 80. The COF of NiCr50 films does not vary much with load up to 200 °C, however it starts to increase beyond that point. For NiCr200 coating, the average COF value at different load remains almost constant, showing minimum effect from normal load up to 300 °C, but shows fluctuation at 400 °C. Fig. 80a also indicates that lower normal load resulted in higher COF at higher temperature, which can be attributed to the higher dependency of COF on adhesion at higher temperatures (and lower normal loads).

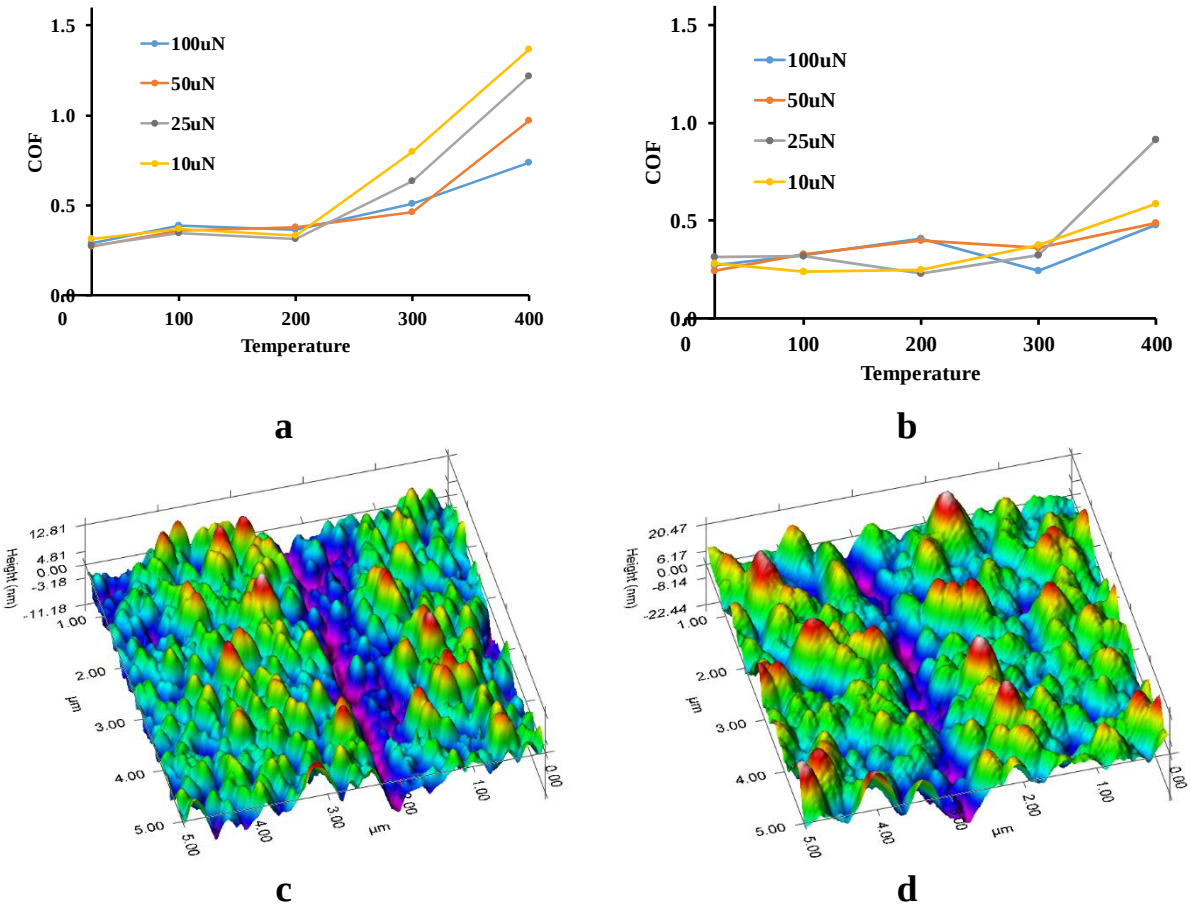

Fig. 80 Variation of COF with normal load and temperature at sliding velocity of 0.6 μm/s, for 6 μm scratch length (a) NiCr50, (b) NiCr200; 3D SPM image (using the same tip as for the scratch) of the post-scratch surface at 400 °C (c) NiCr50, (d) NiCr200.

Fig. 81 shows the normal displacement for 100 μN constant normal force scratch experiments for different temperatures during pre-scratch, in-situ, and post scratch conditions for NiCr200. The residual scratch depths were measured using the post scratch scans by the same tip. All the data is presented in Table 10. From the data, the average in-situ scratch depth values are similar with a slight increase with temperature for both coatings. However, the COF increases with the temperature, especially for coating NiCr50. This increase in COF could be the effect of increased adhesion portion of the friction. In simplified form the total COF can be written as [13]:

$$\text{Total friction coefficient } (\mu) \approx \mu_a + \mu_d \qquad (10.1)$$

where μ_a is the adhesion friction coefficient, which is the inherent part dependent on the material and adjacent conditions. Plowing (deformation) friction takes place when a harder asperity plows a softer surface. Using a spherical asperity geometry scratching a flat surface, ploughing friction coefficient (μ_d) can be simplified as [13]:

$$\text{Ploughing friction coefficient } (\mu_d) = 0.6 \times \sqrt{\frac{h}{R}} \qquad (10.2)$$

where R is the tip radius (here R ≈ 900 nm) and h is the in-situ scratch depth. All the measured and calculated data is shown in Table 10. For NiCr200 the ploughing portion of friction ranges from 0.102 at RT to 0.113 at 400 °C, whereas the total COF increases from 0.27 to 0.47 and is much higher than the ploughing friction for the normal load of 100 µN. This suggests that the adhesive friction has higher impact on the total COF for these coatings. Comparing the two coatings, NiCr50 has better scratch resistance and recovery than NiCr200, but the total COF is much higher at 400 °C for NiCr50.

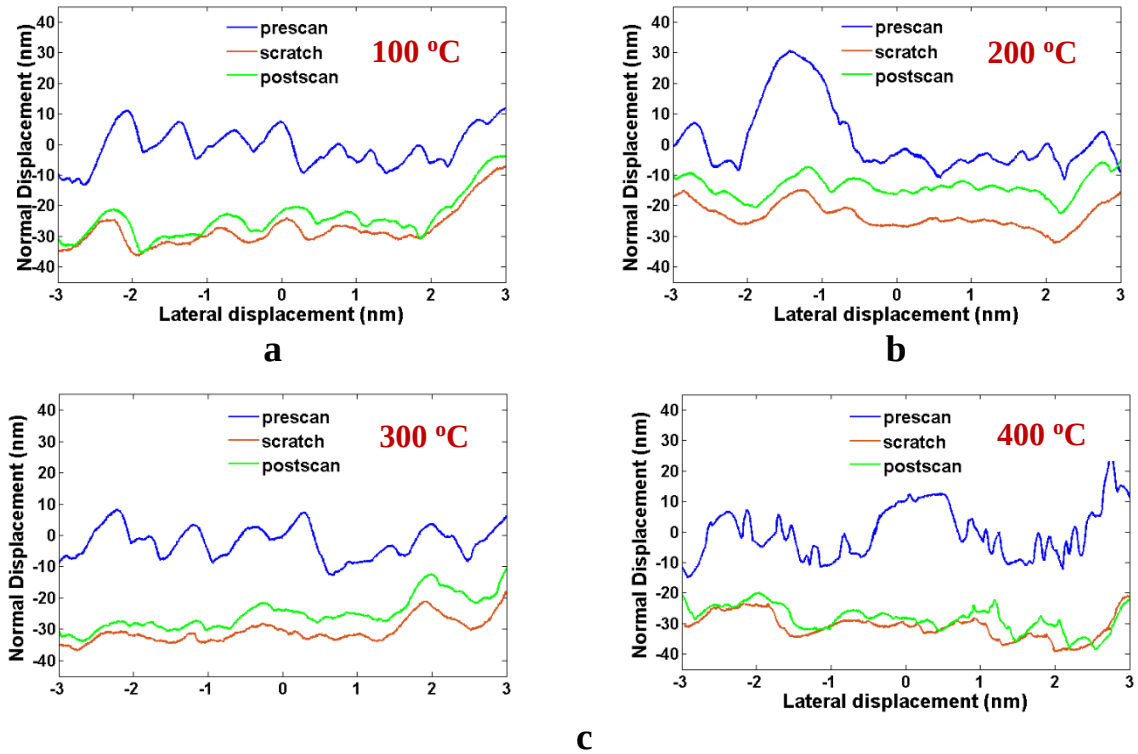

Fig. 81 Scratch profile of NiCr200 with a normal load of 100 µN at (a) 100 ºC, (b) 200 °C, (c) 300 ºC, (d) 400 °C.

Table 10
100 μN Constant Load Scratch Experiments

Coating	Temperature (^oC)	In-situ scratch Depth (nm)	Residual Depth (nm)	Recovery (%)	COF, μ	μ_d
NiCr50	25	13.873	10.102	27	0.287	0.074
	200	15.723	11.382	28	0.362	0.079
	300	18.262	12.837	30	0.509	0.085
	400	20.03	14.767	26	0.736	0.09
NiCr200	25	25.933	21.884	16	0.270	0.102
	200	21.305	15.804	26	0.408	0.092
	300	28.361	23.049	19	0.343	0.107
	400	31.946	27.465	14	0.476	0.113

9.3. Macro Tribological Experiments

The same NiCr50 and NiCr200 Ni/Cr multilayer coatings of 1.6 μm total thickness were deposited on the surface of alloy 800HT and Inconel 617. The surface was prepared by electropolishing before the coating was deposited. The pin-on-disk tribo experiments were conducted in the specialized high temperature tribometer (HTT) simulating VHTR He environmental conditions. For the counterpart a 55.3 mm diameter spherical pin made out of 800HT (against coating surface with 800HT substrate disk) and Inconel 617 (against coating surface with Inconel 617 substrate disk) were used. The surface of the pins was prepared by polishing to have roughness (R_q) in the range of 30 to 40 nm. The experiments were conducted at 750 °C for 800HT and 800 °C for Inconel 617 in He close to the representative environments for HTGR/VHTR. The tribo-experiments were performed under 5 N normal load and at a sliding velocity of 0.04 m/s.

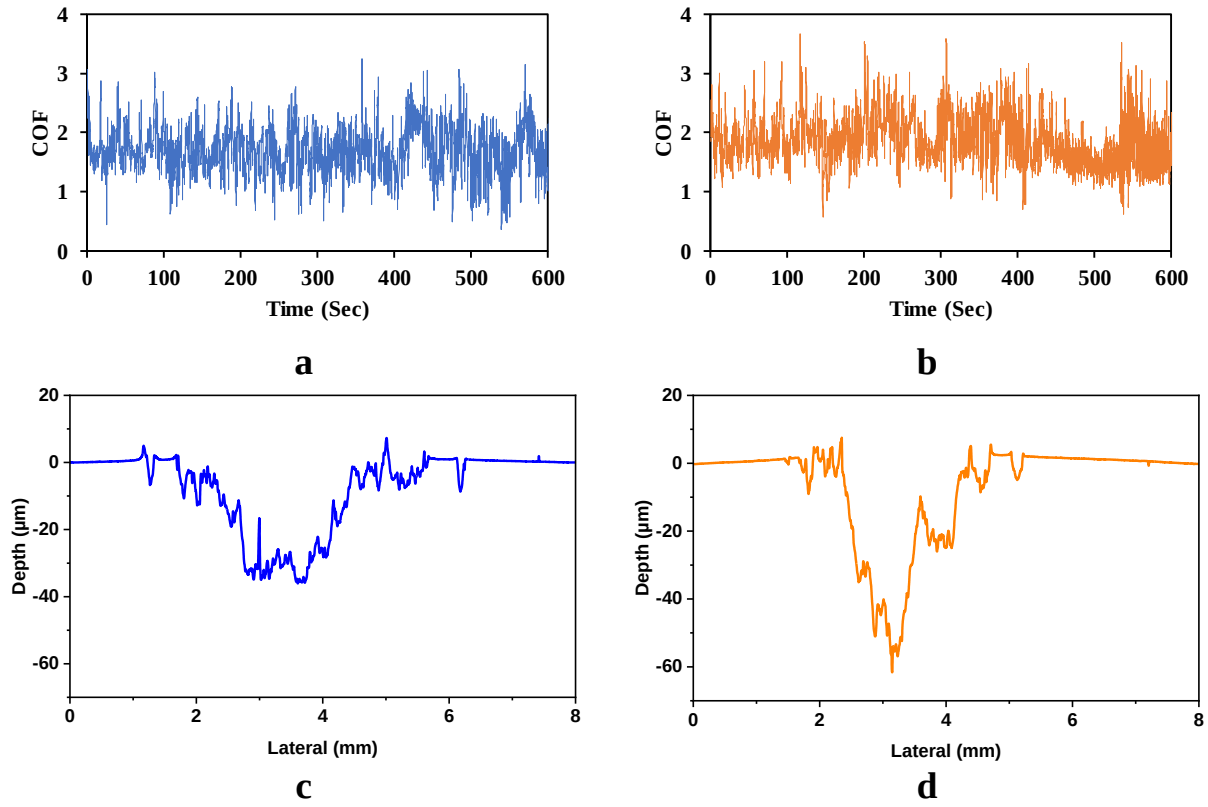

Fig. 82 In-situ COF of (a) NiCr50, (b) NiCr200 in He at 750 °C under 5 N normal load and sliding velocity of 0.04 m/s; Representative wear track line profiles of (c) NiCr50, (d) NiCr200.

Fig. 82 a&b depict the in-situ COF of alloy 800HT coated by multilayer Ni/Cr. The average COF for the NiCr50 coated disk was found to be 1.69 and for NiCr200 to be 1.8. Comparing to COF of untreated surfaces (which was 1.66), this indicates that the coatings were unable to improve the tribological properties of the alloy. The wear tracks were scanned using a contact-based stylus profiler and depicted in Fig. 82c&d. The graphs show clear penetration through the coating and into the substrate for both coatings. Although the coatings survived the scratch experiments at 400 °C under high contact pressure, it could not provide any resistance at 750 °C under macro-scale conditions. Similar results were also observed with the coated samples of Inconel 617 resulting in average COF of 1.36 for NiCr50 and 1.5 for NiCr200. The findings for Inconel 617 are summarized along with those of 800HT in Fig. 83.

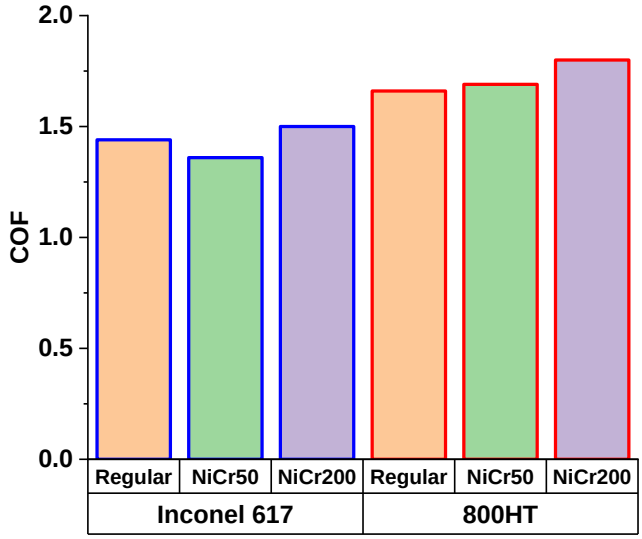

Fig. 83 Average COF of NiCr50 and NiCr200 coated Inconel 617 at 800 °C and alloy 800HT at 750 °C compared with uncoated (designated as "regular") samples.

9.4. Alternative Surface Treatment Approach

Several other alternatives to coatings for alloy 800HT and Inconel 617 were searched in the literature and Laser Shock Peening (LSP) was selected as a potential promising remedy. LSP utilizes short intensive laser pulses to create a plasma in a confined geometry. This results in a very high strain rate plastic deformation leading to a significant increase in the dislocation density through formation of dislocation entanglements and slip bands associated with compressive residual stress and low amount of cold work. The compressive stress field is usually accompanied with increased hardness along with the modified microstructure with a high density of dislocations. The enhanced microstructure creates a shield at the surface where a crack will need much more energy to initiate and propagate. To investigate the effect of LSP on the tribological property of Ni-based alloys in VHTR environment, Inconel 617 samples were LSPed three times and then tested in He at 800°C under 5N normal load, 0.04 m/s sliding velocity and against flat regular (untreated) Inconel 617 pin. Remarkably, the preliminary results show more than 30% reduction in COF and 70% reduction in wear due to LSP process itself, as shown in Fig. 84. This proves LSP

to be a promising technique for enhancing tribological properties of these Ni-based super alloys in future nuclear reactors. This of course opens a new path of research focused on LSP of Ni-based alloys for high temperature tribological applications.

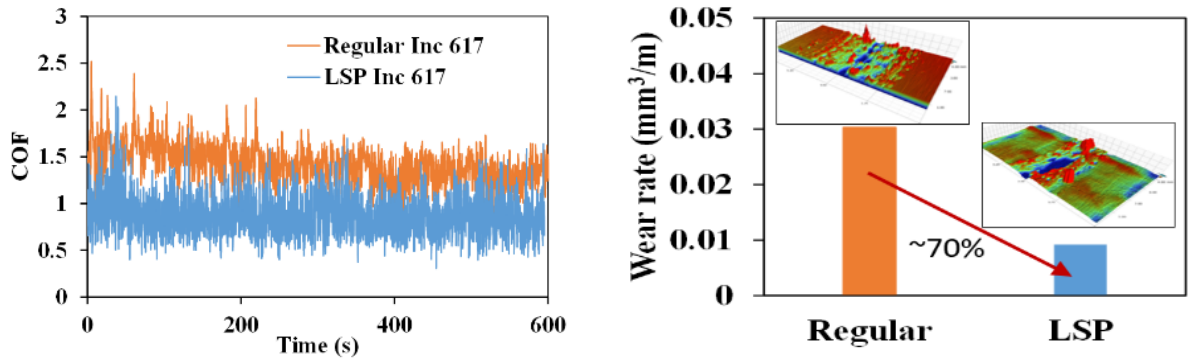

Fig. 84 COF and wear results of untreated and LSPed Inconel 617 in 800°C He atmosphere under 5N load.

9.5. Summary

The objectives of minor milestone #8 were achieved by depositing Ni/Cr multilayer coatings and then subjected to nanoscratch and macro tribological experiments at elevated temperatures. In addition, a relatively new technique to improve the tribological properties at relevant nuclear reactor conditions was investigated showing promising results. The following conclusions can be drawn based on the observations and analysis:

- The developed Ni/Cr multilayer coatings exhibited acceptable performance up to 400 °C under nanomechanical and nano-tribological experiments.
- The same coatings on alloy substrates 800HT and Inconel 617, however, could not protect the surface or improve the tribological properties under macro tribological experiment in realistic VHTR conditions.

- A fairly new surface treatment technique, LSP was applied on Inconel 617 surface. The LSPed samples resulted in 30% reduction in COF and 70% reduction in wear performance, indicating a promising path for the future.

CHAPTER X
CONCLUSIONS AND RECOMMENDATIONS

10.1. Conclusions

This research systematically evaluated the tribological response of 800HT and 617 alloys at relevant reactor operating temperatures (700-950°C) and in the presence of He coolant. The work aimed to address the need for a clear and inclusive understanding of the tribological performance of Ni based alloys in high temperature gas cooled reactors HTGR/VHTR operational environment as well as a further enhancement in HT durability and environmental compatibility of tribological components operating in HTGR-He coolant.

Under this study, a comprehensive experimental plan was performed to investigate and compare the friction, surface damage (wear, self-welding, oxidation) and contact response of tribo-pairs consisting of alloys 800HT and 617 in simulated HTGR He and also in air (room and high temperatures). The results generated here contributes to the design and licensing of HTGR/VHTR in Nuclear Regulatory Commission (NRC) especially with the forthcoming addition of Alloy 617 to the ASME Code for HTGR/VHTR. Besides, micro/nano-mechanical testing and material characterization were performed in high temperatures to obtain a fundamental knowledge of failure mechanisms and tribological response as well as to develop predictive models. The research project also investigated different solutions such as optimizing the operating conditions, and surface modifications, such as surface treatments (e.g., LSP), and HT coatings to mitigate tribological problems with these materials under HTGR/VHTR conditions. The following conclusions have been drawn:

- The oxidation behavior of the alloy 800HT and Inconel 617 was investigated under VHTR operating condition and compared with ambient condition. Both alloys follow parabolic

trend of oxidation over time for the investigated temperatures and time under both air and He atmosphere. Inconel 617 has almost same oxidation rate in He and air at 950 °C, whereas alloy 800HT has lower rate of oxidation in He at 750 °C. The parabolic rate constants for alloy 800HT in air and He conditions are 1.23×10^{-12} and 3.87×10^{-13} $g^2\,cm^{-4}\,s^{-1}$, respectively. For Inconel 617, the rates are 2.27×10^{-12} and 2.31×10^{-12} $g^2\,cm^{-4}\,s^{-1}$ in He and air respectively for aging in 950 °C.

- In HTGR/VHTR condition at high temperatures, both alloys exhibit very high friction. Inconel 617 at 950 °C in He shows static coefficient of friction of around 2.28 and steady state sliding friction coefficient of 1.42 under 5N load and 0.04 m/s sliding velocity. Normal load has minimal effect on the friction behavior under the investigated sliding velocity range (corresponding to VHTR application). In HT He, friction and wear are higher than in air due to the instability of the surface oxide layer and crack initiation/propagation in low oxygen partial pressures, generating larger size wear debris. In air, as temperature increases, friction decreases due to the formation of a protective glazed layer on the tribosurface, formed by wear debris compaction.
- Cr-rich oxide is dominant on the surface of Inconel 617 in both air and He. In He, Cr-oxide, namely Cr_2O_3 is being found on the top surface above Ni-Cr mixed spinel oxide layer. On the other hand, in air, a very thin Ni-Co mixed oxide is found on the very top surface above the Cr_2O_3 and Ni-Cr mixed spinel oxide layer.
- Alloy 800HT at 750 °C in He showed very high COF of 1.66 during sliding whereas the static COF is found to be 3.74, which is around 2.5 times higher than the dynamic COF. At 500 °C and 750 °C He, friction and wear stay high for all conditions due to the surface oxide instability, its brittleness and subsequent crack initiation/propagation through oxide

layer in low oxygen partial pressure, resulting in the generation of larger size wear debris. In He atmosphere, under all contact loads studied here, the specific wear rate shows a linear increasing trend with load, while the COF does not show any specific correlation with contact force. No significant change in wear rate or COF values in He atmosphere is observed for the sliding velocities examined here. However, in air environment, higher sliding velocities influence the formation of the compacted glaze layer and as a result, reduce friction and wear.

- On the surface of alloy 800HT, Fe-rich oxide [(Fe,Ni)Cr_3O_4, Fe_3O_4] is found to be dominant with Cr_2O_3. The very top surface in He and air is more Fe-rich. Although on the surface in He wear track (Fe,Ni) Cr_3O_4 spinel is found, on the wear track surface in air (Fe,Ni)Cr_2O_3 corundum is observed.

- Hardness of the oxide layer is much higher than that of the bulk of Inconel 617. This is due to formation of several hard oxide layers on top of Inconel 617 during aged process. The yield strength through of the oxide of aged Inconel is 10 GPa at RT reducing dramatically to 120 MPa at 600 °C. The high yield strength at RT is close to other metal oxides at RT. Activation energy of oxide is much lower than the bulk of Inconel as less energy is needed for ion/voids to move through the boundaries. Creep deformation at high temperature is dependent on diffusion through the grain rather than dislocation climb dominant for the bulk of Inconel 617 and depend on oxygen diffusivity in the oxide. Based on the extracted properties, mechanical properties of the bulk cannot be used to measure and predict the tribological response of the surface which oxidized during holding stages.

- In general, Inconel 617 exhibits higher tribological stability with lower COF and wear rate at 950 °C compared to alloy 800HT at 750 °C under the investigated contact pressures.

Alloy 800HT shows slightly improved frictional performance under higher contact pressure and sliding speed, especially in air. But for Inconel 617, contact pressure or sliding velocity effect is concluded to be minimal.

- Both alloys did not show any variation in friction/wear behavior with surface roughness (R_q 0.3 and 0.04 µm) as well as three impurity concentrations He.
- The developed Ni/Cr multilayer coatings exhibited acceptable performance up to 400 °C under nanomechanical and nano-tribological experiments. But the same coatings on alloy substrates 800HT and Inconel 617 cannot protect the surface or improve the tribological properties under macro tribological experiment in realistic VHTR conditions.
- A fairly new surface treatment technique, laser shock peening (LSP) was applied on Inconel 617 surface. The LSPed samples resulted in 30% reduction in COF and 70% reduction in wear performance, indicating a promising path for the Inconel 617 surface property enhancement that needs in-depth study in the future.
- Overall, comparing Inconel 617 and alloy 800HT at their peak temperature, both exhibited very high friction but relatively low wear rate. Especially Inconel 617, being investigated under 950 °C exhibited well wear resistant performance with lower COF compared to 800HT. ***The static and dynamic COF values and low wear rate of Inconel 617 make it more favorable than alloy 800HT for the HTGR/VHTR applications.***

10.2. Optimum Design/Operating Conditions

Based on the conclusions from this study, the relevant optimum parameters influencing the tribo-pairs performance in reactors have been identified. Here, the overall effect of all these parameters to help in design and material/operating condition selections are summarized.

Temperature:

Both alloys exhibited the lowest COF at the intermediate temperature of approximately 500ºC and the highest at very high temperatures of 800ºC and higher for Inconel 617 and 750ºC for alloy 800HT. Maximum temperatures were selected based on the suggested operating temperature range of VHTR. According to several experiments at both air and He environments, Inconel 617 exhibits higher tribological stability with lower COF and wear rate at 950 °C compared to alloy 800HT at 750 °C. *These findings suggest Inconel 617 as the favorable choice over alloy 800HT for HTGR/VHTR applications.*

Contact Pressure

The study has been conducted in between 5 N to 20N normal load, which corresponds to 0.16 MPa and 0.64 MPa nominal contact pressures. In the case of Inconel 617 in He condition at 950 °C, the change in contact pressure did not have any effect on the gross behavior of the friction. The intermediate load, 10N exhibited the lowest COF consistently and also the specific wear rate. However, for alloy 800HT, the intermediate load of 10 N resulted in the highest COF and specific wear rate. Alloy 800HT exhibited the lowest COF and wear rate at the highest normal load of 20 N at HT of 750 °C in He condition. Experimental observations show that for relative HTGR/VHTR conditions tribo-contact consisting of Inconel 617 performs best around 0.32 MPa at 950 °C and alloy 800HT around 0.64 MPa nominal contact pressure at 750 °C. However, since the vairation

are minimal and overall COF is generally more than 1.0, the effect of contact pressure is concluded to be insignificant.

Sliding velocity

The sliding velocity range was selected based on the sliding speed calculated for the valve operating in the He pipeline. During the study it is observed that Inconel 617 does not show any dependency on sliding velocity in the investigated range (0.04 m/s to 0.15 m/s). Similarly, for alloy 800HT, sliding velocity did not show any effect on the tribo-contact behavior up to intermediate 0.32 MPa contact pressure. However, as the contact pressure increased to 0.64 MPa, the COF showed a decreasing trend with the raise of sliding velocity, whereas minimal change in wear rate was observed. This generally indicates that alloy 800HT performance increases under higher contact pressure and sliding speed, but for Inconel 617, sliding velocity effect is concluded to be minimal.

Surface roughness

The tribo-study has been conducted for two surface roughness values: Rq 0.3 μm and 0.04 μm. Both alloys did not show any variation in friction/wear behavior with surface roughness. This is due to the high impact of thick surface oxide layer on tribological behavior which is formed/reformed during running-in as well as steady state conditions at high temperatures. Generally, the steady-state condition and the oxide layer morphology/chemistry/thickness was not influenced by initial roughness and therefore, long-term friction/wear behavior showed no dependency on initial roughness.

Helium impurity

To study the effect of the impurities, present in the coolant He, the experiments were performed using three different combinations of impurities which were kept aligned with the reported impurities in the VHTR/HTGR test facilities.

He1 -99.9999% pure (ppm): N_2(0.5),) H_2O(0.2) O_2(0.5), CO(0.1), CO_2(0.1), CH_4(0.1)

He2 -99.999% pure (ppm): N_2(5) H_2O(1), O_2(1), CO(1), CO_2(1), CH_4(0.5)

He3 – 99.99% pure (ppm): H_2(200), CO(20), CH_4(10)

Majority of studies here, were focused on He2, whereas He1 and He3 were used as the two other combination of impurities were found before in the test facilities. None of the impurity combinations resulted in better tribological behavior for any of the alloys. Both He1 and He3 resulted in slightly higher COF at high temperature. Therefore, it can be concluded that the investigated impurity combination within the current range of HTGR/VHTR does not have considerable effect on the tribological behavior of the studied alloys.

Surface modification – Coating/LSP

Coating

To improve the tribological properties of the alloy, a NI/Cr multilayer coating of different layer thickness were deposited on the alloy surface and tested under VHTR simulated tribometer. Although the coatings performed well under high temperature nanoindentation and scratch experiments, they could not offer any improvement to the alloys while under sliding contact in tribometer resulted in similar COF and wear as untreated surfaces. Accordingly, Ni/Cr layered coating is not suggested for the VHTR condition application.

LSP

Several other surface treatment alternatives for alloy 800HT and Inconel 617 were searched and laser shock peening (LSP) was selected and utilized on Inconel 617 surface. The samples were then tested in He at 800°C under 5N normal load and 0.04 m/s sliding velocity and against flat regular Inconel 617 pin. Interestingly, the preliminary results show more than 30% reduction in COF and 70% reduction in wear. *This proves LSP to be a promising technique to enhance tribological properties of these Ni-based super alloys in future nuclear reactors, however, in-depth analysis concentrated on LSP is required for several operating conditions. This, of course, opens a new path of research focused on LSP of Ni-based alloys for high temperature tribological applications.*

10.3. Future Work Recommendations

Current research used a He gas with blend of impurities. For complete understanding of the effect of the gas impurities, it would be better if the materials can be exposed to only one impurity at a time to investigate and isolate the effect of the gas composition on the tribological behavior. For VHTR, understanding the effect of CO_2/CO and H_2O is most important.

Laser shock peening shows promising result in improving friction and wear behavior of Inconel 617 in He atmosphere at high temperature. This study needs to be expanded to investigate the mechanism of improvement and its limitations.

Air aged shows promising possibility to work as a surface treatment method in reducing the friction of Inconel 617, which later can be used in He atmosphere. This surface treatment method needs to be further investigated.

High temperature indentation is very challenging, especially on very reactive material like Ni-based superalloys. Further investigation needs to be done to identify an ideal probe material that can be used for indenting on reactive material without facing the significant challenges.

REFERENCES

[1] Very-high-temperature reactor 2021. https://en.wikipedia.org/wiki/Very-high-temperature_reactor.

[2] Brinkmann G, Vanvor D. Test Facilities in Germany Test Facilities in Germany 2015:1–27. https://www.briva-tech.de/projects.php.

[3] Kim D, Sah I, Kim D, Ryu W, Jang C. High Temperature Oxidation Behavior of Alloy 617 and Haynes 230 in Impurity-Controlled Helium Environments. Oxid Met 2011;75:103–19. doi:10.1007/s11085-010-9223-5.

[4] Wheeler JM, Armstrong DEJ, Heinz W, Schwaiger R. High temperature nanoindentation: The state of the art and future challenges. Curr Opin Solid State Mater Sci 2015;19:354–66. doi:10.1016/j.cossms.2015.02.002.

[5] Cabet C, Terlain A, Lett P, Guétaz L, Gentzbittel JM. High temperature corrosion of structural materials under gas-cooled reactor helium. Mater Corros 2006;57:147–53. doi:10.1002/maco.200503901.

[6] Richard N W. Kinetics of Gas Reactions and Environmental Degradation in NGNP Helium. 2006. doi:10.2172/911710.

[7] Wright RN. Summary of Studies of Aging and Environmental Effects on Inconel 617 and Haynes 230 2006:27. doi:10.2172/911722.

[8] Roy AK, Virupaksha V. Performance of alloy 800H for high-temperature heat exchanger applications. Mater Sci Eng A 2007;452–453:665–72. doi:10.1016/j.msea.2006.11.082.

[9] Natesan K, Purohit A, Tam SW. Materials Behavior in HTGR Environments. 2003. doi:NUREG/CR-6824.

[10] Hasan MH. Effects of mechanical and metallurgical variables on creep , fracture toughness and crack growth behavior of Alloy 617 2009:163.

[11] Ren W, Swindeman R. A Review of Alloy 800H for Applications in the Gen IV Nuclear Energy Systems. ASME 2010 Press. Vessel. Pip. Conf. Vol. 6, Parts A B, ASME; 2010, p. 821–36. doi:10.1115/PVP2010-25278.

[12] Wright JK, Lybeck NJ, Wright RN. Tensile Properties of Alloy 617 Bar Stock 2013.

[13] Quadakkers WJ, Schuster H. Corrosion of High Temperature Alloys in the Primary Circuit Helium of High Temperature Gas Cooled Reactors. -Part I: Theroetical Backround 1985;150:141–50.

[14] Kim D, Jang C, Ryu WS. Oxidation characteristics and oxide layer evolution of Alloy 617 and Haynes 230 at 900 °c and 1100 °c. Oxid Met 2009;71:271–93. doi:10.1007/s11085-

009-9142-5.

[15] Jang C, Lee D, Kim D. Oxidation behaviour of an Alloy 617 in very high-temperature air and helium environments. Int J Press Vessel Pip 2008;85:368–77. doi:10.1016/j.ijpvp.2007.11.010.

[16] Christ HJ, Künecke U, Meyer K, Sockel HG. High temperature corrosion of the nickel-based alloy Inconel 617 in helium containing small amounts of impurities. Mater Sci Eng 1987;87:161–8. doi:10.1016/0025-5416(87)90374-0.

[17] Langevoort JC, Sutherland I, Hanekamp LJ, Gellings PJ. On the oxide formation on stainless steels AISI 304 and incoloy 800H investigated with XPS. Appl Surf Sci 1987;28:167–79. doi:10.1016/0169-4332(87)90062-6.

[18] Birol Y. High temperature sliding wear behaviour of Inconel 617 and Stellite 6 alloys. Wear 2010;269:664–71. doi:10.1016/j.wear.2010.07.005.

[19] Birol Y. Inconel 617 and Stellite 6 alloys for tooling in thixoforming of steels. Trans Nonferrous Met Soc China (English Ed 2010;20:1656–62. doi:10.1016/S1003-6326(09)60354-X.

[20] Beech DJ, May R. Gas Reactor and Associated Nuclear Experience in The UK Relevant to High Temperature Reactor Engineering. Proceedings, Oecd 1999:57.

[21] Corwin W. Nuclear Energy University Programs (NEUP) Fiscal Year (FY) 2015 Annual Planning Webinar-Advanced Structural Materials (RC-3) 2014:5.

[22] Reed TB. Transparent Furnace. 3626154, 1971.

[23] Rouillard F, Cabet C, Wolski K, Terlain A, Tabarant M, Pijolat M, et al. High temperature corrosion of a nickel base alloy by helium impurities. J Nucl Mater 2007;362:248–52. doi:10.1016/j.jnucmat.2007.01.049.

[24] Mankins WL, Hosier JC, Bassford TH. Microstructure and Phase Stability of Inconel Alloy 617. Met Trans 1974;5:2579–90. doi:10.1007/BF02643879.

[25] Kimball. OF, Lai GY, Reynolds H. Effects of thermal aging on the microstructure and mechanical properties of a commercial Ni-Cr-Co-Mo alloy (inconel 617) 2000;7:2–3.

[26] Pauschitz A, Roy M, Franek F. Mechanisms of sliding wear of metals and alloys at elevated temperatures. Tribol Int 2008;41:584–602. doi:10.1016/j.triboint.2007.10.003.

[27] Inman IA, Rose SR, Datta PK. Development of a simple ‘ temperature versus sliding speed ’ wear map for the sliding wear behaviour of dissimilar metallic interfaces 2006;260:919–32. doi:10.1016/j.wear.2005.06.008.

[28] Stott FH, Lin DS, Wood GC, Stevenson CW. The tribological behaviour of nickel and nickel-chromium alloys at temperatures from 20° to 800 °C. Wear 1976;36:147–74.

doi:10.1016/0043-1648(76)90002-8.

[29] Buckley DH. Adhesion and Wear Resistance of Materials. 1986. doi:NASA-TM-87239.

[30] Zum Gahr K-H. Microstructure and wear of materials. Elsevier B.V; 1987.

[31] Buckley DH. Friction, Wear, And Lubrication in Vavuum. NATIONAL AERONAUTICS AND SPACE ADMINISTRATION; 1971.

[32] Stott FH, Lin DS, Wood GC, Stevenson CW. The Tribological Behavior of Nickel and Nickel-Chromium Alloys At Temperature From 20 to 800'C. Wear 1976;36:147–74.

[33] Blau PJ. Elevated-temperature tribology of metallic materials. Tribol Int 2010;43:1203–8. doi:10.1016/j.triboint.2010.01.003.

[34] Crone W, Cao G, Sridhara K. Assessment of Embrittlement of VHTR Structural Alloys in Impure Helium Environments. 2013. doi:10.2172/1087120.

[35] Hrutkay K. Evolution of Microstructure of Haynes 230 and Inconel 617 Under Mechanical Testing At High Temperatures. University of South Carolina, 2013.

[36] Jiang J, Stott FH, Stack MM. The effect of partial pressure of oxygen on the tribological behaviour of a nickel-based alloy, N80A, at elevated temperatures. Wear 1997;203–204:615–25. doi:10.1016/S0043-1648(96)07421-2.

[37] Soda N, Kimura Y, Tanaka A. Wear of some F.C.C. metals during unlubricated sliding part IV: Effects of atmospheric pressure on wear. Wear 1977;43:165–74. doi:10.1016/0043-1648(77)90111-9.

[38] Mishina H. Atmospheric characteristics in friction and wear of metals. Wear 1992;152:99–110. doi:10.1016/0043-1648(92)90207-O.

[39] Rahman MS, Ding J, Beheshti A, Zhang X, Polycarpou AA. Elevated temperature tribology of Ni alloys under helium environment for nuclear reactor applications. Tribol Int 2018;123:372–84. doi:10.1016/j.triboint.2018.03.021.

[40] Inman IA, Datta PS. Studies of high temperature sliding wear of metallic dissimilar interfaces IV: Nimonic 80A versus Incoloy 800HT. Tribol Int 2011;44:1902–19. doi:10.1016/j.triboint.2011.08.004.

[41] Landauer AK, Barnhill WC, Qu J. Correlating mechanical properties and anti-wear performance of tribofilms formed by ionic liquids, ZDDP and their combinations. Wear 2016;354–355:78–82. doi:10.1016/j.wear.2016.03.003.

[42] Yoshizawa H, Chen Y, Israelachrilio J. Fundamental Mecbanisms of Interfacial Friction . 1 . Relation between Adbesion and Friction. Methods 1993:4128–40.

[43] Kato K, Adachi K. Wear Mechanisms. 2001. doi:10.1201/9780849377877.ch7.

[44] Chen LH, Rigney DA. Transfer during unlubricated sliding wear of selected metal systems. Wear 1985;105:47–61. doi:10.1016/0043-1648(85)90005-5.

[45] A Pauschitz, M Roy FF. Identification of the Mechanisms of Wear during Sliding of Metallic Materials at Elevated 2004:721–30.

[46] Cabet C, Chapovaloff J, Rouillard F, Girardin G, Kaczorowski D, Wolski K, et al. High temperature reactivity of two chromium-containing alloys in impure helium. J Nucl Mater 2008;375:173–84. doi:10.1016/j.jnucmat.2007.11.006.

[47] Meschter PJ, Grabke HJ. Kinetics of the water-gas shift reaction on an "FeO" surface. Metall Trans B 1979;10:323–9. doi:10.1007/BF02652502.

[48] M. Hansel, W. J. Quadakkers DJY. Role of water vapor in chromia-scale growth at low oxygen partial pressure. Oxid Met 2003;59:285–300. doi:10.1023/A:1023040010859.

[49] Pieraggi B, Rolland C, Bruckel P. Morphological characteristics of oxide scales grown on H11 steel oxidised in dry or wet air. Mater High Temp 2005;22:61–8. doi:10.1179/mht.2005.007.

[50] Choudhry KI, Mahboubi S, Botton GA, Kish JR, Svishchev IM. Corrosion of engineering materials in a supercritical water cooled reactor: Characterization of oxide scales on Alloy 800H and stainless steel 316. Corros Sci 2015;100:222–30. doi:10.1016/j.corsci.2015.07.035.

[51] Bsat S, Huang X. Corrosion Behaviour of Alloy 800H in Low Density Superheated Steam. ISIJ Int 2016;56:1067–75. doi:10.2355/isijinternational.ISIJINT-2015-651.

[52] Behnamian Y, Mostafaei A, Kohandehghan A, Amirkhiz BS, Serate D, Sun Y, et al. A comparative study of oxide scales grown on stainless steel and nickel-based superalloys in ultra-high temperature supercritical water at 800 °C. Corros Sci 2016;106:188–207. doi:10.1016/j.corsci.2016.02.004.

[53] Zeng Z, Natesan K, Grimsditch M. Effect of Oxide Scale Compositions on Metal Dusting Corrosion of Fe-Based Alloys. CORROSION 2004;60:632–42. doi:10.5006/1.3287838.

[54] Wang W, Ding Z, Zhao X, Wu S, Li F, Ming Yue, et al. Microstructure and magnetic properties of MFe2O4 (M = Co , Ni , and Mn) ferrite nanocrystals prepared using colloid mill and hydrothermal method. J Appl Phys 2015;117:1–5. doi:10.1063/1.4917463.

[55] Bates HGA. Corrosion behavior of high-temperature alloys during exposure for times up to 10,000 h in prototype nuclear process helium at 700 to 900 °C. Nucl Technol 1984;66:415–28. doi:10.13182/NT84-A33444.

[56] Cappelaere M, Perrot M, Sannier J. Behavior of Metallic Materials Between 550 and 870°C in High-Temperature Gas-Cooled Reactor Helium Under Pressures of 2 and 50 bar. Nucl Technol 1984;66:465–78. doi:10.13182/NT84-A33447.

[57] Tan L, Allen TR, Yang Y. Corrosion behavior of alloy 800H (Fe – 21Cr – 32Ni) in supercritical water. Corros Sci 2011;53:703–11. doi:10.1016/j.corsci.2010.10.021.

[58] Erdemir A. A crystal-chemical approach to lubrication by solid oxides. Tribol Lett 2000;8:97–102. doi:10.1023/A:1019183101329.

[59] Srisrual A. Photoelectrochemical characterization of thermal oxide developed on metal and model alloys Caractérisation photoélectrochimique d ' oxydes thermiques développés sur métaux et alliages modèles 2015.

[60] Srisrual A, Coindeau S, Galerie A, Petit JP, Wouters Y. Identification by photoelectrochemistry of oxide phases grown during the initial stages of thermal oxidation of AISI 441 ferritic stainless steel in air or in water vapour. Corros Sci 2009;51:562–8. doi:10.1016/j.corsci.2008.12.002.

[61] Renusch D. Transient oxidation in Fe-Cr-Ni alloys: A raman-scattering study. Oxid Met 1996;46:365–81. doi:10.1007/BF01048636.

[62] Srisrual A, Petit JP, Wouters Y, Galerie A. The effect of water vapor on thermal oxide grown on inconel 690. Appl Mech Mater 2014;670–671:74–81. doi:10.4028/www.scientific.net/AMM.670-671.74.

[63] Srisrual A, Petit JP, Wouters Y, Pascal C, Galerie A. Photoelectrochemical investigations on individual ferritic and austenitic grains of a duplex stainless steel oxidized in water vapour. Mater High Temp 2011;28:349–54. doi:10.3184/096034011X13190163136192.

[64] Edwards MW, McIntyre NS. Gas phase initial oxidation of incoloy 800 surfaces. Oxid Met 2013;79:179–200. doi:10.1007/s11085-012-9316-4.

[65] Abraham GJ, Bhambroo R, Kain V, Shekhar R, Dey GK, Raja VS. Electrochemical characterization of oxide film formed at high temperature on Alloy 690. Nucl Eng Des 2012;243:69–75. doi:10.1016/j.nucengdes.2011.11.018.

[66] McCarty KF, Boehme DR. A Raman study of the systems Fe3-xCrxO4 and Fe2-xCrxO3. J Solid State Chem 1989. doi:10.1016/0022-4596(89)90245-4.

[67] Zeng Z, Natesan K, Grimsditch M. Effect of Oxide Scale Compositions on Metal Dusting Corrosion of Fe-Based Alloys 2004:632–42.

[68] Srisrual A, Pitaksakorn K, Promdirek P. Influence of Water Vapor on Oxide Scale Morphology of Incoloy800HT at 850°C. Appl Mech Mater 2018;875:36–40. doi:10.4028/www.scientific.net/amm.875.36.

[69] Sakaba N, Hamamoto S, Takeda Y. Helium chemistry for very high temperature reactors. J Nucl Sci Technol 2010;47:269–77.

[70] Stanford MK. A Review of Tribomaterial Technology for Space Nuclear Power Systems. Program 2007.

[71] Chatterjee A, Polycarpou AA, Abelson JR, Bellon P. Nanoscratch study of hard HfB2 thin films using experimental and finite element techniques. Wear 2010;268:677–85. doi:10.1016/j.wear.2009.11.001.

[72] Chechenin NG, Bøttiger J, Krog JP. Nanoindentation of amorphous aluminum oxide films I. The influence of the substrate on the plastic properties. Thin Solid Films 1995;261:219–27.

[73] Pharr GM, Oliver WC. Measurement of thin film mechanical properties using nanoindentation. Mrs Bull 1992;17:28–33.

[74] Humood M, Beheshti A, Meyer JL, Polycarpou AA. Normal impact of sand particles with solar panel glass surfaces. Tribol Int 2016;102:237–48.

[75] Pang X, Gao K, Volinsky AA. Microstructure and mechanical properties of chromium oxide coatings. J Mater Res 2007;22:3531–7.

[76] Humood M, Beheshti A, Polycarpou AA. Surface reliability of annealed and tempered solar protective glasses : Indentation and scratch behavior. Sol Energy 2017;142:13–25. doi:10.1016/j.solener.2016.12.011.

[77] Lee J, Beheshti A, Polycarpou AA. Rough Surface Normal Nanocontact Stiffness: Experimental Measurements and Rough Surface Contact Model Predictions. J Appl Mech Trans ASME 2017;84. doi:10.1115/1.4035524.

[78] Su C, Herbert EG, Sohn S, LaManna JA, Oliver WC, Pharr GM. Measurement of power-law creep parameters by instrumented indentation methods. J Mech Phys Solids 2013;61:517–36. doi:10.1016/j.jmps.2012.09.009.

[79] Cordova ME, Shen Y-L. Indentation versus uniaxial power-law creep: a numerical assessment. J Mater Sci 2015;50:1394–400.

[80] Kang J, Becker AA, Sun W. Determination of elastic and viscoplastic material properties obtained from indentation tests using a combined finite element analysis and optimization approach. Proc Inst Mech Eng Part L J Mater Des Appl 2015;229:175–88.

[81] Takagi H, Dao M, Fujiwara M. Prediction of the constitutive equation for uniaxial creep of a power-law material through instrumented microindentation testing and modeling. Mater Trans 2014;55:275–84.

[82] Gibson JS-L, Roberts SG, Armstrong DEJ. High temperature indentation of helium-implanted tungsten. Mater Sci Eng A 2015;625:380–4.

[83] Wang H, Dhiman A, Ostergaard HE, Zhang Y, Siegmund T, Kruzic JJ, et al. Nanoindentation based properties of Inconel 718 at elevated temperatures: A comparison of conventional versus additively manufactured samples. Int J Plast 2019;120:380–94. doi:10.1016/j.ijplas.2019.04.018.

[84] Zhang Y, Mohanty DP, Seiler P, Siegmund T, Kruzic JJ, Tomar V. High temperature indentation based property measurements of IN-617. Int J Plast 2017;96:264–81. doi:10.1016/j.ijplas.2017.05.007.

[85] Wu ZF, Wang XD, Cao QP, Zhao GH, Li JX, Zhang DX, et al. Microstructure characterization of AlxCo1Cr1Cu1Fe1Ni1(x = 0 and 2.5) high-entropy alloy films. J Alloys Compd 2014;609:137–42. doi:10.1016/j.jallcom.2014.04.094.

[86] Frost HJ, Ashby MF. Deformation mechanism maps: the plasticity and creep of metals and ceramics. Pergamon press; 1982.

[87] Bower AF, Fleck NA, Needleman A, Ogbonna N. Indentation of a power law creeping solid. Proc R Soc Lond A 1993;441:97–124.

[88] Dean J, Bradbury A, Aldrich-Smith G, Clyne TW. A procedure for extracting primary and secondary creep parameters from nanoindentation data. Mech Mater 2013;65:124–34.

[89] Dean J, Wheeler JM, Clyne TW. Use of quasi-static nanoindentation data to obtain stress--strain characteristics for metallic materials. Acta Mater 2010;58:3613–23.

[90] Palma T, Munther M, Damasus P, Salari S, Beheshti A, Davami K. Multiscale mechanical and tribological characterizations of additively manufactured polyamide 12 parts with different print orientations. J Manuf Process 2019;40:76–83.

[91] Monclús MA, Lotfian S, Molina-Aldareguía JM. Tip shape effect on hot nanoindentation hardness and modulus measurements. Int J Precis Eng Manuf 2014;15:1513–9. doi:10.1007/s12541-014-0499-2.

[92] Phani PS, Oliver WC, Pharr GM. On the Measurement of Power Law Creep Parameters from Instrumented Indentation. JOM 2017;69:2229–36.

[93] Phani PS, Oliver WC. A direct comparison of high temperature nanoindentation creep and uniaxial creep measurements for commercial purity aluminum. Acta Mater 2016;111:31–8. doi:10.1016/j.actamat.2016.03.032.

[94] Oliver WC, Pharr GM. An improved technique for determining hardness and elastic modulus using load and displacement sensing indentation experiments. J Mater Res 1992;7:1564–83.

[95] Feng G, Ngan AHW. Effects of creep and thermal drift on modulus measurement using depth-sensing indentation. J Mater Res 2002;17:660–8.

[96] Lee H, Chen Y, Claisse A, Schuh CA. Finite element simulation of hot nanoindentation in vacuum. Exp Mech 2013;53:1201–11.

[97] Shackelford JF, Han Y-H, Kim S, Kwon S-H. CRC materials science and engineering handbook. CRC press; 2016.

[98] Petersen KE. Silicon as a mechanical material. Proc IEEE 1982;70:420–57.

[99] Liu H, Tao J, Xu J, Chen Z, Gao Q. Corrosion and tribological behaviors of chromium oxide coatings prepared by the glow-discharge plasma technique. Surf Coatings Technol 2009;204:28–36. doi:10.1016/j.surfcoat.2009.06.020.

[100] Hidaka Y, Anraku T, Otsuka N. Deformation of iron oxides upon tensile tests at 600-1250°C. Oxid Met 2003;59:97–113. doi:10.1023/A:1023070016230.

[101] Evans B, Goetze C. The temperature variation of hardness of olivine and its implication for polycrystalline yield stress. J Geophys Res Solid Earth 1979;84:5505–24.

[102] Smith GD, Yates DH. Optimization of the Fatigue Properties of INCONEL alloy 617. ASME 1991 Int. Gas Turbine Aeroengine Congr. Expo., 1991, p. V005T12A009--V005T12A009.

[103] Corporation SM. Inconel Alloy 617. Spec Met 2015:Inconel Alloy 617.

[104] Coble RL. A model for boundary diffusion controlled creep in polycrystalline materials. J Appl Phys 1963;34:1679–82. doi:10.1063/1.1702656.

[105] Lifshitz IM. On the theory of diffusion-viscous flow of polycrystalline bodies. Sov Phys JETP 1963;17:909.

[106] Lau JH. Solder joint reliability: theory and applications. Springer Science & Business Media; 1991.

[107] Schneider K, Rekas M. High Temperature Creep of Metal Oxides. Creep 2018. doi:10.5772/intechopen.70876.

[108] Bobji MS, Ramanujan CS, Pethica JB, Inkson BJ. A miniaturized TEM nanoindenter for studying material deformation in situ. Meas Sci Technol 2006;17:1324–9. doi:10.1088/0957-0233/17/6/006.

[109] Anantheshwara K. In situ transmission electron microscope triboprobe for tribological studies of materials at nanoscale. Indian Institute of Science, 2011. doi:10.1.1.629.6462.

[110] Li X, Diao D, Bhushan B. Fracture mechanisms of thin amorphous carbon films in nanoindentation. Acta Mater 1997;45:4453–61. doi:10.1016/S1359-6454(97)00143-2.

[111] Li X, Bhushan B. Measurement of fracture toughness of ultra-thin amorphous carbon films. Thin Solid Films 1998;315:214–21. doi:10.1016/S0040-6090(97)00788-8.

[112] Mikowski A, Carlos Serbena F, Eugnio Foerster C, Roberto Jurelo A, Maurcio Lepienski C. A method to measure fracture toughness using indentation in REBa 2Cu3O7-superconductor single crystals. J Appl Phys 2011;110. doi:10.1063/1.3662121.

[113] B. R. LAWN D. B. MARSHALL. Hardness, Toughness, and Brittleness: An Indentation

Analysis. J Am Ceram Soc 1979;62:1–4.

[114] Yu N, Polycarpou AA, Conry TF. Tip-radius effect in finite element modeling of sub-50 nm shallow nanoindentation. Thin Solid Films 2004;450:295–303. doi:10.1016/j.tsf.2003.10.033.

[115] Rahman MS, Polychronopoulou K, Polycarpou AA. Tribochemistry of inconel 617 during sliding contact at 950 °C under helium environment for nuclear reactors. J Nucl Mater 2019;521:21–30.

[116] Tayebi N, Polycarpou AA. Reducing the effects of adhesion and friction in microelectromechanical systems (MEMSs) through surface roughening : Comparison between theory and experiments Reducing the effects of adhesion and friction in microelectromechanical systems „ MEMSs … thro 2018;073528. doi:10.1063/1.2058178.

[117] Salari S, Rahman MS, Polycarpou AA, Beheshti A. Elevated temperature mechanical properties of Inconel 617 surface oxide using nanoindentation. Mater Sci Eng A 2020;788:139539. doi:10.1016/j.msea.2020.139539.

[118] Lawn BR, Evans AG. A model for crack initiation in elastic/plastic indentation fields. J Mater Sci 1977;12:2195–9. doi:10.1007/BF00552240.

[119] WEIBULL W. A Statistical Distribution Function of Wide Applicability. J Appl Mech 1951;13:293–7.

[120] Mikowski A, Serbena FC, Foerster CE, Lepienski CM. Statistical analysis of threshold load for radial crack nucleation by Vickers indentation in commercial soda-lime silica glass. J Non Cryst Solids 2006. doi:10.1016/j.jnoncrysol.2006.02.112.

[121] Lee KM, Polycarpou AA. Wear of conventional pearlitic and improved bainitic rail steels. Wear 2005;259:391–9. doi:10.1016/j.wear.2005.02.058.

[122] Tromans D, Meech JA. Fracture toughness and surface energies of covalent minerals: Theoretical estimates. Miner Eng 2004;17:1–15. doi:10.1016/j.mineng.2003.09.006.

[123] Dieter GE. Mechanical metallurgy. New York,: McGraw-Hill,; 1961. doi:10.5962/bhl.title.35895.

[124] Hsu C-Y, Juan C-C, Wang W-R, Sheu T-S, Yeh J-W, Chen S-K. On the superior hot hardness and softening resistance of AlCoCrxFeMo0.5Ni high-entropy alloys. Mater Sci Eng A 2011;528:3581–8. doi:10.1016/j.msea.2011.01.072.

[125] Yamamoto Y. Hot-hardness and indentation creep characteristics of pure metals. J Iron Steel Inst Jpn 1986:110–6.

[126] Moschi S, Grau P, Berg G. Nanotribological Measurements on Sol-Gel Derived Silica Films. MRS Proc 1998;522:415. doi:10.1557/PROC-522-415.

[127] Benjamin P, Weaver C. Measurement of adhesion of thin films. Proc R Soc London Ser A Math Phys Sci 1960;254:163–76. doi:10.1098/rspa.1960.0012.

[128] Ashcroft IA, Derby B. Adhesion testing of glass-ceramic thick films on metal substrates. J Mater Sci 1993;28:2989–98. doi:10.1007/BF00354704.

[129] Laugier MT. Adhesion of TiC and TiN coatings prepared by chemical vapour deposition on WC-Co-based cemented carbides. J Mater Sci 1986;21:2269–72. doi:10.1007/BF01114266.

[130] Laugier MT. An energy approach to the adhesion of coatings using the scratch test. Thin Solid Films 1984;117:243–9. doi:10.1016/0040-6090(84)90354-7.

[131] Burnett PJ, Rickerby DS. The scratch adhesion test: An elastic-plastic indentation analysis. Thin Solid Films 1988;157:233–54. doi:10.1016/0040-6090(88)90006-5.

[132] Bull SJ, Rickerby DS, Matthews A, Leyland A, Pace AR, Valli J. The use of scratch adhesion testing for the determination of interfacial adhesion: The importance of frictional drag. Surf Coatings Technol 1988;36:503–17. doi:10.1016/0257-8972(88)90178-8.

[133] Evans HE. Stress effects in high temperature oxidation of metals. Int Mater Rev 1995;40:1–40. doi:10.1179/imr.1995.40.1.1.

[134] Wang JS, Evans AG. Measurement and analysis of buckling and buckle propagation in compressed oxide layers on superalloy substrates. Acta Mater 1998;46:4993–5005. doi:10.1016/S1359-6454(98)00172-4.

[135] Hutchinson JW, Thouless MD, Liniger EG. Growth and configurational stability of circular, buckling-driven film delaminations. Acta Metall Mater 1992;40:295–308. doi:10.1016/0956-7151(92)90304-W.

[136] Marshall DB, Evans AG. Measurement of adherence of residually stressed thin films by indentation. I. Mechanics of interface delamination. J Appl Phys 1984;56:2632–8. doi:10.1063/1.333794.

[137] Rosenfeld LG, Ritter JE, Lardner TJ, Lin MR. Use of the microindentation technique for determining interfacial fracture energy. J Appl Phys 1990;67:3291–6. doi:10.1063/1.345363.

[138] Thouless MD. An analysis of spalling in the microscratch test. Eng Fract Mech 1998;61:75–81. doi:10.1016/S0013-7944(98)00049-6.

[139] Attar F, Johannesson T. Adhesion evaluation of thin ceramic coatings on tool steel using the scratch testing technique. Surf Coatings Technol 1996;78:87–102. doi:10.1016/0257-8972(94)02396-4.

[140] Wheeler JM, Michler J. Invited article: Indenter materials for high temperature nanoindentation. Rev Sci Instrum 2013;84. doi:10.1063/1.4824710.

[141] KOESTER RD, MOAK DP. Hot Hardness of Selected Borides, Oxides, and Carbides to 1900°C. J Am Ceram Soc 1967;50:290–6. doi:10.1111/j.1151-2916.1967.tb15112.x.

APPENDIX A

NANOINDENTATION OF NI-ALLOYS

Nanoindentation experiments were performed using the load curve shown in Fig. A-1a. The holding time of 30s at the peak load was chosen to identify the creep behavior of the material and another holding time of 60s at 10% of the peak load during unloading was utilized to study the thermal drift of the samples at different experimental conditions. A maximum or peak force of 1mN was used, and the average result is based on four indentations across different random sites. A standardized testing protocol was followed for all experiments. After each high-temperature experiment, the tip area function was recalculated by tip calibration to ensure correct measurement of mechanical properties. After the stage and sample reach the desired temperature, the setup was kept inactive for one hour to achieve thermal stability and a lower drift rate.

Fig. A-1b-c shows typical indentation curves at different temperatures. The associated estimated hardness and elastic modulus of Inconel 617 as a function of temperature are shown in Fig. A-1d-e. Both hardness and reduced modulus show a decreasing trend with increasing temperature. The drift rate decreased continuously at each experiment as the tip was in contact with the sample for a longer duration. The observation at both holding times (at peak and then 10% of the peak) clearly shows the competition between thermal drift and creep. Fig. A-1d-e shows the hardness and elastic modulus is calculated from Oliver-Pharr method and applying Poisson's ratio 0.3 for Inconel 617. Both elastic modulus and hardness shows a decreasing trend with increase of temperature. Significant drop in these values is observed at 600 ^{o}C which implies that at a critical temperature the softening rate of the alloy increases sharply.

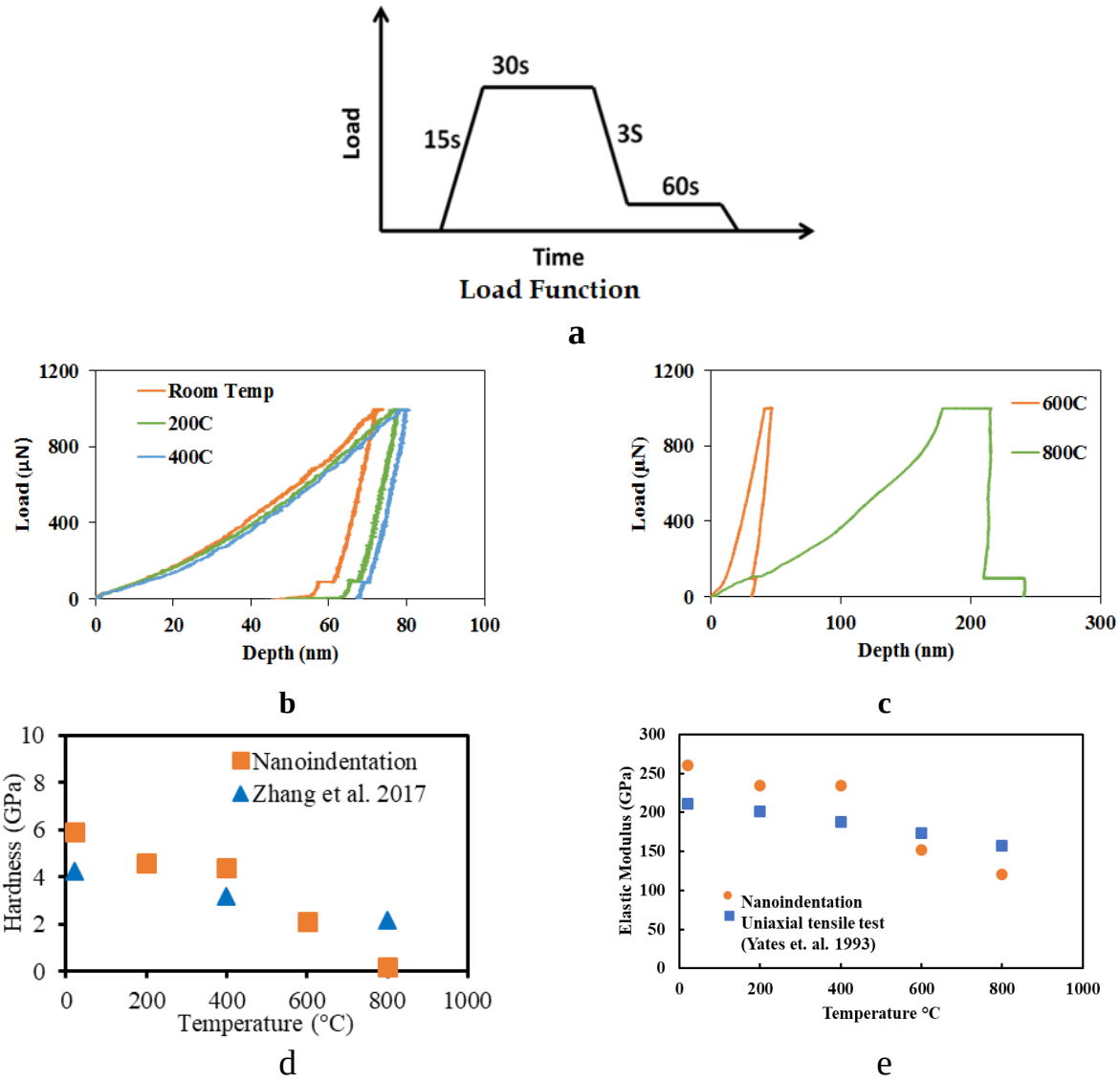

Fig. A-1 (a) Load curve used for HT nanoindentation; Load control indentation curve on Inconel 617 at different temperatures using (b) Diamond tip, (c) Sapphire tip; (d) Hardness and (e) Elastic Modulus of Inconel 617 as a function of temperature

The holding time at peak load is used to identify the creep behavior of the material and another holding time during unloading is used to study the thermal drift of the samples at different experimental conditions. The peak force of 6mN and 1mN is used and the average result is based on four indentations across different sites. A standardized testing protocol is followed for all experiments. After each high temperature experiment the tip area function has been recalculated by tip calibration to ensure correct measurement of mechanical properties. The experiments on

Inconel 617 at high temperature for both 6mN and 1mN load show stable and consistent hardness and reduced modulus results (Fig. A-2a and b). The shallow indentation (70nm) for lower load has lower reduced modulus and higher hardness compared with high load deeper indentation (210nm). The drift rate decreased continuously at each experiment as the tip was in contact with the sample for longer duration. The SPM images in Fig. A-3. show the pile up behavior of the alloy at different temperature. The SPM gradient images in Fig. A-3 shows minimum pile up and clear slip lines, especially under higher load.

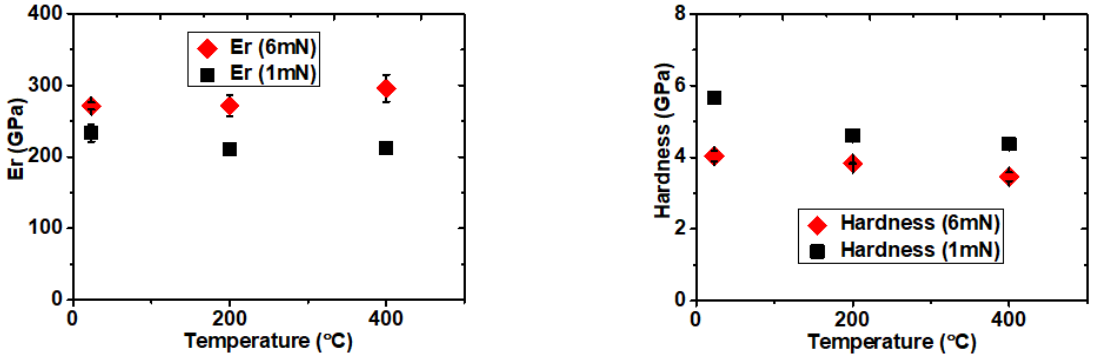

a b

Fig. A-2 Hardness and reduced elastic modulus of Inconel 617

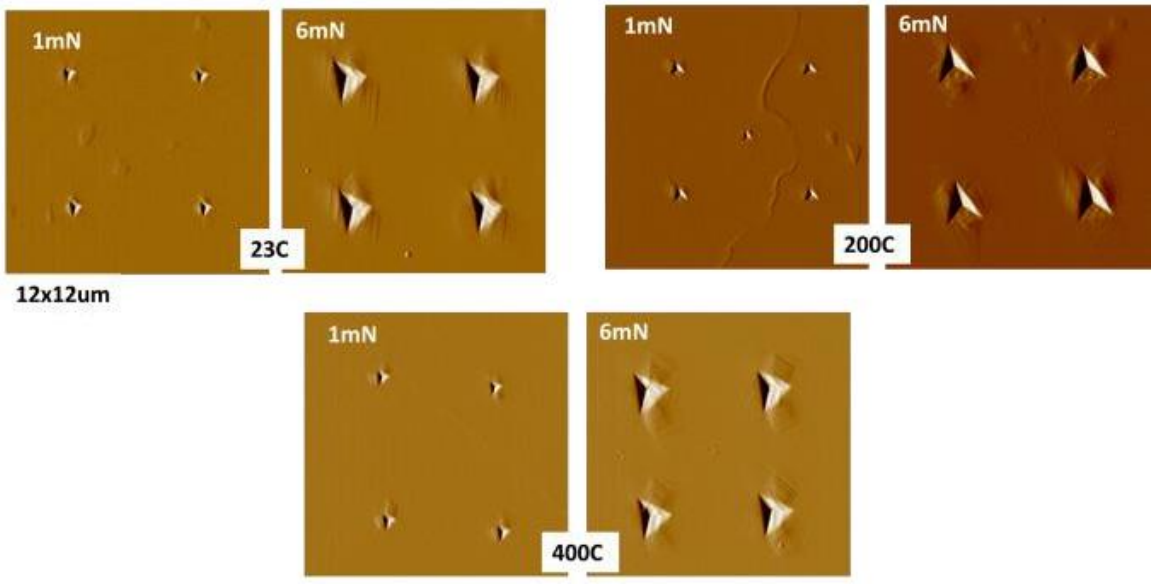

Fig. A-3 SPM images of the indentations performed at different temperatures

The Indentation data on the cross section of the Fig. A-4a shows the RT experimental hardness and elastic modulus of aged Inconel 617 sample. There is a sudden drop in hardness and, to a lesser extent, in elastic modulus when indentations pass the top oxide layer to the bulk material, as expected. Due to high hardness difference between the bulk and the oxide layer, during polishing the cross section, the bulk worn out much faster than the oxide and eventually the oxide layer stays higher than the other region including the Nickel plating. The whitish area in the SPM gradient image indicates the oxide layer in Fig. A-4b.

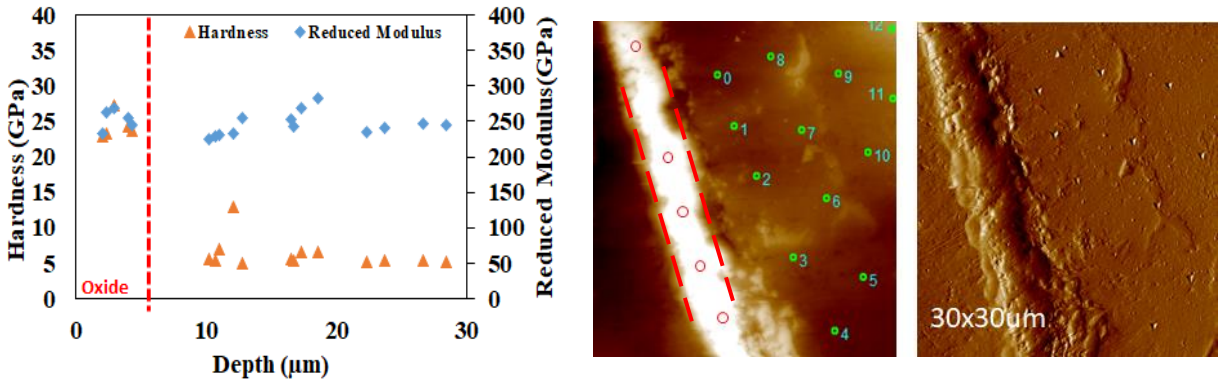

Fig. A-4 (a) Hardness and reduced modulus, (b) SPM images before and after the indentations on the cross section of Inconel 617 samples aged at 950 C for 1 hour. The white area in between the red dash lines in the SPM image is the oxide grown on the surface of the bulk on the right side.

J. H. Westbrook proposed an equation to quantify the softening rate and identifying the critical temperature from the high temperature hardness values [123]:

$$H = Ae^{-BT}$$

Where H = Hardness in Kg mm^{-2}; T = Test temperature in K; A = constant called intrinsic hardness and B = Softening coefficient or thermal coefficient of hardness. Westbrook plotted ln(H) against temperature in K and showed that there are two separate softening zone by linear curve fitting to eq. 1, suggesting two different deformation mechanisms. Applying the eq. 1, two sets of constants A and B are obtained for these softening zones – Low temperature and high temperature. Fig. A-5 shows the ln(H) against temperature as mentioned by Westbrook for Inconel 617 along with precipitation hardened Inconel 718 and Co-based super alloy T-800. The values of transition

temperature and the constants for Inconel 617 are summarized in Table A-1 along with the data of Inconel 718 and T-800 from reference[124]. Inconel 617 exhibits the lowest transition temperature in the comparison whereas the intrinsic hardness at low temperature (A_I) is much higher than Inconel 718 and close to T-800. The softening rate (B_{II}) at high temperature zone is more negative than the comparing materials but it is still two order of magnitude positive than the pure metals[125].

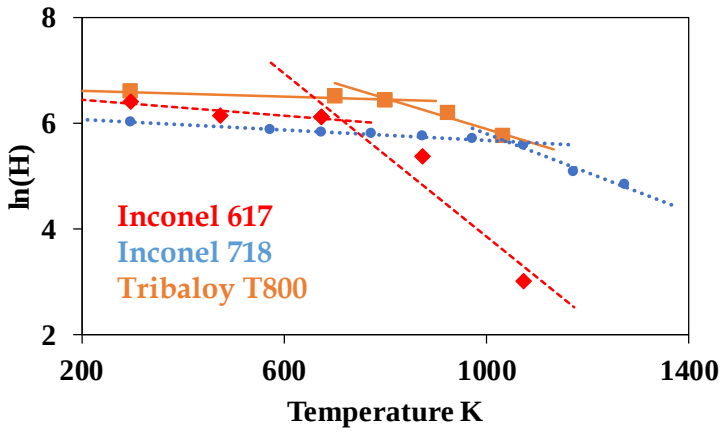

Fig. A-5 Hardness in log scale plotted against temperature for Inconel 617, Inconel 718 and T-800.

Table A-1 Transition temperature, intrinsic hardness, and softening constants from eq. 1 as per Westbrook.

Material	Transition Temperature T_T (K)	Below T_T		Above T_T	
		A_I	B_I	A_{II}	B_{II}
Inconel 617	717	725	-8.00E-04	106937	-7.70E-03
Inconel 718	1037	487	−5.29E−4	13778	−3.74E−3
T-800	818	791	−2.84E−4	8041	−3.12E−3

APPENDIX B

NANOSCRATCH BEHAVIOR OF NI-ALLOYS

Nanoscratch experiments are conducted using the same commercial nanoindenter for nanoindentation test. A conospherical shaped diamond probe with radius 870 nm was used to conduct the nanoscratch tests at room temperature while for all high temperature nanoscratch test, a conospherical shaped diamond probe with radius 5 μm was used. The system has the capability of supplying gas in the chamber to create the required inert environment. All the high temperature nanoscratch tests were performed under the cover of 95% Argon and 5% Hydrogen gas mixture to protect the diamond tip at high temperatures. For nanoscratch testing, the virgin alloy samples were prepared to have roughness values of 0.03 μm to 0.04 μm achieved through mechanical polishing. The samples were then cleaned using acetone in an ultrasonic cleaner and dried before placing inside the nanoindenter. The aged samples were prepared in a vacuum furnace at high temperature (Inconel 617 at 950 °C and 800HT at 750 °C) under He gas environment for 100 hours. The roughness of the samples surface was measured using both AFM and stylus profiler and found to be around 0.45 μm for Inconel 617 aged sample and 0.77 μm for 800HT aged samples (see Figs. B-1a,b). Due to the observed high roughness of the samples surface, it is generally better to use higher load ranges and probes with larger radius. Using SEM imaging shown in Figs. B-1c,d, the oxide layer thickness of the sample after 100hr of aging in He was found to be around 10 μm for Inconel 617 and 8 μm for 800HT.

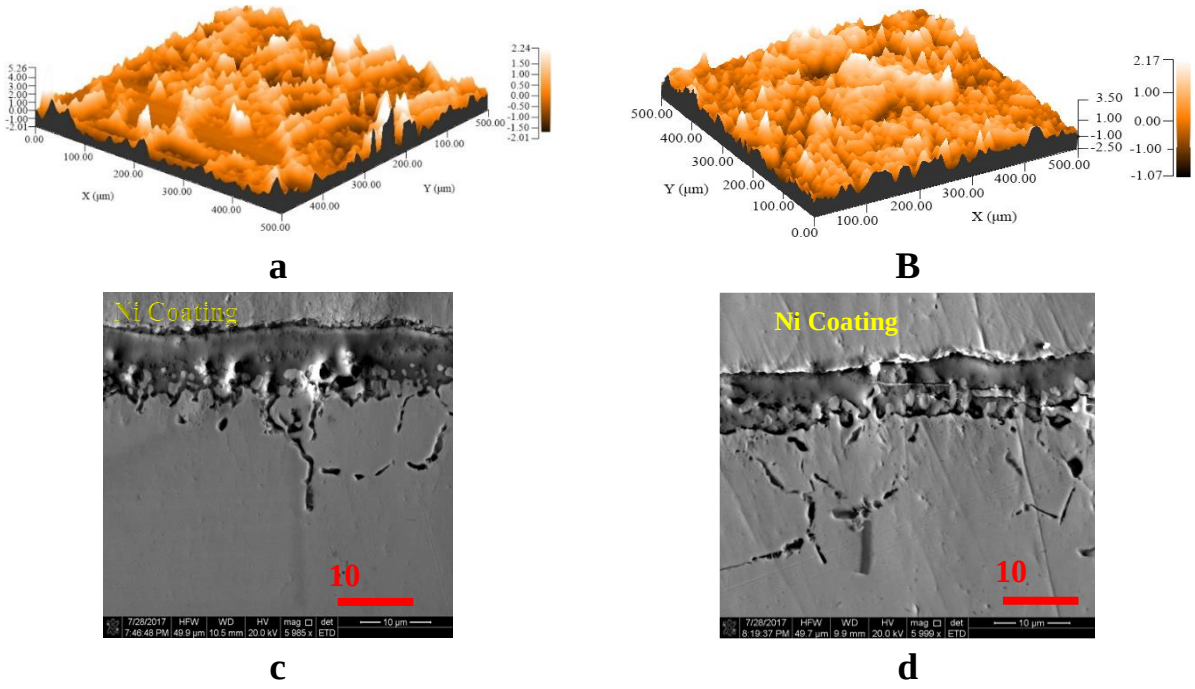

Fig. B-1 3D surface topography image of (a) Aged Inconel 617 (b) Aged 800HT. All dimensions are given in micron; Cross section SEM image of (c) Aged Inconel 617 and (d) Aged 800HT.

For room temperature experiments, the tests were performed with two different sets of constant normal loads – Low load (100 – 500 µN) and High load (1 – 5 mN). The low load normal load set were repeated with varying sliding velocities in the range of 0.3 – 1.2 µm/s to study the effect of sliding velocity and potential frictional heating. The nanoscratch test done at high temperature were limited to only lower normal load set due to higher penetration depth. All scratch lengths were kept constant at 10 µm. The normal force, friction force, normal displacement and lateral displacement were recorded during the scratch tests. A trace and retrace scan were performed using low load of 2 µN before and after the scratch test to be able to do tilt correction and calculate the residual depth due to the scratch. The overall drift rate including the thermal drift was recorded and was kept less than 0.5 nm/s. The system also has a scanning probe microscopy (SPM) capability through which in-situ surface topography can be measured using a low contact force of 2 µN. Table B-1 summarizes the experimental conditions and test parameters.

Table B-1
Experimental conditions for the nanoscratch experiments

Sample	Temperature (ºC)	Normal force (µN)	Sliding velocity (m/s)
Virgin Inc 617, Virgin 800HT, Aged Inc 617, Aged 800HT	25	100 – 500 1000 - 5000	0.3, 0.4, 0.6, 0.85, 1.2
Aged Inc 617, Aged 800HT	200, 400	100 - 500	0.3

B.1. Experimental results

B.1.1. Load dependency of friction

The frictional behavior for both virgin and aged samples was studied at different loads in the range of 100 – 500 µN with constant sliding velocity of 0.3 µm/s. The variation of average friction coefficient as a function of normal load are shown in Fig. B-2 where the error bars designate the standard deviation obtained from three independent measurements. The micro-friction of Inconel 617 (0.13 – 0.23) is slightly lower than 800HT (0.15 – 0.26) in all load conditions. For both materials, the COF shows an increasing trend with higher normal load. The increase in friction force with normal load is an indicator of the larger plowing (deformation) part of friction coefficient [126]. In addition, here, the nanoscratch resistance of the surfaces can be evaluated quantitatively by observing the differences in the residual scratch depth in Fig. B-3. At lower load of 500 µN the residual depth on virgin 800HT is slightly higher than on virgin Inconel 617 while significant higher scratch resistance of Inconel 617 can be seen for the aged samples with the oxide layers on top. Since no considerable residual scratch depth was observed on the aged samples using low load (500 µN), higher load (e.g., 5 mN) was used for the aged samples. As shown in Fig. B-2c,d, the residual scratch depth on the oxide layer of Inconel 617 is around 179 nm whereas on aged 800HT is around 717 nm.

It should be mentioned that the COF reported here were calculated as an average of entire scratch scan length, although the maximum COF during the scratch can be much higher. At high load of

5mN, some of the scratch experiments was abandoned in midway as it crossed the maximum limit of lateral force and normal displacement of the system.

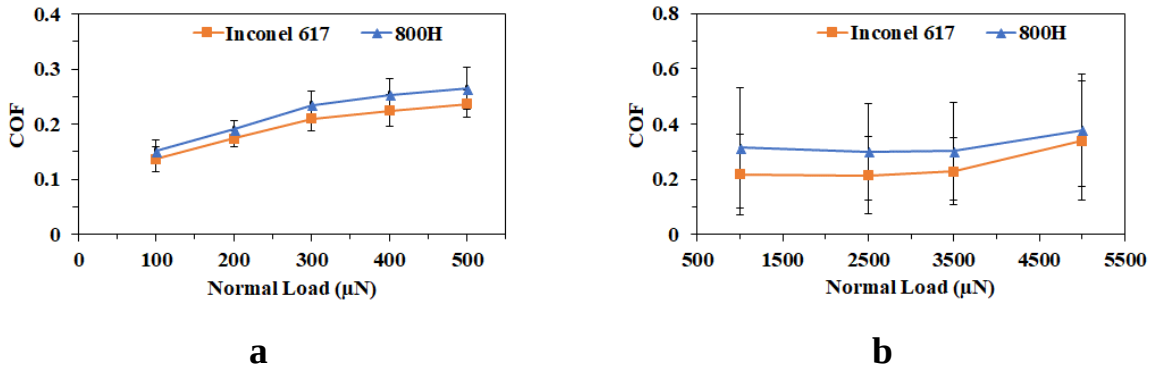

Fig. B-2 Variation of COF with normal load at sliding velocity of 0.3 µm/s on (a) virgin (b) aged samples.

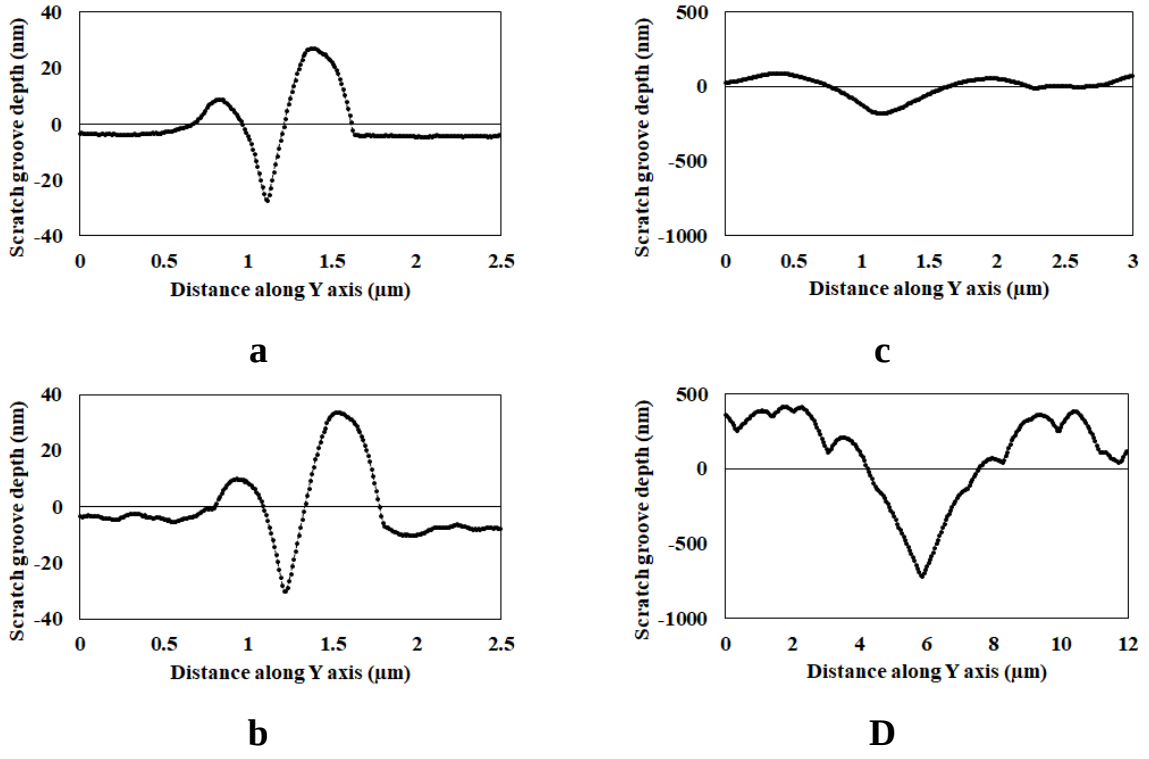

Fig. B-3 Residual scratch groove depth under normal load of 500 µN on virgin samples (a) Inconel 617 (b) 800HT; Residual scratch groove depth under normal load of 5000 µN on aged samples (c) Inconel 617 (d) 800HT.

B.1.2. Sliding velocity dependence of friction

To investigate the effect of sliding velocity and potential associated frictional heating, scratch experiments were performed at different sliding velocity and at constant normal load. Fig. B-4a depicts the variation of COF with varying sliding velocity in the range of 0.3 – 1.2 µm/s at a constant normal load of 500 µN. accordingly, Fig. B-4b shows the SPM image of the residual scratches of the experiments. Both alloys show no significant dependence of COF on sliding velocity.

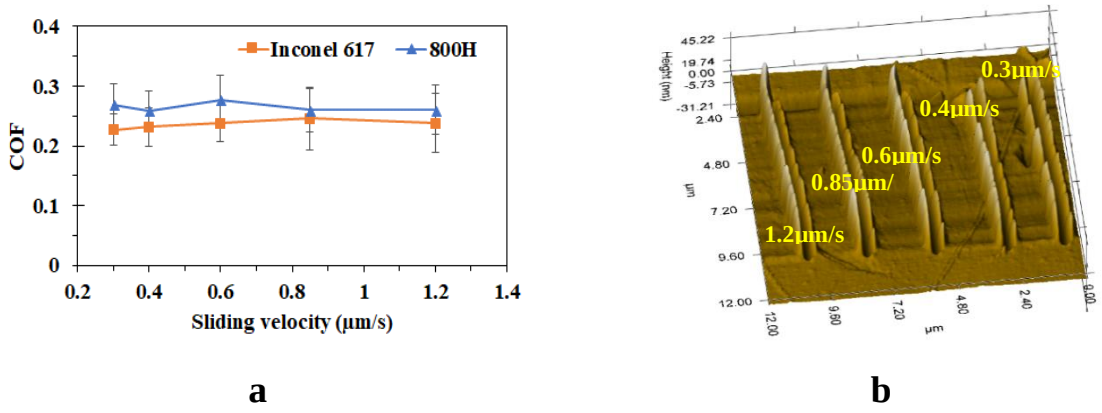

a **b**

Fig. B-4 (a) Variation of COF with sliding velocity at normal load of 500µN on polished virgin samples. (b) SPM image of residual scratches on Inconel 617.

B.1.3. Effect of temperature on friction

High temperature frictional behavior of the aged samples for both materials was observed by conducting HT nanoscratch experiment at 200^{o}C and 400^{o}C with varying normal load in the range of 100 – 500 µN. Depicted in Fig. B-5 is the COF of the oxide layers at HT for aged Inconel 617 and 800HT. For both materials and at all normal loads, COF increases with increased temperature which can be attributed to the effect of combined increased adhesion and more importantly the plowing component due to higher scratch depth on softer oxide layer at higher temperature. On the other hand, both material at 200^{o}C and 400^{o}C shows a lower friction at the load of 500 µN. This variation can also be explained by the dominance of adhesion component of friction at this

load [71]. At high temperature, oxide layer of the aged Inconel 617 shows better frictional behavior and scratch resistance property as compared to 800HT. At 200ºC, COF for Inconel 617 is in between 0.09 and 0.2 whereas for 800HT it is in the range of 0.23 – 0.37. For 400ºC, COF is in the range of 0.29 to 0.38 and 0.37 – 0.51 for Inconel 617 and 800HT respectively. This, in fact, is aligned with our previous findings for high temperature macro-friction of Inconel 617 and 800HT in chapter III & IV. In addition, higher resistance of Inconel 617 is evident as at 400ºC under normal load of 500 µN, the residual depth on the oxide of Inconel 617 is around 763 nm, nearly 30% lower than that of 800HT (residual depth of 1063 nm).

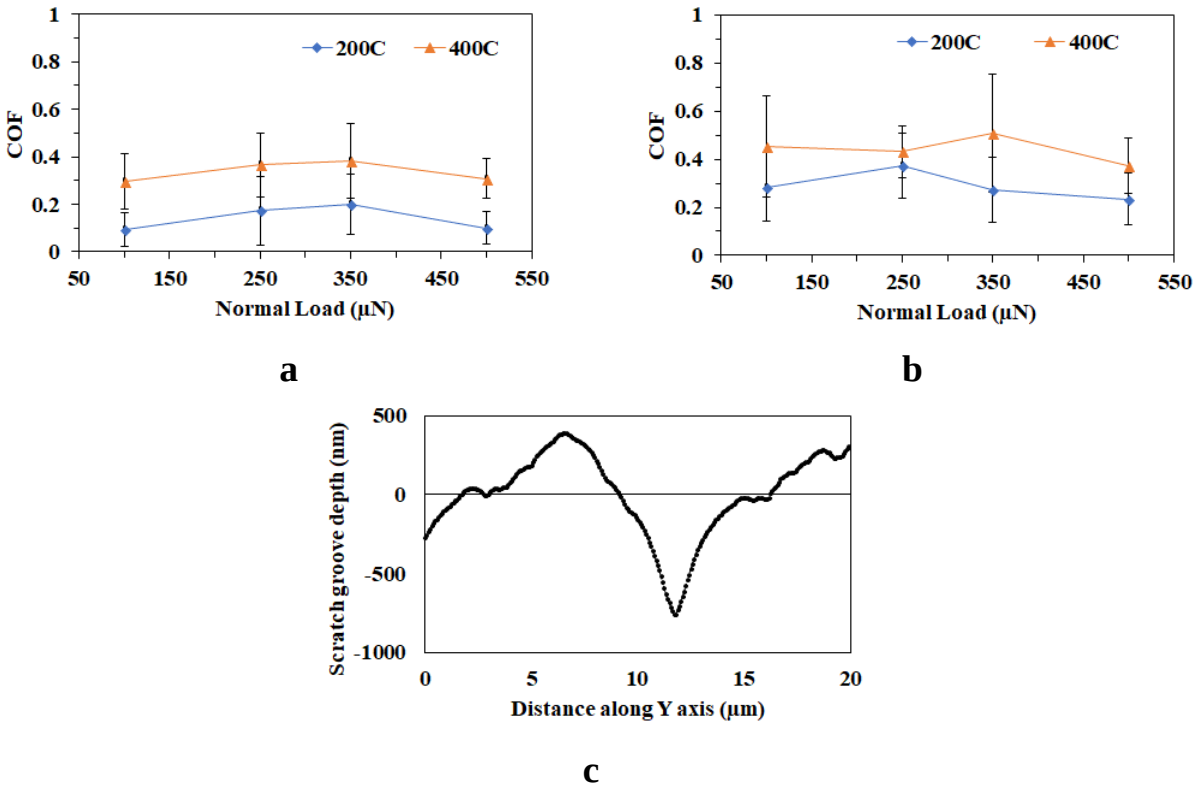

Fig. B-5 Variation of COF with Normal load at elevated temperature at sliding velocity of 0.2 µm/s on (a) Aged Inconel 617 (b) Aged 800HT; (c) Residual scratch groove depth under normal load of 500 µN at 400ºC on aged Inconel 617.

B.2. Nano/micro-scratch summary

- Nanoscratch experiments is conducted with a 870 nm radius conospherical diamond tip at room temperature on virgin samples at high temperature in He. Inconel 617 show lower COF as compared to 800HT.
- HT nanoscratch on the oxidized aged sample is performed with a 5 μm radius conospherical tip under Argon gas environment. Similar to virgin samples, Inconel 617 show lower COF as compared to 800HT.
- None of the material shows significant dependence on sliding velocity at room temperature.
- Although virgin samples show almost identical scratch resistance, the oxide layer on Inconel 617 exhibits much better scratch resistance over 800HT.

Numerical results show that for the current loading condition and geometry the critical stresses remain in the oxide layer with the onset of yielding around 100 nm below the surface. Much higher stresses are observed for the oxide as compared to the virgin sample due to its higher yield strength and elastic modulus.

APPENDIX C

ADHESION AND SHEAR STRENGTH MEASUREMENT

Since the scratch experiments are complex and difficult to interpret based on the complex stress-strain field, failure mode difference and mechanical behavior of film/substrate system is regarded as semi-quantitative comparative investigative technique. Benjamin-Weaver and Ashcroft-Derby [127,128] proposed the relation of interfacial shear strength based on the theory of fully plastic indentation and critical shear force to remove the coating by

$$\tau_c = \sqrt{\frac{HP_c}{\pi\left(r^2 - \frac{P_c}{\pi H}\right)}} \tag{10}$$

where τ_c is the interfacial shear strength (between the film and substrate) in terms of hardness *H*, critical applied load P_c and radius of the probe *r*. This model is applicable for the plastically deformed substrates. Griffith energy balance approach had been used by several models to investigate the interfacial work of adhesion during scratch, which is a measure of chemical bonding between the coating/substrate system. Laugier [129,130] developed a model based on purely elastic analysis of the compressive stress in the coating as a function of the internal stress and applied stresses. The contact radius calculation in this model was performed assuming elastic Hertzian contact between two bodies. Laugier considered local stress σ_c as

$$\sigma_c = \sigma_a + \sigma_{in} \tag{11}$$

where σ_{in} is the internal stress of the coating that could be compressive or tensile which may develop from thermal residual stress, and σ_a is the applied stress developed by the sliding indenter probe, which is expressed as

$$\sigma_a = \frac{2P_c}{\pi d_c^2}\left[(4+\nu_s)\frac{3\pi\mu}{8} - (1-2\nu_s)\right] \tag{12}$$

where σ_a can be expressed as adhesion strength, d_c is the scratch width at the critical load P_c, and μ is the COF between the indenter and the coating. The relation between the work of adhesion and the stored elastic energy in the coating ahead of the indenter is given by [130]

$$W = \frac{\sigma_c^2}{2E} t \tag{13}$$

Burnett-Rickerby [131] and Bull-Rickerby [132] developed another model relating the adhesion energy to the compressive failure modes, buckling and spallation by wedging, which is more related to a hard coating on a soft substrate. The classical buckling theory by Timoshenko was used to develop the buckle failure theory for oxide scales [133–135]. The wedge spallation failure occurs when the compressive shear crack generates through the coating thickness ahead of the indenter and sliding forward movement of the indenter probe propagates the crack, lifts up the coating and a large region ahead of the indenter detaches during the failure of the coating due to the tensile bending stress generated. During this failure, the indenter probe has a significant drop in vertical displacement.

Several models were developed to relate the critical indentation load and interfacial toughness and residual elastic stress [136–138]. The Bull-Rickerby model is based on the elastic-plastic indentation theory considering three components responsible for the coating failure: elastic-plastic indentation stress, tangential frictional stress and residual internal stress. Based on this model, the local compressive stress in the coating in front of the probe generates the critical tensile stress normal to the interface causing the coating to detach. The equation relating the critical load to the work of adhesion is:

$$W = \mu_c^2 P_c^2 . \frac{\nu_f^2 t}{2A^2 E_f} \tag{14}$$

where μ_c is the COF at the critical load; ν_c and E_f are the Poisson's ratio and Young's modulus of the coating; A is the cross-sectional area of the track calculated using the track with d_c measured at the critical load P_c using the indenter radius R:

$$A = R^2 \sin^{-1}\left(\frac{d_c}{2R}\right) - \frac{d_c}{2}\left[R^2 - \left(\frac{d_c}{2}\right)^2\right]^{1/2} \quad (15)$$

This model is later modified by including a combination of shear and tensile stresses in the coating interface ahead of the indenter by Attar and Johanneson [139]:

$$W = \left(\frac{\nu_c \mu_c P_c}{d_c}\right)^2 \cdot \frac{1}{2E_f t} \quad (16)$$

In this model, it is assumed that the friction force acts on the cross section of the coating while simultaneously plastically deforming the substrate. The area under the stress is calculated as $\boldsymbol{A = td}$.

APPENDIX D

HIGH TEMPERATURE PULL-OFF FORCE MEASUREMENT OF INCONEL 617

The high temperature friction behavior of any material is highly impacted by the adhesion force acting between the contacting materials. When two solids approach each other, they experience an attractive force, *i.e.*, van der waals force as well as short-range repulsive forces. When these two solids are in contact and pressed with higher force, the interface can create metallic bonding and the two metals can become welded. This process can be further expedited in the presence of high temperature. Pull-off force in defined as the force required to separate two surfaces in contact. This pull-off force can be very high due to the presence of high temperature.

To understand the high friction behavior of Inconel 617 at high temperature, the adhesion behavior at high temperature was investigated using the instrumented nanoindenter. The capacitive force sensor of the indenter is capable of measuring the forces in the μN range. A diamond conospherical probe with 5μm radius, as shown in Fig. D-1b was used in this adhesion experiments. At the stable temperature, the tip was pushed in contact to the polished sample surface with very low force of 5 μN very slowly. When the tip gets very close to the surface it gets snapped to the surface due to the adhesion force, which is called the Pull-in force. After it reaches the peak load of 5 μN, the probe is retracted again very slowly from the surface. During the tip removal from the surface, due to the high adhesion between the probe material and the sample, it requires much higher force to detach the tip. This is showed as negative force in the data acquisition as the sensor feels the tension. As shown in Fig. D-1, the pull of force increases with the temperature.

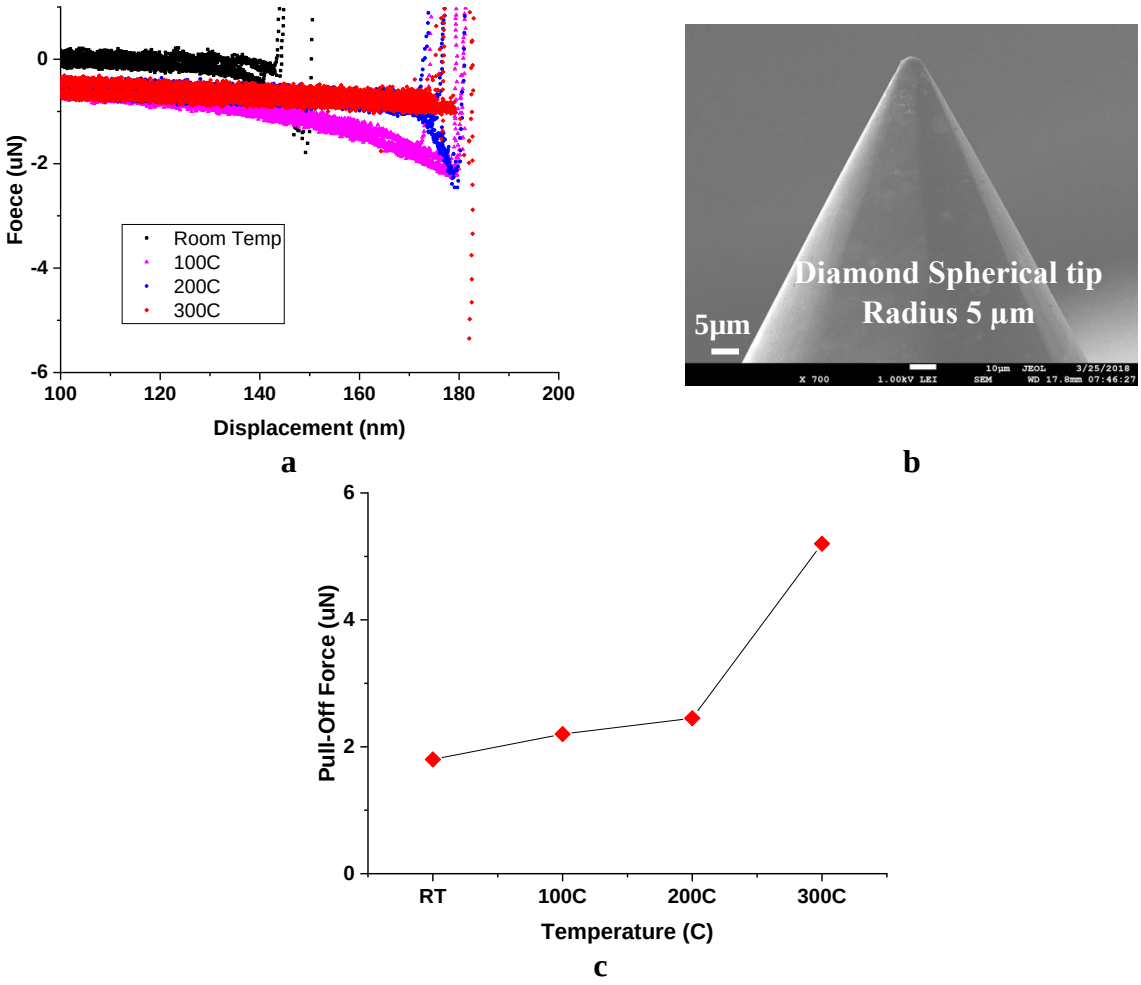

Fig. D-1 (a) In-situ Pull of force measurement at different temperature; (b) Diamond conospherical probe; (a) Pull-off force data against temperature.

The data in Fig. D-1 confirms the rise in adhesion force with temperature. But this data is between Inconel 617 and diamond. To identify the adhesion force between two bodies of Inconel 617, a spherical probe with 350 µm radius shown in Fig. D-2a was fabricated. Higher tip radius was chosen to eliminate the probability of contacting other surfaces than the spherical portion. But unfortunately, this probe can only be used in room temperature as the probe was installed on a

polymeric base. The room temperature adhesion experiments, as shown in Fig. D-2b, resulted in very high pull-off force of almost 30 μN.

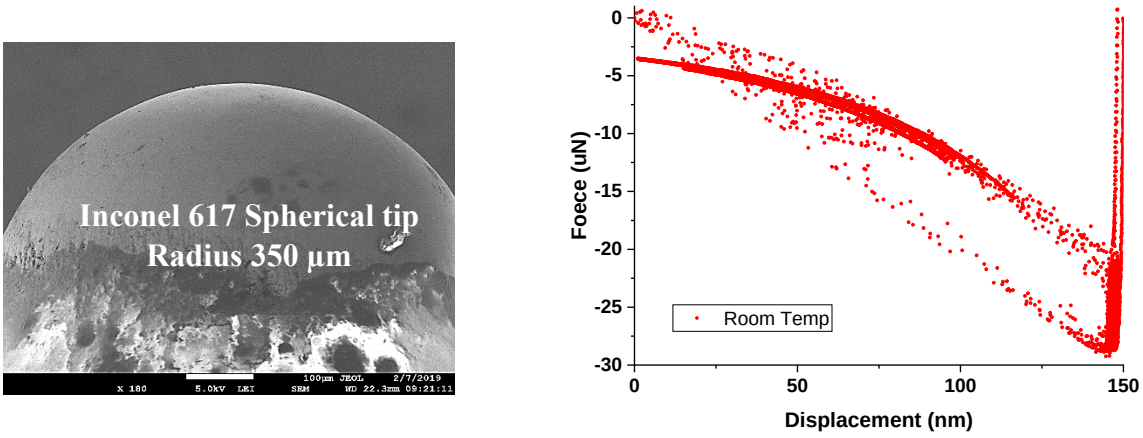

a **b**

Fig. D-2 (a) Inconel 617 spherical probe; (b) In-situ Pull of force measurement at RT.

These experiments need to be further extended to high temperature condition and then correlated with the DMT/JKR model along with rough surface contact model.

APPENDIX E

HIGH TEMPERATURE INDENTATION PROBE MATERIAL

Selecting the correct probe material for instrumented indentation system is high ly important, especially when it involves high temperature. Ideally, the indenter material should be a minimum of 20% higher hardness than the sample to generate plastic deformation. In order to avoid rapid blunting or failure of a sharp indenter tip, the indenter material should be significantly (>100%–1000%) harder than the sample [140]. There are several materials those are currently in use for high temperature indentations up to 800 °C, but the complexity rises exponentially when the sample material happens to be highly reactive. Diamond, cBN, Al_2O_3 and WC have been widely used for high temperature indentations, while all of them having several pros and cons individually. Polycrystalline, sintered boride ceramics such as ZrB2, and HfB2 have been used previously as high temperature indenter materials to good effect [141]. To further study the effectiveness of the materials as probe material, their high temperature property has been studied. The samples were provided by Dr. Gregory E. Hilmas from Missouri University of Science and Technology.

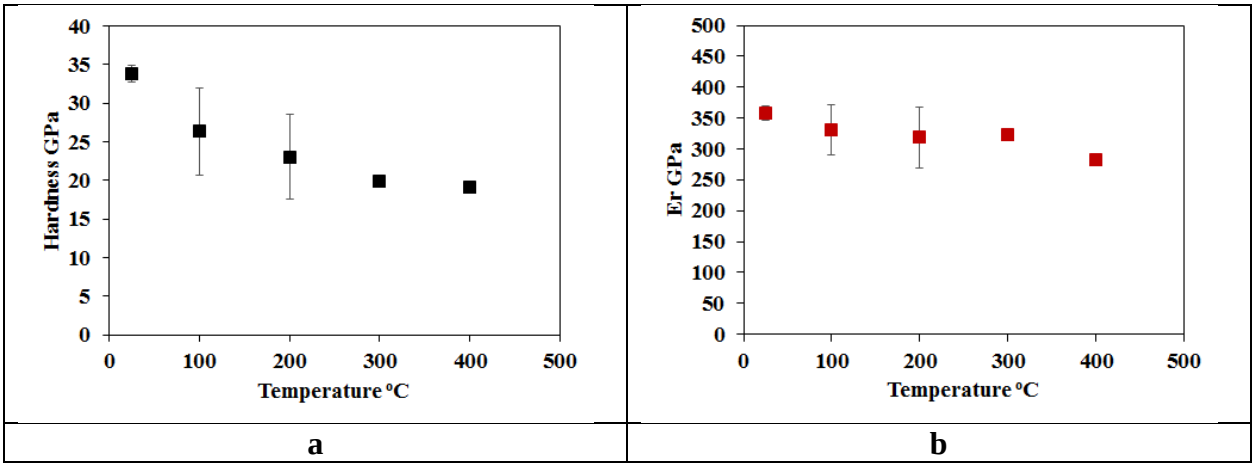

a **b**

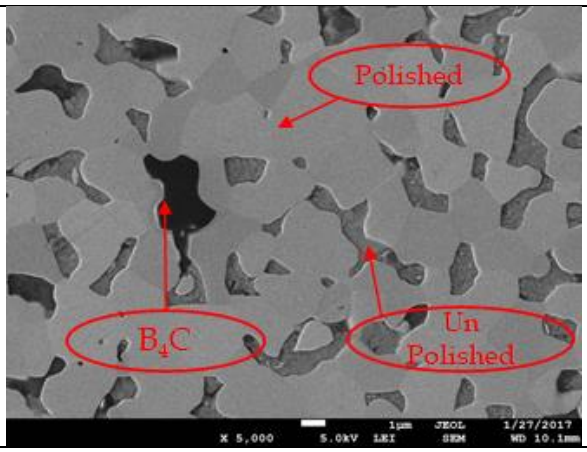

c

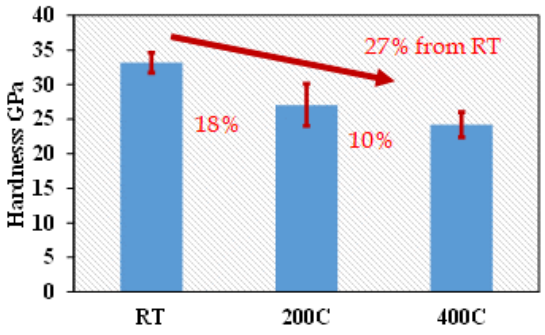

d

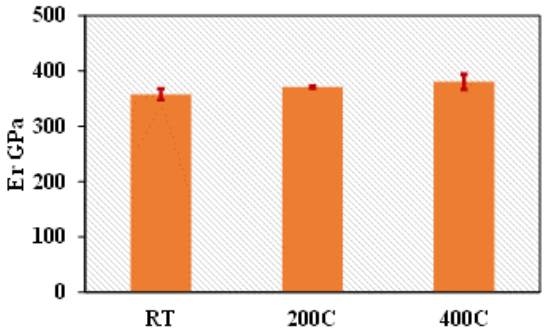

e

Fig. E-1 Nanoindentation properties of HfB_2 at different temperature (a) Hardness, (b) reduced modulus; (c)SEM image of the polished surface of HfB2; Nanoindentation properties of ZrB_2 at different temperature (d) Hardness, (e) reduced modulus

The partial study data shown in Fig. E-1, shows the hardness and elastic modulus of HfB_2 and ZrB_2 up to 400 °C. These indentations were performed using diamond Berkovich probe under Ar-5%H_2 cover gas. For HfB2 in Fig. E-1a and b, the hardness shows steep decrease from around 35 GPa at room temperature to 20 GPa at 400 °C. The reduced modulus stayed in between 300 GPa and 350 GPa in the experimented temperature range. The SEM image in Fig. E-1c shows that the HfB2 surface has lots of unpolished areas, which indicates the presence of cavity or porosity in the structure. It also shows the presence of Boron in the structure. On the other hand, for ZrB_2, Fig. E-1d shows the similar decreasing trend in hardness, but slightly higher hardness retention at 400 °C than HfB_2 is observed. The reduced modulus in Fig. E1e, remains in the range of 350 GPa and 400 GPa.

This study needs to be further extended to higher temperature and requires investigating the oxidation and reactivity study with Ni based super alloys. Silicon nitride is another material of interest that can be useful in case of indenting Ni-based super alloys at high temperature.